Università degli Studi di Milano Bicocca
Dipartimento di Fisica G. Occhialini

Corso di Dottorato in Fisica e Astronomia
Ciclo XXVI

X-ray absorption in Active Galactic Nuclei

Tesi di Dottorato di

Elena Marchese

Tutor:

Monica Colpi

Valentina Braito

Roberto Della Ceca

preparata presso INAF-Osservatorio Astronomico di Brera

Data Dissertazione: 28 Settembre 2015

Anno Accademico 2013-2014

“ Far away there in the sunshine are my highest aspirations.
I may not reach them, but I can look up and see their beauty, believe in them, and try to follow where they lead.”

Louisa May Alcott

Dedico questa tesi a mio padre.

List of Figures

1.1 Composite quasar spectrum . . . 11
1.2 Example of Seyfert 1s and Seyfert 2s spectra . . . 13
1.3 Baldwin diagnostic diagram . . . 14
1.4 Example of FRI and FRII radio galaxies . . . 17
1.5 X-ray spectrum of an AGN, for different column densities . . . 18
1.6 Comparison of the optical spectra of a Sy2, NLS1 and a Sy1 . . . 20
1.7 Example of the optical spectrum of a BL LAC source . . . 21
1.8 Unified Model of AGN scheme . . . 26
1.9 NGC 7582: variability of the X-ray spectrum during *Suzaku*monitoring campaign . . . 29
1.10 NGC 1356: variability of the absorption in the X-ray spectrum . . . 30
1.11 High resolution spectrum of the BAL PHL 5200 . . . 31
1.12 Sketch of the Elvis (2000) model . . . 32
1.13 Sketch of the model by Risaliti et al. (2002) to account for X-ray absorption variability in Seyfert 2s . . . 35
1.14 Classification of AGN in the different unified schemes . . . 37

2.1 Typical X-ray spectrum of a type 1 AGN, showing the various spectral components frequently observed together with the average total spectrum. . . 41
2.2 Left panel: first X-ray spectra of the QSO MR 2251-178. Right panel: Incident and emergent spectra obtained using a warm absorber model. . . . 42
2.3 X-ray reflection spectrum from a neutral, constant density illuminated slab. 45
2.4 Model representing the typical X-ray reflection spectrum where the Fe Kα doublet, the Fe Kβ, the Fe K edge and the Compton hump are shown. . . . 47
2.5 Several effects that act on the profile of an emission line. . . . 49
2.6 Left panel: iron line profile produced by an accretion disc around a non spinning (Schwarzschild) black hole, for three different inclination. The region of the disc producing the profile is assumed to extend from $6r_g$ to $30r_g$. Right panel: comparison of the line profiles produced by a Schwarzschild black hole and a Kerr Black hole. . . . 50
2.7 Reflection spectra produced by an ionized slab (with ionization parameter ξ) 52
2.8 Soft X-ray spectrum (below 2 keV) of the QSO MR2251-178, in the form of residuals with respect to the continuum, as observed by the *Chandra* Medium Energy Grating in 2011. . . . 56
2.9 Schematic diagram of a stratified accretion disc wind. . . . 58

3.1 NGC 454 in a 1.75 × 1.75 arcmin image taken from the Hubble Space Telescope. . . . 62
3.2 NGC 454 as seen by ESO 3.6m telescope . . . 63
3.3 Optical spectrum of NGC 454 East. . . . 64

3.4 Optical spectrum of NGC 454 West. 64
3.5 Left panel:XMM-*Newton* EPIC-pn image (0.5–10 keV) with superimposed the *Suzaku* XIS extraction region. Right Panel: *Digital Sky Survey* (DSS) optical image with overlaid the XMM-*Newton* PN 0.5–10 keV contours. . 66
3.6 Ratio between the *Suzaku* and *Swift* data and the unabsorbed power-law model used to fit *Suzaku* data in the 2–5 keV energy range. 70
3.7 Unfolded *Suzaku* spectrum, showing separately the different components of the best-fit model. 73
3.8 Comparison between the *Suzaku* XIS, HXD, *Swift*-BAT and the XMM-*Newton* data showing the dramatic change in the curvature in the 3–6 keV energy range. 74
3.9 Residuals of the XMM-*Newton* data in the range 4–8 keV with respect to the spectral model discussed in section 3.3.2, showing an absorption feature at about 6.7 keV and a spectral curvature in the 5–6 keV range. . . . 75

4.1 Nordic Optical Telescope images of Mrk 348 84
4.2 *Top panel*: *Digital Sky Survey* (DSS) optical image; *Bottom panel*: Optical spectrum of Mrk 348 as reported by Marcha et al. (1996). 85
4.3 XMM-Newton EPIC-pn and Suzaku XIS-0 images of Mrk 348. 89
4.4 Data/model ratio between the *Suzaku* data and a basic continuum model composed of an absorbed and an additional unabsorbed power law, showing the iron line profile. 91
4.5 Data/model ratio in the soft X-ray energy region to the *Suzaku* data and the model including the reflection component (modelled with PEXRAV). 93
4.6 Data/model ratio in the 4–8 keV energy region between the *Suzaku* data and the model including the reflection component (modelled with PEXMON). 94
4.7 Data/model ratio in the 4–8 keV energy region between the *Suzaku* data and the model including an ionised absorber. 96
4.8 *Suzaku* 0.5–70 keV data and best-fit model of Mrk 348. 99
4.9 Comparison between the X-ray emission measured with *Suzaku* in 2008 (black data points) and XMM-*Newton* (red data points) in 2002. 102
4.10 Comparison of the measured values of $N_{\rm H}$in *ASCA* observation (Awaki et al. 2000), in *RXTE* observation during the time lag from 1997 to 2011 (Akylas et al. 2002 and A. Markowitz in prep. for the 2011 data) and the $N_{\rm H}$ measured from *Suzaku* and XMM-*Newton* observations (this work). . . 105

5.1 Possible absorption scenario for the *Suzaku* (upper panel) and XMM-*Newton* (lower panel) observations of NGC 454 113
5.2 Possible absorption scenario for the *Suzaku* (upper panel) and XMM-*Newton* (lower panel) observations of Mrk 348 114

A.1 Diagram of the XMM-*Newton* spacecraft (adapted from the ESA website). 118
A.2 Representation of the path followed by radiation incident on the XMM-*Newton* X-ray telescope mirrors, with the pn camera in focus. 118

A.3 Operating modes of the MOS-CCD cameras. 120
A.4 PSFs for the MOS1, MOS2 and the pn X-ray telescopes, for the same source. 121
A.5 Design of the RGS (Brinkman et al. 1998) 122
A.6 (a) Schematic image of the Suzaku satellite in orbit (b) Side view of Suzaku with the internal structures (Mitsuda et al. 2007). 126
A.7 Scheme of the XIS CCD 127
A.8 XIS2 field, showing the calibration sources. 128
A.9 Picture and scheme of the HXD (Kokubun et al. 2007). 129
A.10 Scheme of the *Swift* observatory (Gehrels et al. 2004). 131
A.11 Scheme of the *Burst Alert Telescope* (BAT) (Gehrels et al. 2004) 132
A.12 Table reporting the main features of the BAT instrument (Barthelmy et al. 2005). 133
A.13 Scheme of the *Swift X-ray Telescope* (XRT, Burrows et al. 2005). 134
A.14 Table reporting the main parameter of *UVOT* (Roming et al. 2005). 135

List of Tables

1.1 Classification scheme of AGN 22

3.1 Summary of the *Suzaku* and XMM-*Newton* parameters for the best-fit models described in Section 3.3.1, and 3.3.2.1. 72
3.2 Summary of the *Suzaku* and XMM-*Newton* parameters using the MYTORUS model described in Section 3.3.3. 80

4.1 Summary of the X-ray emission lines detected in the 2–8 keV spectrum of *Suzaku*. 98
4.2 Model parameters of the two possible scenarios (described in Sec. 4.3 to explain the variation of the Fe Kα emission line intensity between *Suzaku* and XMM-*Newton* observations. 104
4.3 Summary of the *Suzaku* and XMM-*Newton* parameters for the best-fit models described in section 4.2.1.2, and 4.3. 106

A.1 Main characteristics of XMM-*Newton* (see The XMM-*Newton* Users' Handbook for further details). 124
A.2 Comparison of the main XMM-*Newton* properties with the other X-ray missions 125
A.3 Main features of the *Suzaku* spacecraft and instruments 130
A.4 Table with the main features of the *Swift X-ray Telescope* (XRT, Burrows et al. 2005). 134

Contents

1 Introduction **7**
- 1.1 Active Galactic Nuclei . . . 7
- 1.2 Classification . . . 10
  - 1.2.1 Classification based on bolometric luminosity . . . 10
  - 1.2.2 Classification based on optical spectra: Type 1 and Type 2 AGN . . . 12
  - 1.2.3 Classification based on Radio emission properties . . . 15
  - 1.2.4 X-ray classification . . . 16
  - 1.2.5 Subclasses . . . 19
- 1.3 AGN Unification . . . 22
  - 1.3.1 Unification Scheme . . . 23
- 1.4 Insights on AGN structure from X-ray absorption variability . . . 27
- 1.5 Alternative models . . . 31
  - 1.5.1 Elvis (2000) unified scheme . . . 31
  - 1.5.2 Risaliti (2002) model . . . 34
  - 1.5.3 Elitzur (2007) model: torus model and clumpy unification . . . 34
  - 1.5.4 Torus disk-wind model: basis for a “grand unification scheme”? . . . 37

2 The X-ray spectrum **39**
- 2.1 X-ray primary continuum . . . 40
- 2.2 The reprocessed X-ray spectrum . . . 43
  - 2.2.1 Reflection . . . 44
- 2.3 Fluorescence emission lines . . . 46
  - 2.3.1 Ionised reflection . . . 50
- 2.4 X-ray absorption . . . 51
  - 2.4.1 Cold X-ray absorption: Compton-thin and Compton-thick matter . . . 51
- 2.5 Ionised absorption . . . 53
  - 2.5.1 Warm absorbers . . . 53
  - 2.5.2 Ultrafast outflows . . . 55

3 NGC454: a changing look AGN **59**
- 3.1 NGC454 . . . 60
- 3.2 Observations and data Reduction . . . 61
  - 3.2.1 *Suzaku* data . . . 61
  - 3.2.2 The *Swift*-BAT observation . . . 65
  - 3.2.3 The XMM-*Newton* observation . . . 66
- 3.3 Spectral analysis . . . 68
  - 3.3.1 The *Suzaku* and *Swift* broad band X-ray emission . . . 68
  - 3.3.2 Comparison with XMM-*Newton* data . . . 74
  - 3.3.3 A physical interpretation with *MyTorus* model . . . 78
- 3.4 Constraints on the distance of the ionised absorber . . . 80

3.5 Summary and Conclusion 81

4 The variable ionized absorber in the Seyfert 2 Mrk 348 83
4.1 Observations and data reduction 88
4.1.1 *Suzaku* 88
4.1.2 XMM-*Newton* 90
4.2 Spectral analysis 90
4.2.1 Suzaku spectral analysis 90
4.3 XMM-*Newton* data analysis 100
4.3.1 Reflection scenarios 103
4.3.2 $N_{\rm H}$ past observations 104
4.4 Discussion 107
4.5 Conclusions 108

5 Conclusions and Future prospects 111

A XMM-*Newton* and *Suzaku* 117
A.1 The XMM-*Newton* Observatory 117
A.1.1 EPIC 119
A.1.2 RGS 122
A.2 *Suzaku* 126
A.2.1 XIS 126
A.2.2 Hard X-ray Detector (HXD) 128
A.2.3 Background 129
A.3 *Swift Gamma-ray burst observatory* 131
A.3.1 Burst Alert Telescope (BAT) 131
A.3.2 X-Ray Telescope (XRT) 133
A.3.3 Ultraviolet and Optical Telescope (UVOT) 133

B Modelling AGN X-ray spectra 137

Bibliography 143

Rationale

There are nowadays strong evidences that Supermassive Black Holes (SMBH, $M_{BH} = 10^6 - 10^9 M_\odot$) reside at the center of almost all the galaxies in the local Universe. Moreover, studies performed in the last decades proved the existence of a correlation between the mass of the central SMBH and the properties of the host galaxies bulges, such as the bulge luminosity (Kormendy & Richstone 1995), the velocity dispersion (Ferrarese & Merritt 2000; Gebhardt et al. 2000; Tremaine et al. 2002) and the stellar mass (Marconi & Hunt 2003). These correlations clearly suggest that there shall be a co-evolution between the central black hole and the host galaxy. The mechanism connecting the growth of the SMBH (through accretion of matter, during an "active" phase) and the evolution of the host galaxy (in terms of star formation) is still highly debated and it is referred as *feedback*. To assess the nature and possible origin of *feedback* a profound knowledge on the structure, the physical properties (such as the density, ionisation state, geometry, temperature, etc) of the matter in proximity of the central accreting SMBH is needed. The topic on which I focused during my PhD is the X-ray study of Active Galactic Nuclei (AGN), i.e. the central regions of galaxies where the accretion of matter onto a SMBH is taking place. The X-ray energy band is unique to investigate this topic, because it probes the conditions of the innermost emitting/absorbing regions in the active galaxies.

The phenomenon of AGN characterizes about 10-20% of the galaxies in the local Universe. They are among the most energetic sources in the Universe, with bolometric luminosities ranging from 10^{41} to 10^{48} erg s^{-1}, in most cases outshining the luminosities of their own host galaxies. Their spectra cover a wide wavelength range (from radio to TeV energies) showing a continuum and strong emission lines that cannot be produced by stellar processes. The strong variability, often observed on time scales from months to hours suggests that the central emitting regions is compact ($R\sim 10^{13} - 10^{15}$cm). The AGN "family" has been object of several classifications, since the observed properties of these sources are strongly dependent on the energy band in which they have been found and/or studied. One of the most important classifications is based on the properties of the optical spectrum, designating Type 1 AGN the sources showing both broad and narrow emission lines, and Type 2 AGN those displaying only narrow emission lines. According to the most accredited paradigm, known as Unified Model (Antonucci 1993), the central engine producing the observed properties and the different classes of AGN is intrinsically the same, but it is viewed from different angles. Indeed it envisages that the SMBH is surrounded by an anisotropic uniform absorber of gas and dust, with a toroidal geometry that, depending on the orientation with respect to the line of sight, can intercept the radiation emitted from the innermost region. In this scenario the broad emission lines are produced in a region, called Broad Line Region (BLR), very close to the central SMBH ($R<0.1$ pc), whose view is blocked when we look at the AGN along a direction that intercepts the torus. Therefore, along this direction, we only see the narrow emission lines produced in the most external region (Narrow Line

Region, NLR, R~ hundreds of pc) and we designate the source as Type 2 AGN. When instead we observe the source at small angles with respect to the torus axis, then we are able to observe both the BLR and the NLR, and the object is classified as a Type 1 AGN.

Even if on a general level the Unified Model can be retained valid (in the sense that at the origin of the differences among type 1 and type 2 sources there is the anisotropy of the absorbers), recent studies in distinct energy bands suggest the presence of several non-uniform absorbers, located at different distances from the SMBH, and at different physical states. These findings, leading to the formulation of alternative models, are:

- the presence of strongly blueshifted broad absorption lines in the UV spectra of some quasar, indicating the existence of outflowing winds with velocities from thousands of km/s to 0.2c. A model was proposed by Elvis (2000), in which the torus is replaced by a funnel-shaped thin outflow that, observed on different viewing angles, can provide the observed features.

- the almost ubiquitous variability of the X-ray spectral shape of AGN and the time scales on which variability occurs, which suggest that the underlying absorber is clumpy and located at distances compatible with the BLR (Risaliti et al. 2002).

- the dependence of the fraction of obscured AGN on luminosity: it is thought to indicate that the covering factor of the obscuring material is a function of luminosity ("receding torus model", see e.g. Lawrence 1991; Simpson 2005; Lusso et al. 2013)

- the observation that the IR emission of AGN is almost isotropic despite the anisotropic geometry of the torus (e.g. Lutz et al. 2004; Horst et al. 2006), and the coexistence of strongly different temperatures at the same distance from the SMBH: a model in which the torus is clumpy, with a soft-edge density distribution can explain these patterns (Elitzur 2007).

Besides the numerous evidences of the clumpy nature of the absorber, studies performed in the last years showed that the absorbing material is not always neutral. In fact significant amounts of ionised material have been detected in about ~50% of Type 1 AGN, thanks to the features they imprint in the X-ray spectra, i.e. narrow absorption lines from several ionisation states of a high variety of elements (Kaastra et al. 2000; Kaspi et al. 2000; Blustin et al. 2005). These ionised absorbers are called "warm absorbers" (WA) and have outflow velocities in the range $\sim 100 - 1000$ km/s. WAs present many open points still under analysis, such as their origin (accretion disk or putative torus), their kinetic energy and thus their eventual role in the feedback mechanism. A further complexity is provided by the observations of highly ionised absorbers with high outflow velocities ($v_{\rm out} \gtrsim 0.1$ c, Chartas et al. 2002; Chartas, Brandt, & Gallagher 2003; Pounds et al. 2003; Braito et al. 2007; Reeves et al. 2009; Gofford et al. 2011; Lobban et al. 2011; Dauser et al. 2012; Gofford et al. 2013), that have been classified under the name of "ultrafast outflows" (UFOs, Tombesi et al. 2010b). Finally, although the Unified Model of AGN is valid at the zeroth order, according to recent models of AGN-galaxy co-evolution, the presence

of obscuration (hence Type 2 versus Type 1 AGN) may be linked to a specific (initial) phase of the evolution of the AGN. At this stage the central BH is still growing and is surrounded by large amounts of dust, probably related to an intense star-forming activity in the central part of the host galaxy. In this phase its radiation is mostly hidden to our view. In a later phase, the outflows driven by the central AGN expel most of the obscuring material, leaving the active SMBH visible (Type-1 AGN phase). This has been recently used also to explain the relatively high (and increasing) fraction of obscured AGN at high redshift. On a broader extent, it may be related to a higher fraction of mergers at high redshift (Ryan et al. 2008).

Among the most useful "tools" to test the size, structure and composition of the circumnuclear medium there is the observation of absorption variability in the X-ray spectra of AGN. One of the difficulties of this kind of studies is disentangling if the spectral changes are a result of an intrinsic variation of the primary emission or of the absorbing medium or both. Once that a variability of the continuum can be excluded, the time scales on which absorption variability occurs can provide some constraints on the size and the distance of the obscuring clouds from the central SMBH (Ballo et al. 2015). The most extreme cases of AGN showing absorption variability have been classified as "changing look" AGN, i.e sources that, observed in different epochs, are found to vary from a Compton-thin state ($N_{\rm H} < 10^{24}{\rm cm}^{-2}$) to a Compton-thick state ($N_{\rm H} \gtrsim 10^{24}{\rm cm}^{-2}$). Among these sources the best examples are NGC 1365 (Risaliti et al. 2005, 2007, 2009; Risaliti et al. 2009), NGC 4388 (Elvis et al. 2004), NGC 7674 (Bianchi et al. 2005), NGC 4151 (Puccetti et al. 2007), NGC 7582 (Bianchi et al. 2009), UGC 4203 (Risaliti et al. 2010), NGC4051 (Uttley et al. 2004; Lobban et al. 2011) and 1H 0419-577 (Pounds et al. 2004).
Two different approaches can be carried on for testing the numerous models for the internal structure of AGN. One is the systematic study of samples of AGN, in order to estimate the covering factor of these occultation events and the frequency on which absorption variability occurs. Among these works I cite the first statistical survey performed by Markowitz, Krumpe, & Nikutta (2014) and a recent statistical work on X-ray occultations published by Torricelli-Ciamponi et al. (2014).

A second approach, that is also the one performed in this thesis, is the accurate study of single objects, thanks to multi-epoch or monitoring X-ray observations, with the aim of defining a more detailed scenario of the geometry, size and physical state of the obscuring medium, and compare this outcome with the Unified Model and the current alternative schemes.

In this context, during my thesis I focused on the analysis of two AGN, for which multi-epoch X-ray observations are available and reveal interesting features for the understanding of the structure of the circumnuclear material and for testing the validity of the Unified Model. In particular, starting from the *Swift* BAT-70 months sample[1], a subsample of 31 interacting galaxies, of which at least one component is active, was defined during the master degree thesis of a student (Elisa Sala), carried out at INAF-Osservatorio Astronomico di Brera. These galaxies were chosen because they either show signs of per-

[1] http://swift.gsfc.nasa.gov/results/bs70mon/

turbed morphology in the optical images or they show the presence of one or more nearby galaxies with which they could be interacting. They all have redshift z< 0.03, high galactic latitude (| b |> 15°), signal to noise ratio S/N> 5 and flux in the 15-150 keV higher than 8.0×10^{-12}erg cm^{-2} s^{-1}. Interacting galaxies are among the most promising sources when searching for the initial phase of AGN activity, since we expect large amount of gas available for feeding (and allowing the growth) of the central black hole. The two sources involved in this work are:

- NGC 454E, a red elliptical Seyfert 2 galaxy part of an interacting system, at z=0.0122. X-ray good quality data (from XMM-*Newton* and *Suzaku*) were public and available. A first inspection on these data immediately revealed a very different spectral shape, for which a detailed spectral analysis was worth. The high variability in column density of the neutral absorber allowed me to include this source in the class of "changing look" AGN, which is still limited to a few sources so far.
- Mrk 348 (NGC 262), a bright Compton-thin Seyfert 2 galaxy at z=0.015. For this source a *Suzaku* observation was obtained by our research group (PI Valentina Braito), since the existing results obtained with XMM-*Newton* observation revealed complexity in the X-ray spectrum. Indeed in both XMM-*Newton* and *Suzaku* observations I could determine the presence of multiple absorbers, some of which featuring variability.

In Chapter 1 I illustrate in more detail what are AGN, their physical nature and classification, the Unified Model and the most recent alternative models of their structure. In Chapter 2 I focus on the X-ray emission produced in the innermost regions of AGN and on the reprocessing and absorption observed in the X-ray spectra of these sources.
In Chapter 3 I describe the analysis performed on NGC 454E, where I compare the X-ray spectrum observed first with *Suzaku* and 6 month later with XMM-*Newton*, and detect a dramatic change in the spectral curvature between 3 keV and 6 keV. The origin of the variability relies in a significant change of the neutral absorber column density, occurred during the 6 months separating the two observations. Indeed the columns density changes from $\sim 1 \times 10^{24}$cm^{-2}(*Suzaku*) to $\sim 1 \times 10^{23}$cm^{-2}(XMM-*Newton*), allowing to classify NGC 454E as a "changing-look" AGN. Besides the strong variation of the neutral absorber, the XMM-*Newton* spectrum also showed clear signatures of the presence of an ionised absorber, that is absent during *Suzaku* observation. An upper limit on its distance was inferred to be $\sim 10^{-3}$ pc, consistently with being located inside the BLR.
In Chapter 4 I concentrate on the study on Mrk 348, that displays less extreme features with respect to NGC 454, but shows a very complex absorbing system. It is indeed characterized by three different absorbers, of which one neutral and two ionised, with different densities and ionisation states, but with approximately the same outflow velocity ($\sim$ 0.05c). The distances of the ionised absorbers from the central emitting region are likely to be different, indeed the upper limits I find are 0.026 pc for the highly ionised absorber ($log\xi \sim 3.8$ erg cm s^{-1}), and 2.72 pc for the mildly ionised one ($log\xi \sim 2$ erg cm s^{-1}). I conclude that a variation of the column density is present also for Mrk 348, both for the neutral absorber ($\Delta N_H \sim 5.5 \times 10^{22}$cm^{-2}) and for the mildly ionised absorber

($\Delta N_H \sim 6.7 \times 10^{22} cm^{-2}$).
The results of these two studies were published in Marchese et al. (2010) and Marchese et al. (2014), for NGC 454 and Mrk 348 respectively. Both these studies are a step forwards in the definition of an alternative model to the "basic" Unified Scheme, for which more and more evidences are being collected suggesting that the absorbing material is not homogeneously distributed, but it is likely composed by multiple and multiphase absorbers at different distances, densities and ionisation states. A further improvement in the comprehension of the physics very close to the SMBH can be provided by additional observations of these same sources, that may give a higher level of detail on their structure, and the finding of other sources displaying similar features. I finally remark that such studies are very important also in the framework the general understanding of the galaxy formation and evolution, as proved by the strong correlation between SMBH masses and host galaxy properties.

During the PhD I was also involved in two works carried out with a research group at Osservatorio Astronomico di Brera. These were connected to my Master degree thesis, that concerned the computation of the optical-UV-X-ray spectral energy distribution of a sample Type 1 AGN extracted from the *XMM*-Newton Bright Serendipitous sample (XBS, Della Ceca et al. 2004; Caccianiga et al. 2008), in order to infer bolometric luminosities and bolometric corrections. Physical parameters, such as SMBH masses, accretion rate and bolometric luminosity have been inferred from the available optical-UV-X-ray data and have been used to investigate the link between the hot corona (producing X-rays via Inverse Compton Scattering of optical-UV photons emitted from the accretion disk) and the phenomenon of accretion on the central SMBH. In the final pages of this thesis I have attached the relevant papers reporting the main results reached so far. I will resume hereafter the topics they cover:

- **Caccianiga et al. (2013)**: in this paper the masses of the central SMBHs of 154 AGN belonging to the XMM-*Newton* Bright Serendipitous Survey (XBSS) were derived, by using the "single-epoch"relations, based on Hβ and MgIIλ2798 Å. For the same sources the accretion rate was derived from the bolometric luminosities, computed starting from the optical-UV-X spectral energy distribution. The masses found for these AGN are comprised in the range $10^7 - 10^{10} M_\odot$ and the accretion rates range from ~ 0.05 to $\sim 50 M_\odot$/yr (assuming an efficiency of 0.1).

- **Fanali et al. (2013a,b)**: the two works published by Fanali et al. 2013 focus on the relation between the X-ray emission in radio quiet AGN and the accretion rate $\dot{M}$, for a sample of 71 AGN belonging to the XBS. In this work a dependence of the X-ray spectral index Γ on the accretion rate normalized to the Eddington luminosity ($\lambda = \frac{L_{bol}}{L_{Edd}}$) was found. This could be explained with the effect of cooling of the electrons in the corona: higher accretion rates imply a larger number of photons produced in the accretion disc, determining a faster cooling of the coronal electrons, resulting in steeper X-ray spectra. Both the bolometric correction $k_{bol} (= \frac{L_{bol}}{L_{2-10keV}})$

and the two-point spectral index α_{ox}[2] index are found to depend on λ and $\dot{M}$. These correlations suggest the presence of a link between the disc/corona luminosity ratio and the accretion rate.

[2] $\alpha_{ox} = \frac{\mathrm{Log}(f_0/f_X)}{\mathrm{Log}(\nu_0/\nu_X)}$ where f_0 and f_X are, respectively, the rest-frame monochromatic fluxes at $\nu_0 = 1.20 \times 10^{15}$ Hz (meaning $\lambda_0 = 2500$ Å) and $\nu_X = 4.84 \times 10^{17}$ Hz (meaning E = 2 keV)

Chapter 1

Introduction

Contents

1.1 Active Galactic Nuclei 7
1.2 Classification 10
1.2.1 Classification based on bolometric luminosity 10
1.2.2 Classification based on optical spectra: Type 1 and Type 2 AGN . . 12
1.2.3 Classification based on Radio emission properties 15
1.2.4 X-ray classification 16
1.2.5 Subclasses 19
1.3 AGN Unification 22
1.3.1 Unification Scheme 23
1.4 Insights on AGN structure from X-ray absorption variability 27
1.5 Alternative models 31
1.5.1 Elvis (2000) unified scheme 31
1.5.2 Risaliti (2002) model 34
1.5.3 Elitzur (2007) model: torus model and clumpy unification 34
1.5.4 Torus disk-wind model: basis for a “grand unification scheme”? . . 37

1.1 Active Galactic Nuclei

In the local Universe about 10%-20% of the galaxies show at their center the presence of a compact and luminous source of energy, reason for which they are designated as Active Galactic Nuclei (AGN). In many cases the luminosity of the AGN outshines the starlight of its host galaxy, appearing as a bright and pointlike source (whose luminosity ranges from 10^{41} to 10^{48} erg/s, in a wavelength interval going from the radio to the γ-ray band).

Following the definition given by Netzer (1990) we can refer to a source as an AGN if one of the following criteria is satisfied:

- it contains a nuclear compact source, emitting more energy than the corresponding region of a galaxy of the same morphological type;
- its continuum emission is not produced by stellar processes;
- it shows strong emission lines in the IR-optical-UV band, due to non-stellar excitation processes;

- it exhibits strong and rapid variability, both in the continuum and line emission, that indicates that the emitting region is very compact (R$\sim 10^{13} - 10^{15}$cm). The involved timescales range from a few months (at radio wavelengths), to a few days (at optical wavelengths and in the X–rays). In some cases X-ray variability timescales of the order of one hour (Aharonian et al. 2007) or minutes (in the TeV energy band, Aleksić et al. 2014) have been observed .

What can be the origin of all these unusual (at least for a "normal" galaxy) features? The strong energy output and variability of AGN requires an energy generation mechanism with high efficiency in a region with a size comparable to the Solar System. The most accredited model for describing such phenomenon is that this emission is produced by accretion onto a Supermassive Black Hole (SMBH, Rees 1984, $M_{\rm BH} \sim 10^6 M_\odot - 10^9 M_\odot$) located at the center of the AGN. Since the interstellar gas possesses angular momentum it cannot fall radially onto the black hole, therefore it forms an accretion disk. In this disk, matter loses angular momentum through viscous and turbulent processes, converting gravitational energy into radiation emitted at optical-UV and soft X-ray wavelengths (<2 keV). These photons interact with a corona of optically thin plasma (surrounding the internal region of the accretion disk) by inverse Compton scattering, therefore they gain energy and are observed in the hard X-ray band. In addition broad and narrow emission lines are produced in regions containing clouds moving at different velocities and distances from the central engine. The emission from the higher velocity clouds (located nearer to the central black hole), together with the accretion disc emission, is in turn absorbed along a certain range of directions by an optically thick structure with high covering fraction, presumably with a toroidal geometry. The inner regions of the disc also produce highly collimated jets of plasma. These jets are composed by charged particles that interact with the magnetic field, emitting synchrotron radiation. They are also responsible for inverse Compton scattering, extending the emission to higher energy bands (GeV and TeV).

One important finding of recent years was the discovery of the presence of SMBHs in almost all galaxies, through measurements of star proper motions (Genzel, Eisenhauer, & Gillessen 2010), radial velocities of single gas clouds (H_2O maser emission at $\lambda = 1.35$ cm, e.g. NGC 4258, Herrnstein 1999), gas kinematics (velocity inferred from emission lines from ionized gas, e.g. Davis et al. 2013) and stellar dynamics (e.g. Walsh et al. 2012). The existence of a SMBH may have a strong influence on the host galaxy's properties, even in the cases where the SMBH is not any more manifesting its presence by accreting matter (Kormendy & Richstone 1995; Magorrian et al. 1998; Ferrarese & Merritt 2000). Indeed the discovery of strong correlations between the black hole mass and some of the host galaxy properties was a confirmation of this hypothesis, introducing the concept of co-evolution of black hole and host galaxy. When reliable measurements of the masses of SMBH were available, the following correlations were found: (1) a correlation between the black hole mass and the bulge luminosity M_{BH} -L_{bulge} (Kormendy & Richstone 1995); (2) a correlation between the black hole mass and the velocity dispersion of their host bulges, of

the form $M_{BH} \propto \sigma^4$, known as the $M_{BH}-\sigma$ relation (Ferrarese & Merritt 2000; Gebhardt et al. 2000; Tremaine et al. 2002); (3) a similar correlation between the black hole mass and the bulge stellar mass, leading to the relation $M_{BH} \sim 10^{-3} M_{bulge}$ (Marconi & Hunt 2003).

The process through which the growth of black holes and the assembly of galaxies take place together and influence each other is known as AGN *feedback*. This mechanism from one end puts a constraint on the growth of the SMBH due to its dependency on the local environment, and from the other end it determines the proportionality between the star formation rate and the SMBH mass.
Feedback processes can be grouped in two main modes, *radiative* and *kinetic* mode. The dominant one is the radiative mode, also known as quasar or wind mode, that is obtained when the the accretion onto the black hole is radiatively efficient and close to the Eddington limit. In these conditions, high velocity outflows are expected to be driven from the central region of the AGN (King 2003, 2005). The standard models for radiative feedback (Fabian, 1999; Fabian, Wilman, & Crawford, 2002; King, 2003, 2005; Murray, Quataert, & Thompson, 2005; King & Pounds, 2015) assume that when the black hole reaches a certain mass, the surrounding material will be blown out from the host galaxy, both causing the accretion of gas onto the black hole to stop and preventing further star formation (Springel, Di Matteo, & Hernquist, 2005; Di Matteo, Springel, & Hernquist, 2005). For this reason this mechanism is also known as "negative feedback". However feedback from the black hole can also have an opposite role in the evolution of the host galaxy, triggering star formation, thus contributing to the growth of the galaxy (Ishibashi & Fabian 2012). This is known as "positive feedback".
The second, and less common, feedback mode is the *kinetic* mode, also known as radio jet mode, that typically occurs when the accreting black hole produces collimated jets that release energy through mechanical processes. These jets, that are likely produced by magnetic forces (Blandford & Znajek 1977), inject heat into the IGM and cause the generation of big lobes of strong radio emission extending up to $\sim$ Mpc scales from the host galaxy. This process releases a huge amount of energy, of the order 10^{60} erg, that can be responsible for interrupting star-formation and heating the gas (Böhringer et al. 2002; Fabian 2012).

Before understanding the processes causing AGN feedback, it is essential to investigate the structure and the physical processes occurring in the central region of these galaxies. For this reason I was involved in the X-ray spectral analysis of two Type-2 AGN, showing interesting features in their spectra. In particular, I focussed on the material causing absorption of the primary emitted radiation, on its physical state, geometry and location with respect to the central black hole, and on the implications for the validity of the Unified Model of AGN. This material may be outflowing and thus it may be responsible for the feedback process that I described previously. As I will show, this study goes in the direction of confirming the necessity of a more complex model to describe the phenomenon of AGN.

1.2 Classification

First observations of AGN showed the existence of a wide range of different properties, among which different luminosities, and the presence in their spectra of narrow and/or broad optical-UV emission lines. Therefore, AGN were divided into different classes, according to the properties they displayed. Since they emit over the full electromagnetic spectrum, they were discovered and classified separately at different wavelengths, as technological improvements allowed to investigate new parts of the electromagnetic spectrum. A first general classification is based on the optical luminosity and designates *Seyfert galaxies* the lower luminosity AGN, and *quasar* the more luminous ones (Section 1.2.1). In general quasars have bolometric luminosities between $L_{bol} \approx 10^{44} - 10^{48}$erg s^{-1}, while Seyferts have $L_{bol} \approx 10^{42} - 10^{44}$erg s^{-1}. A second distinction can be made on the base of the properties of their optical spectra: type 1 AGN show broad and narrow optical/UV emission lines while type 2 AGN show only narrow emission lines (Osterbrock & Ferland 2006). Finally, the strength of the radio emission with respect to the optical flux divides AGN into *Radio Loud* or *Radio Quiet*. Each of these classes includes a variety of subclasses.
Nowadays the attention is concentrated on a distinction based on the effective physical properties, such as black hole mass, luminosity, Eddington ratio (L_{bol}/L_{Edd} [1]) and radio power, rather than observational features. I will now go through the general characteristics of the main classes of AGN.

1.2.1 Classification based on bolometric luminosity

1.2.1.1 Seyfert Galaxies

The first description of the optical spectrum of an AGN was made by Fath (1909) who highlighted the presence of strong emission lines in the nuclear spectrum of NGC1068. However, the first systematic study of a sample of AGN was done by Seyfert (1943) who analysed the nuclear regions of six unusual spiral galaxies. Optical images showed that, differently from non active galaxies, they display a bright, central, point-like core and unusual emission lines properties (such as narrow and/or broad emission lines from highly ionised matter). For this reason they were considered as a new class of galaxies, designated as Seyfert galaxies. Seyfert galaxies are lower luminosity AGN, with absolute magnitudes by definition fainter than $M_B = -23$ mag (where M_B is the absolute B band magnitude, Schmidt & Green 1983), corresponding to luminosities fainter than $\sim 5 \times 10^{44}$ erg s^{-1}. For this reason their host galaxies, typically spiral or lenticular galaxies (Weedman 1977), are clearly detectable. What makes Seyfert galaxies distinguishable with respect to normal galaxies, is the observable contrast between the luminosity of central region and the luminosity of the host galaxy.

[1] The Eddington luminosity L_{Edd} is the maximum luminosity achieved by a source in hydrostatic equilibrium : $L_{Edd} = \frac{4\pi GMm_p c}{\sigma_T} \sim 1.3 \times 10^{38} \frac{M}{M_\odot}$erg s^{-1}, where σ_T is the Thomson scattering cross-section, and m_p is the mass of a proton.

1.2.1.2 Quasars

In the late 1950s and early 1960s large sky surveys using radio telescopes were carried out. Many of the observed sources could not be identified with known classes of objects, and in the optical images appeared as blue stars, thus they were labelled as *quasi stellar radio sources*, or quasars. Optical spectroscopy of these sources lead to the discovery of strong redshifted emission lines (Schmidt 1963), suggesting that quasars constituted the more distant equivalent of Seyfert galaxies. Since they are much brighter than Seyfert galaxies (brightness is such that it dominates over the emission of the host galaxy), quasars can be detected at higher distances. Unlike Seyferts, quasars are typically found in elliptical galaxies and are those AGN with absolute magnitudes brighter than $M_B = -23$ mag (Schmidt & Green 1983). In Fig. 1.1 a combined quasar spectrum, obtained as an average of more than 700 individual quasar spectra, is shown (Francis et al. 1991).

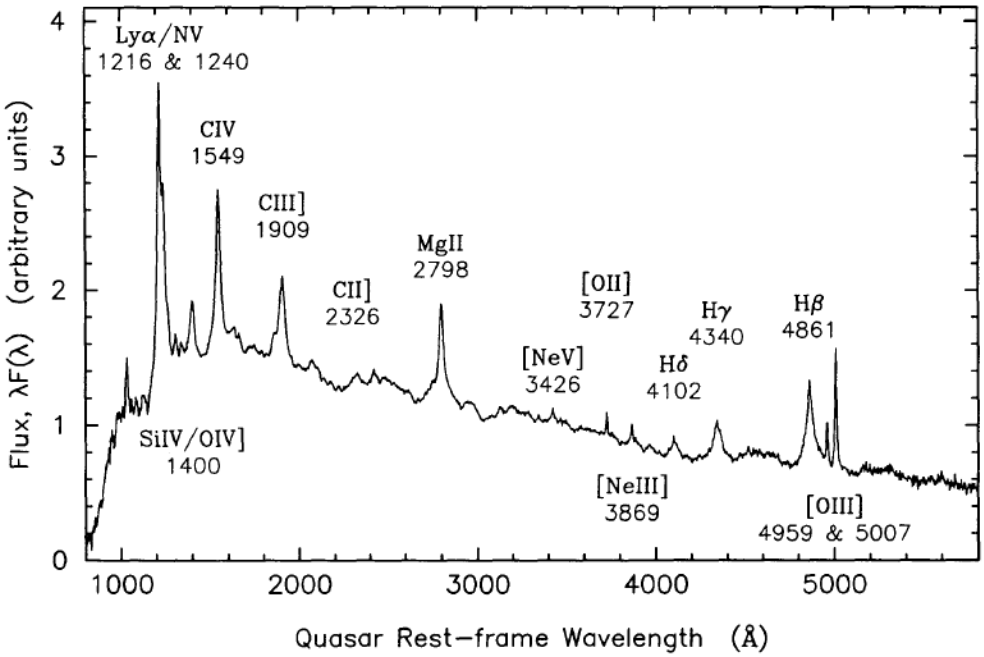

Figure 1.1: *Composite quasar spectrum derived as an average of 718 quasar spectra from the Large Bright Quasar Survey. The spectrum shows the clear presence of both strong and weak broad emission line features, typical of quasars. In particular we note the hydrogen Lyα λ1216+NVλ1240 blend, some of the hydrogen Balmer-series lines (Hβλ4861 and Hγλ4340 blended with [O III]λ4363) and the lines of the most abundant ions (MgIIλ2798 and Al IIIλ1858 + CIII]λ2798, CIVλ1549). Data and image adapted from Francis et al. (1991).*

1.2.2 Classification based on optical spectra: Type 1 and Type 2 AGN

A detailed study of the spectra of Seyfert galaxies by Khachikian & Weedman (1974) found two distinct types of optical spectra. All the spectra exhibited narrow and unresolved emission lines from highly ionized material, but only some of them also showed broad emission lines. They classified Seyferts in two types, according to the relative widths of narrow (forbidden) lines and Balmer lines. This classification designated as Seyfert 1 galaxies those galaxies where the Balmer lines (mainly Hα, Hβ, Hδ) appeared broader (FWHM $>$ 1000 km s^{-1}) than the forbidden lines, like the Oxygen [OII] and [OIII] lines, the nitrogen and neon [N II], [Ne III] and [Ne IV] lines. Instead in Seyfert 2 galaxies both the forbidden and Balmer lines were narrow. The narrow lines arise from low density gas (electron density $n_e \simeq 10^3 - 10^6 \mathrm{cm}^{-3}$) and velocities of maximum $\sim$ 1000 km s^{-1}. The broad Balmer lines are instead typical of dense matter ($n_e \simeq 10^8 - 10^{10} \mathrm{cm}^{-3}$) at velocities of $10^3 - 10^4$ km s^{-1}. Moreover, while in Seyfert 1s we observe a strong and variable optical-UV continuum, in Seyfert 2s this continuum is rather weak with respect to the stellar continuum emitted by the host galaxy. Two typical spectra of the two classes of Seyfert galaxies are shown in Fig. 1.2. The classification into type 1 or type 2, based on the properties of the optical emission lines, is applicable also to Quasars. That is why we can generally speak about of Type 1 and Type 2 AGNs.

The classification of a galaxy as a Seyfert 1 rather than a normal galaxy is straightforward due to the presence of the broad emission lines indicating the existence of high velocity clouds illuminated by a strong radiation field. On the contrary, for Seyfert 2s we observe narrow emission lines of elements that are also present in the HII regions of star-forming galaxies. Spectroscopic methods allow to disentangle the two processes since the emission lines show signatures of what is the main excitation mechanism, which is different for stars and AGN. In fact the ionizing emission of all stars show generally a cut off near the He II edge (54.4 eV), while AGNs are typically strong X-ray emitters. In AGN we expect an increase of both high- and low-ionization lines, with respect to HII regions. This is because:

- the material in inner regions of AGN is more strongly ionized and therefore emits strong high ionization lines.

- the high energy photons go deeper into the circumnuclear gas (due to the dependence of the absorption cross-section on energy, $\sigma_\nu \propto \nu^{-3}$) and extended regions of partially ionized gas are formed. In these regions it is observable the emission of collisionally excited low-ionization lines.

Baldwin, Phillips, & Terlevich (1981) first proposed a diagnostic diagram (now known as the BPT diagram) using the [NII]/Hα versus [O III]/Hβ line ratios to distinguish HII regions, planetary nebulae, and the circumnuclear regions of AGN, which are photoionized by higher energy photons. This diagram (Fig. 1.3) shows that the different populations are located in different regions without overlapping, allowing to easily identify them.

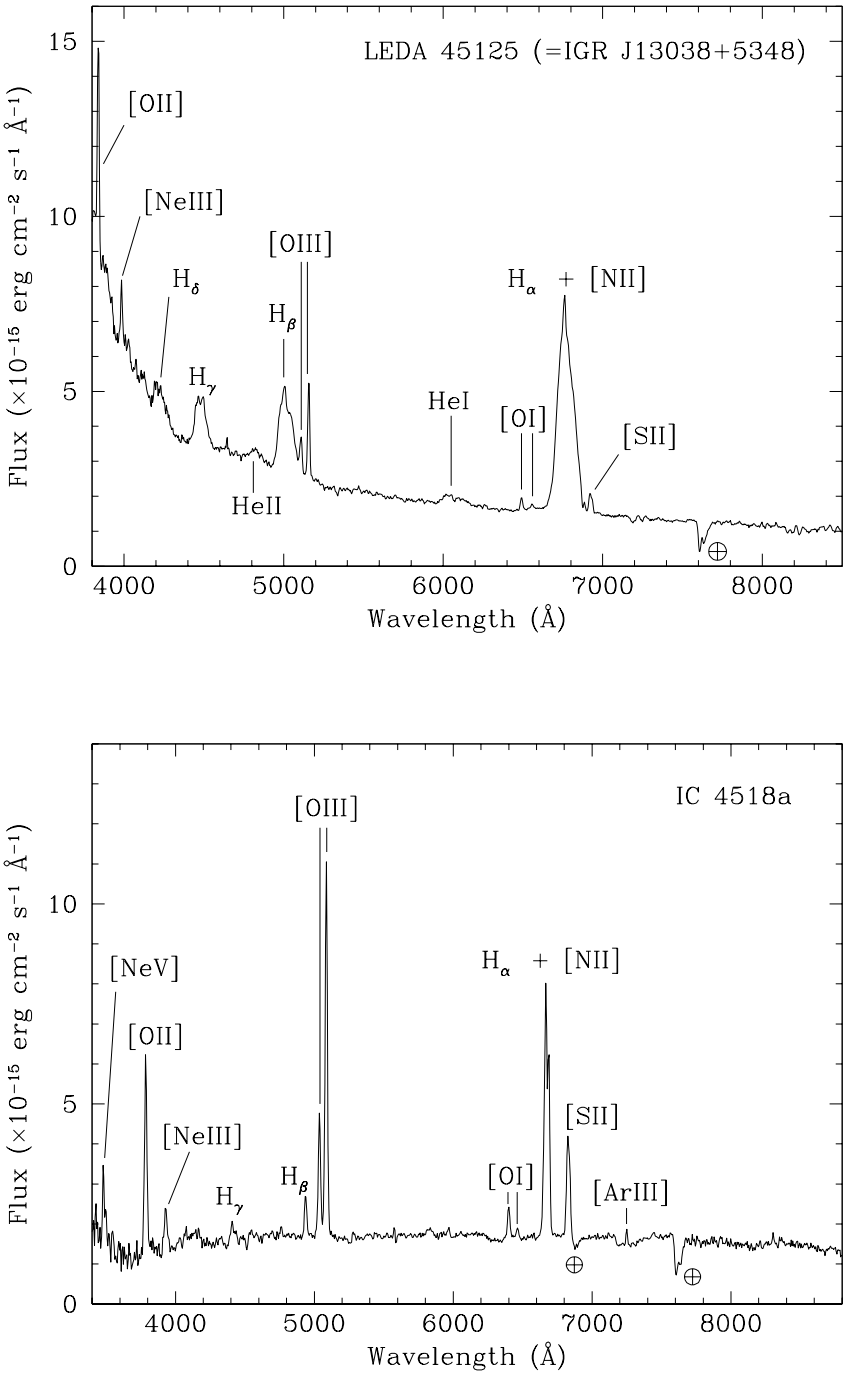

Figure 1.2: Upper panel*: optical spectra of a typical Seyfert 1 galaxy (LEDA 45125) where the stronger broad emission lines (like the Balmer lines) are marked. The classification of LEDA 45125 as a Seyfert 1 galaxy is due to the presence of emission lines with Full Width at Half Maximum (FWHM) of ∼ 4900 km/s.* Lower panel*: optical spectra of a typical Seyfert 2 galaxy (IC 4518a), also showing the most important emission lines, narrower than those typical of Seyfert 1s. Both the figures have been adapted from* Masetti et al. *(2008).*

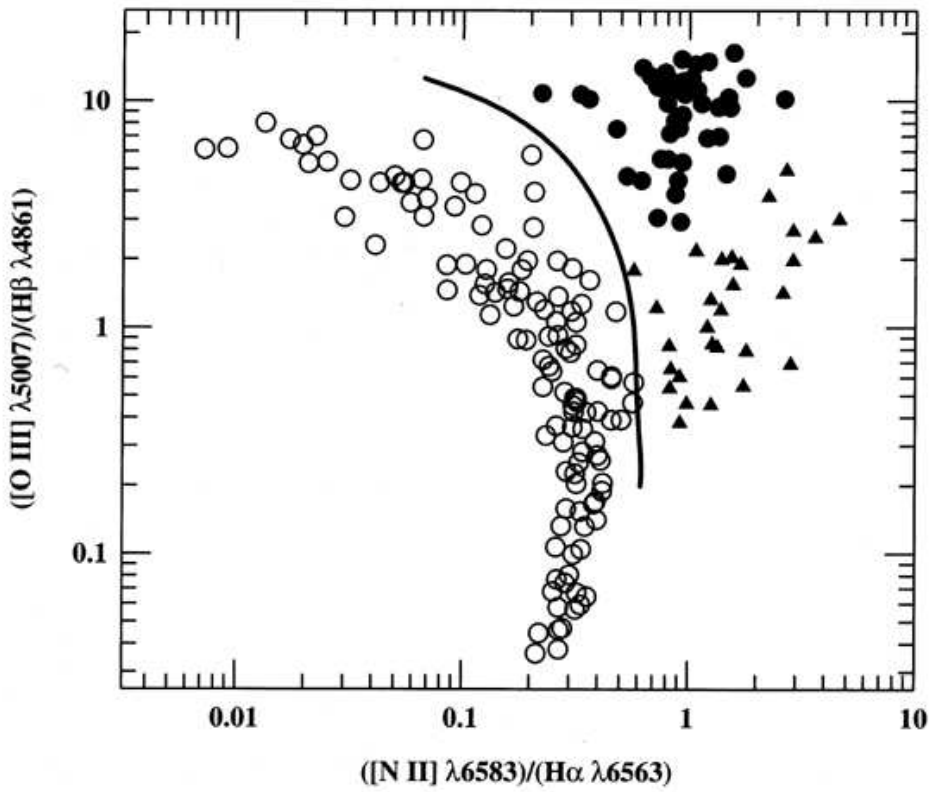

Figure 1.3: *Classification diagram using [OIII]λ5007/Hβ versus [NII]λ6583/Hα. The open circles represent HII regions (and sources ionized by hot stars), closed filled circles are AGN (Seyfert 2s and Narrow Line Radio Galaxies), that are ionized by continua with a higher fraction of high energy photons, and the triangles represent Low-Ionization Nuclear Emission-Line Region (LINERs), a sub-class of highly debated active galaxies, on which the ionizing phenomena originating their spectra are still under discussion (nuclear accretion versus shocks). The solid line divides HII regions from AGN. Image adapted from Peterson (1997).*

1.2.3 Classification based on Radio emission properties

1.2.3.1 Radio Loud and Radio Quiet AGN

Radio galaxies are sources for which we observe bright radio jets and large radio luminosities. The radio emission is produced in two different regions: a compact and an extended region (the latter one is generated by the interaction of the bipolar jets with the external medium). The emission from both these components is synchrotron radiation due to relativistic particles (Lorents factor $\gamma \sim 10^4$) ejected from the central nucleus in an environment with magnetic fields. The compact emission component is unresolved at scales lower than the arcsecond, and it is located in a position approximately coincident with the central black hole.
The designation of *Radio Loud* AGNs is given to those sources where the radio emission constitutes a significant fraction of the total luminosity: $L_{radio} \sim 10^{41} - 10^{46}$erg s^{-1} in the 10^2 MHz and $\sim$ 10 GHz band. The general criteria for classifying a radio source as radio loud or radio quiet is based the ratio R of radio (5 GHz) to optical (B band) fluxes. If R is higher than 10 (Kellermann et al. 1989) then the source is classified as radio loud. These sources constitute a small fraction of the AGN population, approximately 10-20%.
Two subclasses of radio loud AGN can be defined on the base of the appearance of the extended radio emission:

- low luminosity Fanaroff-Riley Class I (FR-I) galaxies (Fanaroff & Riley 1974), that show a relatively compact emission generated close to the core (upper panel of Fig. 1.4). In these sources the outer extremities of the lobes are the faintest regions, likely because the jets decelerate and become sub-relativistic. Although they show the presence of narrow emission lines, most FR-I do not display broad optical/UV emission lines (Urry & Padovani 1995).

- the high-luminosity FR-II sources (Fanaroff & Riley 1974), in which the structure is dominated by the radio lobes and most of the emission appears to come from the most external part of the extended emission, in the form of hotspots (see lower panel of Fig. 1.4). In these sources the jets remain relativistic and supersonic from the core to the hot spots.The optical properties of the associated AGN can be either Seyfert-1 like or Seyfert-2 like: these are known as Broad Line Radio Galaxies (BLRG) and narrow-line radio galaxies (NLRG), respectively.

There is also a quite clear division in luminosity between FR-I and FR-II galaxies: $L_R = 2 \times 10^{33}$erg s^{-1}Hz^{-1} at a frequency of 178 MHz.
Several models have been proposed to explain the FRI versus FRII dichotomoy, among them the different mechanisms of interaction between the jet and the interstellar medium (Bicknell 1995), the role of the spin of the SMBH (causing different kinetic power in the jets, e.g. Meier 1999), the host galaxy environment properties (Smith & Heckman 1990) or the accretion rates (Ghisellini & Celotti 2001), where FRIIs could be characterised by accretion in an optically thick and geometrically thin disc, while FRIs by an optically thin

advection dominated accretion flow (ADAF[2])

The most optically luminous Radio Loud AGN are designated as Radio Loud Quasars (RLQ). They were the first quasars to be discovered, because of high luminosity and strong radio emission. Nevertheless RLQ are only 10% of the total population of quasars. Apart from the strong radio emission, they show similar characteristics as their radio quiet counterparts (variable continuum flux, strong UV component, broad emission lines) but they tend to be located in more massive host galaxies with respect to radio quiet quasars (Dunlop et al. 2003). Radio Loud quasars can be further classified as Flat Spectrum Radio Quasars (FSRQ), having radio spectral index[3] $\alpha_r \gtrsim 0.5$ (between 2.7 and 5 GHz) and Steep Spectrum Radio Quasars (SSRQ), with radio spectral index $\alpha_r \lesssim 0.5$. The former have a compact radio structure, while the latter are dominated by radio lobe emission.

1.2.4 X-ray classification

A distinction into two types of AGN exists also in the X-rays, where the AGN are classified as absorbed or unabsorbed depending on the intrinsic absorption measured in this energy band. While the optical classification into type 1 or type 2 AGN is based typically on the FWHM of the emission lines, with a dividing value assumed to be in the range between 1000 km/s and 2000 km/s (e.g. Page et al., 2006; Caccianiga et al., 2007), in X-rays the dividing line between the two classes is determined by the intrinsic Hydrogen column density $N_{\rm H}$, designating Type 1s the unabsorbed AGN (whose $N_{\rm H}$ lies below a certain threshold), and Type 2 those AGNs whose primary emission is clearly absorbed ($N_{\rm H}$ higher than the threshold). Depending on the published works, the dividing $N_{\rm H}$ value was adopted to be $N_{\rm H} = 4 \times 10^{21}{\rm cm}^{-2}$ (Caccianiga et al., 2007; Della Ceca et al., 2008) or $N_{\rm H} = 10^{22}{\rm cm}^{-2}$ (Garcet et al., 2007; Beckmann et al., 2009.

Focusing on the absorbed AGN, as I will discuss in Section 2.4, the X-ray observed spectrum depends strongly on the amount of absorption (expressed in terms of $N_{\rm H}$) along the line of sight. An important fraction of AGN are obscured in the X-rays ($\sim$ 43% with $N_{\rm H} > 10^{22}{\rm cm}^{-2}$ in the 20-40 keV band, Malizia et al. 2010). It is common to refer conventionally to "Compton-thick" and "Compton-thin" AGN depending on if the $N_{\rm H}$ is higher or lower than the inverse Thomson cross section $\sigma_T^{-1} = 1.5 \times 10^{24}{\rm cm}^{-2}$ respectively. In Fig.1.5 it is shown the resulting X-ray spectra for different values of $N_{\rm H}$, under the hypothesis that the underlying primary emitted continuum is a simple power law with spectral index of 2. In the Compton-thin cases where $N_{\rm H} \lesssim 10^{24}{\rm cm}^{-2}$ the primary X-ray spectrum is visible above a few keV, with a small contribution from the Fe Kα emission line. Instead, when we observe the emission from a Compton-thick AGN with $N_{\rm H} > 10^{24}{\rm cm}^{-2}$, the primary emission is transmitted only above 10 keV; below this energy the spectrum is dominated by the reflected continuum, with a strong fluorescent emission line (EW$\sim$ 1 keV, Matt, Brandt, & Fabian 1996), probably produced in the inner surface

[2] Advection Dominated Accretion Flows (Narayan & Yi 1995): it is a regime in which the radiation efficiency of the accreting matter is too low with respect to the gravitational energy liberated, causing part of this energy to be advected with the infalling matter onto the black hole. The geometry of an ADAF is not a disc, since the height of the flow is proportional to its radius.

[3] $f_\nu \propto \nu^{-\alpha_r}$)

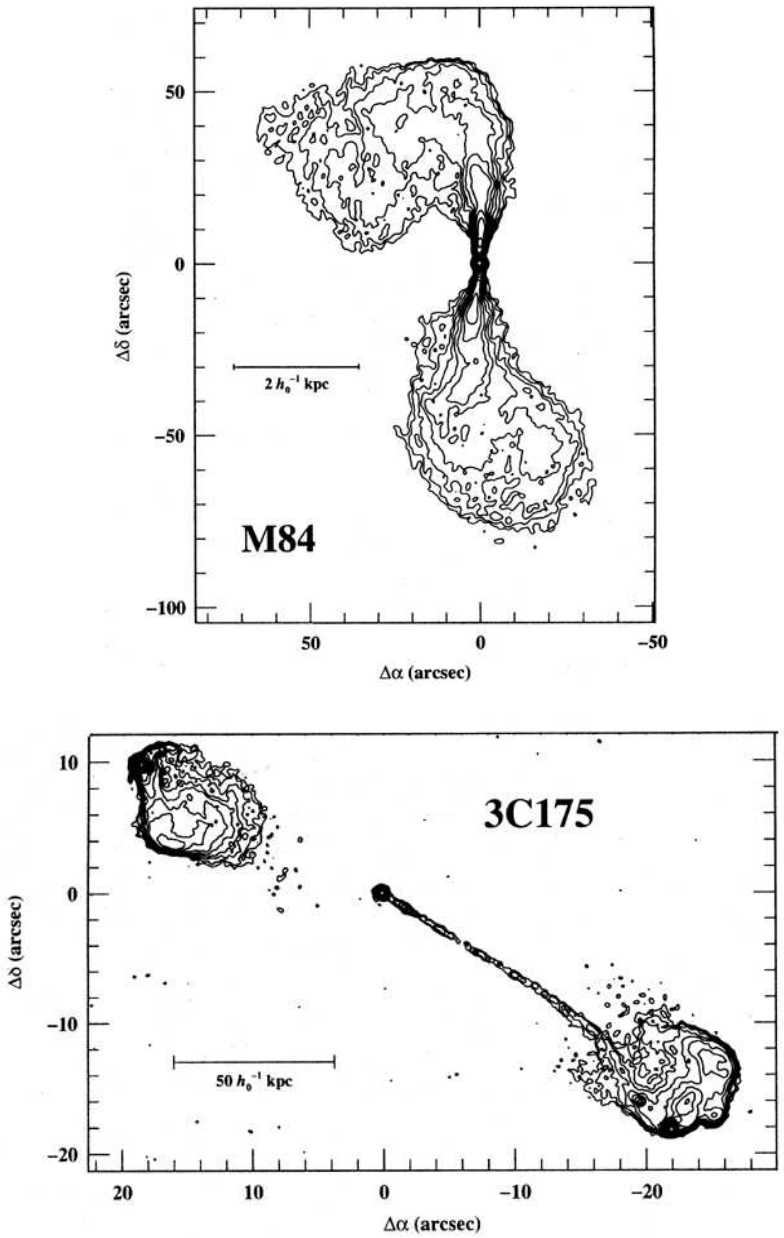

Figure 1.4: Top panel*: Example of a FRI radio galaxy, M84, observed at 5 GHz with the VLA. It is evident that the strongest emission comes from the central region, and it decreases towards the extremities of the lobes. Figure adapted from* Laing & Bridle *(1987).* Lower panel*: The quasar 3C175 (classified as a FRII radio galaxy when observed in the radio wavelength range), observed at 4.9 GHz with the VLA. Differently from FRI radio galaxies, the edges of the lobes produce the strongest emission together with the core.*

of the torus. In the case of $N_H > 10^{25} cm^{-2}$ no emission is transmitted through the absorber also at E> 10 keV, and the spectrum is totally dominated by the reflection component.

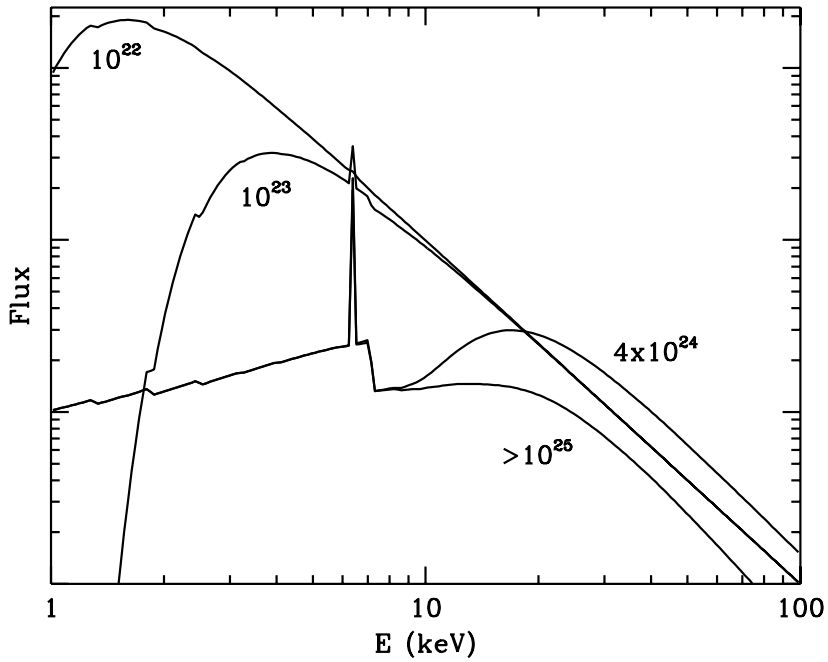

Figure 1.5: *X-ray spectrum of an AGN, for different column densities. Figure adapted from Matt, Guainazzi, & Maiolino (2003).*

Not always the optical classification as a Seyfert 1 or a Seyfert 2 galaxy coincides with the X-ray classification. Indeed in 10-20% of AGN some discrepancies were found, like some optically classified type 2 AGN showing no or low X-ray absorption (Caccianiga & Marchã 2004; Corral et al. 2005) or some optically classified type 1 AGN showing large X-ray absorption (Comastri et al., 2001; Brusa et al., 2003; Garcet et al., 2007). The mismatch between optical and X-ray classification is not explainable through the Unified Model (the presence of a homogeneous dusty torus, surrounding the central engine; see Section 1.3), and thus supports the validity of alternative models (Section 1.5). However it is important to remark that some of these discrepancies can be due to other effects, such as for example X-ray variability, the absence of the Broad Line Region (BLR, Section 1.3.1)

in some AGN (Laor 2003) or a different dust-to-gas ratio with respect to the Galactic one (Risaliti & Elvis, 2004). Thus the reasons behind this mismatch are still highly debated.

1.2.5 Subclasses

The classes of AGN described in the previous paragraphs also includes sources presenting "non standard" features, and that have been thus enclosed in sub-classes. Between these there are the *Narrow Line Seyfert 1 Galaxies* (NLS1). Their first peculiarity with respect to "standard" Seyfert 1 galaxies, is that the permitted optical-UV lines, despite being broader than the narrow lines typical of Seyfert 2 galaxies, are significantly narrower than those of Seyfert 1 galaxies (Fig. 1.6). The criteria used to describe NLS1 are:

- the width of the broad component of their optical Balmer emission lines is $\mathrm{FWHM}_{\mathrm{H}\beta} < 2000$ km/s. Above this threshold they are classified as Broad Line Seyfert 1s (BLS1);
- the relative weakness of the [OIII]λ5007 line flux is such that [OIII]/Hβ <3. This values was adopted by Shuder & Osterbrock (1981) to differentiate Sy1 and Sy2 galaxies;
- they have strong Fe II emission with respect to the Hβ line (Fe II/Hβ); this emission is about twice as strong in NLS1 as compared to other galaxies.

NLS1 constitute about 10-20% of optically selected Sy1s (Williams, Mathur, & Pogge 2004), but the fraction gets higher in soft X-rays selected samples ($\sim$ 50%, Grupe, 1996, 2004). Measurements of the masses of the central BH in NLS1 showed that they have on average lower masses than other Seyferts, in the range $M_{BH} \sim 10^5 - 10^7 M_\odot$ (Peterson et al., 2000; Grupe & Mathur, 2004), despite having comparable bolometric luminosities. This suggests that these sources have higher accretion rates than other Seyferts (**?**).

Other sources worth mentioning are *Blazars*, subclasses of RL sources in which the relativistic jet is pointing towards the observer's line of sight. They display high variability (with timescales $\leq$1 day), high polarization (up to a few percent), superluminal motion, and non-thermal continuum. Their emission covers a large energy range from the radio frequencies to very high energies (above 1 TeV). Blazars can be further divided into *BL Lac objects* and FSRQ, which are in turn divided into Optical Violent Variables (OVV) and Highly Polarized Quasars (HPQ). The distinguishing criterium between FSRQ and BL Lac is the equivalent width[4] of the emission lines (EW< 5Å for BL Lac objects). The fact that in BL LACs usually the emission lines are not seen is due to the dominance of the underlying non thermal continuum.

[4]The equivalent width is the width that the continuum underlying the line must have in order to contain the same flux as the line. It is defined as $\mathrm{EW}_\lambda = \int \frac{\mathrm{F_l}(\lambda) - \mathrm{F_c}(\lambda)}{\mathrm{F_c}(\lambda)} \mathrm{d}\lambda$, where $F_l(\lambda)$ represents the flux across the emission line at the wavelength λ, and $F_c(\lambda)$ is the continuum flux underneath the emission line.

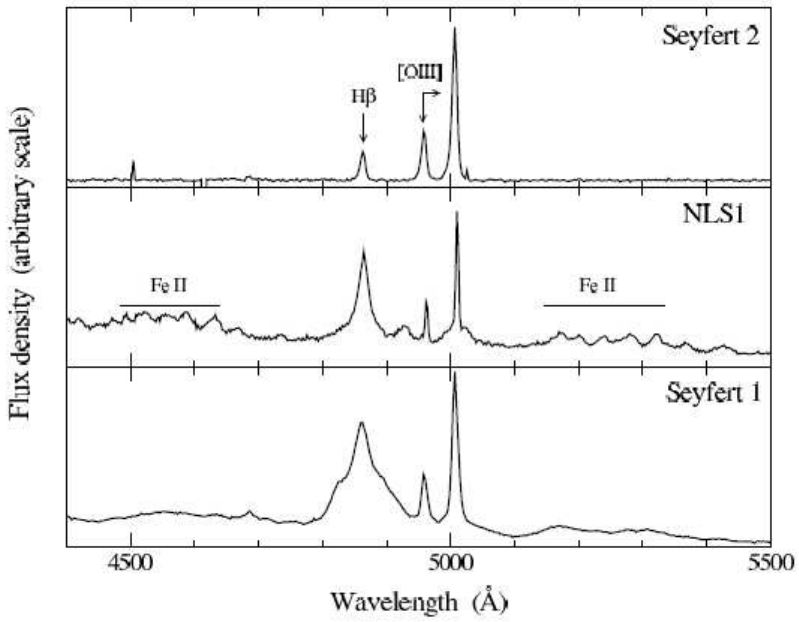

Figure 1.6: *Comparison of the optical spectra of a Sy2 (Mrk 1066), a NLS1 (RX J1251.0+6603) and a Sy1 (NGC3516). It is evident that NLS1 show narrower emission lines than normal Sy1s, even if not as narrow as Sy2. The FeII multiplet emission is visible in both the Sy1 and the NLS1, stronger for the latter one. Image adapted from Gallo (2004).*

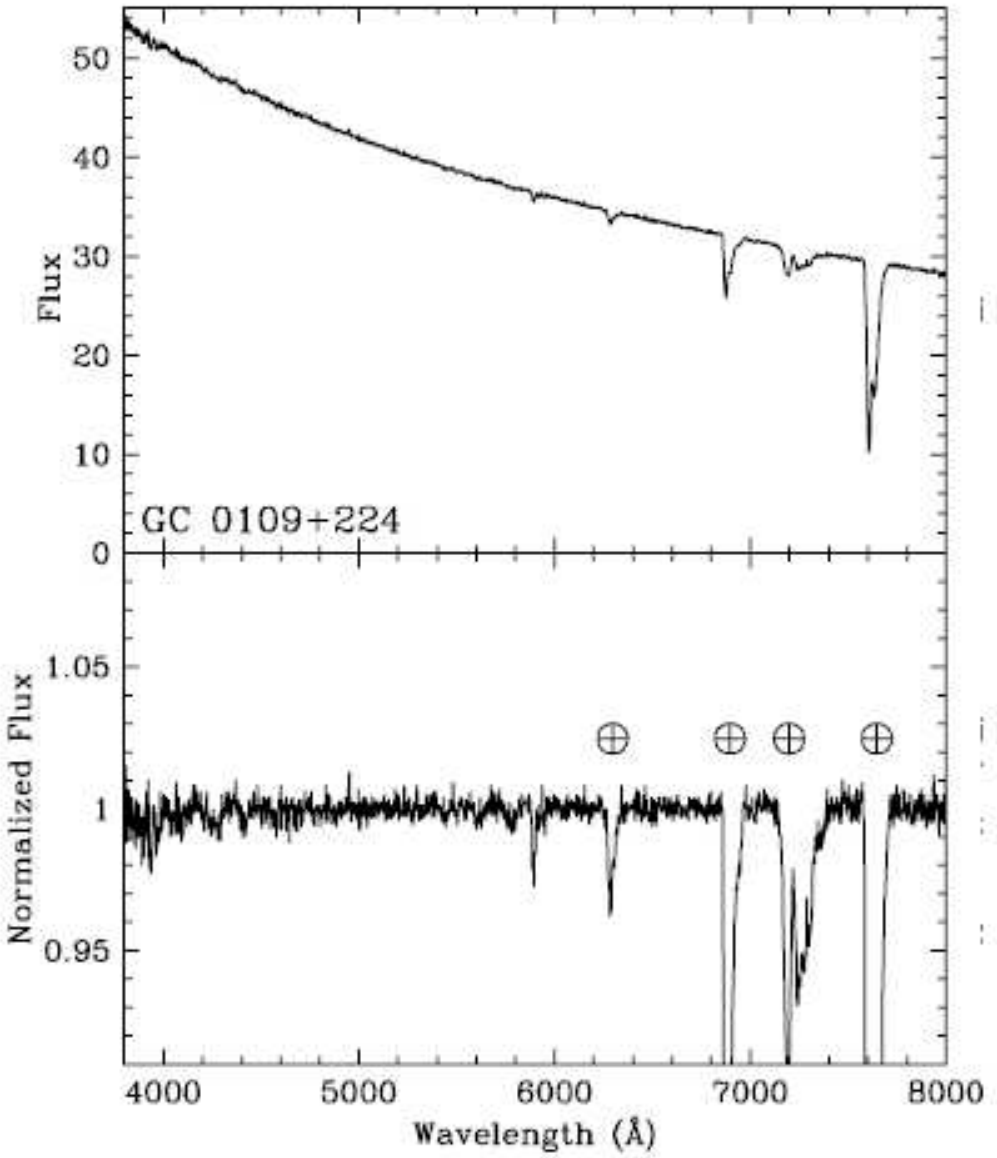

Figure 1.7: *Example of the optical spectrum of a BL LAC source. The top panel is the flux-calibrated dereddened spectra, the bottom panel is the normalized spectrum. With respect to a normal quasar spectrum (Fig.1.1) it is evident the absence (or weakness) of emission lines, due to the relativistically enhanced continuum. The* $\oplus$ *indicate the telluric bands. The flux density is in units of* 10^{-16}erg cm^{-2} s^{-1} Å^{-1} *Figure adapted from* **Sbarufatti et al.** *(2009).*

Table 1.1: Scheme describing the classification of AGN on the base of radio loudness and presence of broad and narrow emission lines.

Radio Loudness	AGN type	Sub Type	Broad Balmer Lines	Narrow Balmer Lines
Radio Loud				
	QSO	Type 1	yes	yes
		Type 2	no	yes
	FRI		some	yes
	FRII	BLRG	yes	yes
		NLRG	no	yes
	Blazar	FSRQ,SSRQ	yes	yes
		BL Lac	no	no
	NLS1		yes	yes
Radio Quiet				
	QSO	Type 1	yes	yes
		Type 2	no	yes
	Seyfert	Type 1	yes	yes
		Type 2	no	yes
	NLS1		yes	yes

1.3 AGN Unification

One of the fundamentals of the unified model is that any intrinsic property that is observed in type 1 AGN should also be present in type 2 AGN, even if modified due to the different viewing angle. The possibility to explain the various observational properties of AGN through different orientations was not so obvious at the beginning. Indeed it was believed for a while that the region producing the broad emission lines was missing from objects showing only narrow lines, therefore making the two objects intrinsically different from each other.

Evidences of unification As discussed, while we observe broad permitted optical emission lines (like Hα and Hβ) only in Seyfert 1 galaxies, high and low ionization narrow lines are common in both Seyfert 1 and Seyfert 2. This seems to indicate that both classes of objects have the same intrinsic engine. The first evidences of unification came from polarisation measurements performed on the Seyfert 2 NGC 1068 (Antonucci & Miller 1985), whose spectrum showed the presence of polarised broad optical emission lines, like the broad permitted lines observed in Seyfert 1s. The implication of this finding was that the BLR is present also in the nuclei of Seyfert 2s, even if it is obscured by the circumnuclear matter, and it becomes visible when the light it emits is scattered towards the line of sight by material on larger scales than the molecular torus. The analysis on the broad polarized lines and the measurement of their polarization angles also allowed to infer the need for an axisymmetric geometry for the absorber. Finally, a strong evidence for the unification of type 1 and type 2 AGN comes from the X ray observations of Seyfert 2s. In fact the X-ray spectra (above few keV) of these sources are characterized by a power law, simi-

lar to Seyfert 1s, indicating that the central engine is intrinsically the same. However in the case of Seyfert 2s the presence of an absorbing medium with column density typically higher than $10^{22}\mathrm{cm}^{-2}$ is manifested in the spectrum by a photoelectric absorption cut-off. In some cases we do not observe such cut-off, but a weaker continuum with a strong Fe Kα 6.4 keV emission line indicates that the primary radiation is totally absorbed by a medium with $N_{\mathrm{H}} > 10^{24}\mathrm{cm}^{-2}$ and we observe only the radiation reflected in our direction by the circumnuclear medium.

1.3.1 Unification Scheme

The advantage coming from the formulation of a "Unified Model" is that the differences due to "external" factors, such as orientation, are distinguished from intrinsic differences, allowing to better understand the basic physics behind the observations.
Various kind of unification models were proposed, some of which, after availability of new data and observations, were rejected and/or revised. The simplest and still actual scheme, that is the base to develop more elaborate models, was proposed by Antonucci in 1993. According to this model, there is no intrinsic difference between broad-line AGN and narrow-line AGN , regardless to their intrinsic luminosity: the observed different properties are determined only by orientation effects. The fundamental components of the Unified Model (Figure 1.8) are:

- **Black hole and accretion disk**
  The central engine producing the high luminosities observed in AGN is a SMBH at the center of the host galaxy. A black hole can be described through some basic parameters. Among them the gravitational radius (r_g) and the Schwartzschild radius (r_s):
  $$r_g = \frac{GM_{BH}}{c^2}\ ,\ r_s = 2r_g \simeq 3\left(\frac{M_{BH}}{10^8 M_\odot}\right)\times 10^{13}\mathrm{cm} \tag{1.1}$$
  The radius of the *Innermost Stable Circular Orbit* (ISCO, radius at which the material free falls into the BH) strongly depends on whether the BH is spinning (Kerr black hole) or not (Schwarzschild black hole) and, in the first case, also on the direction of motion of the accreting particle with respect to the direction of BH rotation (co-rotation or counter-rotation). For a non spinning Schwarzschild black hole the ISCO occurs at
  $$r_{isco} = 6r_g = 3r_s \tag{1.2}$$
  For a maximally co-rotating black hole, the ISCO radius is (Jefremov, Tsupko, & Bisnovatyi-Kogan 2015):
  $$r_{isco} = r_g \tag{1.3}$$
  In an AGN the central SMBH is accreting matter through an optically thick and geometrically thin accretion disk (Shakura & Sunyaev 1973) where matter is losing angular momentum through viscous and turbolent processes. Since the orbital velocity of the material in the disc is much faster than its inward flow speed, the material must lose energy and angular momentum due to the internal disc viscosity. By this

mechanism the angular momentum is transported outwards throughout the disc and the excess energy heats the gas and is radiated away. Matter reaches temperatures of $\sim 10^5 - 10^6 K$ and produces thermal emission in the optical-UV range (from $\sim$ 7000Å to $\sim$ 100Å). The emissivity of the disk can be described by a multitemperature blackbody where the temperature scales with the distance from the central black hole as $T(R) \propto R^{-3/4}$. Thus the inner ring temperature is the highest, emitting at the highest frequencies with respect to the more external regions. Moreover, the temperature increases with the accretion rate but decreases with the mass of the central object:

$$T(R, \dot{M}, M) \propto R^{-3/4} \dot{M}^{1/4} M^{-1/4} \tag{1.4}$$

If we assume a SMBH with $M_{BH} \sim 10^7 M_\odot$ the temperature at a distance of $10 r_S$ at the Eddington accretion rate[5] is $kT = 50$ eV, which at zero redshift corresponds to frequencies in the extreme ultraviolet band (or very soft X-rays). This makes the peak temperature difficult to observe since the galaxy becomes opaque in that spectral region. The region surrounding the accretion disk is thought to host a *corona* of optically thin and very hot (T$\sim 10^9 K$) plasma of high energy electrons. This region is responsible for the production of the X-ray emission, through inverse Compton scattering of the optical-UV photons emitted in the accretion disk with the coronal electrons.

- **Broad Line Region (BLR)**
  This region is composed of high velocity (~3000-10000 km/s) clouds in the potential well of the central BH. These clouds produce strong and broad optical emission lines due to photoionization from the central radiation emitted in the accretion disk. The BLR clouds are assumed to be in photoionization equilibrium, that means that the rate of photoionization is balanced by the rate of recombination. Therefore if two or more lines of different ionization states are observed it is possible to infer physical parameters. The temperature is estimated to be of order of 10^4 K and the density is believed to be very high ($n_e \sim 10^9 \mathrm{cm}^{-3}$, Netzer 1990), as required by the observed ratio between the permitted and forbidden emission line transitions. The distance of these clouds, as deduced from the variability of the broad emission lines and from their high velocities, is of 0.01-0.1 pc (Netzer, 1990; Peterson, 1998; Kollatschny, 2003). The structure of an individual cloud is thought to be such that the side of the cloud facing the central engine will be highly ionized and, depending on its column density the opposite side will be less ionized or mostly neutral. This manifests observationally in the coexistence of high ionization lines from ions such as He II, He I, O VI, N V and C IV, and low ionization lines from Mg II, Ca II, O I and Fe II.

- **Narrow Line Region (NLR)**
  Narrow emission lines, which are also commonly observed in AGN, have much smaller widths (of the order of several hundreds up to 1000 kms^{-1}) than broad lines

[5] The Eddington accretion rate is the one for which the central SMBH reaches the Eddington luminosity: $\dot{M}_{Edd} = L_{Edd}/\varepsilon c^2$, where ε is the accretion efficiency.

(as term of comparison the typical FWHM produced by stars in galaxies are $\sim$ 400 km/s). They are also produced by clouds that are photoionized by the central radiation source, but they are located further away from the central black hole, on scales of typically $\sim$100 pc, as inferred from their smaller keplerian velocities. The presence of forbidden as well as semiforbidden and permitted lines of, for example, oxygen, neon, magnesium and sulfur, suggest gas densities of $\sim 10^3 - 10^6 \mathrm{cm}^{-3}$ (Netzer 1990). In fact, at these low densities, collisions among ions and other particles occur rarely, implying that an ion can maintain its excited level until there is a spontaneous radiative decay. The emission line spectra of NLR is characterized by a wide range of ionization states, due to the presence of both strong low ionization lines (such as [OI]λ6300) and high ionization lines (such as [OIII]$\lambda\lambda$4959,5007).

- **Obscuring molecular torus**
  The key element of the Unified Model is the presence of a toroidal shaped optically thick obscuring medium surrounding the central engine, composed of dust and molecular gas and extending from $\sim$ 1 pc up to at least a few times 100 pc (Jaffe et al., 2004; Burtscher et al., 2013). The location and geometry of the torus is such that the emission from the NLR is expected to be detected by any observer, independently from the viewing angle. Instead, the emission coming from the BLR is detectable only if the line of sight does not intercept the torus.

1.3.1.1 The overall picture

According to the Unified Model model (Antonucci 1993), all AGN have regions very close to the nucleus producing broad emission lines (BLR) and featureless continuum radiation, and farer away regions producing narrow emission lines (NLR). When in a given object the toroidal material is face-on relative to the line of sight, so that both the BLR and the NLR are observed together with the emission from the accretion disk, then the source is classified as a Type 1. Otherwise only the narrow emission lines, produced in the the region outside the torus are seen directly, and we classify the source as a Type 2. Nevertheless, the radiation emitted from the nuclear regions can be reflected into the observer's direction due to scattering of electrons, which produces also polarization.

1.3.1.2 Unified Scheme for Radio Loud sources

As we discussed, some radio loud sources exhibit double jets of relativistic particles and lobes extending up to a few Mpc from the center of the host galaxies and with the same orientation as the axis of the torus. The physical process determining the launching of these jets is still quite uncertain, but many studies suggest that magnetic fields play an important role in jet collimation (Blandford 1993). These particles are responsible for the production of strong radio emission through the synchrotron process, and their bulk motion is relativistic, at least near the nucleus, with similar Lorentz factor in all sources. If the axis of a radio loud source is directed along the line of sight, then the spectrum observed is

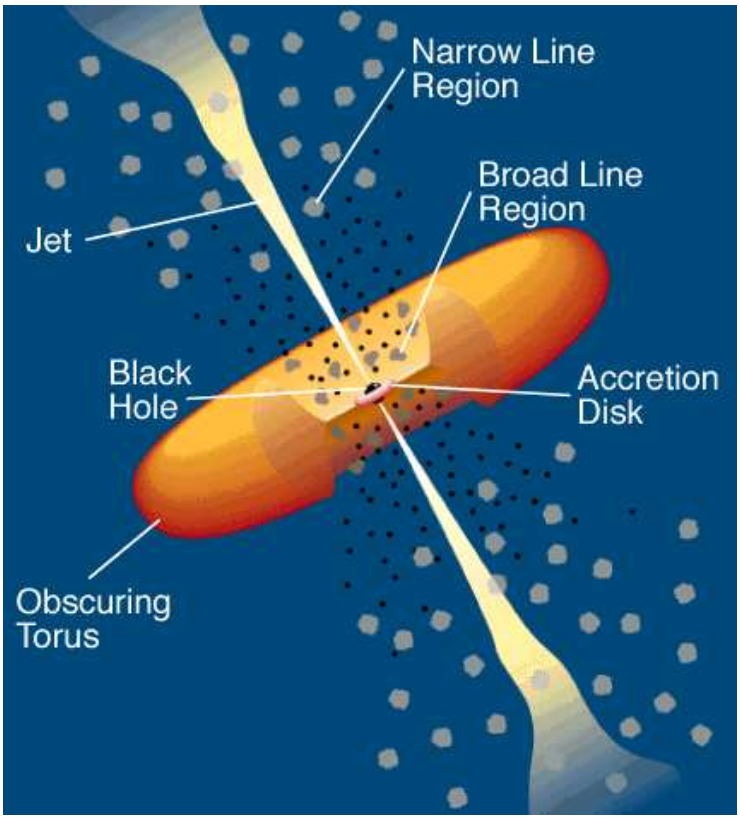

Figure 1.8: *Schema representing the AGN phenomenon according to the unified model, where the type of AGN depends on the viewing angle, whether or not the AGN produces a significant jet emission, and how powerful the central engine is. Figure adapted from Urry & Padovani (1995).*

constituted of a continuum with superimposed broad and narrow emission lines plus the emission produced by a one-sided jet, likely with superluminal motion. When the jet is observed at acute angles with respect to its axis, or directly down it, then we observe a rapid variable Blazar. When instead the AGN is observed perpendicularly with respect to the jet emission, then a NLRG is observed, with radio lobes. In the intermediate angle cases, if the source is observed closer to the jet it will be classified as a core-dominated FR-I radio galaxy, while a lobe-dominated FR-II will be observed at angles intercepting the torus. However, as discussed in Section 1.2.3.1, the division into FRI and FRII could be attributed to different intrinsic properties, such as a lower accretion efficiency in FRI with respect to FRII (Ghisellini & Celotti 2001).
We will see in more detail in the next sections that not all the properties of the different AGN fit into this simple picture, and that some evidences suggest that the scenario of intrinsically different AGN cannot be excluded at all.

1.4 Insights on AGN structure from X-ray absorption variability

The observation of both short and long time scale X-ray absorption variability in AGN is increasingly common. The variability of the observed X-ray spectra of AGN can be explained by two possible scenarios. The first one is an intrinsic variation in the primary ionizing continuum, that propagates through an homogeneous absorber and that produces a change in the ionization state of the intervening matter, determining a variation of the X-ray spectrum. The second and most probable explanation is that there is a change in the absorber column density, and not in the continuum emission. This alternative implies that the absorber is clumpy and that the observed variation timescale is linked to the time taken by a cloud to cross along the line of sight. A coexistence of both phenomena is also possible. The second scenario has been deeply discussed by Risaliti et al. (2002), showing that these variations are not in agreement with one of the basis of the unified model, i.e the homogeneity of the obscuring parsec-scale torus.
In particular, the rapid variability of the absorbing column density detected in the so called "changing look" AGN, i.e. AGN that have been observed both in Compton-thin and reflection dominated states (Risaliti et al. 2002), implies that, besides being clumpy, the absorbing material must be located at much smaller distance than the conventional obscuring "torus" with velocity, distance and size from the central X-ray source of the same order of those of the Broad Line Region (BLR) clouds. Up to now, we can count only a few "changing look" AGN where such a variability has been discovered on time-scales from a few days down to a few hours: NGC 1365 (Risaliti et al. 2005, 2007, 2009; Risaliti et al. 2009; Braito et al. 2013), NGC 4388 (Elvis et al. 2004), NGC 7674 (Bianchi et al. 2005), NGC 4151 (Puccetti et al. 2007), NGC 7582 (Bianchi et al. 2009), UGC 4203 (Risaliti et al. 2010), NGC4051 (Uttley et al. 2004; Lobban et al. 2011) and 1H 0419-577 (Pounds et al. 2004).
In Fig.1.9 an example of X-ray spectra showing N_H variability is shown, for the Seyfert 2 galaxy NGC 7582. It is evident how the curvature of the X-ray spectrum changes signifi-

cantly on time scales of a few days.
In the most extreme cases, like for NGC 1365 (Fig. 1.10), the spectral change exhibits a transition from a Compton-thin state ($N_{\rm H}$ in the range of $10^{23}{\rm cm}^{-2}$) to a reflection dominated state ($N_{\rm H} \sim 10^{24}{\rm cm}^{-2}$) in time scales of less than a day (Risaliti et al. 2005, 2007; Risaliti et al. 2009; Braito et al. 2013). The rapidity of these occultations implies that the cloud must be moving at velocities v> 10^3 km/s, at distances of $\sim 10^4 R_g$ from the central BH. Risaliti et al. (2009) estimated the distance from the X-ray source and density of the clouds to be $\sim 10^{16}$cm and $\sim 10^{10} - 10^{11}{\rm cm}^{-3}$ respectively. These parameters suggest that the clouds providing the obscuration are located at the BLR distance, therefore they could be both responsible for the X-ray absorption and the broad emission lines in the optical-UV bands.
X-ray variability studies are useful to investigate the clumpy structure of the BLR, but they cannot give information on the clumpiness of the Compton-thick parsec-scale absorber. Indeed, the existence of the parsec-scale absorber can be inferred in the X-ray band through the Fe kα emission line and the Compton hump, giving also information on its geometry. However, the expected variability in the parsec scale torus occurs on longer times scales with respect to the BLR clouds, making its monitoring more difficult.

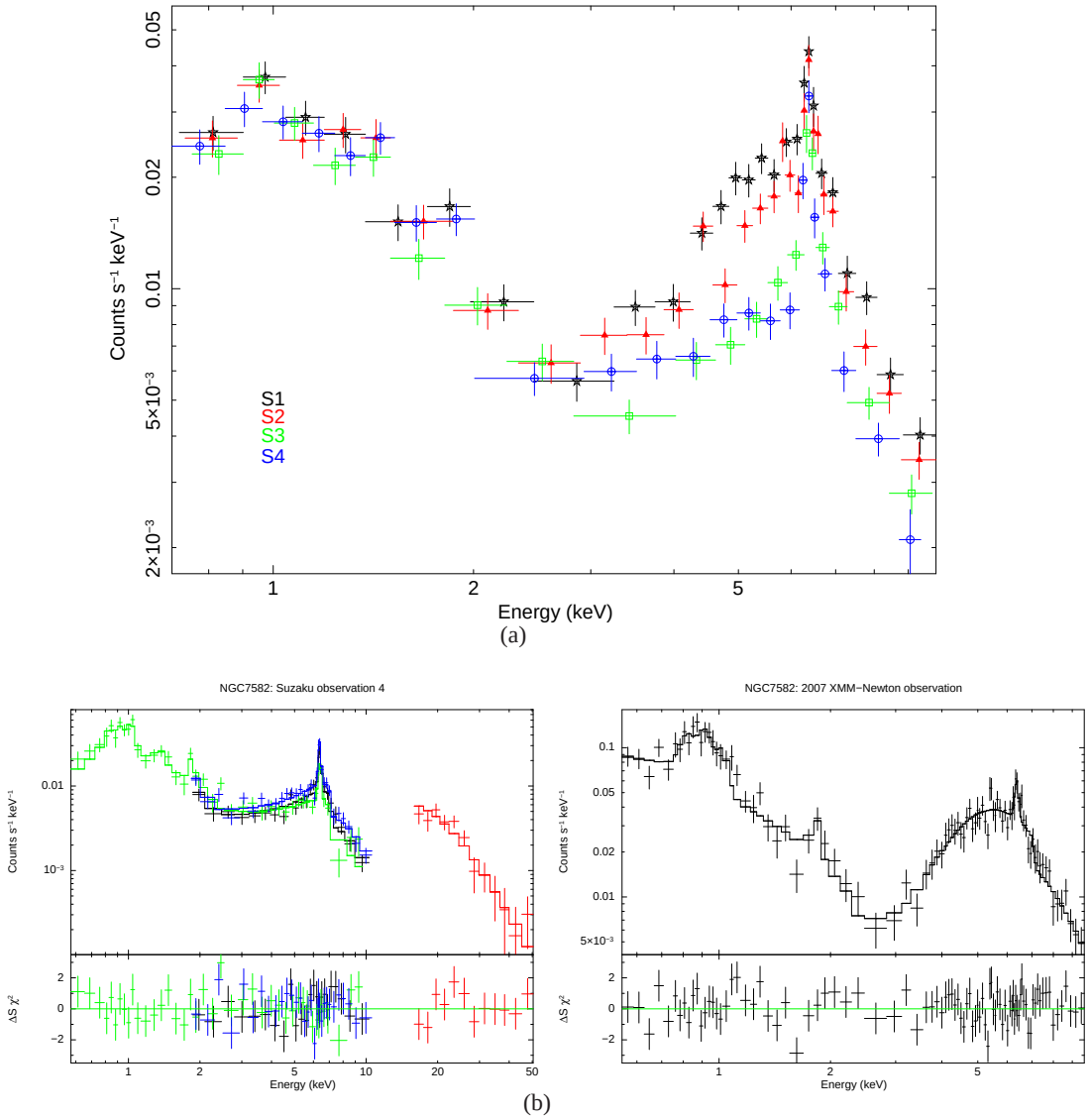

Figure 1.9: *Panel (a):* Suzaku *monitoring campaign of the Seyfert 2 galaxy NGC 7582, that was observed 4 times, on May 1 and 28, and November 9 and 16. The spectra show significant shape variations above 3 keV. Panel (b): comparison between the last* Suzaku *observation (16 November 2007, on the left) and an XMM-*Newton *observations performed on 30 April 2007 (on the right). From a comparison of the two observations it is evident a strong variation in the spectral curvature.* Bianchi et al. *(2009) conclude that most of the variability can be ascribed to rapid (the shortest variability time-scale being 20 hours) changes of the column density ($\Delta N_H \sim 10^{23} cm^{-2}$) of the most internal absorber. Figures adapted from* Bianchi et al. *(2009).*

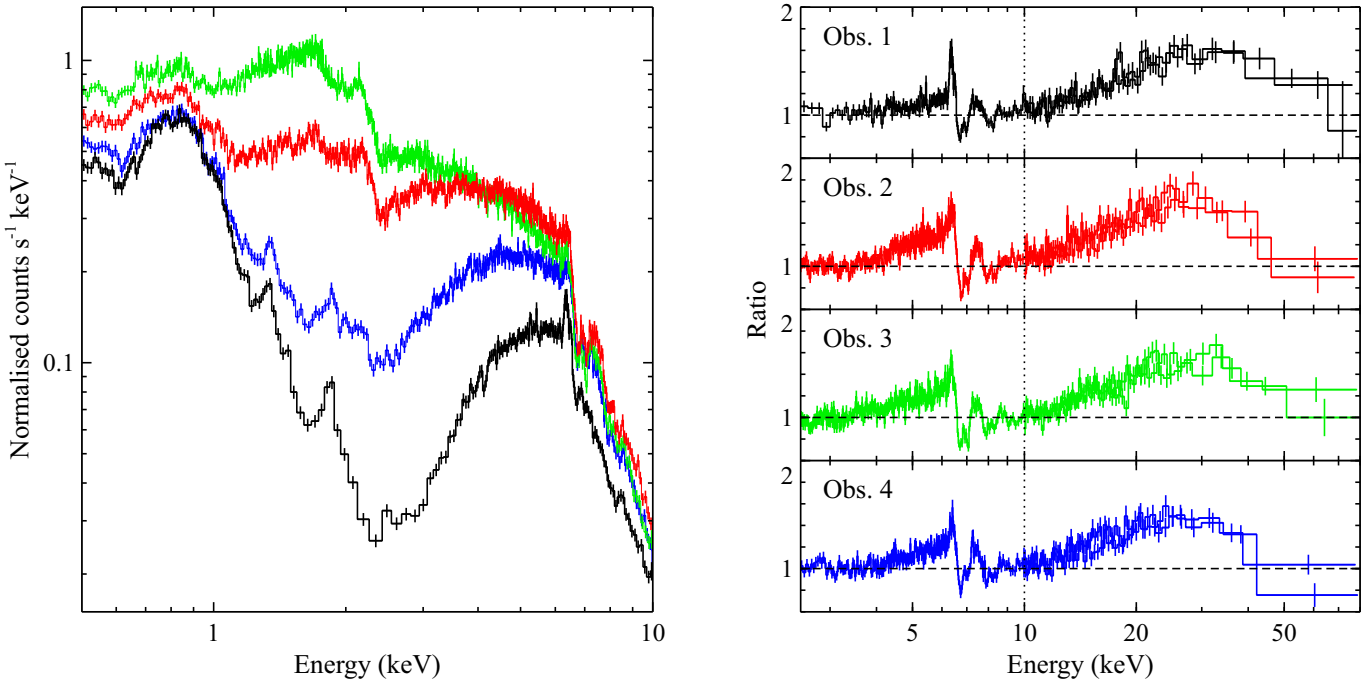

Figure 1.10: *X-ray spectra of the Seyfert galaxy NGC 1365, observed in 4 coordinated* NuSTAR *(Nuclear Spectroscopic Telescope Array,* Harrison et al. 2013*) and XMM-*Newton *observations in July and December 2012, and January and February 2013. The different spectral curvature among the 4 observations shows the extreme variability of the absorption along the line of sight. The panel on the right reports the residuals with respect to a power law with* $\Gamma = 1.75$*, absorbed by partial covering neutral material: the iron line at 6 keV and the Compton hump at 30 keV are observed in all of the four spectra. Figure adapted from* Walton et al. (2014).

1.5 Alternative models

In this section I will describe the main alternative models for the AGN structure, that have been proposed to explain some features and observations that do not completely fit in the Unified Model discussed in Section 1.3.

1.5.1 Elvis (2000) unified scheme

About 10-15% of optically selected quasars belong to a class of objects that hosts strong nuclear outflows, known as Broad Absorption Line Quasars (BAL, Weymann et al. 1991). What characterizes these sources is the presence, in their UV (and in some cases optical) spectrum, of strongly blueshifted broad (FWHM$\geq$ 2000km s^{-1}) absorption lines, due to resonant transitions of ionized metals (e.g. MgII, AlIII, SiIV, CIV, NV, OVI). This indicates the presence of outflowing winds with velocities from thousand of km s^{-1} to 0.2 c (e.g., Turnshek, 1998; Trump et al., 2006). One example of BAL is the quasar PHL 5200 (Junkkarinen, Burbidge, & Smith 1983), whose spectrum is shown in Fig. 1.11.

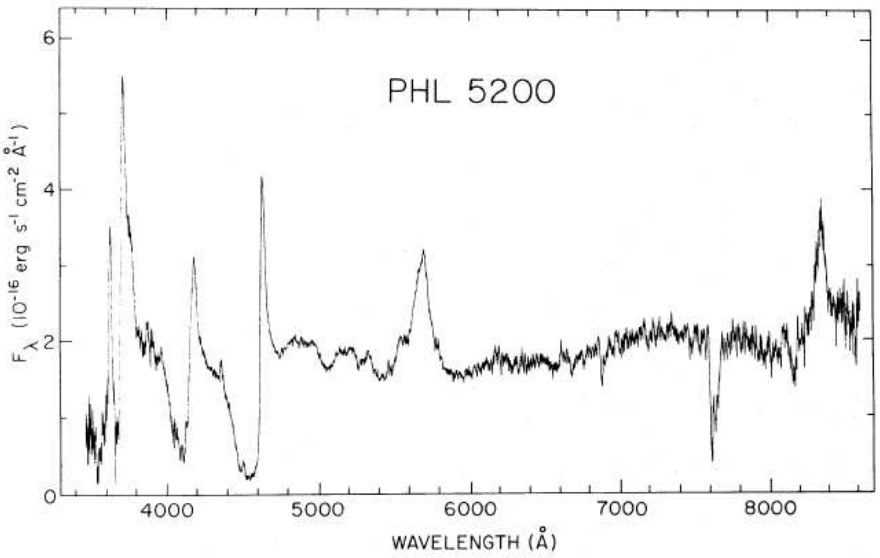

Figure 1.11: *High resolution spectrum of the BAL PHL 5200. With respect to the optical/UV spectrum of a normal quasar (Fig. 1.1 strong blueshifted absorption lines are clearly detectable. Figure adapted from Junkkarinen, Burbidge, & Smith (1983).*

The need of explaining the existence of BALs lead to the formulation of an alternative model to the standard Unified Model. Such model was proposed by Elvis (2000, 2004) and its main ingredient is the presence of a thin shell outflow, whose initial direction is

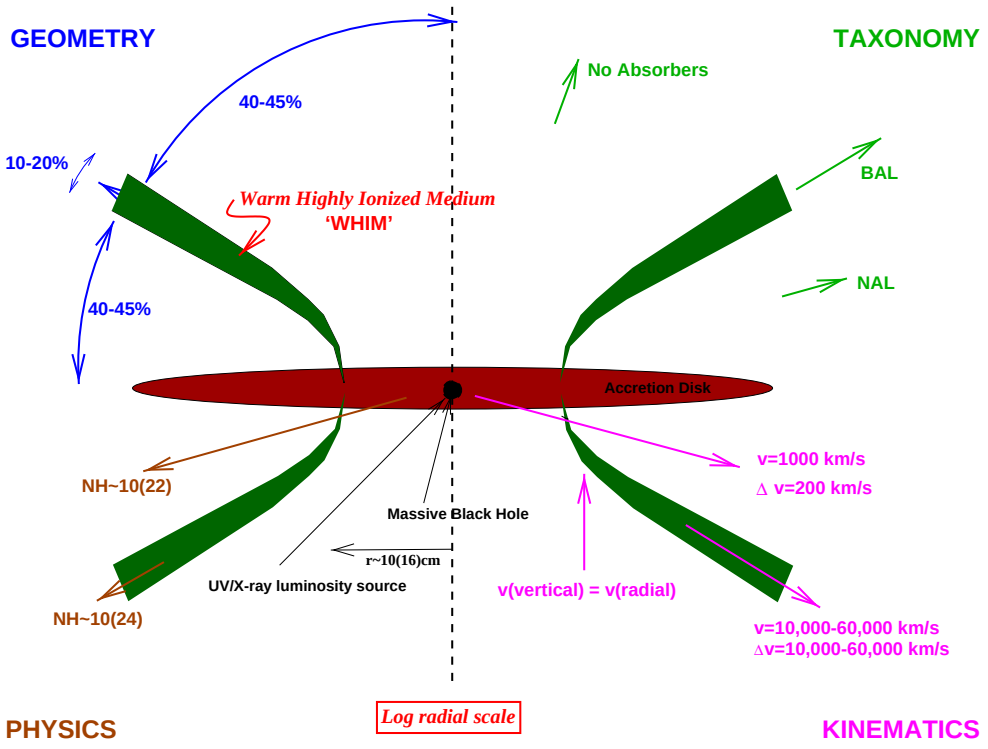

Figure 1.12: *Sketch of the Elvis (2000) model. BALs are seen in the spectrum when the funnel-shaped outflow intercepts the line of sight.*

vertical with respect to the accretion disk, and then is bent outwards by radiation pressure, becoming thicker. The funnel-like geometrical shape of this outflow is shown in Fig.1.12). Depending on the viewing angle, absorbers with different features (or no absorbers) are observed:

- when we observed down the length of the cone, then we detect high velocity and broad absorption lines, typical of BALs;
- when we look across the flow and not along it, only a component of the radial velocity will be directed in the line of sight, therefore we observe lower velocity and narrower absorption lines;
- when we observe the flow from above we do not detect any absorber.

1.5.2 Risaliti (2002) model

As discussed in Section 1.4 it is becoming quite common to observe absorption variability in the X-ray spectra of AGN, often on time scales implying that the absorber responsible for this variability, besides being clumpy, is located at distances compatible with the BLR. The standard unified model cannot explain the X-ray absorption by means of the BLR clouds, since it would predict some unobserved features. Indeed, assuming an isotropic distribution of the BLR clouds, it would predict these clouds to have a covering factor of ∼10% for a type 1 AGN, meaning that multi-epoch observations of the same objects should exhibit X-ray absorption in 10% of the cases. Nevertheless this is not in agreement with the observations, since the fraction of objects changing from type 1 to type 2 is very low. For this reason Risaliti et al. (2002) proposed an alternative scenario, where:

- the absorbing clumpy medium is not spherically symmetric distributed but covers a fraction ∼ 0.8 of the solid angle, according to the actual ratio of Seyfert 2s over Seyfert 1s.
- the number of BLR clouds in Seyfert 2 galaxies is higher than in Seyfert 1s.

A consequence of this is that the difference between type 1 and type 2 AGN is an intrinsic physical property, even if orientation still plays a role, because the X-ray absorber is not spherically symmetric. This model can also explain the absence of IR emission in some type 1 AGN, since it predicts that sources with a quite low number of clouds would almost always be observed as Type 1 objects and their IR emission would be low as compared to the bolometric luminosity.
Risaliti et al. (2002) propose that a possible non-spherical geometry is a biconical one, as described by Elvis (2000). This biconical outflow is a two-phase wind, composed by a warm phase (T∼ 10^5 – 10^6 K), producing scattering phenomena and responsible for X-ray warm absorbers (Section 2.5.1) and a cold phase where the clouds producing the optical broad emission lines are located. The outer layers of the wind are likely composed of dust, transferred from the material inflowing from the host galaxy. With respect to the model proposed by Elvis (2000), they suggest that the BLR clouds inside the wind are more numerous and thus they cover all lines of sights. This model predicts that the variation from type 1 to type 2 is possible only occasionally, when the random motions result in a line of sight free of clouds.

In Fig. 1.13 we report a representation of this model, the features are similar to the Elvis (2000) model, with the addition of dusty inflowing gas reaching the external part of the wind, which is located at higher distances with respect to the outflow invoked by Elvis (2000) model.

1.5.3 Elitzur (2007) model: torus model and clumpy unification

The IR emission characterizing the spectral energy distribution of AGN is a strong indicator of the presence of dust intercepting the primary radiation emitted by the accretion disk. In fact, the radiation absorbed by the obscuring dust is re-radiated at longer wavelengths,

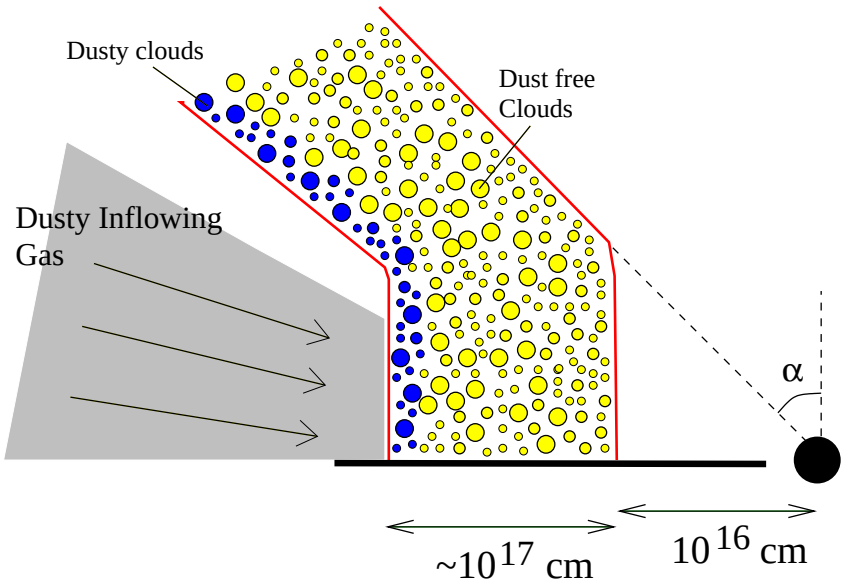

Figure 1.13: *Model proposed by Risaliti et al. (2002) to account for X-ray absorption variability in Seyfert 2s. Both the X-ray continuum produced in the inner regions of the disk, and the broad emission lines (emitted by the dust-free clouds populating the internal region of the outflow) are absorbed by the dusty clouds in the external layer of the wind.*

and we observe it as an IR bump at $\lambda \geq$ micron (Barvainis 1987). The existence in the nuclei of Seyfert 1s of hot dust with temperature close to the sublimation temperature was discovered through various near-IR studies (Storchi-Bergmann, Mulchaey, & Wilson, 1992; Alonso-Herrero et al., 2001; Oliva et al., 1999). For Seyfert galaxies the sublimation radius is on parsec scales, while for quasars it is on sub-parsec scales. Early works, such as the one performed by Krolik & Begelman (1988), already suggested that a smooth distribution of dust could not survive in the proximity of the central engine of AGNs, implying that it should be distributed in a clumpy configuration, which is the model that is recently more accredited.

A lot of observational and theoretical evidences (summarised below) lead to the conclusion that the torus is clumpy, instead of having a smooth distribution:

- **Similarity of the IR emission of Type 1 and Type 2 AGN**
  One of the basis of the Unified Model is that the torus emission is highly anisotropic. Nevertheless its observed emission appears to be almost isotropic (Lutz et al. 2004; Horst et al. 2006). This issue was solved by the clumpy model (Nenkova et al. 2008a,b), which can produce strongly anisotropic obscuration of the AGN together with almost isotropic IR emission, as observed.

- **Torus size and temperature**
  A puzzling result of high resolution IR observations of some AGN (the best studied

one being NGC 1068) is the coexistence of high gradients of dust temperature at the same distance from the central engine. The solution to this problem comes with a torus composed of dusty and optically thick clouds, where the temperature is much higher on the side directly exposed to the radiation with respect to the opposite side (Nenkova, Ivezić, & Elitzur 2002).

Clumpiness introduces the concept of probability of directly observing the central engine as main driver of the difference between type 1 and type 2 AGN (Elitzur 2007, 2008; Nenkova et al. 2008a,b). This means that we cannot exclude to observe a source with a type 2-like orientation as a type 1 source, and inversely. In case of a single cloud obscuration, when the cloud moves out of the line of sight than we would observe directly the nucleus and thus a transition from a type 2 to a type 1 spectrum.
A sharp-edge density distribution for the clumpy torus (left panel of Fig. 1.14) has been ruled out by observations (Nenkova et al. 2008a,b) in favour of soft-edge distributions (right panel of Fig. 1.14), where at each viewing angle the probability of obscuration increases with the number of clouds. The conclusion derived by Elitzur (2007) is that there are two factors determining the fraction of obscured sources: the torus angular width and the average number of clouds along the line of sight.

The fact that the obscuring torus of AGN could not be the same for AGN with the same luminosity (due to the high spread of possible properties of the torus itself) has consequences also on the AGN classification. Indeed, a study performed by Elitzur (2012) highlights that the classification of AGN depends not only on orientation, but also on a higher/lower probability due to higher/lower covering factors of the torus, where by "covering factor" we mean the fraction of the sky covered by the obscuring material at the AGN center. This means that if we consider a sample of AGN with a certain distribution of covering factors C_T, those with larger C_T will have a higher probability to be observed as type 2 sources. Therefore the distribution of covering factors has an high impact on the classification of AGN, with type-1 belonging preferentially to the lower end of the distribution and type-2 to the higher end. The model of Elitzur provides a possible explanation also to other features, such as the results of recent studies (Maiolino & Risaliti 2007; Della Ceca et al. 2008) showing that the fraction of obscured AGN decreases as a function of luminosity, consistently with the hypothesis of a reduction of the covering factor of the circumnuclear dust component as a function of luminosity. A model known as "receding torus model", in which the torus angular width decreases with luminosity (Lawrence 1991; Simpson 2005; Lusso et al. 2013) was proposed in order to explain these observations. According to this model the inner radius of the torus is determined by the dust sublimation radius, which increases with the luminosity of the source. This model assumes a sharp edge obscuration, while instead adopting a soft edge one would add a new parameter, that is the number of clouds. This means that the observed relation between fraction of obscured AGN and luminosity, could also be reproduced by the existence of a dependence of the number of clouds on luminosity, at constant torus angular width, instead of a simple dependence of angular width on luminosity.

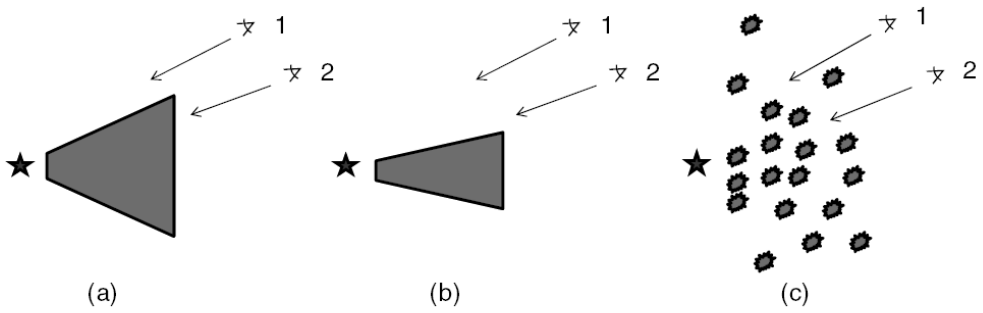

Figure 1.14: *Adapted from Elitzur (2012). Scheme showing the classification of AGN in the unified models. (a) Standard Unified model of an homogeneous torus, where every observer located inside the opening angle (such as observer 2) will see the source as a type 2 AGN. (b) if the covering factor of the torus decreases (e.g. it is a decreasing function of luminosity, Lawrence 1991; Simpson 2005), then more observers will see the source as a type 1 AGN. (3) if the torus is clumpy the probability of observing directly the central engine of the AGN decreases away from the axis, but it is always not null.*

1.5.4 Torus disk-wind model: basis for a "grand unification scheme"?

In the last years many observations and theoretical works seem to indicate that the torus is just a smooth continuation of the BLR (Elitzur & Ho 2009; Netzer & Laor 1993). Thus, according to these works, the torus is a region, located beyond the dust sublimation radius, where the clouds start to contain an important amount of dust, besides the gas content characterizing the BLR clouds. Some of the evidences leading to these hypotheses were:

- The finding of the so called "true" type 2 AGN (Laor 2003), i.e. Seyfert galaxies in which the BLR is not obscured, but it is actually missing (Nicastro, 2000; Elitzur & Ho, 2009).

- In agreement with what already proposed by Netzer & Laor (1993), a work presented by Suganuma et al. (2006) measured the inner radius of the dusty torus for a sample of four Seyfert 1 galaxies and found evidence that the BLR extends until this boundary. The conclusion of this work is that, when the inner radius of the torus is reached, a physical transition takes place, and dust gets embedded in the clouds, suppressing line emission and absorbing the ionizing radiation coming from the central regions.

- Risaliti et al. (2002) observed that the X-ray variability due to the motion of clouds along the line of sight has the same behaviour on a big range of time-scales, that

can be attributed both to the passage of dust-free BLR clouds or more distant dusty clouds belonging to the torus.

According to these studies the BLR clouds and the torus are a unique structure, characterized by clouds at different distances and composition. Therefore there are not physically different regions producing X-ray obscuration, broad emission lines and dust obscuration, but they all are a continuous distribution of clouds, where the different composition and ionization state of the material at different distances determines the variety of observed features.
This attempt of unification is in good agreement with Elvis et al. (2004) model. Indeed in this scenario the torus is a region in a clumpy wind coming from the accretion disk (from here the name "disk-wind model"), rather than being produced by accretion of material from the galaxy (as proposed by Gaskell 2009).

In agreement with observations, the disk wind scenario predicts that at low luminosities ($< 10^{42}$ erg/s) the torus might not exist any more, due to the low accretion rate that cannot provide the necessary outflow rate. Besides, it is expected that when L decreases still further, also the outflow from the inner ionized zone decreases, implying that also the BLR disappears (Nicastro, 2000). This seems to be in agreement with the observation of some "true" type 2 sources, among AGN with L$< 10^{42}$ erg/s (Laor 2003).

Despite the many detailed theories proposed in order to explain the complexity of the phenomenon of AGN, up to now there is still not a prevalent one. All of them confirm the existence of an axisymmetric circumnuclear inhomogenous absorber. I will discuss in detail in the next chapter the importance that X-rays observations have in the framework of confirming/refusing the validity of these models, being the energy band that better allows to study the most internal region of AGN.

Chapter 2

The X-ray spectrum

Contents

2.1 X-ray primary continuum 40
2.2 The reprocessed X-ray spectrum 43
2.2.1 Reflection 44
2.3 Fluorescence emission lines 46
2.3.1 Ionised reflection 50
2.4 X-ray absorption 51
2.4.1 Cold X-ray absorption: Compton-thin and Compton-thick matter . 51
2.5 Ionised absorption 53
2.5.1 Warm absorbers 53
2.5.2 Ultrafast outflows 55

Observing AGN in the high energy bands (X-rays and γ rays) provides a lot of information that other bands do not show. In particular the X-rays originate from very close to the central black hole, thus they offer the possibility to study the innermost regions of SMBHs and the still poorly understood accretion process that feed them.
Figure 2.1 shows the typical X-ray spectrum of a Seyfert 1 galaxy with the various spectral components:

- The dominant component of the X-ray spectrum is a power law with an exponential cut off at high energies. This component is produced by Compton up-scattering of soft optical-UV photons emitted by the accretion disc with relativistic electrons of the corona located above the disc. The exponential cut-off at high energies is produced when the scattered photons reach their maximum energy, that is the energy of the electrons.

- Being isotropic, a fraction of the radiation produced in the corona is directed towards the disc, where it is scattered generating a secondary emission characterized by a peak between 20 keV and 40 keV (Guilbert & Rees, 1988; Lightman & White, 1988; George & Fabian, 1991), plus fluorescence lines, the prominent one being the 6.4 keV Kα fluorescent line produced by neutral iron. The bump in the 20–40 keV energy range, also known as “reflection hump” is due to two processes: at energies < 10 keV the photoelectric absorption is the dominant interaction mechanism, while at higher energies (> 50 keV) the Compton down-scattering (in the Klein-Nishina regime) induce the energetic photons to lose energy in favour of the lower energy electrons on which they scatter (so the spectrum falls down at high energies).

- For many AGN the nuclear radiation intercepts a partially ionized optically thin plasma, called "warm absorber" (Reynolds, 1997; Fabian, 1999; George et al., 2000; **?**; Blustin et al., 2005), which imprints the main absorption features observed in the soft X-ray spectrum. The first source in which the presence of such intervening medium was first discovered in QSO MR 2251-178 (Halpern 1984, Fig. 2.2). This phenomenon is easily observed in Type 1 AGN.

- In most sources the X-ray spectrum shows an "excess" of emission with respect to the extrapolation of the primary power law in the soft X-ray band (below 1 keV), known as "soft excess" (Holt et al., 1980; Pravdo et al., 1981; Singh, Garmire, & Nousek, 1985; Arnaud et al., 1985). The origin of this soft X-ray component, that can be phenomenologically modelled with a blackbody with effective temperature of $\sim 0.1 - 0.2$ keV (Vasudevan et al. 2014), is still unclear. The first hypothesis of being the high energy tail of the optical-UV disc emission has been ruled out by observations (see e.g. Ponti et al. 2010 and references therein), since different temperatures should be observed depending on the mass of the central black hole and on the accretion rate. Instead the observed temperature is much higher than what foreseen for a standard accretion disc and it does not show strong dependence on the SMBH mass. Some processes that have been proposed in order to explain soft excess are:

  1. ionised reflection in the inner regions of the accretion disc, where the X-ray lines undergo relativistic blurring (Ross & Fabian 2005);
  2. relativistically smeared absorption occurring at high energies (above $\sim$ 0.7 keV). The high velocity of the absorbing clouds make undistinguishable their atomic spectral features, resulting in an apparent soft excess, which represents the real power law at low energies (Gierliński & Done, 2004), and a harder spectrum at higher energies.
  3. the existence of two Comptonizing regions, a hotter one responsible for high energy emission, and a colder one producing the soft X-rays (Laor et al., 1997; Magdziarz et al., 1998).

  Soft excess could also result from the combination of emission lines of collisionally ionised ions and thermal radiation produced by hot gas in the host galaxy, especially if the galaxy has a significant star formation activity.

2.1 X-ray primary continuum

As anticipated, the primary broadband X-ray spectrum (1–300 keV) of AGN can be well described using a power law. It is common in X-ray astronomy to use as unit of measurement the photon flux per unit energy F(E) (photons per keV) instead of the energy per unit of frequency:

$$F(E) \propto E^{-\Gamma} e^{-\frac{E}{Ec}} \text{photons} \cdot \text{cm}^{-2} \cdot \text{s}^{-1} \cdot \text{keV}^{-1} \tag{2.1}$$

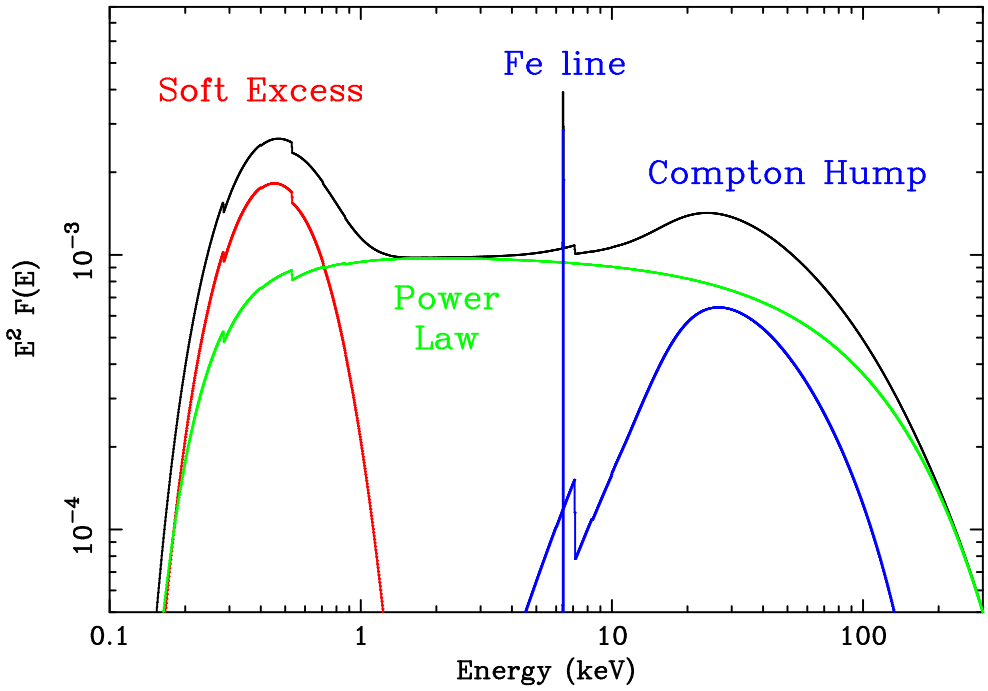

Figure 2.1: *Typical X-ray spectrum of a type 1 AGN, showing the various spectral components frequently observed. The components are: 1) the primary continuum component (green), represented by a power law with an high energy cut-off at E ∼ 100 keV, absorbed at soft energies; 2) a cold reflection component (blue) 3) the neutral iron FeKα emission line at ~6.4 keV (blue); 4) a "soft excess" modelled with a black body component (red). The thick black line is the final resulting X-ray spectrum. Image adapted from* Fabian *(2006).*

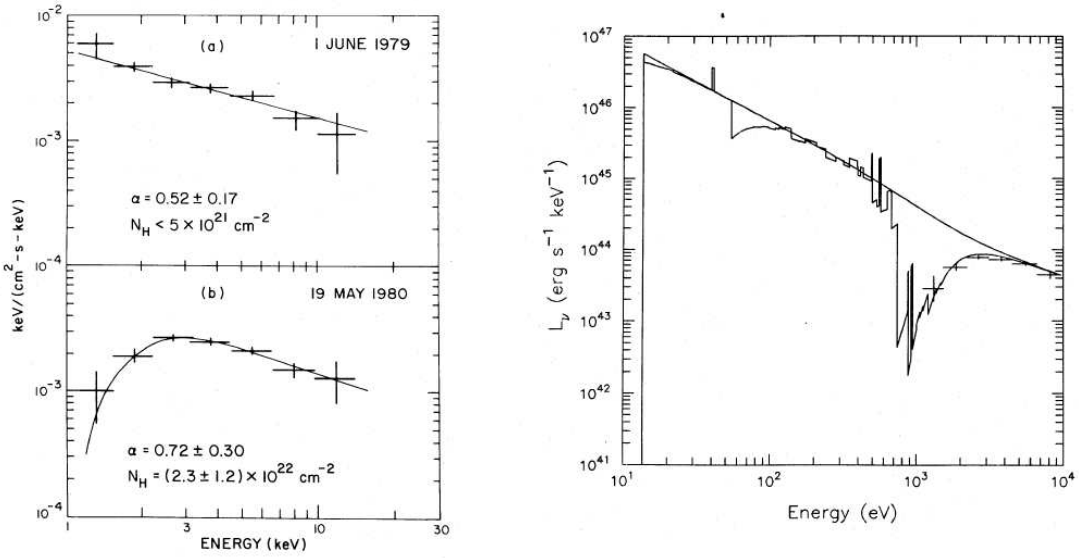

(a)

Figure 2.2: *Left panel: first X-ray spectra of the QSO MR 2251-178, observed in two occasions (June 1979 and May 1980) by the* Einstein Observatory *(Giacconi et al. 1979). Halpern (1984) explained the increase in absorption column density between the two observations with a model where the primary continuum intercepts and ionises a cloud. Right panel: Incident and emergent spectra obtained using a warm absorber model that, differently from a neutral absorber, is not totally opaque at energies below 1 keV, and shows absorption edges due to O* VII *(739 eV) and O* VIII *(870 eV). Figures adapted from Halpern (1984). It is interesting to compare this spectra with the more recent one shown in Fig. 2.8.*

where Γ is the photon index of the power law, related to the spectral index α by $\Gamma = \alpha + 1$ and E_c is the high energy cut-off, which I'll discuss in the end of this section. The photon index is on average in the range $\Gamma \sim 1.8 - 2$ (e.g. Dadina 2008; Beckmann et al. 2009). We have seen in Section 1.3.1 that the simplest mode of accretion (through a disc) leads to the production of a strong optical-UV continum (Shakura & Sunyaev 1973). Thus, the thermal emission from the disc cannot be responsible for the radiation emitted in the X-rays. Furthermore, the rapid variability observed in the X-rays indicates that they originate in the innermost regions of AGN. Since the X-ray luminosity represents an important fraction (about 5–40%, Marchese et al. 2010) of the bolometric luminosity, this mechanism must be efficient in transferring the energy released in the accretion disc to a hotter plasma, emitting higher energy radiation. The model explaining the power law shape of the X-ray spectrum is based on Compton up-scattering of soft (optical-UV) photons on a corona of relativistic electrons in the inner regions of the accretion disc (Haardt & Maraschi 1991, 1993). How the heating of the electrons in the corona is produced is still under debate, however one possible explanation is that the energy transfer from the accretion disc is due to the presence of magnetic fields, via reconnection of magnetic loops extending out of the accretion disc. Since the maximum energy that the scattered photon can acquire is related to the thermal energy of the electrons in the corona, the cut-off of the primary power law depends on the plasma temperature. The high energy cut-off is observed in the range $\sim 50-200$ keV (Malizia et al. 2014; Dadina 2008). An estimate of the plasma temperature was provided in several works (see e.g. Petrucci et al. 2001; Molina et al. 2009) and recently confirmed by Malizia et al. (2014) to be in the range from 20 to 100 keV (or $2-12\times 10^8$ K) [1]. The recent launch of the X-ray mission *Nustar* (Harrison et al. 2013), observing in the 3-79 keV energy band with a lower background than *Suzaku* and a higher effective area than XMM-*Newton* above 6 keV, is providing accurate measurements (or lower limits) to the high energy cut-off for several AGNs: MGC-5-23-16 (116±6 keV; Baloković et al. 2015), IC 4329A (186±14 keV; Brenneman et al. 2014), SWIFT J2127.4+5654 (108±11 keV; Marinucci et al. 2014), 3C 382 (214^{+147}_{-63} keV) in one of the two NuSTAR pointings, and > 190 keV in the other pointing, Ballantyne et al. 2014), Ark 120 (>190 keV; Matt et al. 2014), and in NGC 2110 (>210 keV; Marinucci et al. 2015), NGC 5506 (>350 keV, Matt et al. 2015).

2.2 The reprocessed X-ray spectrum

Since the AGN corona is likely to be located at distance of a few tens of R_g, the X-ray continum could undergo reprocessing due to the gas present in different locations, from very near to the central black hole to the outer regions. If we assume isotropy in the X-ray continuum photons emitted by the corona, then some of them could escape along the line of sight and likely interact with material along their path, some of them may instead irradiate the accretion disc, being then reflected towards the observer. This implies that the observed spectrum is a combination of the primary and the reprocessed X-ray continuum.

[1] As described in Malizia et al. (2014) , when the optical depth is $\tau \leq 1$ the plasma temperature kT_e is estimated as $kT_e = E_c/2$, instead when $\tau >> 1$ a better estimate is given by $kT_e = E_c/3$ (Petrucci et al., 2001).

2.2.1 Reflection

The designation of Compton "reflection" refers to those photons that are scattered "back" towards the observer, thus they maintain the initial direction. The optically thick material responsible for the reflection can be located near to the central engine (the accretion disc) or further away (like the putative molecular torus).

Let's assume an X-ray photon incident upon a semi-infinite slab of uniform density, covering 2π sr of the sky with respect to the X-ray source. The photon can undergo one of the following interactions:

- Compton down scattering with free electrons
- Photoelectric absorption, either resulting in a fluorescent emission line or followed by Auger decay

The predominance of a process between photo-electric absorption and scattering is determined by two factors: the initial energy of the photon and the relation between the cross sections of the two mechanisms. At energies below 10 keV, photoelectric absorption is the dominant process in neutral material, since its cross section decreases as E^{-3}, becoming equal the to Thomson scattering cross section at around 10 keV. At this energy the cross sections of the two processes are approximately equal, while above ∼10 keV the reflection fraction increases and dominates over the fraction of absorbed photons, due to the higher scattering cross section.

At even higher energies, the photon energy is such that Compton down scattering is important, so the reflection is no longer elastic and the incident photons lose energy in the process. The amount of energy lost due to Compton down scattering gets larger for higher energy photons (Murphy & Yaqoob 2009; Antonucci 1993). Typically the energy lost by a photon during a Compton scattering is $\Delta E/E \simeq 2/m_e c^2$, thus at energies higher than 30 keV it is more than 10%. Considering all these processes, neutral reflection gives rise to a flattening of the spectrum (with respect to the primary power law) at energies 5-50 keV and to a very characteristic peak between 20-50 keV, where lower energy photons are photo-electrically absorbed (George & Fabian 1991; Matt, Perola & Piro 1991).
Differently from photo-electric absorption, Compton-scattering depends on the geometry of the absorber. Indeed the reflection hump produced by a toroidal absorber with a given opening angle is weaker than the one produced by a sphere. In fact the amount of reflection is proportional to the solid angle irradiated by the central source and to the surface area of the absorber seen by the observer (Murphy & Yaqoob 2009; Brightman & Nandra 2011). In this thesis I will adopt a reflection model (PEXRAV, Magdziarz & Zdziarski 1995) that describes the radiation reflected out of the line of sight by a semi-infinite slab of cold material subtending an angle defined by the parameter R (Magdziarz & Zdziarski 1995), that in case of an isotropic source represents the solid angle subtended by the material producing reflection:

$$R = \Omega/2\pi \tag{2.2}$$

The value of the parameter R has also a dependence on the inclination angle *i* between the perpendicular to the reflector and the line of sight, i.e. when *i* is small the observed reflection component is larger. Besides the PEXRAV model, throughout the thesis I also used the MYTORUS model, which models the complex transmission and reflected spectrum of AGN over a broad energy range and for a large range of absorbing column densities. The geometry assumed in the two models is different, in fact while PEXRAV assumes the geometry of a reflecting semi-infinite slab, MYTORUS is based on a toroidal geometry with a half opening angle of 60°. A detailed description of these models can be found in Section 3.3.3.

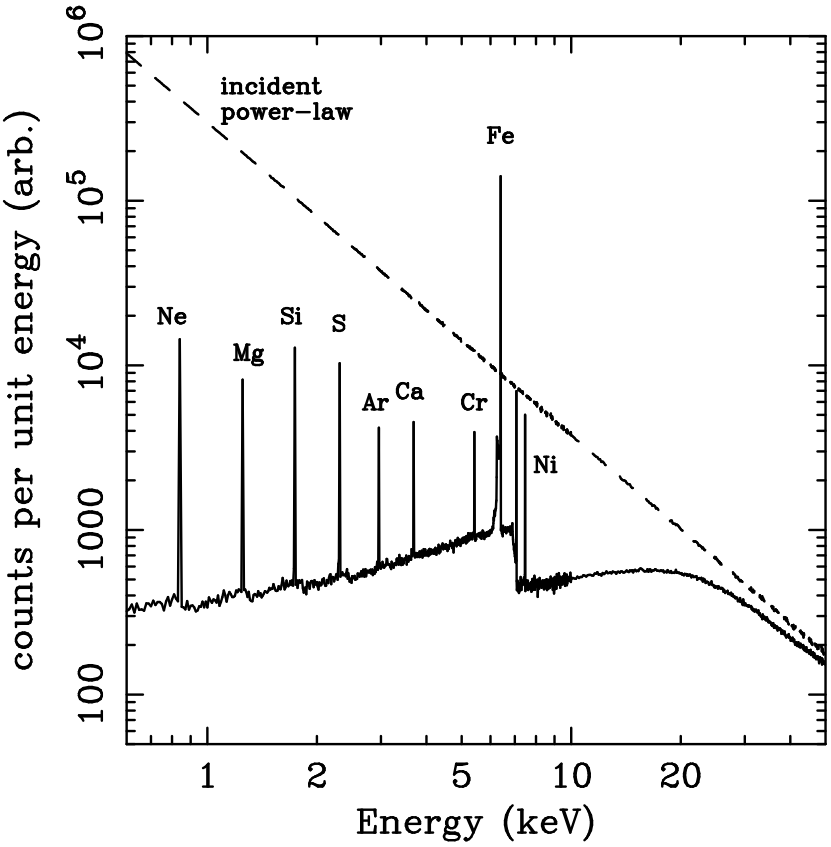

Figure 2.3: *X-ray reflection spectrum from a neutral, constant density illuminated slab. The dashed line shows the incident continuum and solid line shows the reflected spectrum (integrated over all angles). Most of the radiation below 20 keV is absorbed by the metals and re-radiated at lower energies. Solar abundances are assumed. Figure adapted from Reynolds 1997.*

2.3 Fluorescence emission lines

The reflection spectrum shown in Fig. 2.3 is characterized by several emission lines. They are generated when an incident X-ray photon is photoelectrically absorbed by a neutral or partially ionised atom. This will result in either a fluorescent emission line or the ejection of an Auger electron. The probability that an excited ion will de-excite through a fluorescent line emission versus the Auger effect is given by the fluorescent yield. The strongest fluorescent lines observed in AGN are from iron, due both to its high abundance and its high fluorescence yield (which scales as Z^4, where Z is the atomic number). The production of the iron fluorescent lines occurs when one of the two electrons in the K shell (n=1) is ejected, due to the absorption of an X-ray photon. The threshold for this absorption (the so called "absorption edge") corresponds to the binding energy of the inner shell, thus it depends on the ionization state of the atom. To higher ionization states correspond higher energy absorption edges (since the electrons are more tightly bound). For neutral iron the absorption edge is at 7.1 keV. Once the photon has been absorbed and the inner shell electron has been ejected, an L-shell (n = 2) electron can drop into the K-shell (in a 2p→1s transition), releasing 6.4 keV [2] of energy (in the case of neutral iron) either as an emission line photon (34% probability) or an Auger electron ejected from the ion (66% per cent probability, Fabian et al. 2000). There is also a Kβ line at 7.06 keV, when an n=3 (M shell) electron drops to fill the hole in the K-shell (3p→1s transition) ; the Kα:Kβ flux ratio is approximately 13.5% (Palmeri et al 2003).
In case of Helium-like iron (FeXXV) the Kα line is emitted at ~6.7 keV , while for Hydrogen-like iron (FeXXVI) the Lyα line is emitted at ~6.97 keV.

Since reflection can be produced both by the accretion disc and by a more distant reprocessing structure, there is a certain complexity in the observed fluorescent emission lines. Indeed a "narrow" (FWHM<5000 km s^{-1}, Murphy & Yaqoob 2009) Fe Kα line is always observed (Yaqoob & Padmanabhan 2004), presumably produced by the outer regions of the accretion disc of from matter locater far from the black hole. Since the peak of this narrow Fe Kα line is at ~ 6.4 keV in most of the cases this provides an evidence that it is produced by cold material (Nandra et al. 1997a; Nandra et al. 1997b; Reeves et al. 2003; Levenson et al. 2006). Besides the narrow Fe Kα line also a component called "Compton shoulder" is often observed. In fact, once a Fe Kα line is emitted it can undergo Compton scattering, loosing part of its energy, so the "narrow core" of the line gets spread downwards in energy. In a few cases, Fe Kα line photons undergo more than one Compton scattering and a red wing at energies < 6 keV is formed (Matt, Perola & Piro 1991, George & Fabian 1991; Leahy & Creighton 1993, Sunyaev & Churazov 1996). In the majority of the cases the biggest contribution to the Compton shoulder is given by photons scattered only once, and its EW is expected to be about 10-20 % of the Fe Kα EW (Matt 2002; Yaqoob & Murphy 2010). In Fig. 2.4 it is reported a typical X-ray reflection spectrum from neutral material, where the Compton shoulder is visible.
A further complexity in some cases is due to the detection of a broad Fe Kα

[2] The FeKα is the results of the blending of a doublet, the Kα1 at 6.404 keV and Kα2 at 6.391 keV (see Fig. 2.4), that currently cannot be disentangled with the current X-ray instruments.

(FWHM~30,000 km s^{-1} or even more, Murphy & Yaqoob 2009), likely originating in proximity to the central engine, and thus presenting gravitational and Doppler energy shifts. However such extreme cases are highly debated, since when the line profile is so broad it is difficult to disentangle the contribution from the emission line and the underlying continuum.

The profile of the Fe Kα emission line can be used to study what is the motion and the gravitational field of the matter in the location where the line emission takes place. The intensity of the line gives insight into the amount of the absorbing/reflecting material, while the peak energy of the line gives information on the ionisation state of the emitting material (as we discussed for neutral material $E_{FeK\alpha} \sim 6.4$ keV, while for FeXXVI $E_{FeK\alpha} \sim 6.97$ keV). Finally, line broadening can give indication on the relative motion with respect to the observer. If the line-emitting material is moving in keplerian motion, then the line profile will show Doppler broadening. Besides, as I will discuss in next section, the profile of the line can show features indicative of relativistic effects.

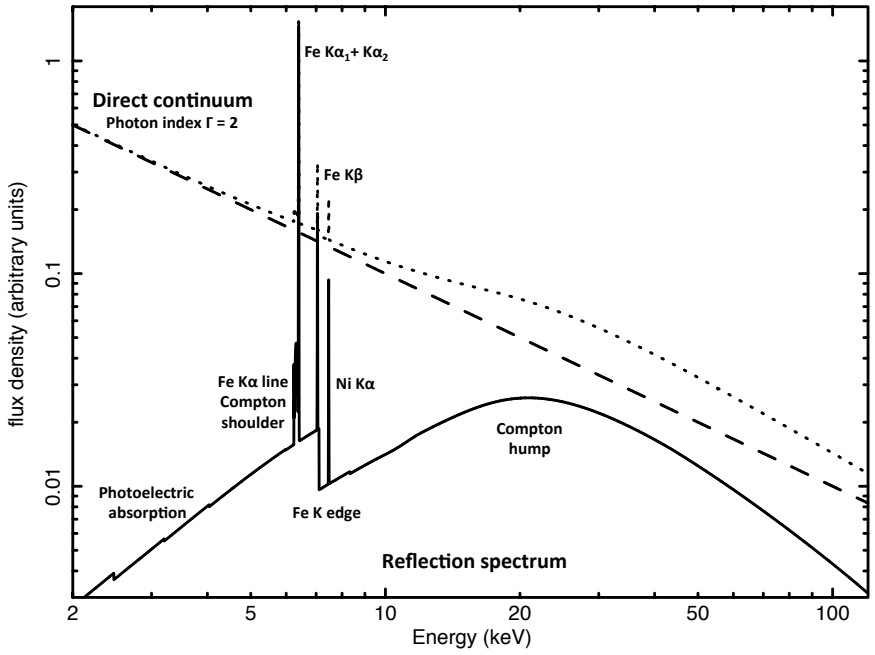

Figure 2.4: *Model representing the typical X-ray reflection spectrum where the Fe Kα doublet, the Fe Kβ, the Fe K edge and the Compton hump are shown. Figure adapted from Ponti et al. (2013)*

2.3.0.1 Relativistic effects on the Fe Kα profile

The distance of the line-emitting material with respect to the black hole determines the importance of relativistic effects affecting the profile of the line. If the region producing the emission line is located near the black hole, like in proximity of the innermost region of accretion disc, its shape also depends on the inclination of the emitting region with respect to the line of sight and on the spin of the central black hole. In summary (Fabian et al. 2000):

- a double horn profile is produced even in a non relativistic disc, due to the matter whose motion along the line of sight is approaching (blueshift) or receding (redshift). The broader component of the line is due to faster moving matter, thus matter located in the inner regions of the disc (first panel of Fig. 2.5);
- closer to the black hole, the effect of special relativity is to increase the contribution of the blue peak of the line (second panel of Fig. 2.5). Besides, the transverse Doppler effect produces the shift of the emission coming from each radius to a lower energy;
- the gravitational redshifting (implying that "clocks run slowly") also produces a further shift to lower energies, as shown in the third panel of Fig. 2.5. The final line profile produced by the combination of the above cited effects is shown in the fourth panel of Fig. 2.5;
- when the line emitting region is close to the black hole the line profile is dependent on the inclination. This is because the beaming is a strong function of the inclination of the disc, thus the blueshifted tail of the line increases with inclination (left panel of Fig. 2.6);
- finally, the extension of the red wing of the line depends on the inner radius of the disc (right panel of Fig. 2.6), and therefore on if the BH is spinning. Indeed, when the inner radius is smaller, the gravitational reddening is stronger and thus the line is broader "redwards".

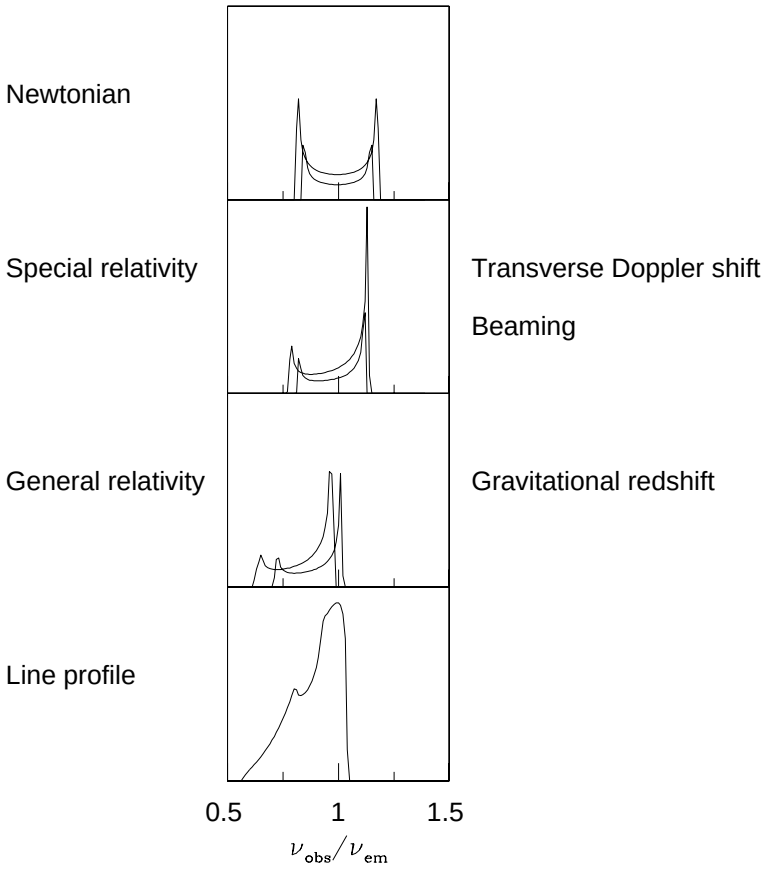

Figure 2.5: *These panels show separately the several effects that act on the profile of the line: the Newtonian motion in the disc determines a symmetric double peak (upper panel), the relativistic beaming enhances the peak bluewards (second panel) and finally gravitational redshift and transverse Doppler effect shift the energies redwards (third panel). The resulting line profile is shown in the lower panel. Figure adapted from* Fabian et al. *(2000).*

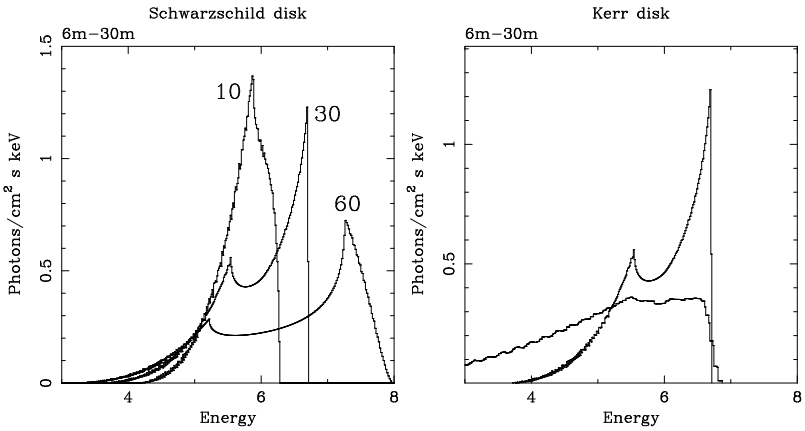

Figure 2.6: *Left panel: iron line profile produced by an accretion disc around a non spinning (Schwarzschild) black hole, for three different inclination: 10°, 30°, 60°. It is observable that to higher inclinations corresponds a higher extent of the high energy tail of the line profile. Right panel: comparison of the line profiles produced by a Schwarzschild black hole (narrower profile) and a Kerr Black hole. The different distances of the innermost radius (*$6r_g$ *and* $1.25r_g$ *respectively) have the effect of increasing the redshift and the width of the line. Figures adapted from* Fabian et al. (2000).

2.3.1 Ionised reflection

As we discussed at the beginning of Section 2.2.1 reflection can be produced either by neutral material or ionized matter, showing different features. I will now describe what are the characteristics of the reflection spectrum produced by ionised matter. First of all, when the reprocessing matter is ionized, there is a lower contribution from photoelectric absorption, and thus the emission below 10 keV is higher. I introduce here the ionisation parameter, defined as

$$\xi = L_{\rm ion}/nR^2 \tag{2.3}$$

where $L_{\rm ion}$ is the 1–1000 Rydberg[3] ionising luminosity, n is the electron number density and R is the distance of the ionising source from the absorbing clouds. This parameter is a measure of the ratio of the ionizing radiation to the gas density, thus it is a measure of the degree of ionization. In figure 2.7 I show the expected reflection spectra for different ionization parameters. As shown by several works (Matt, Fabian, & Ross 1993; Matt, Brandt, & Fabian 1996; Fabian et al. 2000), there are different regimes of X-ray reflection depending on the ionization state of the material. I will describe them here and graphically in Fig. 2.7:

- when reflection is produced in weakly ionized ($\xi < 100$ erg cm s^{-1}) material in the accretion disc, most of the X-ray emission is absorbed below ~10 keV, and the

[3] 1 Ry=13.605 eV

spectrum is characterized by a cold iron line at 6.4 keV and a small iron absorption edge at 7.1 keV.

- when the disc is moderately ionised (100 erg cm s^{-1} < ξ < 500 erg cm s^{-1}) the low energy spectrum exhibits strong emission lines (e.g. lines due to Oxygen, Carbon, Nitrogen, Neon, Iron L-shell transitions). The presence of partially ionised iron with a vacancy in the L shell (n=2) increases the occurrence of resonant absorption of Kα photons so that these photons are mostly trapped in the surface of the disc, making iron Kα emission line is very weak (Fabian et al. 2000).

- when the ionisation state rises until $\xi \sim 5000$ erg cm s^{-1} almost all elements with the exception of iron are fully ionised, thus the spectrum in the soft X-rays shows only weak spectral features. The iron emission line (at $\sim$ 6.8 keV) is very strong, due to the higher fluorescence yeld and lower Auger effect.

- when the disc is highly ionized ($\xi \geq 5000$ erg cms^{-1}) all the elements (included iron) are completely ionized, no emission lines are produced and no absorption edges are produced. The reflection component of the spectrum resembles the primary power law, thus the reflecting medium behaves like a perfect mirror.

2.4 X-ray absorption

2.4.1 Cold X-ray absorption: Compton-thin and Compton-thick matter

The most important broad spectral feature observed in the X-ray spectra of Seyfert galaxies is the cut-off in the soft X-ray region due to photoelectric absorption, which is produced mainly by the circumnuclear material in the active galaxy and in lower part by the interstellar medium. The absorbing matter is not only constituted by the molecular torus, but also other absorbing components can contribute: the BLR, the host galaxy (dust lanes and starburst regions). This material suppresses the primary X-ray continuum and thererfore allows to detect features (such as the emission from the NLR) that would be too weak or hidden in Seyfert 1 galaxies.
By measuring the energy at which photoelectric absorption occurs it is possible to infer what is the column density of the absorbing material. The observed values for the intrinsic absorption column density span from $N_{\rm H} \sim$ few $\times 10^{20}$ cm^{-2} up to $N_{\rm H} > 10^{25}$ cm^{-2} with a distribution peaked at $\sim 10^{23-24}$ cm^{-2}, as reported by Risaliti, Maiolino & Salvati (1999) for a large sample of local Seyfert 2s, thus for AGN where the line of sight intercepts absorbing material.

In Compton-thick sources a fraction of the primary radiation is still observable at energies above 10 keV, but when the column density reaches $N_{\rm H} > 10^{25} cm^{-2}$ then the radiation is totally blocked, even at hard X-rays. At this high values of $N_{\rm H}$ the Compton down scattering acts on high energy photons, which are subsequently photoelectrically absorbed. Even when the primary radiation is totally absorbed (at least at energies below 10 keV) it is still possible to observe its presence because a fraction is reflected along our line of

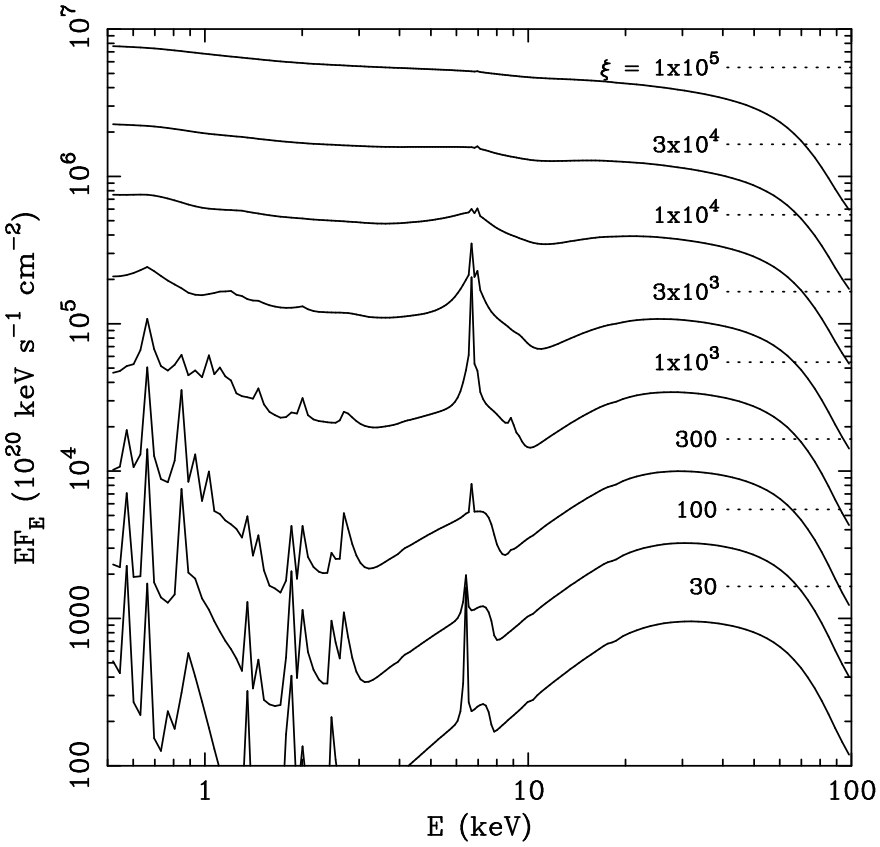

Figure 2.7: *The figure shows the reflection spectra produced by an ionized slab (with ionization parameter ξ). The dotted lines on the right part of the plot show the primary ($\Gamma = 2$) power laws. When the gas is lowly or moderately ionised ($\xi < 500$ erg cms^{-1}) below about 1-2 keV there is a strong contribution due to soft X-ray lines (such as e.g. Oxygen, Carbon, Nitrogen, Neon, Iron L). The upper spectra of the plot represent the cases in which the disc becomes more ionized, which has a strong influence on the importance and the shape of the spectral features. Adapted from Fabian (2000).*

sight from neutral or ionised gas. As this component is more than one order of magnitude fainter than the primary emission, Compton thick sources are usually more difficult to find, especially at higher redshifts.

Type 2 AGN are those sources where the direct radiation is intercepted by the torus, implying that the EW of the Fe $K\alpha$ is expected to be larger. For the case of Compton-thick sources, for example, the primary radiation is completely absorbed, leaving only the reflection component to be observed. Instead, in Compton-thin sources, where the primary continuum is less diluted by the absorbing matter, we observe a weaker emission line. In particular, for Compton-thin sources the equivalent width of this emission line does not exceed a few hundred of eV, while for Compton-thick sources it can reach values of more than 1 keV.

2.5 Ionised absorption

2.5.1 Warm absorbers

The existence of ionized material along the line of sight was discovered for the first time in the '80s from the analysis of the *Einstein Observatory* spectrum of QSO MR 2251-178, that presented a large absorption feature at $\sim$ 1 keV (Halpern, 1984, Fig. 2.2).

The first works analysing this ionized absorbing gas were based only on the detection of broad absorption edges, due to the low energy resolution of X-ray instruments. Indeed observations obtained with ASCA revealed the presence of deep O VII and O VIII edges at 0.74 keV and 0.87 keV respectively (e.g. George et al 1997), which were interpreted as evidence of ionized absorbing gas. Later on, a great improvement in understanding the nature of this absorbing gas was allowed by the advent of X-ray missions such as *XMM-Newton* and *Chandra*, where grating spectrometers became available. Nowadays, the so called "warm absorber" (WA) is observed to be present in about 50% (e.g. Piconcelli et al. 2005) of type 1 AGN, where the primary radiation intercepts gas and photoionizes it, resulting in a partially ionized plasma. The soft X-ray spectra of luminous type 1 AGN observed with these instruments show the presence of many narrow blueshifted absorption lines from several ionization states (Kaastra et al. 2000; Kaspi et al. 2000; Blustin et al. 2005) of a wealth of elements, especially iron, oxygen, carbon, nitrogen, neon, silicon and sulphur, that can be associated with the presence of WAs. Some of the best examples of sources showing the presence of WAs are NGC 3783 (Kaspi et al. 2001, 2002; Krongold et al. 2003; Netzer et al. 2003) and NGC 5548 (Kaastra et al. 2000, 2014).

Detailed studies (i.e. Kaastra et al. 2000; Kaspi et al. 2000; Blustin et al. 2005; Young et al. 2005; Miniutti et al. 2007; Reeves et al. 2013) showed that the physical parameters of WAs are:

- column density in the range $N_{\rm H} \sim 10^{20} - 10^{22} {\rm cm}^{-2}$;
- ionisation parameter $\log\xi \sim 0 - 2$ erg cm s^{-1};

- outflow velocity $v_{\rm out} \sim 100 - 1000$ km s^{-1}.

An example of the soft X-ray spectrum with the typical signatures of a WAs is shown in figure 2.8 for the QSO MR2251-178, as a modern view of the first X-ray observations of the same source shown in Fig. 2.2.

Besides understanding the ionisation level, outflow velocity and column densities of WAs, and how they depend on the type and luminosity of the AGN, a big open issue is where WAs originate. There are two main scenarios concerning their origin. The first one suggests that they are generated outside the accretion disc, at distances comparable to the obscuring torus (Blustin et al. 2005), presumably by radiation-driven evaporation occurring in the inner part of the torus (Krolik & Kriss 2001). The second model proposes that warm absorbers are winds ejected from the accretion disc, after reaching larger distances (Proga & Kallman 2004).
It is possible to estimate the lower and upper limits on the the distance of the absorber, once we known the outflow velocity. An estimate of the minimum radius can be given by assuming that the outflow velocity must be higher or equal to the escape velocity ($v_{esc} = \sqrt{\frac{2GM}{R}}$):

$$r_{\rm min} \equiv \frac{2GM_{\rm BH}}{v_{\rm out}^2} \tag{2.4}$$

The maximum distance of the absorber can be estimated using the definition of ionisation parameter ξ (Equation 2.3). Assuming that most of the absorbing mass is concentrated in a layer of thickness Δr smaller than its distance to the black hole ($\frac{\Delta r}{R} \leqslant 1$). The relation between the line-of-sight absorbing column density $N_{\rm H}$ and the density of the material $n(R)$ is:

$$N_{\rm H} \sim n(R) C_{\rm v} \Delta r \tag{2.5}$$

where $C_{\rm v}$ is the volume filling factor. Combining this expression with the definition of ξ (Equation 2.3) gives:

$$\frac{\Delta r}{R} \sim \frac{\xi R N_{\rm H}}{L_{\rm ion} C_{\rm v}} \xrightarrow{\frac{\Delta r}{R} \leqslant 1} R \leqslant \frac{L_{\rm ion} C_v}{\xi N_{\rm H}} \tag{2.6}$$

Finally, assuming that the volume filling factor C_v is equal to 1 (for the case of a homogeneous flow) the maximum distance of the outflow is obtained:

$$r_{\rm max} \equiv \frac{L_{\rm ion}}{\xi N_{\rm H}} \tag{2.7}$$

The low ionisation parameters ξ and the low velocities characterizing warm absorbers suggest that they are located at quite large distances (from ~pc up to ~kpc) with respect to the black-hole.

Another question is the role of WAs in terms of feedback. As anticipated in Section 1 the injection of large amounts of kinetic energy (in the form of outflows launched from the accretion disc) into the interstellar medium can be responsible for the process known as

"feedback", explaining the observed correlation between host galaxy properties and central SMBH. In order to understand what can be the contribution of WAs to the feedback mechanism, it is necessary to estimate how much energy they carry and if this energy is a significant fraction of the total energy output of the AGN. A parameter that is used to infer this contribution is the mass outflow rate $\dot{M}_{\rm out}$ that, for a uniform radial outflow (volume filling factor $C_{\rm v} = 1$), is defined as

$$\dot{M}_{\rm out} = 4\pi C r^2 n m_p v_{\rm out} \tag{2.8}$$

where n is the gas density of the absorber, r is the distance from the central engine, m_p is the proton mass and $C = \Omega/4\pi$ is the covering fraction (Blustin et al. 2005). Once the mass outflow rate is known, it is possible to estimate the kinetic luminosity, i.e. the kinetic energy that the outflow carries away per unit time $L_{kin} = \frac{1}{2}\dot{M}_{\rm out}v^2$. Thus the kinetic energy depends on the covering factor, the filling factor, the distance of the WAs and its velocity. Depending on the filling and covering factor the $\dot{M}_{\rm out}$ can be high, but the relatively low velocities imply a low kinetic power, compared to the bolometric luminosity, typically $\ll 1\%L_{\rm bol}$ (Blustin et al. 2005; McKernan, Yaqoob, & Reynolds 2007; Tombesi et al. 2013). This means that they are not expected to contribute significantly in the feedback process affecting the host galaxy properties. Indeed, in order to affect the galaxy their mechanical power should be of the order of $\sim 0.5\%L_{\rm bol}$ (Hopkins & Elvis 2010). Whether the role of WAs is important in the feedback process is still matter of debate, and it cannot be excluded that some of them could play a significant role in the process. Indeed a recent study by Crenshaw & Kraemer (2012) found that in a sample of 10 Seyfert 1s with WAs, in three of them the integrated kinetic energy of WAs can reach levels in the range $\sim 0.1\%L_{\rm bol} - 0.5\%L_{\rm bol}$, meaning that in some cases they can have the potential to influence the host galaxy environment.

2.5.2 Ultrafast outflows

Recently, observations at harder X-rays lead to the detection of ionised absorbers showing highly ionised Fe K-shell (transition 1s→2p of the ions FeXXV and FeXXVI) absorption lines at $E \geq 7$ keV, characterized by high blueshift (Chartas et al. 2002; Chartas, Brandt, & Gallagher 2003; Pounds et al. 2003; Braito et al. 2007; Reeves et al. 2009; Gofford et al. 2011; Lobban et al. 2011; Dauser et al. 2012; Gofford et al. 2013). Tombesi et al. (2010b) performed the first systematic search for such features in a sample of 42 Seyferts at $z \leq 0.1$ observed with *XMM-Newton* and found that these absorbers are detected in $\sim 40\%$ of the sources in the sample. The higher velocities of these absorbers with respect to WAs ($v_{\rm out} > 3000$ km/s), lead to classify them under the name of *Ultrafast-Outflows* (UFOs). These absorbers are characterised by:

- column density ($N_{\rm H}$) $\simeq 10^{22-24}$ cm^{-2};
- ionisation parameter log$\xi \simeq 3 - 6$ erg cm s^{-1};
- mildly relativistic outflow velocities in the range $\sim 0.01 - 0.3$c ($\sim 3,000 - 100,000$ km s^{-1}, (Tombesi et al. 2013).

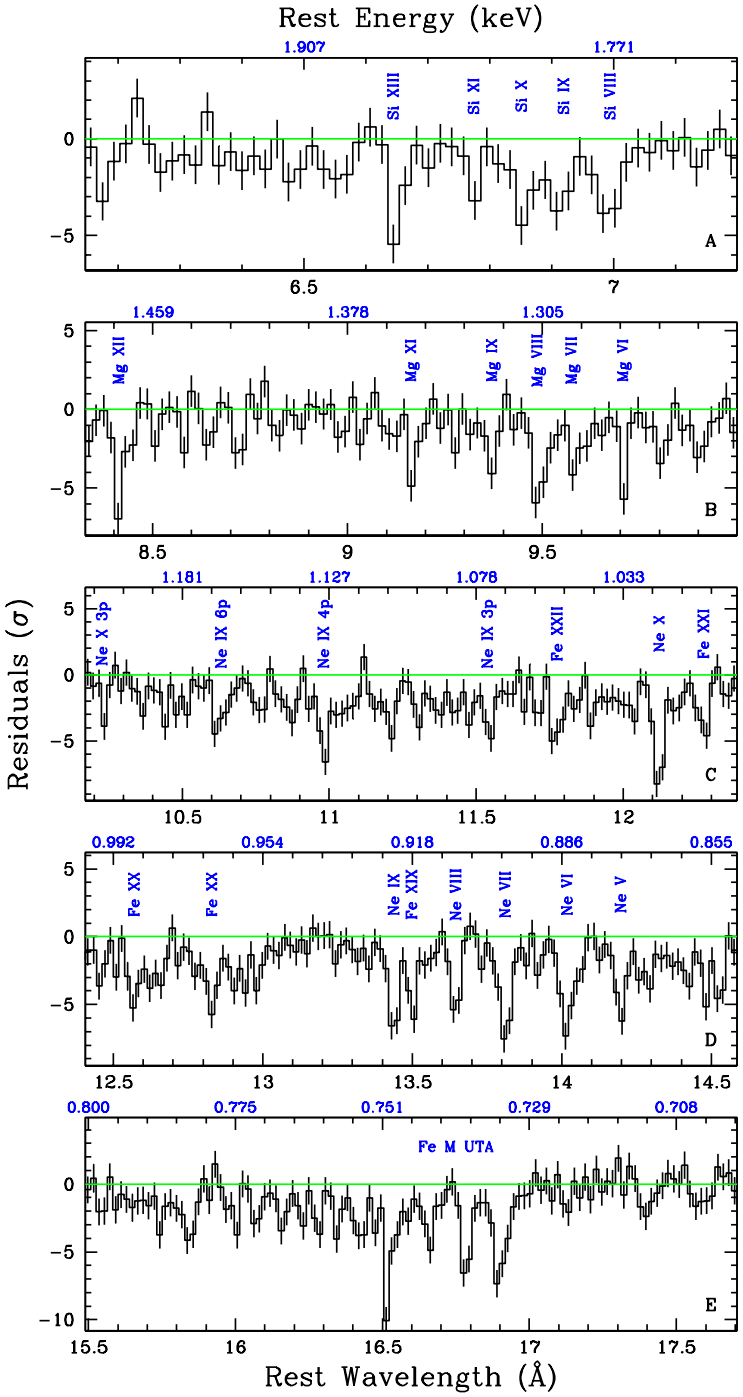

Figure 2.8: *Soft X-ray spectrum (below 2 keV) of the QSO MR2251-178, in the form of residuals with respect to the continuum, as observed by the* Chandra *Medium Energy Grating in 2011. The bottom axis of the plot reports the rest frame wavelength, while the upper axis is the rest energy. In the different panels are shown absorption features from the Si K band (first panel), the Mg K band (second panel), Ne* IX*, Ne* X *and L-shell Fe (third panel), inner shell absorption from Ne V-Ne IX (fourth panel) and the iron M-shell UTA band (last panel). The source was also observed by* XMM-Newton *Reflection Grating Spectrometer in the same year. It is remarkable the high level of details detectable in this spectrum, with respect to the first observations performed with the* Einstein Observatory *(Fig. 2.2), where X-ray grating spectroscopy was still not available. Figure adapted from Reeves et al. (2013).*

The high ionisation state and high velocity imply that UFOs are observed at sub-parsec distances from the central engine. For these absorbers the ratio between mass outflow and accretion rate, which depends on the covering factor (see Equation 2.8), may reach values close or higher than 1. This means that UFOs could potentially determine significant mass loss and energy loss from the central regions and that their mechanical power could constitute a fraction >few% of the bolometric luminosity. However, the covering factor plays an important role in understanding the validity of this hypothesis, and its estimates are still uncertain and valid for only few sources. A confirmation of the potential role played by the UFOs in the *feedback* mechanism comes from a recent study, published by Nardini et al. (2015). It consists of a detailed X-ray spectral analysis of the luminous quasar PDS 456, that highlighted the presence of a nearly spherical outflow, originated in the accretion disc and expelled with relativistic speed (terminal velocity of $\sim 0.35c$). The X-ray observations of this source (performed with *XMM*-Newton and *NuStar*) allowed to determine the solid angle Ω filled by the wind ($\Omega \sim 3.2\pi$ sr) and its starting point (a few hundreds of R_g). After estimating a mass outflow rate of $\dot{M}_{\rm out} \sim 10 M_{\odot}$/year the kinetic power is inferred to be $\sim 2 \times 10^{46}$erg/s, corresponding to 20% of the bolometric luminosity of the quasar, enough to produce significant feedback on the host galaxy. Another recent work Tombesi et al. (2015) detected the presence of an accretion disc wind with velocity $\sim$ 0.25c in the Ultraluminous Infrared Galaxy (ULIRG) IRAS F11119+3257 in the X-ray band. For this source a powerful ∼300 pc-scale molecular outflow was also detected in the IR band, with an outflow velocity of $\sim$ 1000 km s^{-1} and an estimated kinetic power of $\sim$ 2% of the bolometric luminosity. A further observational result by Feruglio et al. (2015) is the finding in the ultra-luminous IR galaxy Mrk 231 of a powerful kpc-scale outflow, traced by CO(2-1) observations, together with a highly ionized UFO with velocity $\sim$ 2000 kms^{-1}: they find that the kinetic energy released by the UFO is almost completely transferred to the kpc-scale outflow, that undergoes an adiabatic expansion. These findings allowed to relate the large scale molecular outflows observed in ULIRGs to the activity of AGN, since they support the hypothesis that AGN winds can transfer significant amounts of energy to the surrounding interstellar medium. Indeed, according to theoretical models, large molecular outflows could be the result of energy-conserving flows originating from fast accretion disc winds. The energy-conserving flow is one of the possible theoretical regimes of interaction between a mildly relativistic disc wind and the surrounding interstellar matter. According to it, the result of this shock (between the wind and the interstellar matter) is a flow where the cooling is inefficient and the gas expands adiabatically (conserving its energy). Oppositely to this mode and ruled out for this source, there is the momentum-conserving flow, where the gas cools efficiently and the kinetic energy is mostly irradiated.

Furthermore a study performed by Tombesi et al. (2013) showed that when comparing parameters (such as ionisation, column density, velocity and distance) of both WAs and UFOs together, significant correlations are observed. In fact WAs and UFOs appear to lie at the opposite ends of the same correlations. The implication of this result is that even if they have been classified as different types of absorbers, they could just be different components of a unique large scale outflow observed at different location along the line of sight (Fig. 2.9).

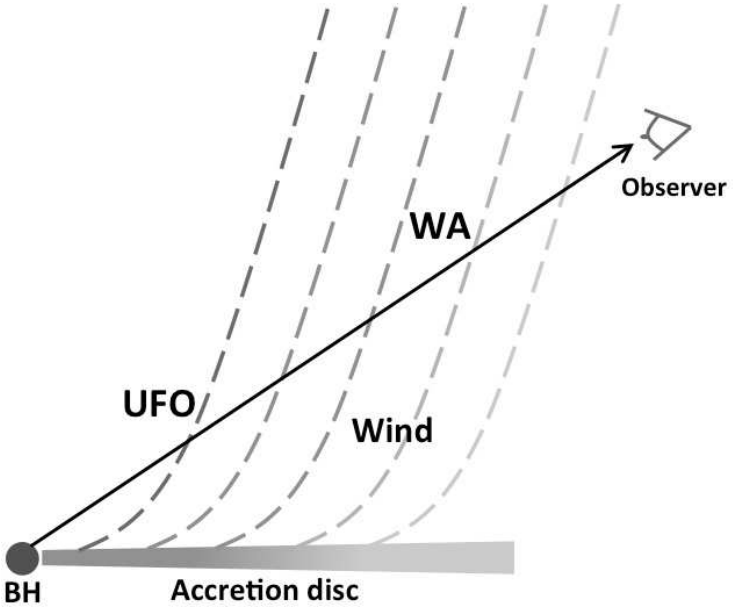

Figure 2.9: *Schematic diagram of a stratified accretion disc wind. The torus, which is not shown here, could be an extension of the outer accretion disc itself. Figure taken from Tombesi et al. (2012).*

We note that in case of WAs, even if their location is inferred to be of the order of the parsec scale torus, their origin is not necessarily there. Indeed some theories suggest that the torus itself is the most external part of a stratified wind (Elvis 2000; Kazanas et al. 2012). The hypothesis that WAs and UFOs are the same physical system is still highly debated. Indeed, some works (Laha et al. 2014) do not find that UFOs follow the same correlations as WAs, in the parameter space defined by ξ, $N_{\rm H}$ and v_{out}. However the same authors conclude that the low statistical quality of UFOs observations cannot exclude that WAs and UFOs are the same astrophysical system. They also claimed the lack of detection of UFOs in a sample of sources, whose presence was instead revealed by a previous analysis (Tombesi et al. 2010b). This study was followed by a work by Tombesi & Cappi (2014) who indicated that the reason for the different results is attributable to the use of single events only (and not also double events) in the study of Laha et al. (2014), that reduced by 40% the total counts. In conclusion, even if this is still a disputed topic, more and more evidences are being collected favouring the potential role of AGN driven outflows in determining co-evolution between SMBH and host galaxy.

CHAPTER 3

NGC454: a changing look AGN

Contents

3.1 NGC454 60
3.2 Observations and data Reduction 61
3.2.1 *Suzaku* data 61
3.2.2 The *Swift*-BAT observation 65
3.2.3 The XMM-*Newton* observation 66
3.3 Spectral analysis 68
3.3.1 The *Suzaku* and *Swift* broad band X-ray emission 68
3.3.2 Comparison with XMM-*Newton* data 74
3.3.3 A physical interpretation with *MyTorus* model 78
3.4 Constraints on the distance of the ionised absorber 80
3.5 Summary and Conclusion 81

As discussed in the previous chapter the X-ray spectra of AGN are complex and constituted by multiple components related to the still poorly understood condition of the matter near the active nucleus. In particular, the significant variability of the absorbing column density ($N_{\rm H}$) detected in the so called "changing look" AGN, i.e. AGN that have been observed both in Compton-thin ($N_{\rm H}$=10^{23}cm^{-2}) and Compton-thick states ($N_{\rm H}$> 10^{24}cm^{-2}) (Risaliti et al. 2002), implies that the absorbing material has to be clumpy and probably at much smaller distance than the conventional obscuring "torus" with velocity, distance and size from the central X-ray source of the same order of those of the Broad Line Region (BLR) clouds.

Up to now, we can count only a few "changing look" AGN where such a variability has been discovered on time-scales from a few days down to a few hours: NGC 1365 (Risaliti et al. 2005, 2007, 2009; Risaliti et al. 2009), NGC 4388 (Elvis et al. 2004), NGC 7674 (Bianchi et al. 2005), NGC 4151 (Puccetti et al. 2007), NGC 7582 (Bianchi et al. 2009), UGC 4203 (Risaliti et al. 2010), NGC4051 (Uttley et al. 2004; Lobban et al. 2011) and 1H 0419-577 (Pounds et al. 2004). Among them we also recall NGC2992 (Weaver et al. 1996): for this source one year monitoring with RXTE (Murphy et al. 2007) unveiled the presence of short-term flaring activity rather than a change in the covering of the absorber.

Working within a research group having availability of observational data of nearby objects, in particular the X-ray spectra of some of the most luminous AGN in the *Swift* BAT-70

months sample[1], I took responsibility of the analysis of two peculiar objects, NGC 454 and Mrk 348. They were drawn from a subsample of 31 interacting galaxies, of which at least one component is active. The sample was defined during the master degree thesis of Elisa Sala (Università di Milano-Bicocca), selecting the galaxies either with signs of perturbed morphology in the optical images, or with the presence of one or more nearby galaxies with which they could be interacting, . They all have redshift z< 0.03, high galactic latitude (| b |> 15°), a signal to noise ratio S/N> 5 and flux in the 15-150 keV higher than 8.0×10^{-12}erg cm^{-2} s^{-1}. Interacting galaxies are interesting sources when searching for AGN activity, since large amount of gas is predicted to be available for feeding and allowing the growth of central black hole. The X-ray spectral analysis I performed allowed me to classify NGC 454 (discusses in this chapter) as a changing-look AGN. Mrk 348 is a source for which a *Suzaku* observation was proposed within our research group (PI Valentina Braito), since the existing results obtained with XMM-*Newton* observation revealed complexity in the X-ray spectrum. As I will discuss in Chapter 4, Mrk 348 is a source whose X-ray spectra changes in a less extreme way with respect to NGC 454, but with evidences of multiple absorbers with different column densities and ionization states. The detailed study of both sources will provide insight on the presence of absorbing material along the line of sight and on its physical state, it will then give estimates on its distance and thus on where it has originated. The results of these two studies were published on *Monthly Notices of the Royal Astronomical Society* (Marchese et al. (2012, 2014)).

3.1 NGC454

Optical studies (Arp & Madore 1987; Johansson 1988; Stiavelli et al. 1998) of the interacting system NGC454 (see Figure 3.1,3.2 and 3.5, right panel) describe it as a pair of emission line galaxies consisting of a red elliptical galaxy (eastern component, hereafter NGC454E) and a blue irregular galaxy (western component, hereafter NGC454W, see Fig. 3.1), at redshift z=0.0122. The distorted morphology of both these galaxies, together with the spectroscopic (Fig. 3.3 and 3.4) and photometric evidence of a young stellar population, is a clear sign of the interacting nature of the system. Furthermore, three very blue knots (Fig. 3.2; discussed in section 3.2.3.1), probably Strömgren spheres[2] surrounding clusters of very hot newly formed stars, are located (and likely related) to the south of NGC454W. *HST* observations of the system, performed with the Wide Field Planetary Camera 2, confirmed that NGC454 is in the early stages of interaction (Stiavelli et al. 1998). The above authors stated also that an important fraction of gas has drifted to the center of the eastern component, but it has yet not produced any significant visible star formation activity; a population of young star clusters has formed around the western component.
The optical spectrum of NGC454E is consistent with that of a Seyfert 2 galaxy (Véron-Cetty & Véron, 2001) as seen by its [O III]λ5007 much stronger with respect to the Hβ,

[1] http://swift.gsfc.nasa.gov/results/bs70mon/

[2] Strömgren spheres, also called HII regions, are spherical regions of interstellar gas, composed of almost completely ionized hydrogen (HII) with a thin outer shell of HI. Such regions surround hot stars (typically present in galaxies with high star formation), that are able to produce large amount of UV radiation (energy above 13.6 eV), capable to ionize the surrounding hydrogen atoms.

and its [N II]λ6583 stronger than the Hα, although none of the high excitation lines, e.g. HeII lines, can be seen. Instead, no optical evidence of an AGN is present in the spectrum of NGC454W which is fully consistent with that of a star-forming galaxy (Johansson 1988).

3.2 Observations and data Reduction

3.2.1 *Suzaku* data

NGC454 was observed on April 29, 2009 by the Japanese X-ray satellite *Suzaku* (Mitsuda et al., 2007) for a total exposure time of about 130 ksec. *Suzaku* carries on board four X-ray Imaging Spectrometers (XIS, Koyama et al. , 2007), with X-ray CCDs at their focal plane, and a non-imaging hard X-ray detector (HXD-PIN, Takahashi et al. , 2007). At the time of this observation only three of the XIS were working: one back-illuminated (BI) CCD (XIS1) and two front-illuminated (FI) CCDs (XIS0 and XIS3). All together the XIS and the HXD-PIN cover the 0.5–10 keV and 12–70 keV bands respectively. The spatial resolution of the XIS is $\sim$ 2 arcmin (HEW), while the field of view (FOV) of the HXD-PIN is 34 arcmin radius. Further details on the *Suzaku* satellite can be found in Appendix A. Data from the XIS and HXD-PIN were processed using v2.1.6.14 of the *Suzaku* pipeline[3] (for a manual on *Suzaku* data analysis we referred to the ABC guide: *http://heasarc.gsfc.nasa.gov/docs/suzaku/analysis/abc/abc.html*) and applying the standard screening parameters. The screening filters all events within the South Atlantic Anomaly (SAA) as well as with an Earth elevation angle (ELV) $< 5^\circ$ and Earth day-time elevation angles (DYE_ELV) less than 20°. Furthermore also data within 256s of the SAA were excluded from the XIS and within 500s of the SAA for the HXD. Cut-off rigidity (COR) criteria of > 8 GV for the HXD data and > 6 GV for the XIS were used.

3.2.1.1 The *Suzaku* XIS data reduction

The XIS data were selected in 3×3 and 5×5 editmodes using only good events with grades 0,2,3,4,6 and filtering the hot and flickering pixels with the script *sisclean*; the net exposure times are 103 ksec for each of the XIS. The XIS source spectra were extracted from a circular region of 2.2′ radius centered on the source, and the background spectra were extracted from two circular regions with the same radius of the source region, offset from the source and the calibration sources. The XIS response (rmfs) and ancillary response (arfs) files were produced, using the latest calibration files available, with the *ftools* tasks *xisrmfgen* and *xissimarfgen* respectively. The spectra from the two FI CDDs (XIS 0 and XIS 3) were combined to create a single source spectrum (hereafter XIS–FI), while the BI (the XIS1) spectrum was kept separate and fitted simultaneously. The net 0.5–10 keV count rates are: (0.0117 ± 0.0005) cts/s, (0.0142 ± 0.0005) cts/s, (0.0132 ± 0.0006) cts/s for the XIS0, XIS3 and XIS1 respectively. The energy ranges considered for the data are 0.5–10 keV for the XIS–FI and 0.6–7 keV for the XIS–BI (because the XIS–BI is optimized

[3] http://heasarc.gsfc.nasa.gov/docs/suzaku/processing/

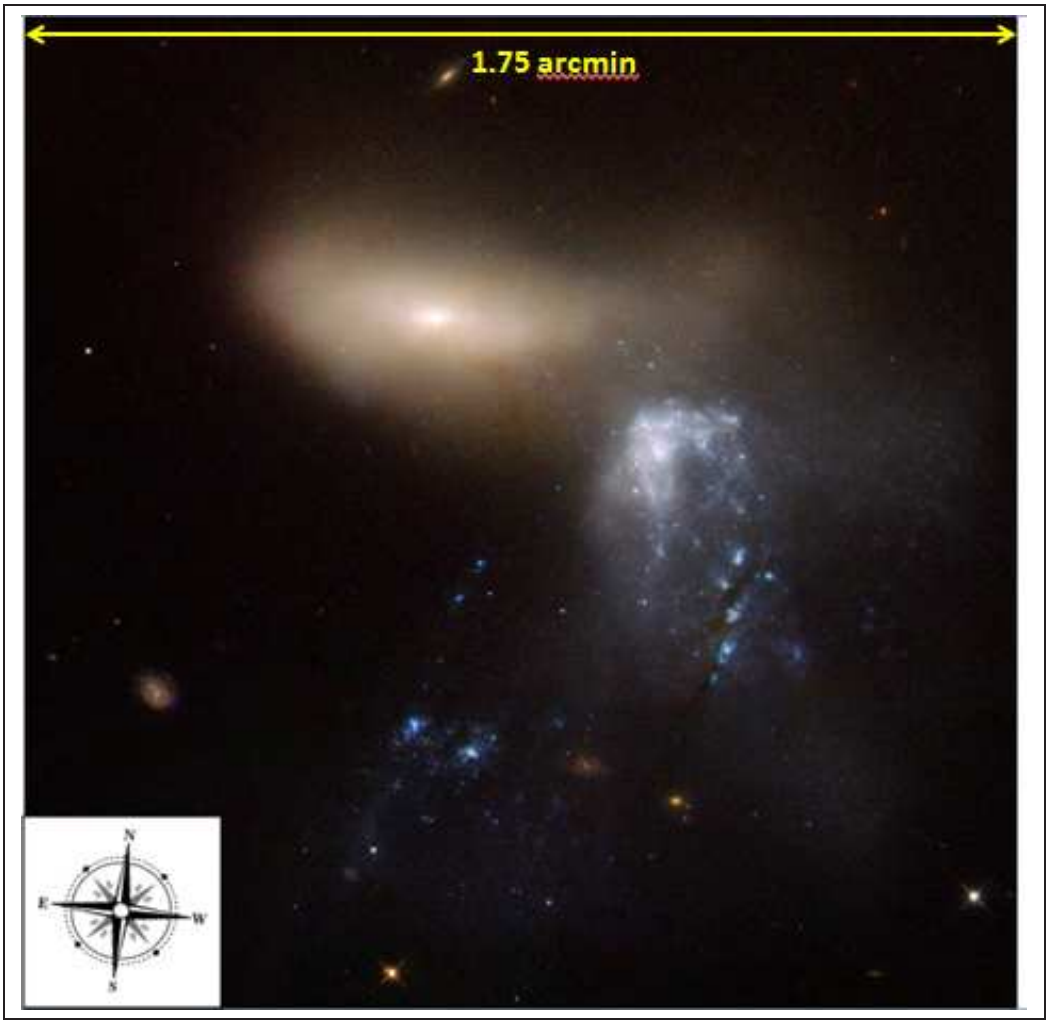

Figure 3.1: *NGC 454 in a* 1.75×1.75 *arcmin image taken from the Hubble Space Telescope, as a part of a collection of 59 images of merging galaxies published for its 18th anniversary. NGC 454 is an interacting system of galaxies, composed by an elliptical galaxy and an irregular blue galaxy. This system is in the first phases of interaction, and thus the two galaxies show evident features of morphological distortion. On the bottom left, three blue knots are visible, and are presumably newly formed globular clusters, related to the irregular galaxy. The pair is located at a distance of approximately 164 million light years away. The filters used in this image are B (at 435 nm, in blue), V (at 555 nm, in green), Infrared (814 nm, in red).*

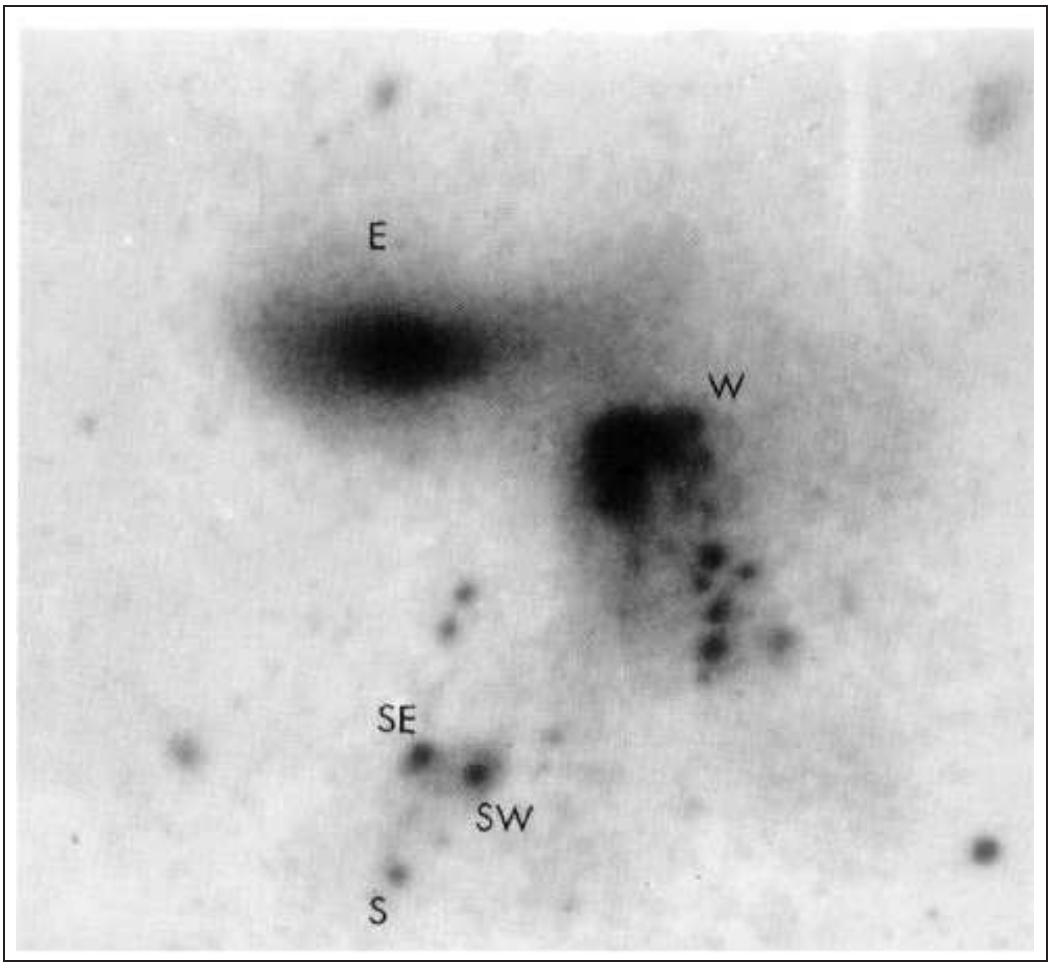

Figure 3.2: *NGC 454 as seen by ESO 3.6m telescope, in the U bandpass. In this image there are the following sources indicated: NGC454E (label E), NGC454W (label W) and the three blue knots (labels SE, SW and S) that in the XMM-*Newton *pn image (Fig. 3.5) are commonly indicated with the name "XS". These latter three regions are presumably newly formed globular clusters, related to NGC454W (Johansson 1988). Figure adapted from Johansson (1988).*

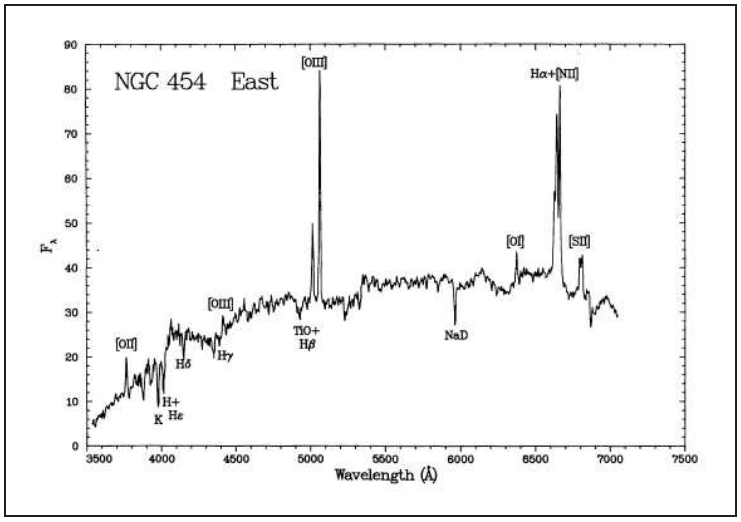

Figure 3.3: *Optical spectrum of the central 4"×2" (corresponding to 1.0 × 0.5 kpc) of NGC 454 East, as observed by Image Dissector Scanner (IDS, ESO 3.6 m telescope) in 1979. The spectrum is dominated a stellar continuum typical of an elliptical galaxy, with strong forbidden emission lines. The flux density is in unit of* $10^{-19}\mathrm{Wm}^{-2}\text{Å}^{-1}$. *Image adapted from Johansson (1988).*

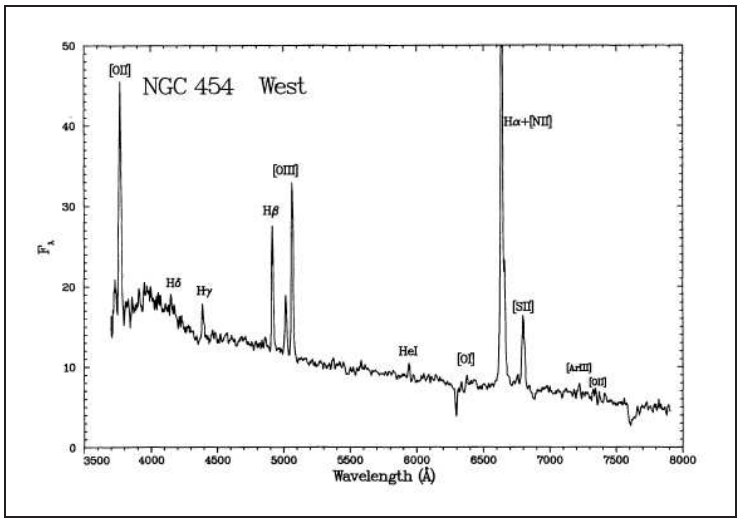

Figure 3.4: *Optical spectrum of the central 4"× 3" (corresponding to 1.0 × 0.7 kpc) of NGC 454 West as observed by Image Dissector Scanner (IDS, ESO 3.6 m telescope) in 1979. The spectrum is dominated by a blue stellar continuum and strong emission lines, with line widths less than* $\sim$ 250km s^{-1}. *The flux density is in unit of* $10^{-19}\mathrm{Wm}^{-2}\text{Å}^{-1}$. *Image adapted from Johansson (1988).*

for observing below ∼ 7 keV). For both the XIS-FI and XIS-BI the band 1.6–1.9 keV was ignored, due to instrumental calibration uncertainties.

The net XIS source spectra were then binned to a minimum of 50 counts per bin.

3.2.1.2 The *Suzaku* HXD-PIN data reduction

For the HXD-PIN data reduction and analysis I followed the latest *Suzaku* data reduction guide (the ABC guide Version 2[4]), and used the rev2 data, which include all 4 cluster units. The HXD-PIN instrument team provides the background (known as the "tuned" background) event file, which accounts for the instrumental "Non X-ray Background" (NXB; Kokubun et al. 2007). The systematic uncertainty of this "tuned" background model is ±1.3% in 15-40 keV (at the 1σ level for a net 20 ksec exposure[5]).
The source and background spectra were extracted using the same common good time interval. Besides, the source spectrum was corrected for the detector dead time. The net exposure time after the screening was 106 ksec. Then a spectrum for the cosmic X-ray background counts (Boldt 1987; Gruber et al. 1999) was simulated and added to the instrumental one.

NGC454 is detected at a level of 3.4 % above the background and the net count rate in the 15–30 keV band is 0.01 ± 0.002 cts/s. For the spectral analysis the source spectrum was rebinned in order to have a signal-to-noise ratio $\geqslant 3$ in each energy bin. I fit the *Suzaku*-HXD spectrum with a single power-law component with a photon index fixed to $\Gamma = 1.9$ and derived an observed 15–30 keV flux of $\sim 3.4 \pm 0.9 \times 10^{-12}$erg cm^{-2} s^{-1}.

3.2.2 The *Swift*-BAT observation

NGC454 was also detected with the BAT detector on board of *Swift* (Gehrels et al. 2004). BAT is a coded aperture imaging camera that operates in the 14–150 keV energy range; it has a large field of view (1.4 steradian half coded), and a point spread function (PSF) of 18 arcmin (HEW). *Swift*-BAT is devoted mainly to the monitoring of a large fraction of the sky for the occurrence of gamma ray bursts (GRBs); while waiting for new GRBs, it continuously collects spectral and imaging information in survey mode, covering a fraction between 50% and 80% of the sky every day.
NGC454 (BAT name: SWIFT J0114.4-5522) is part of the Palermo *Swift*-BAT 54 Month hard X-ray catalogue (Cusumano et al. 2010) and the *Swift*-BAT 70-Month Hard X-ray Survey (heasarc.gsfc.nasa.gov/docs/swift/results/bs70mon/ ; Baumgartner et al. 2013). This latter survey detected 1171 sources in the 14–195 keV band down to a significance level of 4.8σ, reaching a flux level of 1.03×10^{-11}erg cm^{-2} s^{-1}over 50% of the sky (and 1.34×10^{-11}erg cm^{-2} s^{-1}over 90% of the sky).
The 14–195 keV flux of NGC454 is $(1.90 \pm 0.5) \times 10^{-11}$erg cm^{-2} s^{-1}(Baumgartner et al. 2013) and the photon index is $\Gamma = 1.80 \pm 0.3$; this is in good agreement with the expected

[4] http://heasarc.gsfc.nasa.gov/docs/suzaku/analysis/abc/
[5] ftp://legacy.gsfc.nasa.gov/suzaku/doc/hxd/suzakumemo-2008-03.pdf

14–195 keV flux ($\sim 1.6\times10^{-11}$erg cm^{-2} s^{-1}) extrapolated from that measured with *Suzaku* in the 15–30 keV range and the photon index of $\Gamma \sim 1.92$.

3.2.3 The XMM-*Newton* observation

NGC454 was observed with XMM-*Newton* on November 5, 2009 for a total exposure time of about 30 ksec. The XMM-*Newton* Observatory (Jansen et al. 2001) carries, among its onboard instruments, three 1500 cm^2 X-ray telescopes, each with EPIC (European Photon Imaging Camera) imaging spectrometers at the focus. Two of the EPIC use MOS CCDs (Turner et al. 2001) and one uses a pn CCD (Strüder et al. 2001). These CCDs allow observations in the range ∼0.5–10 keV. The spatial resolution of the 2 MOSs is $\sim 14''$ (HEW), and $\sim 15''$ (HEW) for the pn (Ehle et al. 2001).

During this observation the pn, MOS1, and MOS2 cameras had the medium filter applied and they were operating in full frame Window mode. The data have been processed and cleaned using the Science Analysis Software (SAS ver. 6.5) and analysed using standard software packages (FTOOLS ver. 6.1 and XSPEC ver. 11.3). Event files have been filtered for high-background time intervals, and only events corresponding to patterns 0–12 (MOS1, MOS2) and to patterns 0–4 (pn) have been used. The net exposure times at the source position after data cleaning are ∼23.9 ksec (pn), ∼29.1 ksec (MOS1) and ∼29.2 ksec (MOS2).

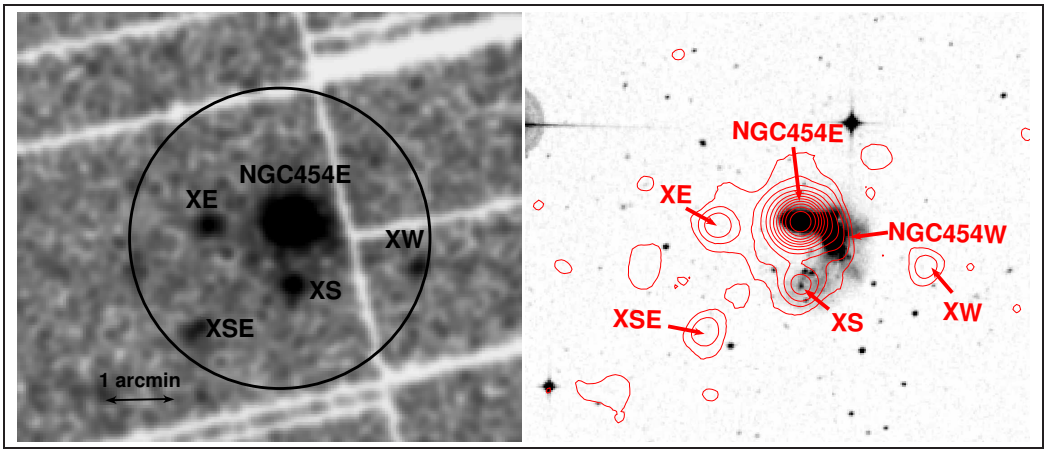

Figure 3.5: *Left panel: XMM-*Newton *EPIC-pn image (0.5–10 keV) with superimposed the* Suzaku *XIS extraction region. Right Panel:* Digital Sky Survey *(DSS) optical image with overlaid the XMM-*Newton *PN 0.5–10 keV contours. I marked the main X-ray sources discussed in this thesis. It is evident that the main X-ray source is positionally coincident with NGC454E (classified as a Seyfert 2) while no X-ray emission is detected at the position of NGC454W. Since the distance between the two nuclei is only 28", at the XMM-*Newton *spatial resolution we were unable to estimate a flux upper limit for NGC454W. The two figures have the same scale on sky.*

In the right panel of Figure 3.5 I report the optical DSS image of the system NGC454,

together with the XMM-*Newton* 0.5–10 keV contours (red) from EPIC-pn. It is evident that the bulk of the X-ray emission is positionally coincident with NGC454E (the galaxy spectroscopically classified as a Seyfert 2) while no strong X-ray emission is detected at the position of NGC454W (the source spectroscopically classified as a star-forming galaxy). A weak X-ray source (labelled XS) is also detected to the south of NGC454, which is positionally coincident with one of the three very blue knots discussed above, likely a star forming region belonging to NGC454W.

The pn, MOS1 and MOS2 source spectra were extracted from a circular region of 0.46 arcmin radius centered on the source (NGC454E), while the background spectra were extracted from two circular regions with 0.5 arcmin radius offset from the source. The MOS1 and MOS2 spectra were combined together, then both the EPIC-pn and EPIC-MOS spectra were grouped with a minimum of 30 counts per channel.

3.2.3.1 Contamination from unresolved sources in the *Suzaku* (XIS, HXD) and *Swift*-BAT extraction region/field of view

In the left panel of Figure 3.5 I show the XMM-*Newton* 0.5–10 keV pn image along with the *Suzaku* extraction region (circle with 2.2′ radius). As discussed above the main X-ray source is centered on NGC454E but given the XMM-*Newton* better angular resolution (14″–15″ HEW) as compared to *Suzaku* (120″ HEW), four other X-ray sources are clearly distinguishable, besides NGC454E, entering in the *Suzaku* XIS extraction region. The XMM-*Newton* spectra for the three brighter sources (XS, XE and XSE, marked in Figure 3.5 for clarity) were extracted and analysed in order to estimate their possible contribution to the *Suzaku* spectrum; the remaining source (XW) has only ~ 80 counts detected in the $\sim 0.5-10$ keV band (see below).

XS is well fitted with a power law, modified only by Galactic absorption, plus a thermal component (MEKAL) with a resulting photon index $\Gamma \sim 1.6$, $kT \sim 0.2$ keV and a 2–10 keV flux $F_{[2-10]keV} \sim 2.2 \times 10^{-14}$erg cm^{-2} s^{-1}; the extrapolated flux in the 14–70 keV band is $F_{[14-70]keV} \sim 3.1 \times 10^{-15}$erg cm^{-2} s^{-1}. As said above this source is likely associated with a star forming region related to NGC454W; if so, assuming $z = 0.0122$, its 2–10 keV luminosity is $L_{[2-10]keV} \sim 7.8 \times 10^{39}$ erg s^{-1}. It is not possible to establish if this luminosity is due to one or more sources and thus speculate on its/their nature, because we lack both the spatial resolution and a good enough sampling to assess its variability and spectral properties. This 2-10 keV luminosity, converted into star formation rate (SFR), yields SFR$\sim$ 1.8 $M_{\odot}$/yr (depending on the relation between $L_{[2-10]keV}$ that it is used: 1.6 $M_{\odot}$/yr using Ranalli, Comastri, & Setti 2003 relation, and 2 $M_{\odot}$/yr using the relation inferred by Persic & Rephaeli 2007). This is in good agreement with the SFR inferred from the $H\alpha$ luminosity (Johansson 1988) using the relation by Kennicutt (1983), which yields SFR$\sim$ 1.2 $M_{\odot}$/yr. The source to the East of NGC454E (hereafter XE) can be fitted with a power-law and a thermal component, yielding $\Gamma \sim$1.6, $kT \sim 0.3$ and $F_{[2-10]keV} \sim 1.3 \times 10^{-14}$erg cm^{-2} s^{-1}($F_{[14-70]keV} \sim 1.18 \times 10^{-15}$erg cm^{-2} s^{-1}). The source to the South-East of NGC454E (hereafter XSE) can be fitted with an absorbed power law ($N_{\rm H}\sim$ 2.2×10^{22} cm^{-2}) with photon index set to 1.8 and

$F_{[2-10]keV} \sim 2.7 \times 10^{-14}$erg cm^{-2} s^{-1}($F_{[14-70]keV} \sim 3.4 \times 10^{-15}$erg cm^{-2} s^{-1}). Finally, the fourth source located to the West of NGC454E (hereafter XW) has not enough counts for a meaningful spectral analysis ($\sim$ 80 counts) and its estimated fluxes are $F_{[2-10]keV} \sim 2.0\times10^{-14}$erg cm^{-2} s^{-1}and $F_{[14-70]keV} \sim 2.5 \times 10^{-15}$erg cm^{-2} s^{-1}(adopting $\Gamma \sim 1.9$). According to the extragalactic logN-logS distributions computed by Mateos et al. (2008), at this flux level the number of random 2–10 keV sources in the *Suzaku* extraction region is ~ 2, thus the sources XE, XSE and XW are probably those expected by "chance". For XE, XSE and XW there is no identification available from source archives (NED[6] and SIMBAD[7]).

The combined 2–10 keV flux of all these 4 possible contaminating sources ($F_{[2-10]keV} \sim 8.2\times10^{-14}$erg cm^{-2} s^{-1}) imply that they will provide a negligible contribution to the *Suzaku* XIS spectrum of NGC454 ($F_{[2-10]keV} \sim 6\times10^{-13}$erg cm^{-2} s^{-1}), unless significant variability is present. More importantly, their estimated $F_{[14-70]keV}$ are well below the *Suzaku* HXD-PIN or Swift-BAT sensitivity. On the other hand this check is still not sufficient for these two latter instruments since their FOV is larger than that of the *Suzaku* XIS instrument. Assuming that the X-ray emission above 10 keV detected with the HXD-PIN or the Swift-BAT is associated to the same source, as the good agreement of the measured fluxes strongly suggests, I used the instrument with the smaller FOV (*Swift*-BAT) to perform further checks. In particular using known catalogues or archives (NED and SIMBAD) I performed a search for bright X-ray/optical sources within 6 arcmin radius error circle (corresponding to 99.7% confidence level for a source detection at 4.8 standard deviations, Cusumano et al. 2010) that could be responsible of the observed X-ray emission above 10 keV. No plausible contaminant source was found and, in the following, I will assume that the emission above 10 keV comes from NGC454E. I note that I'm also assuming a negligible contribution to the emission above 10 keV from the companion galaxy in the interacting system, NGC454W. While a confirmation of this assumption has to wait for direct imaging observations above 10 keV with adequate spatial resolution, I stress that no emission was detected below 10 keV from NGC454W, while a contribution would be expected even in the case of a deeply buried AGN (see e.g. Della Ceca et al. 2002). I thus conclude that a significant contamination is not expected from the nearby sources to the *Suzaku* and *Swift* spectra.

3.3 Spectral analysis

3.3.1 The *Suzaku* and *Swift* broad band X-ray emission

As a first step the X-ray spectrum of NGC454E in the 0.5–100 keV band was considered by fitting simultaneously the *Suzaku* XIS, *Suzaku* HXD and *Swift*-BAT data. The cross-normalisation factor between the HXD and the XIS-FI was set to 1.18, as recommended for HXD nominal observation processed after 2008 July (Manabu et al. 2007; Maeda et al.

[6] http://ned.ipac.caltech.edu/
[7] http://simbad.u-strasbg.fr/simbad/

2008[8]), while the cross-normalisation between *Swift* and XIS was allowed to vary.
In the subsequent sections the χ^2 statistics was used for the fit, the errors are quoted to 90% confidence level for 1 parameter of interest and all the spectral parameters are quoted in the rest frame of the source.

The continuum was fitted with a redshifted power-law model, modified only by Galactic ($N_{\rm H}$= 2.73×10^{20} cm^{-2}, Dickey & Lockman , 1990, model WABS in XSPEC) absorption. This model did not provide an adequate description of the broadband spectrum of NGC454E (χ^2/dof=522.6/122). When fitting only the 2–5 keV continuum, thus excluding possible complexity in the soft energy range and near the Fe K emission line complex, a very flat photon index ($\Gamma \sim 0.15$) is found, strongly suggesting that NGC454E is an absorbed AGN, in agreement with its optical spectral classification.

The residuals with respect to this simple unabsorbed power-law model, which are shown in Figure 3.6, allowed to infer the main features of the observed spectrum. An excess at energies below 1 keV, an emission line feature at ~6.4 keV (likely associated with Fe Kα), together with a line-like feature at ~7 keV, and an excess at energies between 10 and 20 keV are clearly evident. The residuals in the soft X-rays suggest the presence of a thermal component probably related to the host galaxy. The simultaneous occurrence of a strong Fe Kα emission line at ~6.4 keV (figure 3.6 upper and lower panel), a very flat observed Γ and an excess in the hard X-rays (above 10 keV) is the distinctive spectral signature of a highly absorbed source, with a possible strong Compton reflected component. The excess observed at ~7 keV (Figure 3.6 lower panel) is likely due to the combination of the Fe Kβ emission line (7.06 keV), the Fe XXVI (~6.97 keV) and the Fe edge (~7.11 keV).

In order to include in the model the features observed in the residuals described in Fig. 3.6 the broad band fit was performed according to the following steps:

1. I used a model composed by a primary intrinsically absorbed power law and an unabsorbed power law (representing the fraction of primary X-ray radiation that is scattered into our line of sight). The photon indices of the two power laws were tied to each other. The absorber was modelled by a combination of the CABS and ZPHABS models in XSPEC, assuming the same column density, since they represent the same medium producing two different effects (i.e. the non-relativistic Compton scattering out of the line of sight and photoelectric absorption of the primary radiation, respectively). This fit is still poor and yields χ^2/dof= 241.5/108 and $N_{\rm H} \sim 4 \times 10^{23}$cm^{-2}.

2. Due to the residual emission that it is still found in the soft X-ray band, a thermal component was added (modelled with the MEKAL model, Mewe et al. , 1986), leading to an improvement of the fit by $\Delta\chi^2 = 23$ for 2 d.o.f, with kT~0.5 keV.

3. Two Gaussian components were added, to account for the ~6.4 keV (Fe Kα) and 7.06 keV (Fe Kβ) emission lines.The energy of the Fe Kβ was kept fixed to 7.06

[8]http://www.astro.isas.jaxa.jp/suzaku/doc/suzakumemo/suzakumemo-2007-11.pdf; http://www.astro.isas.jaxa.jp/suzaku/doc/suzakumemo/suzakumemo-2008-06.pdf

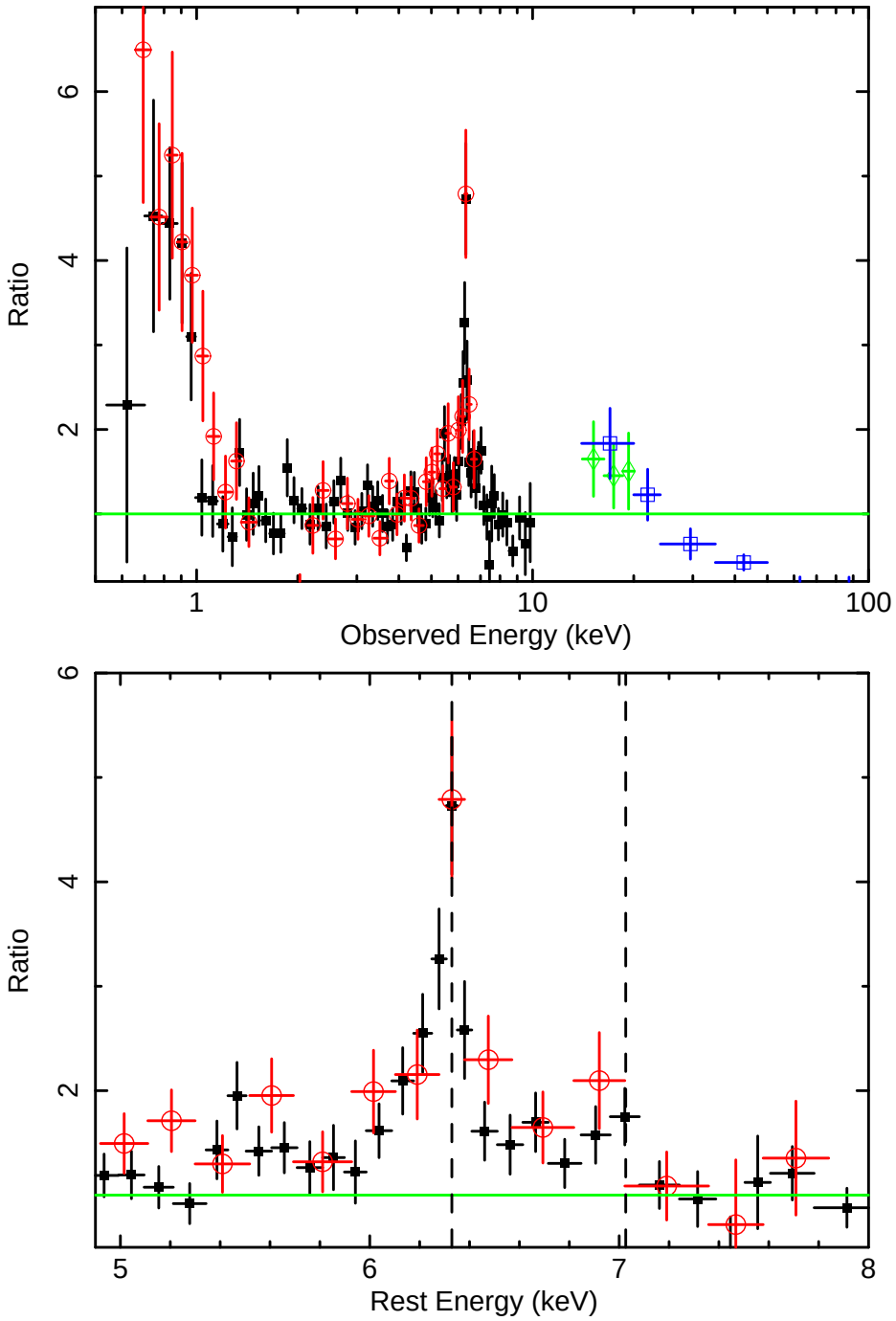

Figure 3.6: *Upper panel: ratio between the* Suzaku *and* Swift *data (XIS-FI: black filled squares; XIS1: red open circles; HXD: green rhombs; and BAT:blue open squares) and the unabsorbed power-law model used to fit* Suzaku *data in the 2–5 keV energy range. Lower panel: zoom into the 5–8 keV energy range (XIS-FI: black filled squares, XIS1: red open circles). It is visible at 6.4 keV the excess characteristic of the Fe Kα emission line and at ~ 7 keV, the combined contribution of the Fe Kβ emission line (7.06 keV), Fe XXVI (~6.97 keV), and the reflector edge. The central energies of the Fe Kα and Fe Kβ are marked with dashed vertical lines.*

keV, its intrinsic width (σ) was tied to the width of the corresponding Fe Kα line and its flux fixed to be 13% of the Fe Kα flux, consistent with the theoretical value (Palmeri et al. 2003). The resulting fit improves significantly ($\Delta\chi^2$ = 75 for 2 d.o.f), yielding χ^2/dof= 142.5/104. The energy centroid for the Fe Kα line is E=$6.38^{+0.02}_{-0.02}$ keV.

4. Finally I added a Compton reflected component, modelled with the PEXRAV model in XSPEC (Magdziarz & Zdziarski , 1995), which represents a power-law spectrum (with a cut-off) reflected from a infinite slab of neutral material. The parameters of the reflected component are: an inclination angle i fixed to 60° [9] (see Noguchi et al. 2010), abundance Z=$Z_\odot$, a reflection fraction (defined by the subtending solid angle of the reflector $R = \Omega/2\pi$) fixed to be -1 (i.e. pure reflection)[10], the cut-off energy (fixed at 200 keV, Dadina 2008) and the normalisation. The fit including the reflection component improves by $\Delta\chi^2$ = 38 for 1 d.o.f (χ^2/dof= 104.5/103).

The final model setup is thus:

WABS$_{Gal}$×[MEKAL + ZPOWERLW + ZGAUSS + ZGAUSS + PEXRAV + CABS×ZPHABS×(ZPOWERLW)]

This model provides a good representation of the X-ray emission of NGC454E (χ^2/dof= 104.5/103). The resulting best-fit parameters are reported in table 3.1 and the unfolded spectrum is shown in Fig. 3.7. In particular, this best-fit model yielded $\Gamma = 1.92^{+0.29}_{-0.36}$, $N_{\rm H}= 2.05^{+4.25}_{-1.38} \times 10^{24}$ cm^{-2}. The rest-frame energy of the Fe Kα is $E_{K\alpha} = 6.38 \pm 0.02$ keV and its equivalent width with respect to the observed continuum is EW=340^{+60}_{-80}eV. At the *Suzaku* spectral resolution this emission line is unresolved; leaving the width σ free to vary it was found to be $\sigma \lesssim 70$ eV (at the 90% confidence level), thus it was fixed to be $\simeq$ 10 eV. The cross-normalisation factor between the *Swift*-BAT and the XIS-FI is $1.05^{+0.64}_{-0.39}$. I remark that a different choice of the cut-off energy in the range between 100 and 300 keV does not affect significantly the best-fit reflection parameters obtained in this work. The relative importance of the reflection component is given by the ratio between the normalizations of the primary absorbed power-law and the reflection component; in our case this ratio is $0.5^{+0.5}_{-0.1}$, which at first order would correspond to a reprocessor covering a solid angle π. The fraction of scattered radiation is $\sim$ 0.1%. The observed 2–10 keV flux is $\sim 6.3\times10^{-13}$erg cm^{-2} s^{-1}while the intrinsic 2–10 keV luminosity obtained with this model is 7.2×10^{42}erg s^{-1}.

[9] In the PEXRAV model, 0° represent a face on configuration thus, considering that the quality of the data does not allow to constrain both i and the normalization at the same time, we assumed an inclination angle of a typical Sy2 (which is ~60 °). A change in the assumption on the inclination angle could have an impact only the normalization of the PEXRAV component and not on the geometry (see Appendix B for further details on PEXRAV). However, for our purposes, it is important to detect an eventual change of normalization between *Suzaku* and XMM-*Newton* observations, so we kept as starting point the same inclination angle in the two observations.

[10] Since in the "pure reflection" PEXRAV model there is a degeneracy between R and the normalisation, the reflection scaling factor was set to -1 and the normalisation was allowed to vary.

Table 3.1: Summary of the *Suzaku* and XMM-*Newton* parameters for the best-fit models described in Section 3.3.1, and 3.3.2.1.

Model Component	Parameter	*Suzaku*	XMM-*Newton*
Power law	Γ	$1.92^{+0.29}_{-0.36}$	$1.99^{+0.11}_{-0.07}$
	Normalisation[a]	$7.39^{+30.00,b}_{-4.39}$	$2.77^{+0.71}_{-0.65}$
Scattered Component	Normalisation[a]	$8.55^{+5.48}_{-4.52} \times 10^{-3}$	$1.62^{+0.29}_{-0.22} \times 10^{-2}$
Absorber	N_H	$2.05^{+4.25}_{-1.38} \times 10^{24}$ cm^{-2}	$1.0^{+0.1}_{-0.2} \times 10^{23}$ cm^{-2}
Thermal emission	kT	$0.62^{+0.10}_{-0.17}$ keV	$0.62^{+0.11}_{-0.11}$ keV
	Normalisation[c]	$6.94^{+2.40}_{-2.22} \times 10^{-6}$	$3.49^{+1.52}_{-1.50} \times 10^{-6}$
Neutral reflection	Normalisation[a]	$3.46^{+2.14}_{-1.61}$	$3.55^{+1.52}_{-1.81}$
Fe Kα	Energy	$6.38^{+0.02}_{-0.02}$ keV	$6.36^{+0.03}_{0.03}$ keV
	EW	340^{+60}_{-80} eV	120^{+40}_{-40} eV
	Normalisation[e]	$3.62^{+0.79}_{-0.78} \times 10^{-3}$	$4.75^{+1.35}_{-1.40} \times 10^{-3}$
Fe Kβ	Energy	7.06 keV (frozen)	7.06 keV (frozen)
	EW	40 eV	16 eV
	Normalisation[e]	fixed to 13% Fe Kα	fixed to 13% Fe Kα
Ionised Absorber	N_H	..	$6.05^{+8.95}_{-4.10} \times 10^{23}$cm^{-2}
	logξ	..	$3.55^{+0.49}_{-0.25}$erg cm s^{-1}
	v_{turb}	..	300 km s^{-1}
	χ^2/dof	104.5/103	190.7/197
	F $^{mekal}_{(0.1-3)\mathrm{keV}}$	$\sim 1.7 \times 10^{-14}$erg cm^{-2} s^{-1}	$\sim 8.5 \times 10^{-15}$erg cm^{-2} s^{-1}
	F $_{(0.5-2)\mathrm{keV}}$	$\sim 4.9 \times 10^{-14}$erg cm^{-2} s^{-1}	$\sim 5.8 \times 10^{-14}$erg cm^{-2} s^{-1}
	F$_{(2-10)\mathrm{keV}}$	$\sim 6.3 \times 10^{-13}$erg cm^{-2} s^{-1}	$\sim 1.9 \times 10^{-12}$erg cm^{-2} s^{-1}
	F $_{(14-150)\mathrm{keV}}$	$\sim 1.4 \times 10^{-11}$erg cm^{-2} s^{-1}	$\sim 1.3 \times 10^{-11}$erg cm^{-2} s^{-1}
	L $^{mekal}_{(0.1-3)\mathrm{keV}}$	$\sim 5.6 \times 10^{39}$erg s^{-1}	$\sim 2.8 \times 10^{39}$erg s^{-1}
	L $_{(0.5-2)\mathrm{keV}}$	$\sim 4.7 \times 10^{42}$erg s^{-1}	$\sim 2 \times 10^{42}$erg s^{-1}
	L$_{(2-10)\mathrm{keV}}$	$\sim 7.2 \times 10^{42}$erg s^{-1}	$\sim 2.5 \times 10^{42}$erg s^{-1}
	L$_{(14-150)\mathrm{keV}}$	$\sim 1.4 \times 10^{43}$erg s^{-1}	$\sim 4.8 \times 10^{42}$erg s^{-1}

[a] units of 10^{-3} photons keV^{-1} cm^{-2} s^{-1}.
[b] Due to a degeneracy between the normalisations of the primary power law and PEXRAV, the errors were computed fixing the reflection normalisation to its best-fit value.
[c] The normalisation of the thermal component is defined as $K = \frac{10^{-14}}{4\pi(D_A(1+z))^2} \int n_e n_H dV$ where D_A is the angular diameter distance, z is the redshift, n_e and n_H are the electron and hydrogen density (cm^{-3}) respectively, and dV is the volume from which the deprojected emission originates.
[d] The line is unresolved; the intrinsic width has been fixed to be $\simeq$ 10 eV.
[e] units of 10^{-3} photons cm^{-2} s^{-1}.
For a comparison on the luminosities measured in *Suzaku* and XMM-*Newton* see Section 3.3.3.

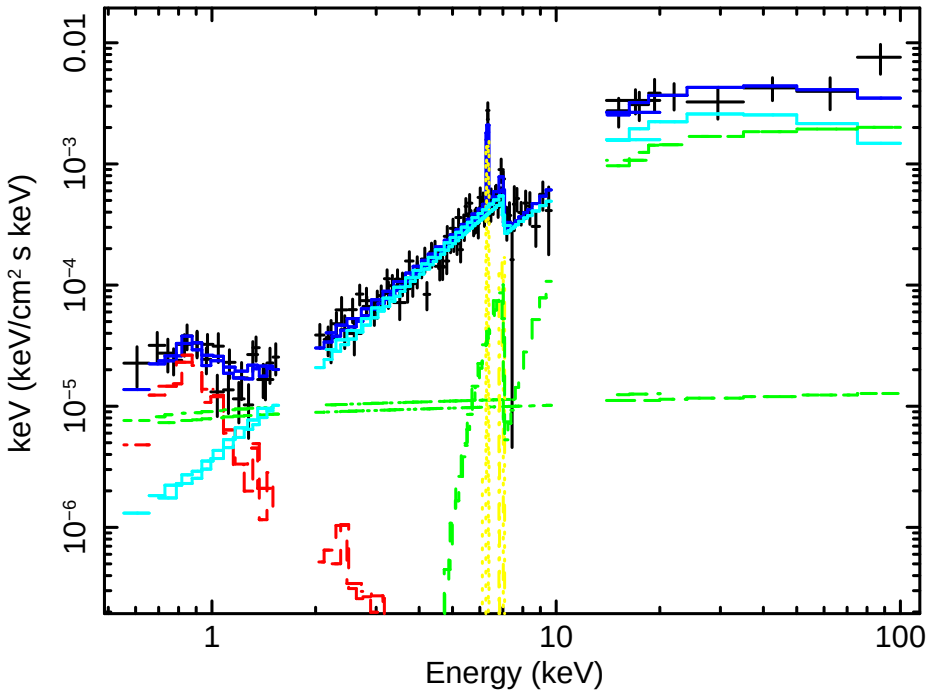

Figure 3.7: *Unfolded* Suzaku *spectrum, showing separately the different components of the best-fit model: in green the scattered power-law and the primary absorbed power-law, in red the soft thermal component, in yellow the iron Kα and Kβ emission lines, in light blue the reflection component, and in blue the total resulting spectrum.*

3.3.2 Comparison with XMM-*Newton* data

In Figure 3.8 I report the *Suzaku* XIS (black, lower spectrum), HXD (black) and *Swift*-BAT spectra (green). In red (upper spectrum) I also show the XMM-*Newton* pn and MOS data, revealing a dramatic change in the spectral curvature between 3 and 6 keV. This variation is most likely due to a change in the amount of absorption of the primary radiation. To test this hypothesis the *Suzaku* best-fit model was applied to the XMM-*Newton* spectra, leaving only the absorbing column density ($N_{\rm H}$) free to vary. Also, both the cross-normalisation factors between the pn and the MOS spectra and between *Swift*-BAT and pn data were left free to vary; they were found to be 1.02 ± 0.04 and $1.06^{+0.14}_{-0.16}$ respectively.

During the XMM-*Newton* observation the $N_{\rm H}$ decreased by about one order of magnitude (from $\sim 2.1\times10^{24}{\rm cm}^{-2}$ to $\sim 2.6\times10^{23}{\rm cm}^{-2}$); this change in the amount of absorption is sufficient to explain the bulk of the differences between the observed XMM-*Newton* and *Suzaku* spectra.

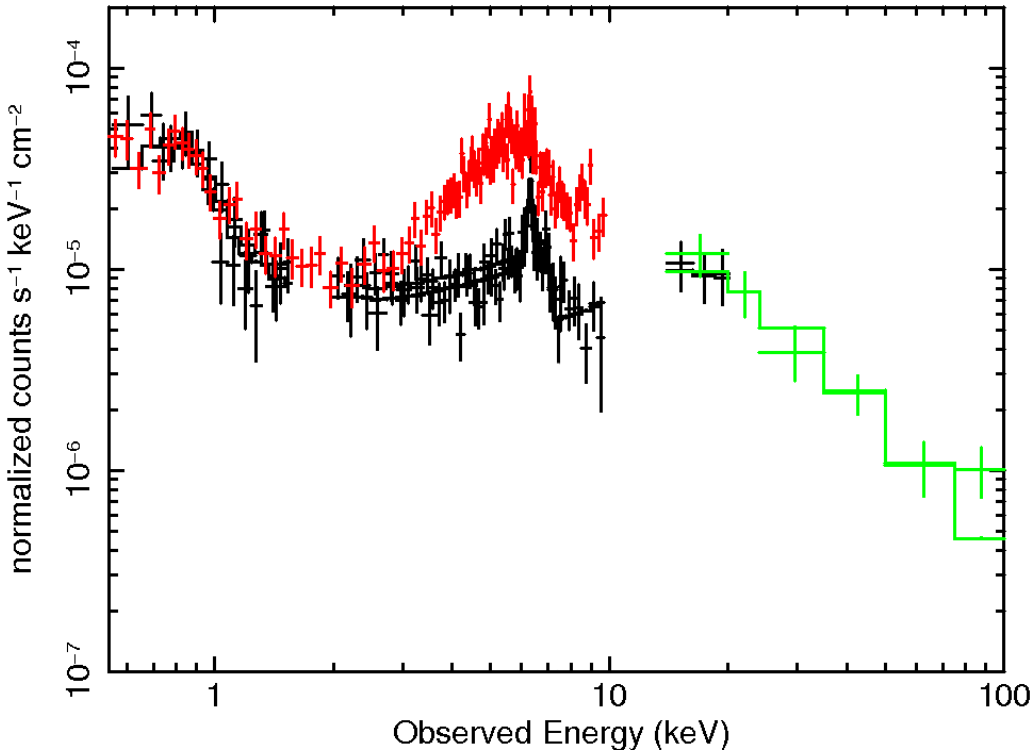

Figure 3.8: *Comparison between the* Suzaku *XIS (black, lower spectrum), HXD (black),* Swift*-BAT (green) and the XMM-*Newton *(red, upper spectrum) data showing the dramatic change in the 3–10 keV energy range. The underlying model (black and green line) is the one obtained fitting only the* Suzaku *XIS (black) and* Swift*-BAT data (green).*

For completeness, also the photon index (Γ), the normalisation of both the power law components, the thermal component and the Kα energy and normalisation were allowed to vary. The fit yielded χ^2/dof=213.9/199 and the only parameter changing well beyond the *Suzaku* errors is, as expected, the $N_{\rm H}$, decreasing to $2.78^{+0.16}_{-0.17} \times 10^{23}$ cm^{-2}. This confirms that the strong variation between XMM-*Newton* and *Suzaku* is due to a change in column density of $\Delta N_{\rm H} \sim 1.8 \times 10^{24}$ cm^{-2}.
Prompted from this result, I carried out the analysis of the 3 *Swift*-X-ray Telescope (XRT) observations taken in 2006 with a time lag of the order of 1–2 days from each other. It was found that the source was in a state similar to that observed by XMM-*Newton*. The exposure time of each of the observations is less than 10 ksec (8713, 8661 and 3667 sec respectively), thus the relatively low statistics does not allow to establish if there is a variability between the single observations.

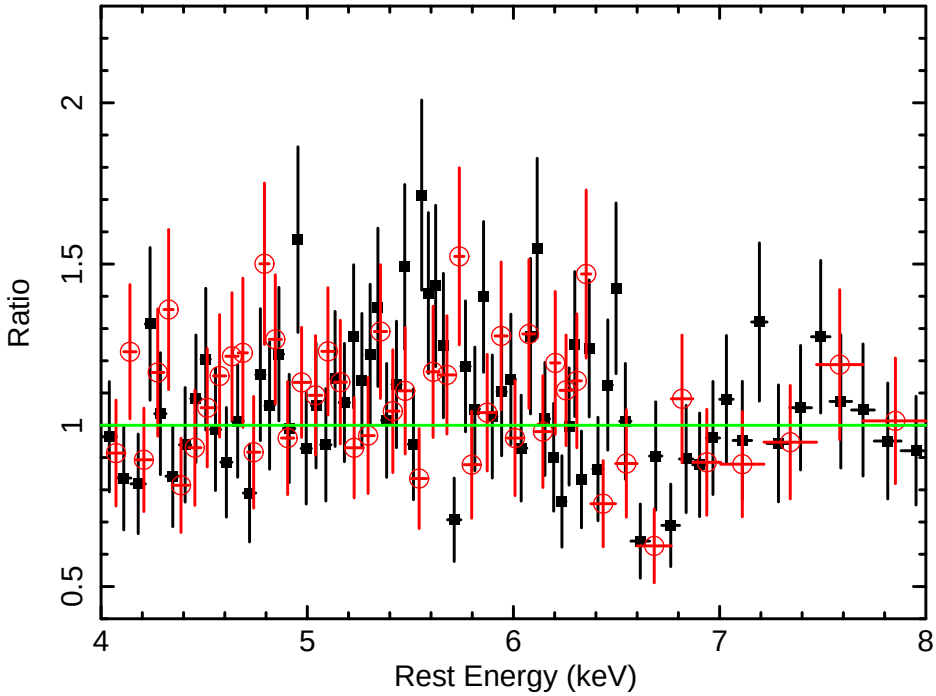

Figure 3.9: *Residuals of the XMM-*Newton *data (pn data are the black filled squares and MOS data are the red open circles) in the range 4–8 keV with respect to the spectral model discussed in section 3.3.2. An absorption feature at about 6.7 keV and a spectral curvature in the 5–6 keV range are clearly present.*

A closer inspection of the residuals in the 4–8 keV energy range to this best-fit model showed some residual curvature between 5 and 6 keV, together with a clear absorption feature centered at ∼ 6.7 keV (see Figure 3.9), which is present in both the pn and MOS spectra and is suggestive of a more complex and likely ionized absorber. After checking the significance of this absorption line, an additional ionized absorber (see section 3.3.2.1)

was included in the model. I remark that, after accounting for the absorption feature at ~6.7 keV, the excess of curvature in the range 5–6 keV is not present anymore.

The final parameters of the XMM-*Newton* best-fit model are reported in table 3.1 and the final model setup is described in section 3.3.2.1. The difference in the best-fit normalisations of the thermal and scattering component between *Suzaku* and XMM-*Newton* are likely due to a degeneracy between these two parameters. Indeed the 0.5–2 keV flux did not strongly vary between the two observations.
The fraction of scattered radiation is $\sim$ 5%. The observed 2–10 keV flux is $\sim 1.9 \times 10^{-12}$erg cm^{-2} s^{-1}, while the intrinsic 2–10 keV luminosity, $L_{(2-10)\mathrm{keV}}$, is $\sim 2.5 \times 10^{42}$erg s^{-1}, about a factor 2.8 below the intrinsic luminosity computed using only the *Suzaku* data. Although such a variation of the intrinsic luminosity is not unusual in AGN, part of this difference could be due to the geometry assumed by the models adopted for the high column density absorber. Indeed I will show in section 3.3.3 that this difference is smaller (a factor 1.7) when the *Mytorus* code is used for the absorber.

3.3.2.1 The $\sim$ 6.7 keV absorption feature in the XMM-*Newton* observation

As a first step to model the absorption feature in the 6–7 keV band a Gaussian absorbing component was added; setting $\sigma = 0.05$ keV, the centroid of the line is found at E=$6.75^{+0.06}_{-0.04}$ keV, the normalisation is $-3.75^{+1.12}_{-1.13} \times 10^{-6}$ and $\Delta\chi^2$=24 for 2 dof. The absorption line appears to be marginally resolved; however leaving its width free to vary only an upper limit $\sigma < 0.3$ keV can be inferred (corresponding to an upper limit on the broadening velocity of ~0.044c), while the energy centroid E=$6.77^{+0.08}_{-0.06}$keV is found to be consistent within the errors. The energy of this absorption line suggests an association with absorption from highly ionized Fe (i.e. Fe xxv at E~6.7 keV) and thus a clear signature of the presence of an ionized absorber. The presence of an ionized absorber is not exceptional, as discussed in Section 2.5.1. Indeed recent sensitive observations with *Chandra*, XMM-*Newton*, and *Suzaku* unveiled the presence of red- and blue-shifted photoionized absorption lines both in type 1 and type 2 AGN as well as in Radio Quiet and Radio Loud AGN (Tombesi et al. 2010b; Tombesi et al. 2011). Thus, it appears that there is a substantial amount of ionized gas in the nuclei of AGNs, which may be linked to gas outflowing on parsec scales with velocities from hundreds of km/s up to $v_{\mathrm{out}} \sim 0.04 - 0.15c$ (Tombesi et al. 2010b). Red- and blue-shifted absorption lines are predicted in several theoretical models of failed disk winds (Proga & Kallman 2004; Sim et al. 2010) or of aborted jet (Ghisellini et al. 2004). However, before proceeding with any further modelling of the absorption feature I checked its significance.

To assess the significance of the absorption feature, extensive Montecarlo simulations were performed, as detailed below. The assumed null hypothesis model is the best-fit model discussed at the end of section 3.3.2, and S=3000 spectra were simulated (with the *fakeit* command in XSPEC), with the same exposure time as the real data. Each one of these simulated spectra was then fitted with the null hypothesis model to obtain a χ^2 value, searching systematically for an absorption line in the 2–10 keV energy range,

stepping the energy centroid of the Gaussian in increments of 0.1 keV and refitting at each step. For each simulated spectrum a minimum χ^2 was obtained and allowed to create a distribution of 3000 simulated values of the $\Delta\chi^2$ (compared to the null hypothesis model). This indicates the fraction of random generated absorption features in the 2–10 keV band that are expected to have a $\Delta\chi^2$ greater than a threshold value. If N of these simulated values are greater than the real value, then the estimated detection confidence level is 1-N/S. Using this analysis it is possible to conclude that the line detection is significant at >99.97% level, i.e. only 0.03% of the simulated spectra show a $\Delta\chi^2$ higher than the real value.

In order to obtain a physical description of the absorber the Gaussian absorption line was replaced with a model representing a photoionized absorber, which has been produced using a multiplicative grid of absorption model generated with the XSTARV 2.1 code (Kallman et al., 2004). This grid describes an ionized absorber parametrised by its column density ($N_{\rm H}$), and its ionisation parameter (ξ). Since there is no apparent broadening of the absorption line a turbulence velocity of $v_{\rm turb}$ = 300 km s^{-1} was assumed.
The inclusion of this ionized absorber significantly improved the fit (χ^2/dof=190.7/197, $\Delta\chi^2$ = 25 for 2 dof), with a column density of $N_{\rm H} = 6.05^{+8.95}_{-4.10} \times 10^{23}$ cm^{-2}and an ionisation of $\log(\xi/\mathrm{erg\ cm\ s^{-1}}) = 3.55^{+0.49}_{-0.25}$. The improvement in the χ^2 is determined solely by fitting the absorption feature in the 6–7 keV band, since an ionised absorber with such a high level of ionization does not produce any feature below 2 keV.

The parameters of the XMM-*Newton* best-fit model are reported in table 3.1 and the model setup is the following:

WABS×[MEKAL + ZPOWERLW + ZGAUSS + ZGAUSS + PEXRAV + XSTAR *CABS *ZPHABS ×(ZPOWERLW)]

Since this absorption feature is not observed in the *Suzaku* spectrum, a Gaussian absorption line was added to the *Suzaku* best-fit model, using the same parameters obtained with the XMM-*Newton* data. The lower limit for the detection of an absorption line with central energy of 6.75 keV and width of 0.05 keV, is -1.18×10^{-6} for the *Suzaku* data. Thus, being the normalisation of this line -3.75×10^{-6} in the XMM-*Newton* spectrum, one can infer that the ionised absorber should be detectable by *Suzaku*. The simplest interpretation is that also the ionized absorber is variable; which is not surprising since there are several reported cases of variable absorption feautures (Tombesi et al. 2010b; Tombesi et al. 2011; Braito et al. 2007; Cappi et al. 2009; Dadina et al. 2005; Risaliti et al. 2005). Moreover instability of the outflowing ionized absorbers is predicted both in disk winds models (Proga & Kallman 2004; Sim et al. 2010) or of aborted jet (Ghisellini et al. 2004). This will cause the presence of transient absorption features and variability of the derived outflowing velocities and their EW as observed in several sources (see e.g. Tombesi et al. 2010b)

3.3.3 A physical interpretation with *MyTorus* model

The models discussed so far, which are based on spectral components largely used from the astronomical community, do not treat both fluorescent emission lines and continuum components self-consistently. Furthermore all these spectral components may be deficient in one or more aspect of modelling the complex transmission and reflected spectrum of AGN over a broad energy range and for a large range of absorbing column densities (see section 2 of Murphy and Yaqoob, 2009 for a critical discussion of these points).

In order to alleviate these problems and, thus, to further assess the possible geometry and/or nature of the variable absorber, I tested the model for the toroidal reprocessor [11] as descried by Murphy & Yaqoob (2009). This model, recently included in the XSPEC software package, is valid for column densities in the range 10^{22} to 10^{25} cm^{-2} and for energies up to 500 keV (the relativistic effects being taken into account); more importantly the reprocessed continuum and fluorescent line emission are treated self-consistently. This model assumes that the absorber geometry is toroidal with a half opening angle of 60° (corresponding to a covering factor $\Delta\Omega/(4\pi) = 0.5$), and cosmic abundances of Anders & Grevesse (1989). Among the free parameters there are the viewing angle and the column density (see http://www.mytorus.com/manual/index.html). I remark, as a point of difference, that the PEXRAV model assumes that the reflector has the geometry of a slab, therefore its parameters don't give information on the geometry of the toroidal material surrounding the AGN. The MYTORUS model is composed by three tables:

- MYTORUSZ: a multiplicative table that, applied to the primary power-law, describes the zeroth order continuum, i.e. the spectrum resulting from the photons that do not interact with the intervening matter. This spectrum is distorted with respect to the direct continuum, because of photoelectric absorption (at low energies) and Klein-Nishina scattering (at higher energies, due to the energy dependence of the Klein-Nishina scattering cross section).

- MYTORUSS: an additive table describing the scattered/reflected continuum towards the line of sight

- MYTORUSL: an additive table describing the emission lines (Fe kα, Fe kβ and the Compton shoulder)

Since we are clearly seeing a variation of the absorbing column density along the line of sight I used a spectral configuration of *MyTorus* that can *mimic* a clumpy absorber and which also takes into account the fact that the Fe Kα is rather constant (see table 3.1). This has been done by decoupling the direct (unscattered) continuum passing through the reprocessor and the reflected/scattered continuum from reprocessor. In practice this means decoupling the inclination angle parameters for the direct continuum and the reflected/scattered continuum, and leaving the column densities of these two components independent from each other (meaning that the $N_{\rm H}$ responsible for absorption along the line of sight can be different with respect to the $N_{\rm H}$ responsible for reflection/scattering towards the line of sight).

[11] http://www.mytorus.com/

Therefore, for the direct continuum I fixed the inclination angle between the line of sight and the axis of the torus to be 90 degrees, as for a configuration of edge-on torus. Then, I assumed a patchy reprocessor in which the scattered continuum is observed from reflection in matter on the far-side of the X-ray source, without intercepting any other "clouds," (while the intrinsic continuum is filtered by clouds "passing" through our line-of-sight to the central engine). This configuration can be parametrized with the MYTORUSS component, fixing the inclination angle to 0 degrees, i.e. face-on, which represents the back-scattered radiation without intercepting any absorbing matter. Finally, since the XMM-*Newton* spectrum unveiled the presence of an additional ionized absorber, which affects the line-of-sight continuum, also an ionized absorber was included, which is modelled adopting the same XSTAR grid as described in section 3.3.2.1.

The best-fit model obtained using the MYTORUS model is:

PHABS (ZPOWERLW * XSTAR * MYTORUSZ + A_S * MYTORUSS + A_L* GSMOOTH* MYTORUSL+ MEKAL + CONSTANT * ZPOWERLW)

The XSPEC model GSMOOTH is a gaussian convolution model that allows to leave the line width as free parameter, since the MYTORUSL is characterised by an intrinsic velocity width of 10 km/s. A_S and A_L are the relative normalizations of the reflected continuum and of the emission lines, respectively. Also a soft power law component was included, in order to account for the scattering due to optically-thin ionised gas.

Applying this model to the the XMM-EPIC and *Swift*-BAT spectra a good fit was found, with the same absorbing column density ($N_{\rm H} = 2.75^{+0.05}_{-0.04} \times 10^{23}{\rm cm}^{-2}$; χ^2/dof=201/192) filtering the line-of-sight intrinsic continuum and producing the scattered component (including the production of the fluorescent emission lines). The parameters of the ionized absorber are: $N_{\rm H} = 6.46^{+5.04}_{-1.96} \times 10^{23}{\rm cm}^{-2}$and $\log\xi = 3.26^{+0.20}_{-0.21}$erg cm s^{-1}; these values are in good agreement with those found with the best-fit model described in table 3.1, together with the parameters of the thermal component (MEKAL). The photon index of the primary power-law component is now $\Gamma = 1.86^{-0.11}_{+0.17}$ and the intrinsic emitted luminosity is $L_{[2-10]{\rm keV}} \sim 1.4 \times 10^{42}$erg s^{-1}. Using the *Suzaku* and *Swift* data, a good fit can be obtained with an absorber producing the reflected components having an $N_{\rm H}$ statistically consistent with that obtained using the XMM-*Newton* data (thus suggesting that this component is likely associated with the distant reflector or torus), while our line of sight to the central engine intercepts a column density $N_{\rm H} = (0.88 \pm 0.09) \times 10^{24}$ cm^{-2}. The photon index of the primary power-law component is $\Gamma = 1.8^{+0.12}_{-0.12}$, consistently with what found for XMM-*Newton*. The parameters of the MEKAL remain in good agreement with the values reported in table 3.1.

In summary this analysis, which is based on a model which takes into account consistently the physical process in place within the X-ray absorber, shows that the change of state of NGC454E can be understood simply by a change in the line-of-sight obscuration ($\Delta N_{\rm H} \sim 6 \times 10^{23}$ cm^{-2}) while the global obscurer remains unchanged.

The intrinsic luminosity derived from the *Suzaku* data is $L_{[2-10]{\rm keV}} \sim 2.4 \times 10^{42}$erg s^{-1}. Using *Mytorus* the derived change of the intrinsic luminosity between the two data sets are in better agreement (a factor 1.7) with respect to those found in Section 3.3.2. However, with the present statistic and the complexity of the observed spectra, it is not possible to rule

Table 3.2: Summary of the *Suzaku* and XMM-*Newton* parameters using the MYTORUS model described in Section 3.3.3.

Model Component	Parameter	*Suzaku*	XMM-*Newton*
Power law	Γ	$1.80^{+0.12}_{-0.12}$	$\Gamma = 1.86^{-0.11}_{+0.17}$
	Normalisation[a]	$2.93^{2.56}_{-0.83}$	$3.22^{+1.36}_{-1.03}$
MYTorusZ	N_H	$0.88^{+0.08}_{-0.09} \times 10^{24}$ cm^{-2}	$2.75^{+0.05}_{-0.04} \times 10^{23}$cm^{-2}
	Inclination	90°	90°
MYTorusS	N_H	$6.22^{+1.65}_{-1.36} \times 10^{22}$ cm^{-2}	$3.13^{+8.26}_{-3.13} \times 10^{22}$ cm^{-2}
	Inclination	0°	0°
Thermal emission	kT	$0.53^{+0.09}_{-0.17}$ keV	$0.58^{+0.07}_{-0.08}$ keV
	Normalisation[b]	$6.21^{+4.00}_{-2.84} \times 10^{-6}$	$7.68^{+4.19}_{-4.97} \times 10^{-6}$
Ionised Absorber	N_H	..	$6.46^{+5.04}_{-1.96} \times 10^{23}$cm^{-2}
	logξ	..	$3.26^{+0.20}_{-0.21}$erg cm s^{-1}
	v_{turb}	..	300 km s^{-1}
	χ^2/dof	107.6/108	201/192
	$L_{(2-10)keV}$	$\sim 2.4 \times 10^{42}$erg s^{-1}	$\sim 1.4 \times 10^{42}$erg s^{-1}

[a] units of 10^{-3} photons keV^{-1} cm^{-2} s^{-1}.
[b] The normalisation of the thermal component is defined as $K = \frac{10^{-14}}{4\pi(D_A(1+z))^2} \int n_e n_H dV$ where D_A is the angular diameter distance, z is the redshift, n_e and n_H are the electron and hydrogen density (cm^{-3}) respectively, and dV is the volume from which the deprojected emission originates.

out or confirm a possible variation in luminosity of about a factor 2, frequently observed in AGN; indeed by comparing the 54-months and 9-months BAT high energy (14–195 keV) spectra of this source, the intensity is found to be higher in the 9-months spectrum. However, fitting the spectra with a single absorbed power-law component, a constant flux is also well within the errors on the best-fit normalizations of this primary power-law.

3.4 Constraints on the distance of the ionised absorber

Using very simple considerations it is now possible to estimate what is the maximum distance of this ionised absorber from the central black hole, relating the ionisation parameter, the density of the absorber and the continuum luminosity L_{ion} through Eq. 2.3 and Eq. 2.7. In this case, after extrapolating the measured power law below 0.5 keVc , L_{ion} (in the energy range between 13.6 eV and 13.6 keV) is 7.3×10^{42} erg s^{-1}. Assuming that the thickness of the absorber $\Delta R = N_H/n$ is smaller than the distance R_{ion} ($\Delta R/R_{ion} < 1$), the upper limit to the distance is:

$$R_{ion} = \frac{L_{ion}\Delta R}{N_H \xi R} < \frac{L_{ion}}{N_H \xi} = 2.3 \times 10^{15}\text{cm} \approx 7.5 \times 10^{-3}\text{pc} \quad (3.1)$$

This maximum distance of $\sim 10^{-3}$pc is consistent with a location of the ionised absorber within the Broad Line Region of the AGN. Indeed an estimate of the BLR size R_{BLR} for NGC454E can be inferred by using the relation between R_{BLR} and the monochromatic luminosity at 5100 Å, $L_{5100Å}$ (Kaspi et al. 2005, $\frac{R_{BLR}}{10\ lt-days} = 2.45 \times (\lambda L_{\lambda}(5100Å))^{0.608}$). Since the luminosity of the optical continuum cannot be measured directly from the spectrum, because of the strong absorption, $L_{5100Å}$ is estimated from the intensity of the [OIII]5007Å line flux, assuming a mean F[OIII]5007Å/F(5100Å) ratio. This ratio has been inferred from the AGN template presented in Francis et al. (1991) ($F(5100Å) = 0.059F([OIII])$). Using the [OIII]5007Å flux published in Johansson (1988) we obtain $L_{5100Å} \sim 1 \times 10^{41}$erg s^{-1} Å^{-1} and, thus, an approximate size of the BLR of 0.05 pc, i.e. about 50 times R_{ion}.

3.5 Summary and Conclusion

In this chapter I discussed the results of *Suzaku*, XMM-*Newton* and *Swift* observations of the interacting system NGC454 (z=0.0122). The bulk of the measured 2–10 keV emission comes from the active galaxy NGC454E ($L_{[2-10]keV} \sim 2 \times 10^{42}$erg s^{-1}); no emission from the center of the companion galaxy (NGC454W) in the interacting system is detected. The nuclear X-ray emission of NGC454E is filtered by an absorbing column density typical of a Type 2 AGN, in agreement with the optical classification as Seyfert 2 galaxy.

No variability in the light curves has been observed during the length of *Suzaku* and XMM-*Newton* observations respectively. A comparison between the two observations (taken 6 months later) revealed a significant change in the spectra of NGC454E in the energy range between 3 and 6 keV. This variation can be well explained by a variability of about an order of magnitude in the absorbing column density along the line of sight: from $\sim 1 \times 10^{24}$cm^{-2}(*Suzaku*) to $\sim 1 \times 10^{23}$cm^{-2}(XMM-*Newton*). In this work I also used the most recent model for the toroidal reprocessor (Murphy & Yaqoob 2009), which takes into account consistently the physical processes in place within the X-ray absorber. Furthermore, regarding the XMM-*Newton* spectrum, I detected a statistically significant absorption feature a $\sim$ 6.7 keV, a clear signature of the presence of a ionised absorber, with ionisation parameter $\log(\xi/\text{erg cm s}^{-1}) = 3.55$ and column density $N_{\rm H} = 5.31 \times 10^{23}$ cm^{-2}. The absence of this feature in the *Suzaku* spectrum, despite its detectability, implies that it has varied between the two observations. Absorption lines associated with ionized iron have been now observed in several sources and there is also a clear evidence that these lines are variable as in the case of NGC454. Furthermore, in some cases the measured blue-shifts of the energy centroids imply a large velocity of these absorbers and a likely association with powerful disk winds (King & Pound 2003), while in other cases there is no measurable motion as in our case.

In summary, NGC454E is a new member of the class of "changing look" AGN, i.e. AGN that have been observed in both Compton-thin ($N_{\rm H}$=10^{23}cm^{-2}) and Compton-thick

states ($N_{\rm H}> 10^{24}{\rm cm}^{-2}$). A possible scenario is that a stable and likely distant absorber responsible for the iron emission line is present. However, there is also a clear variation of the $N_{\rm H}$ of the line of sight absorber, probably indicative of the clumpy nature of the rather neutral absorber itself. Unfortunately the comparison between different observations, typically performed at intervals of months to years (as those discussed here), provides only upper limits to the intrinsic time scales of $N_{\rm H}$ variations and thus on the possible location of the thicker obscuring material (obscuring “torus" vs. Broad Line Region clouds). The low exposure of the *Swift* XRT 2006 observations, when the source was in a state similar to the XMM-*Newton* one, did not allow us to establish the $N_{\rm H}$ variability on smaller time scales (i.e. intra-day) of the single observations. An improvement of the estimates of velocity, distance and size from the central X-ray source of the obscuring material could be obtained only through monitoring observational campaigns within a few days or weeks and/or through the search for $N_{\rm H}$variations within single long observation. For what concerns the ionised absorber, as derived from my first order estimate of its distance from the central black hole (i.e. within 10^{-3} pc), the most likely location for this absorber is much closer in than the stable and rather neutral one.

CHAPTER 4

The variable ionized absorber in the Seyfert 2 Mrk 348

Contents

4.1 Observations and data reduction 88
4.1.1 *Suzaku* 88
4.1.2 XMM-*Newton* 90
4.2 Spectral analysis 90
4.2.1 Suzaku spectral analysis 90
4.3 XMM-*Newton* data analysis 100
4.3.1 Reflection scenarios 103
4.3.2 $N_{\rm H}$ past observations 104
4.4 Discussion 107
4.5 Conclusions 108

Mrk 348 (NGC 262) is a bright Seyfert 2 galaxy (R=13 mag) at z=0.015 (corresponding to 84 Mpc, Khachikian & Weedman 1974; de Vaucouleurs et al. 1991). It is one of the brightest sources in the BAT catalogue ($F_{(14-195\ \rm keV)} \sim 1.6\times10^{-10}$erg cm^{-2} s^{-1}, Baumgartner et al. 2013) and for which the availability of *Suzaku* data allows to perform for the first time a detailed analysis of the spectrum above 10 keV. The optical spectrum is characterized by narrow, high-excitation emission lines (Fig. 4.2, Marcha et al. 1996) and a hidden BLR was revealed through the detection of a broad Hα emission line (~7500 km/s) in the polarized spectrum (Miller & Goodrich 1990).
To the east of Mrk 348 a companion galaxy at the same redshift is present, at a distance of ~ 22.2 kpc. The optical images of Mrk 348 published by Antón et al. (2002) (taken with the Nordic Optical Telescope) in Fig. 4.1 reveal that Mrk 348 is a spiral galaxy, where the end of one disrupted arm reaches the eastern companion galaxy, confirming that they are interacting on large scale, as already proposed by Simkin et al. (1987) using radio observations. Interestingly the region of the eastern component nearer to the external arm of Mrk 348 is bluer, as if star formation has been triggered by the interaction between the two galaxies.

Mrk 348 is a relatively strong radio emitter and was observed by the Very Large Array (VLA) and the Multi-Element-Radio-Linked-Interferometer-Network (MERLIN, Unger et al. 1984; Antón et al. 2002). It is characterised by a flat radio spectrum continuing well into the infrared, as well as a core-dominated radio structure and rapid radio variability

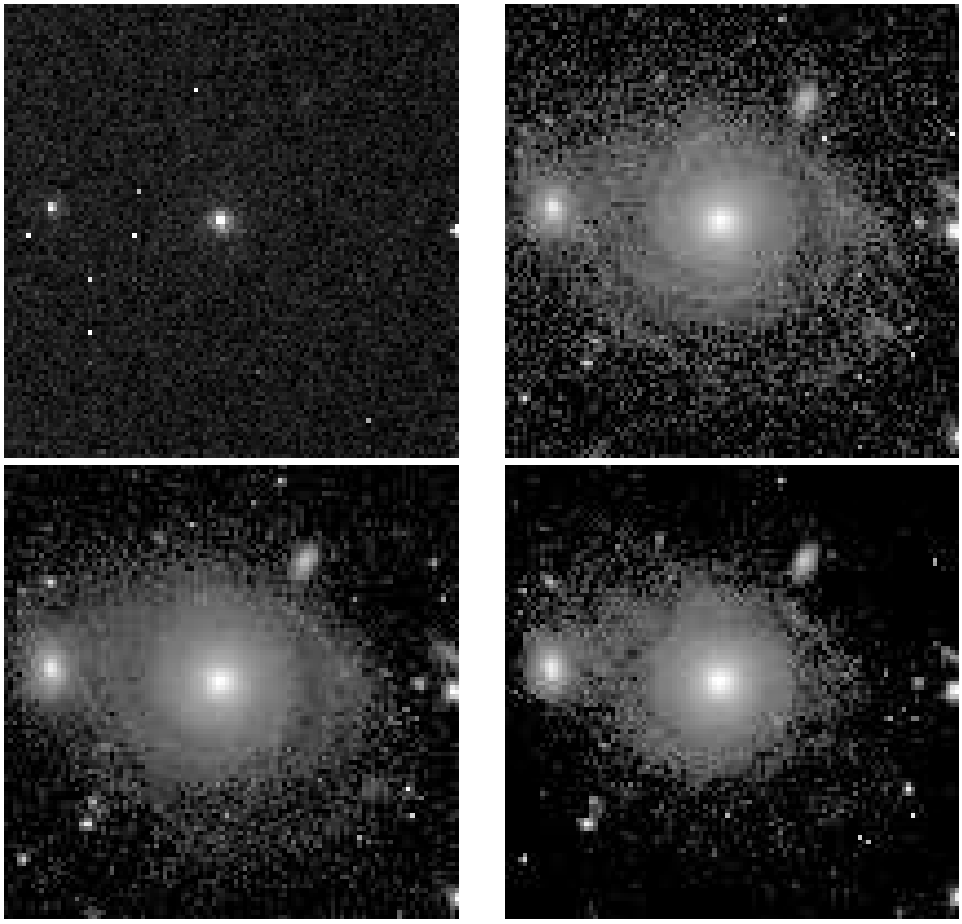

Figure 4.1: *Mrk 348 and its companion galaxy, as observed by the Nordic Optical Telescope, in the U (top left), B (top right), R (bottom left) and I (bottom right) bands. For each image the field of view is 3.3'×3.3', the North is up and the East is on the left. The B,R and I images also show the spiral arms, appearing very symmetric in the internal region and with a slightly more disturbed morphology in the external part. Images adapated from Antón et al. (2002).*

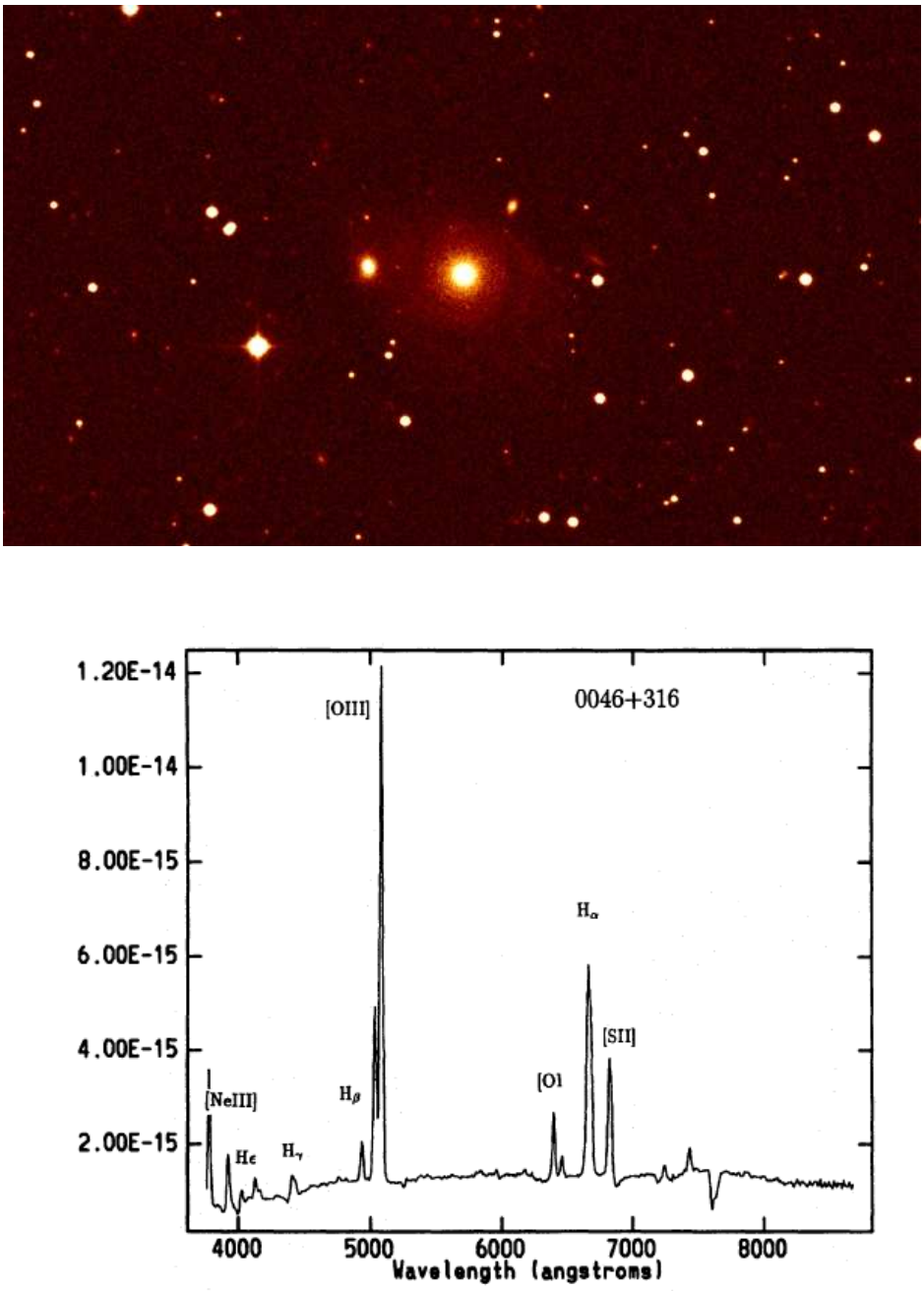

Figure 4.2: Top panel*:* Digital Sky Survey *(DSS) 11.7 × 6.8 arcmin optical image, based on photographic data obtained using the Oschin Schmidt Telescope on Palomar Mountain and the UK Schmidt Telescope.* Bottom panel*: Optical spectrum of Mrk 348 as reported by Marcha et al. (1996). The presence of narrow emission lines allows to classify the source as a Seyfert 2 galaxy.*

(Neff & de Bruyn 1983). The complex radio properties of this source and the difficulties in determining its orientation with respect to the line of sight make its classification as a radio-quiet or as a radio loud source uncertain, however according to the standard radio classification (Section 1.2.3.1) it belongs to the class of Radio Quiet sources (Xu, Livio, & Baum 1999).

The first X-ray observation of this source was performed by *Ginga*, and provided evidence of an absorbed ($N_{\rm H}\sim 10^{23}{\rm cm}^{-2}$) X-ray source, with photon index $\Gamma\sim$1.7 (Warwick et al. 1989). Mrk 348 was also observed with the *Rossi X-Ray Timing Explorer* (*RXTE*) mission in twelve observations during the period December 29, 1996 to July 12, 1997. Smith et al. (2001) analysed these spectra and described the resulting time–averaged 3–20 keV spectrum with a power-law continuum ($\Gamma\sim 1.8$) absorbed by a column density of $N_{\rm H}$ $\sim 10^{23}{\rm cm}^{-2}$, plus a Fe K$\alpha$ emission line with equivalent width $EW\sim 100$ eV, plus a Compton reflection component. They found variations in the intrinsic column density occurring over periods of typically weeks to months, with the largest change ($\Delta N_{\rm H}\sim 10^{23}{\rm cm}^{-2}$), taking place on a time-scale of $\sim$ 70 days. They also found X-ray continuum variations with the shortest observed timescale of $\sim$ 1 day. Smith et al. (2001) also found that the Fe Kα line flux did not change significantly during the multiple observations, deducing that much of the line emission is produced in a layer of material with a rather constant sky coverage and thickness, as viewed from the nucleus. They modelled the Compton reflection component using PEXRAV (Magdziarz & Zdziarski 1995), finding that the data were consistent with a reflection strength of $R\sim 0.3-0.8$. The 2–10 keV luminosity measured in these observations was, depending on the observed $N_{\rm H}$ of each observation, in the range 0.8–3.4$\times10^{43}$erg s^{-1} (for $H_0 = 50$; $q_0 = 0.5$), a factor 3 higher than that measured by *Ginga*. Smith et al. (2001) suggested that the absorber in Mrk 348 could consist of individual clouds; motions in and out of the line of sight could explain the observed variations in $N_{\rm H}$. Akylas et al. (2002) analyzed the same data as Smith et al. (2001) but with additional 25 *RXTE* observations taken in May–June 1996. This analysis confirmed the spectral variability already observed by Smith et al. (2001).

Finally, a more recent work by Singh et al. (2011) on the X-ray spectral properties of a sample of Seyfert galaxies, analysed the 0.5–10 keV XMM-*Newton* EPIC-pn spectrum of Mrk 348. They suggested the presence of two absorbers intercepting the primary radiation, a fully covering absorber, with $N_{\rm H}\sim 7\times10^{22}{\rm cm}^{-2}$and a partial covering component, with $N_{\rm H}\sim 1\times10^{23}{\rm cm}^{-2}$ and covering fraction of $C_f\sim 0.84$. They also found a narrow Fe Kα line with $EW\sim$34 eV.

In this work I analysed the *Suzaku* and XMM-*Newton* spectra of Mrk 348, finding a variability in the spectral curvature between them. In both cases the structure of the absorbers intercepting the primary radiation is quite complex: three layers of absorption, of which one is neutral and two are ionized. I engaged in the study of which are the physical parameters responsible for the observed variability. As I will discuss in detail in this chapter, I found that Mrk 348 is characterized by a variation in the column density of both the neutral and one of the ionized absorbers, together with a variation in the ionization level of the same absorber. The results of this work have been published on *Monthly Notices*

of the Royal Astronomical Society (Marchese et al. 2014).

4.1 Observations and data reduction

4.1.1 *Suzaku*

Mrk 348 was observed by *Suzaku* (Mitsuda et al. 2007) on 28th June 2008 for a total exposure time of about 88 ks.
A detailed description of the *Suzaku* telescope and instruments is presented in Appendix A.

4.1.1.1 The *Suzaku* XIS data reduction

The XIS data were selected in 3×3 and 5×5 editmodes using only good events with grades 0, 2, 3, 4, 6 and filtering the hot and flickering pixels with the script *sisclean*. The XIS response (rmfs) and ancillary response (arfs) files were produced, using the latest calibration files available, with the *ftools* tasks *xisrmfgen* and *xissimarfgen* respectively. The net exposure times are 76 ks for each of the XIS. The XIS source spectra were extracted from a circular region of 2.9′ centered on the source, and the background spectra were extracted from two circular regions with radius 2.3′, offset from the source and the calibration sources. The spectra from the two FI CDDs (XIS 0 and XIS 3) were combined to create a single source spectrum (hereafter XIS–FI), while the BI (the XIS1) spectrum was kept separate and fitted simultaneously. The net 0.5–10 keV count rates are: (0.793 ± 0.003) counts s^{-1}, (0.829 ± 0.003) counts s^{-1}, (0.709 ± 0.003) counts s^{-1} for the XIS0, XIS3 and XIS1 respectively. We considered data in the range 0.6–10 keV for the XIS–FI and in the range 0.6–9 keV for the XIS–BI (ignoring the band 1.6–1.9 keV, due to the presence of instrumental calibration uncertainties). The difference on the upper boundary for the XIS1 spectra is because this CCD is optimised for the soft X-ray band, with higher background at higher energies.

The net XIS source spectra were physically binned at the *Suzaku* energy resolution, then they were further grouped to a minimum of 20 counts per bin in order to use χ^2 statistics.

4.1.1.2 The *Suzaku* HXD-PIN data reduction

For the HXD-PIN data reduction and analysis I followed the latest *Suzaku* data reduction guide (the ABC guide Version 2[1]), and used the rev2 data, which include all 4 cluster units. The HXD-PIN instrument team provides the background (known as the "tuned" background) event file, which accounts for the instrumental "Non X-ray Background" (NXB; Kokubun et al. 2007). The systematic uncertainty of this "tuned" background model is ±1.3% (at the 1σ level for a net 20 ks exposure, Fukazawa et al. 2009).
The source and background spectra were extracted using the same common good time interval, and corrected the source spectrum for the detector dead time. The net exposure time after screening was 73 ks. I then simulated a spectrum for cosmic X-ray background counts (Boldt 1987; Gruber et al. 1999) and added it to the instrumental one. Mrk 348 was detected at a level of 36.8% above the background.

[1] http://heasarc.gsfc.nasa.gov/docs/suzaku/analysis/abc/

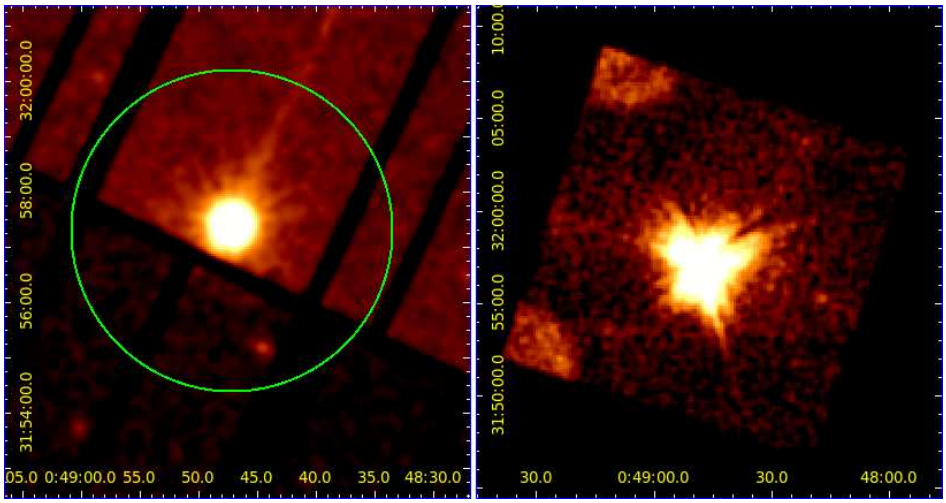

Figure 4.3: Left panel*: XMM-Newton EPIC-pn image (0.5-10 keV) with superimposed the Suzaku XIS-0 extraction region.* Right panel*: Suzaku XIS-0 image (0.5-10 keV), where the illuminated areas in the two left corners are caused by the* ^{55}*Fe calibration sources illuminating each XIS sensor.*

Fitting this spectrum with a power law we obtain a photon index $\Gamma = 1.50^{+0.09}_{-0.09}$ and $F_{(14-70\ \mathrm{keV})} \sim 1.5 \times 10^{-10}$erg cm^{-2} s^{-1}. The extrapolation of this flux in the 14–195 keV band (using the best-fit photon index) gives $F_{(14-195\ \mathrm{keV})} \sim 3.4 \times 10^{-10}$erg cm^{-2} s^{-1}.
Mrk 348 was also detected with the BAT detector on board of *Swift* (Gehrels et al. 2004). Its BAT name is SWIFT J0048.8+3155 and it is part of the *Swift*-BAT 70-Month Hard X-ray Survey (heasarc.gsfc.nasa.gov/docs/swift/results/bs70mon/ ; Baumgartner et al. 2013). The flux obtained by fitting the *Suzaku* HXD spectrum is higher than the *Swift*–BAT flux, which is $F_{(14-195\ \mathrm{keV})} \sim 1.6 \times 10^{-10}$erg cm^{-2} s^{-1} (Baumgartner et al. 2013). We also note that *Swift*–BAT observation provides a different photon index, $\Gamma \sim 1.9$, probably due to the wider energy range. If we fit simultaneously *Suzaku* HXD-PIN and *Swift*–BAT spectra, fixing the photon indexes to the same value, we find $\Gamma \sim 1.8$; if we extrapolate the flux in the 14–195 keV band from *Suzaku* HXD observation we find $F^{HXD}_{14-195\mathrm{keV}} \sim 2.3 \times 10^{-10}$erg cm^{-2} s^{-1}, while the flux measured with *Swift*–BAT is $F^{BAT}_{(14-195\ \mathrm{keV})} \sim 1.6 \times 10^{-10}$erg cm^{-2} s^{-1}. The variation could be explained by the fact that *Swift*–BAT spectrum is an average of the observations made during 70 months, while the HXD observation provides a snapshot of the spectrum, when the flux was possibly higher, therefore it is not surprising to find intrinsic variations between them. It is very unlike that this variation could be due to background issues. For comparison I verified that the background for this observation deviates less than 5% from the one observed in the HXD observation of NGC 454. This background variation is much lower than the flux variation between HXD and *Swift*–BAT spectra.

4.1.2 XMM-*Newton*

XMM-*Newton* observed Mrk 348 on July 18, 2002 for a total duration of about 50 ks.

During this observation the pn, MOS1, and MOS2 cameras (operating in Full Frame Window mode) had the medium filter applied. The data have been processed using the Science Analysis Software (SAS ver. 6.5) and analysed using standard software packages (FTOOLS ver. 6.1). Event files have been filtered for high-background time intervals, and only events corresponding to patterns 0–12 (MOS1, MOS2) and to patterns 0–4 (pn) have been used. The net exposure times at the source position after data cleaning are ~31.5 ks (pn), ~38.3 ks (MOS1) and ~38.2 ks (MOS2). The net count rate in the 0.5–10 keV band is 2.078±0.008 counts s^{-1} (pn), 0.647 ± 0.004 counts s^{-1} (MOS1) and 0.650±0.004 counts s^{-1} (MOS2). The effect of pile-up for this source is negligible.
The results of the analysis of the XMM-*Newton* observation were already published in past works (Singh et al. 2011; Guainazzi et al. 2011), describing a best-fit model composed of a fully covering absorber ($N_{\rm H} \sim 7 \times 10^{22}{\rm cm}^{-2}$), and a partial covering component with $N_{\rm H} \sim 10.5 \times 10^{22}{\rm cm}^{-2}$and covering fraction of $C_f \sim 0.84$. Therefore in this work for simplicity only the pn data were used (the MOS spectra are consistent with it), in order to compare it to the new *Suzaku* spectra.

4.2 Spectral analysis

All the models were fitted to the data using standard software packages (XSPEC ver. 12.6.0, Arnaud 1996) and including Galactic absorption ($N_{\rm H,Gal} = 5.86 \times 10^{20}{\rm cm}^{-2}$; Kalberla et al. 2005). In the following, unless otherwise stated, fit parameters are quoted in the rest frame of the source at z=0.015 and errors are at the 90% confidence level for one interesting parameter ($\Delta\chi^2 = 2.71$).

4.2.1 Suzaku spectral analysis

For the analysis a simultaneous fit of the *Suzaku* spectra from the XIS-FI (0.6–10 keV), the XIS1(0.6–9 keV) and HXD-PIN (14–70 keV) was performed. The cross-normalization factor between the HXD and the XIS-FI spectra was set to 1.16 (allowing it to vary by ±5%), as recommended for XIS nominal observation processed after 2008 July[2]. The cross normalization factor between the XIS-FI and the XIS1 spectra was allowed to vary.

As a starting point the data were fitted by a simple model composed of an absorbed primary power-law component and an unabsorbed power law, representing the fraction of primary X-ray radiation that is scattered into our line of sight. The photon indices of these two components were tied to each other. At this first stage only the continuum was fitted, excluding the data between 5 and 7.5 keV where the Fe Kα emission complex is expected. This model provided a poor fit with a χ^2 of 411.4 for 266 degrees of freedom (*d.o.f.*), with a photon index Γ ~1.57 and $N_{\rm H}$~ 1.24 $\times 10^{23}{\rm cm}^{-2}$. When including the data in the 5–7.5

[2]http://www.astro.isas.jaxa.jp/suzaku/doc/suzakumemo/suzakumemo-2007-11.pdf; http://www.astro.isas.jaxa.jp/suzaku/doc/suzakumemo/suzakumemo-2008-06.pdf

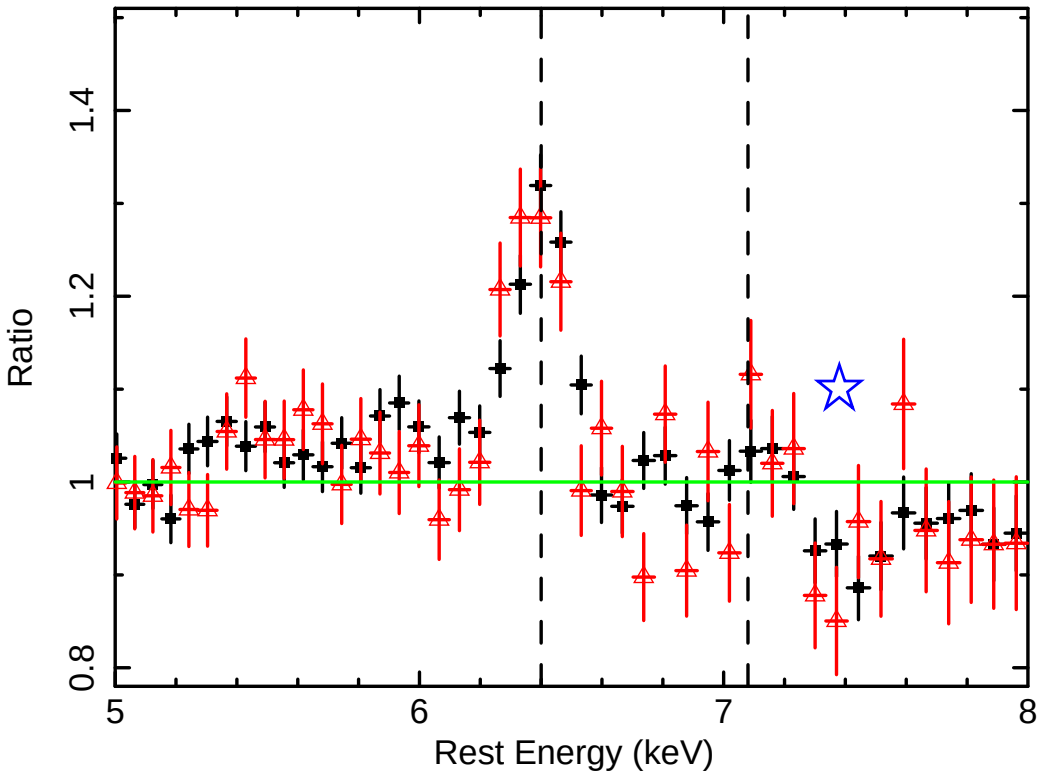

Figure 4.4: *Data/model ratio between the* Suzaku *data (XIS-FI: black filled squares; XIS1: red open triangles) and a basic continuum model composed of an absorbed and an additional unabsorbed (scattered) power law, showing the iron line profile. The two vertical dashed lines correspond to the rest-frame energies of the Fe Kα and Fe Kβ emission lines at 6.4 keV and 7.06 keV respectively. The star indicates a possible absorption feature at ~ 7.4 keV.*

keV energy range a $\chi^2/d.o.f. = 950/344$ is obtained. In Figure 4.4 I report the residuals of this simple model, including all data, which clearly reveal the presence of emission lines at energies corresponding to Fe Kα ($E \sim 6.4$ keV), and to Fe Kβ ($E \sim 7.06$ keV).
Thus two Gaussian components were added, in order to reproduce these emission lines, fixing the normalization of the Fe Kβ line to be 13.5% of the Fe Kα consistent with the theoretical value (Palmeri et al. 2003). The addition of the Fe Kα and Fe Kβ lines improved significantly the fit, yielding as energy centroid for the Fe Kα line E=$6.39^{+0.01}_{-0.01}$ keV and for the Fe Kβ line E=$7.10^{+0.06}_{-0.06}$ keV and a $\Delta\chi^2 = 338.4$ for 3 d.o.f, with respect to the first model applied to all the data (5–7.5 keV). This was still not a good fit ($\chi^2/d.o.f. = 611.6/341$). The equivalent width of the Fe Kα with respect to the observed continuum is $EW = 81.5^{+9.0}_{-8.8}$ eV and the line width is $\sigma = 67.9^{+19.1}_{-21.0}$ eV. Considering that along the line of sight I measured an $N_{\rm H}$ of $\sim 1.2 \times 10^{23}$cm^{-2}, I expect it to produce in transmission an equivalent width of $EW \sim 30$ eV for Solar abundances (Murphy & Yaqoob 2011). Therefore I can suppose that the measured Fe Kα equivalent width ($EW \sim 81$ eV) is mainly due to reflection by Compton thick matter located out of the line of sight.
Given the presence of a flat continuum ($\Gamma \sim 1.57$) and of the Fe Kα emission with an equivalent width of $EW \sim 81$ eV, a Compton reflection component was included in the fit. Fitting the data including this component (modelled by adding the PEXRAV model (Magdziarz & Zdziarski 1995) yields $\chi^2/d.o.f.$=594.0/340 (thus $\Delta\chi^2 = 17.6$ compared to the model with the Fe Kα and Fe Kβ emission lines). The parameters characterizing the reflected component are: an inclination angle i fixed to 60°[3], abundance Z=$Z_\odot$, a reflection fraction found to be $R \sim 0.41$ and a normalisation fixed to the normalisation of the absorbed power law. The fact that the reflection is quite weak is in agreement with the modest equivalent width ($EW \sim 81$ eV) found for the Fe Kα emission line (Ghisellini, Haardt, & Matt 1994; Matt, Brandt, & Fabian 1996).

The model still did not provide a good fit, in particular between 2 and 2.4 keV, as can be observed in Figure 4.5. Thus an emission line at about 2.2 keV and an absorption line at about 2.4 keV were added, even if it cannot be excluded that these features could be instrumental features, such as the Au M edge ($\sim$ 2.2 keV). This provided a better representation of the soft X-ray spectrum, yielding a χ^2 of 534.1 for 336 d.o.f. ($\Delta\chi^2$ of 59.9 for 4 d.o.f.). The energy centroids found for the lines are $E = 2.22^{+0.02}_{-0.02}$ keV and $E = 2.42^{-0.03}_{+0.03}$ keV. The model achieved until this point gives the following best-fit parameters: $\Gamma = 1.75^{+0.06}_{-0.05}$, $R = 0.41^{+0.17}_{-0.16}$, $N_{\rm H}$= $1.29^{+0.28}_{-0.31} \times 10^{23}$cm^{-2}. Since there are still some residuals in the soft X-ray band also a thermal component was added, through the MEKAL model (Mewe et al. 1986) in XSPEC.

As a second step a neutral reflection component PEXRAV was replaced with the PEXMON model (Nandra et al. 2007), which self-consistently includes the Fe Kα, Fe Kβ, Ni Kα and the Fe Kα Compton shoulder. The parameters characterizing PEXMON are: an inclination angle i fixed to 60°, a cut off energy of E =200 keV (Dadina 2008), a scaling reflection

[3]as discussed for NGC 454, we assume the inclination angle of a typical Seyfert 2, as confirmed by the work of Antón et al. (2002), requiring that the inclination angle is higher than 45°.

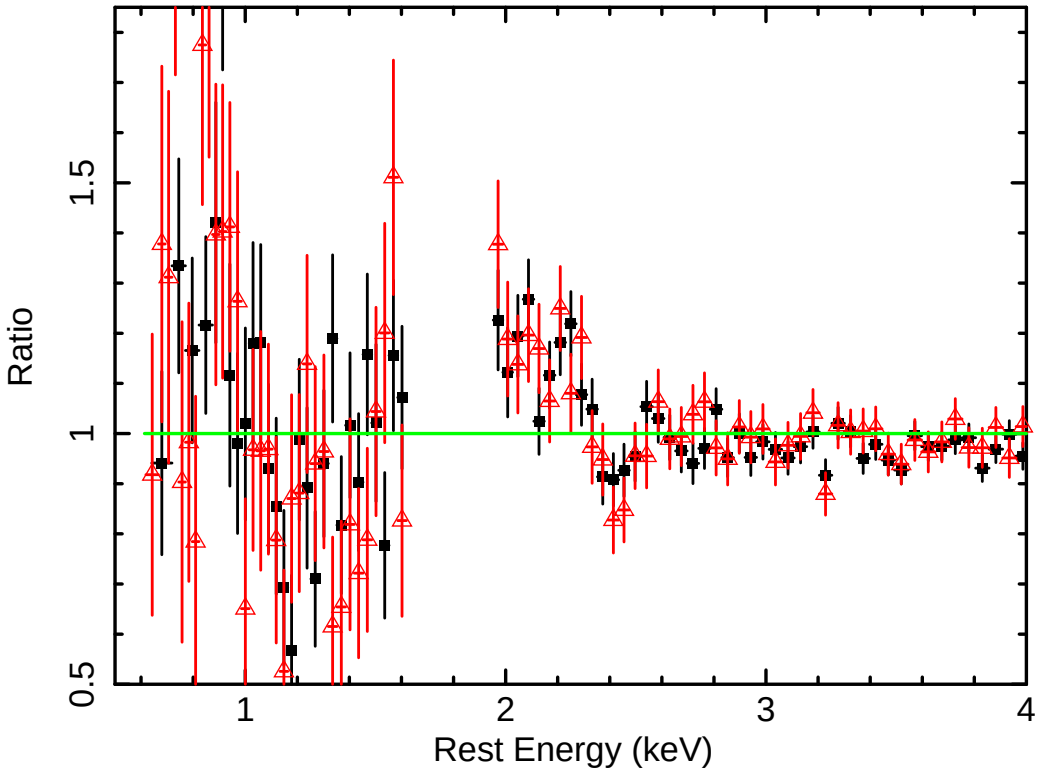

Figure 4.5: *Data/model ratio in the soft X-ray energy region to the* Suzaku *data (XIS-FI: black filled squares; XIS1: red open triangles) and the model including the reflection component (modelled with* PEXRAV*). The band 1.6–1.9 keV was ignored, due to the presence of instrumental calibration uncertainties. These residuals highlight the possible presence of an emission line at ~ 2.2 keV and of an absorption line at ~2.4 keV.*

factor R left free to vary, abundance $Z = Z_{\odot}$, and a reflection normalisation fixed to the normalisation of the absorbed power law. The fit including MEKAL and PEXMON gives a $\chi^2/d.o.f.$=514.3/337, and $R = 0.43^{+0.04}_{-0.04}$. The fit is still poor due to the presence of residuals in the energy range 5–8 keV (see Fig. 4.6). The model at this stage is :

$F(E)$ = wabs×[mekal+(zphabs×pow1)+pexmon+pow2+2.2keV emis.line+2.4keV abs.line)]. (4.1)

and a summary of the values of its main free parameters is reported in Table **??**.

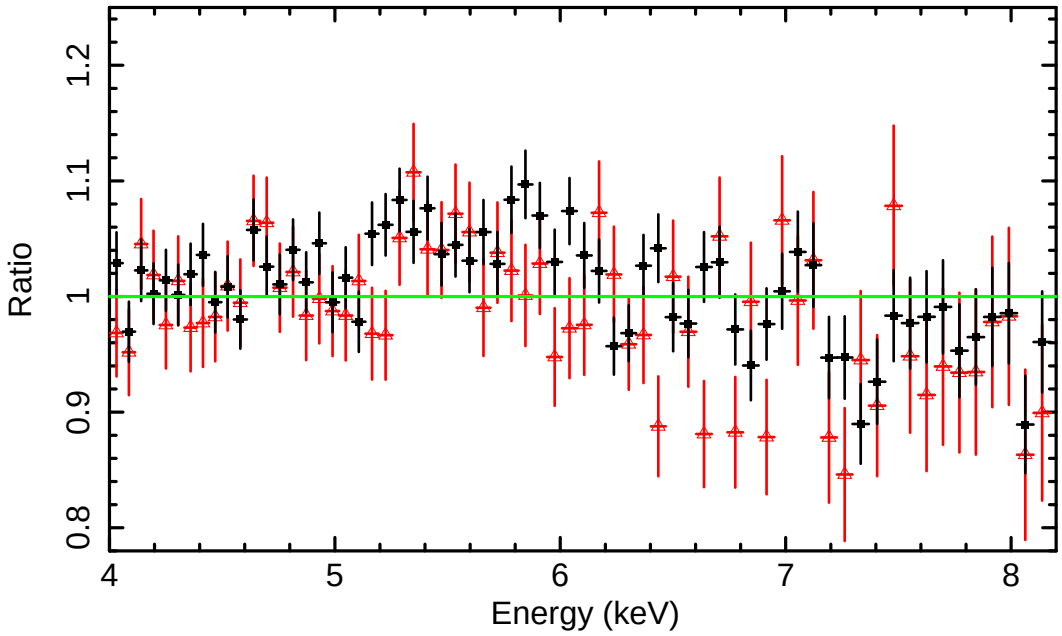

Figure 4.6: *Data/model ratio in the 4–8 keV energy region between the* Suzaku *data (XIS-FI: black filled squares; XIS1: red open triangles) and the model including the reflection component (modelled with* PEXMON*).*

4.2.1.1 Fe K complex

In this Section I discuss the possible presence of emission lines belonging to the Fe K complex and their properties. The search for signatures of ionised emission lines was performed by adding a Gaussian component centered at $E = 6.7$ keV (rest frame) and then at $E = 6.96$ keV (rest frame). The fit did not improve significantly and the upper limit on the equivalent width of each of these lines is less than 10 eV.
However, if we observe Figure 4.6, reporting the residuals of the last model, including the PEXMON component, the presence of a residual weak curvature between 5 and 6 keV and weak absorption lines near 7 keV is noticeable.
First a test was performed for detecting the presence of broadening of the Fe Kα emission

line , due to relativistic effects manifesting when the line is produced in the inner regions of the accretion disk.

Starting from the model including PEXMON, a Gaussian component initially centered at about $E = 6.4$ keV was added, allowing its centroid energy to vary without any constraint. The addition of this component could account for the curvature only through a very broad and implausible (from a physical point of view) emission line centered at $E \sim 5.6$ keV and with $\sigma \sim 1$ keV. Finally, in order to describe more precisely the line emission from a relativistic accretion disk a new component was added, the LAOR model in XSPEC (Laor 1991), representing the emission line profile from around a maximally rotating black hole. The outer radius R_{out} was fixed at 100 R_g, the inclination was constrained to be $> 45°$ (appropriate for a type 2 AGN) and we allowed as free parameters the emissivity index, the innermost radius R_{in} and the normalization. The fit still fails to reproduce the curvature, unless the inclination is allowed to vary, reaching a best-fit value of 25° ($\chi^2/d.o.f.$=398.7/333), but this model produces more than one inconsistency. In fact it represents a face-on orientation (which is in disagreement with the classification of this source as a Sy2 under classical Sy1/Sy2 unification schemes) and the Fe Kα line has an equivalent width of $EW \sim 168$ eV which, without considering the narrow Fe Kα emission line, would imply a reflection fraction of $R \sim 1$, in contrast with what we find ($R \sim 0.4$). Given that the observed curvature appears unlikely to originate from a disk line, in Section 4.2.1.2) I will discuss if it could be due to a more complex absorber.

4.2.1.2 Ionized absorber

Since, as discussed in section 4.2.1.1 and shown in Figure 4.6, the presence of a weak residual curvature and of weak absorption features is clear, I evaluated if a more complex absorber (i.e. partial covering or ionised) was required by the present data.
Firstly, a partial covering absorber was included in the model, in addition to the fully covering one, using the ZPCFABS model (see Appendix B). This results in a significant improvement of the fit, yielding $\Delta\chi^2 = 111.9$ for 2 d.o.f.. The column density of this absorber is $N_{\rm H}=1.20^{+5.11}_{-2.65} \times 10^{23}{\rm cm}^{-2}$and the covering fraction is $f_{cov} = 0.50^{+0.19}_{-0.14}$. Despite this being a better fit, the curvature in the 5–6 keV region is however still present. Then the best-fit values obtained by Singh et al. 2011 (who adopted the same model) were used, fixing the covering fraction to f_{cov}=0.84 and finding $N_{\rm H,part.cov.} = 9.16^{+0.61}_{-0.67} \times 10^{22}$ cm^{-2}and $N_{\rm H,ful.cov.} = 6.79^{+0.33}_{-0.28} \times 10^{22}$ cm^{-2}. However the fit get worse by $\Delta\chi^2 = -11.2$ for 1 d.o.f.

It is thus possible to consider if this feature of the spectrum can be better described using an ionised absorber. This was done through a multiplicative grid of absorption model generated with the XSTAR v 2.1 code (Kallman et al. 2004), as already done for NGC454. The turbulence velocity was assumed to be 5000 km s^{-1} and the outflow velocity was fixed to zero for simplicity.
A significant improvement was obtained, providing a $\chi^2/d.o.f. = 385.6/335$ ($\Delta\chi^2 = 128.7$ for 2 d.o.f with respect to the model described at the end of section 4.2.1); the parameters obtained with this fit are $N_{\rm H}$(neutral absorber) = $5.85^{+0.61}_{-0.66} \times 10^{22}$ cm^{-2},

$N_{\rm H}$(ionized absorber) = $1.49^{+0.10}_{-0.09} \times 10^{23}$cm^{-2} and a photoionization parameter of logξ = $1.83^{+0.15}_{-0.14}$erg cm s^{-1}. The addition of this mildly ionised absorber succeeds in reproducing the curvature in the 5–6 keV energy range (Fig. 4.7).

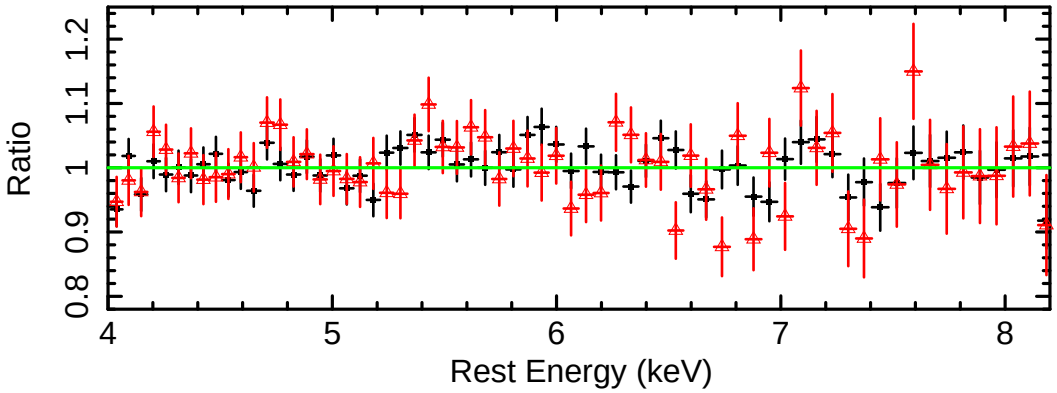

Figure 4.7: *Data/model ratio in the 4–8 keV energy region between the* Suzaku *data (XIS-FI: black filled squares; XIS1: red open triangles) and the model including an ionised absorber. In the range 5–6 keV it is noticeable an improvement with respect to the fit shown in Fig. 4.6, where the ionised absorber was not included, however there are still some residuals in the region 6–7.5 keV, in particular at E∼ 7.4 keV.*

Despite being a better description of the data, this model still leaves some residual features in the region 6–7.5 keV, in particular an absorption feature at ∼ 7.4 keV.
As a first step an absorption line was added, modelled by an inverted Gaussian, with its centroid and width left free to vary. This yielded $\Delta\chi^2$ = 7.8 for 3 *d.o.f.*, corresponding to a significance of 95.5%, with energy of the line E=$7.40^{+0.07}_{-0.06}$ keV and σ ∼ 0.046 keV, which implies a FWHM of ∼4400 km/s. The most likely candidate for this weak feature is blue-shifted (v ∼ 0.05c) absorption due to the 1s→2p transition of H-like Fe (E=6.97 keV), while if it is assumed a lower ionization state of Fe (i.e. Fe xxv) the corresponding blue-shift would be higher (v ∼ 0.1c).
The last consideration lead to investigate if the weak absorption feature could be well described by substituting the inverted Gaussian component with a second more ionized absorber, with turbulence velocity 5000 km/s. The assumption of this turbulence velocity, for the two ionised absorbers, is in agreement with the measured FWHM of the Fe xxv absorption line. At this step, for simplicity, the outflow velocity of the more ionised absorber was tied to the velocity of the mildly ionised one, leaving it free to vary. The resulting fit with this additional component provided $\chi^2/d.o.f.$ = 369.3/332 ($\Delta\chi^2$ = 16.4 for 3 d.o.f), and gives an acceptable model for the absorption feature at ∼ 7.4 keV. Then the outflow velocity of the highly ionised absorber was left free to vary, in order to test for an improvement of the fit, but it did not statistically improve ($\chi^2/d.o.f.$ = 364.6/331). The same is true when fixing the outflow velocity of the more ionised absorber to zero. Thus hereafter

I will make the simple assumption that the two absorbers have the same outflow velocity.

The final "best-fit model" is thus:

$$F(E) = \text{wabs} \times [\text{mekal} + (\text{zphabs} \times \text{ion abs1} \times \text{ion abs2} \times \text{pow1}) + \text{pexmon} + \text{pow2} + 2.2\text{keV emis.line} + 2.4\text{keV abs.line})].$$

This model describes a general scenario in which:

- a thermal emission component (modelled with MEKAL) is observable in the spectrum below 1 keV
- the primary radiation ("pow1") is absorbed by a neutral absorber (ZPHABS) and two ionised absorbers ("ion abs1" and "ion abs2")
- the same radiation is reflected along the line of sight by neutral cold matter (PEXMON)
- the primary radiation is scattered along line of sight from other directions ("pow2").

The main parameters of the best-fit model are: $N_{\rm Hion1} = 1.50^{+0.09}_{-0.09} \times 10^{23}{\rm cm}^{-2}$, $N_{\rm Hneutral} = 4.14^{+0.41}_{-0.40} \times 10^{22}$ cm $^{-2}$, $N_{\rm Hion2} = 1.41^{+0.80}_{-0.79} \times 10^{23}{\rm cm}^{-2}$, $\log\xi_1 = 1.63^{+0.08}_{-0.07}$erg cm s^{-1}, $\log\xi_2 = 3.88^{+0.09}_{-0.28}$erg cm s^{-1} and $v_{\rm ion1,2} = 0.057^{+0.006}_{-0.005}c$. I remark that, being the $N_{\rm H}$ of the two ionised absorbers very similar, it could be due to a stratification of the same absorber with different ionisation states. This model gives a flux in the 2–10 keV energy range of $F_{2-10{\rm keV}} \sim 3.60 \times 10^{-11}$erg cm^{-2} s^{-1} and an intrinsic luminosity of $L_{2-10{\rm keV}} \sim 3.26 \times 10^{43}$erg s^{-1}.
The value of measured outflow velocity ($0.057c$) is in agreement with assuming an absorption feature due to blueshifted Fe XXVI absorption line.

Physically this model describes radiation that intercepts a neutral absorber and two photoionised absorbers that have an outflow velocity of $\sim$ 0.06c, attenuating the primary AGN emission and producing blueshifted absorption lines (Fig. 4.8).

Table 4.1: Summary of the X-ray emission lines detected in the 2–8 keV spectrum of *Suzaku*. The energies of the lines are quoted in the rest frame. Fluxes and identifications are reported in column 2 and 3. The *EW* are reported in column 4 and they are calculated against the total observed continuum at their respective energies. In column 5 the improvement of fit is shown with respect to the continuum model, the value for the model with no lines is χ^2/d.o.f. =950.0/344.

Energy (keV) (1)	Flux (10^{-6}ph cm^{-2} s^{-1}) (2)	ID (3)	*EW* (eV) (4)	$\Delta\chi^2$ (5)
$2.22^{+0.02}_{-0.02}$	$8.2^{+1.9}_{-1.9}$	SKα	$30^{+8.2}_{-8.2}$	54
$2.42^{+0.03}_{-0.03}$	$-4.6^{+2.4}_{-2.5}$	Sxv	$13.6^{+6.6}_{-6.8}$	22
$6.39^{+0.01}_{-0.01}$	$44.8^{+5.0}_{-4.9}$	Fe Kα	$81.5^{+9.0}_{-8.8}$	335
7.06	13.5% Fe Kα	Fe Kβ	10 eV[a]	5
6.7	<4.8	Fe xxv	<12	0
6.97	<5.8	Fe xxvi	<10	0

[a] the normalisation is fixed to 13.5% of the Fe Kα (Palmeri et al. 2003).

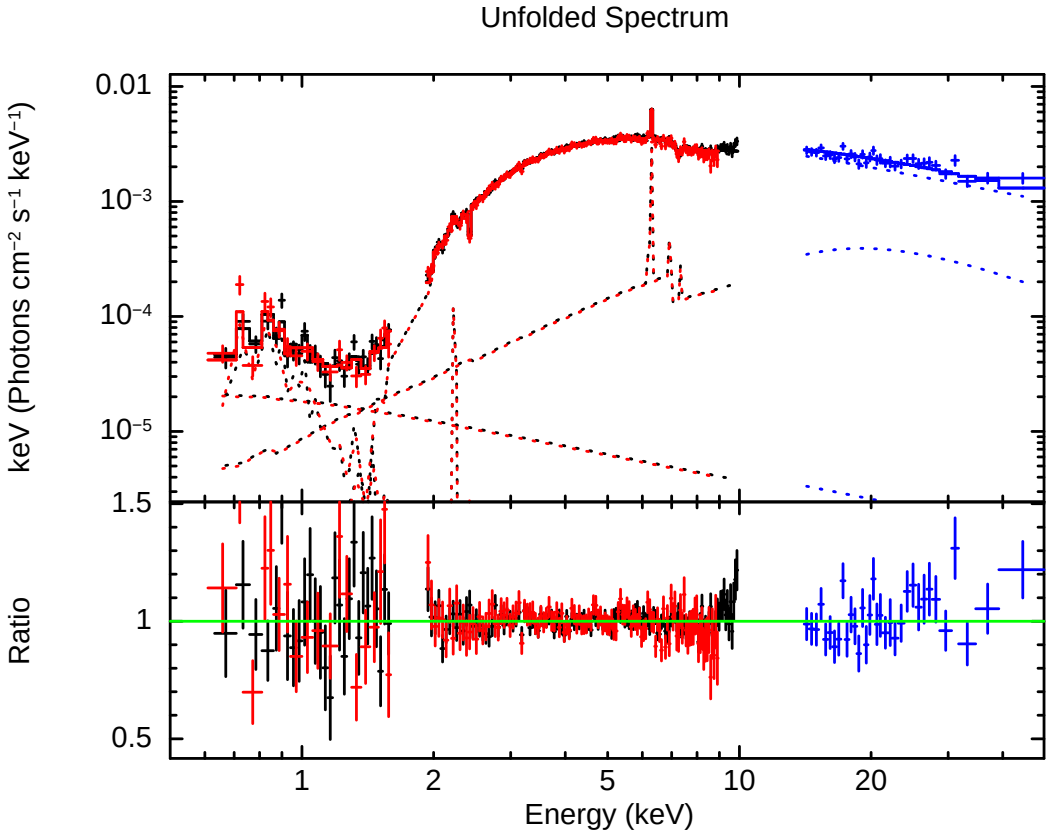

Figure 4.8: Suzaku *0.5–70 keV data and best-fit model (XIS-FI black; XIS1 red; HXD blue) of Mrk 348; data have been rebinned for plotting purposes. The upper panel shows the data and best-fit model described at the end of section 4.2.1.2 (see table 4.3 for the best-fit parameters). The lower panel shows the data/model ratio to this model.*

4.3 XMM-*Newton* data analysis

According to the works by Akylas et al. (2002); Smith et al. (2001); Singh et al. (2011) Mrk 348 is candidate for a variable absorber. The $N_{\rm H}$ measured with *Suzaku* is a factor of 1.8 lower than the $N_{\rm H}$ reported by Singh et al. (2011) from XMM-*Newton*, in agreement with the presence of a variable absorber. Thus I re-analysed the XMM-*Newton* spectra with some of the models used to describe the *Suzaku* spectrum.

At first the simplest model was considered, where the reflection component is represented by PEXRAV plus a Gaussian component for the Fe Kα emission line. When fitting simultaneously the *Suzaku* and XMM-*Newton* data the energy centroid of the Fe Kα was found to be consistent between the two observations, while its normalization changed (from $I^{Suzaku}_{\rm Fe\ K\alpha} = 4.47^{+0.66}_{-0.65} \times 10^{-5}$photons cm^{-2}s^{-1} and $EW^{Suzaku}_{\rm Fe\ K\alpha} = 82^{+10}_{-10}$ eV to $I^{XMM}_{\rm Fe\ K\alpha} = 2.37^{+0.63}_{-0.61} \times 10^{-5}$photons cm^{-2}s^{-1} and $EW^{XMM}_{\rm Fe\ K\alpha} = 47^{+13}_{-12}$ eV).

In Figure 4.9 I plot the *Suzaku* XIS (black, upper spectrum), HXD (blue) and XMM-*Newton* pn (red, lower spectrum) data (using the best-fit model, see below), confirming a change in the spectral curvature between 1 and 6 keV. What are the spectral components that could be responsible for this variation? First of all the model including the partial covering absorber was tested. Fixing the covering fraction of both *Suzaku* and XMM-*Newton* to $f_{cov} = 0.84$ the $N_{\rm H}$ changes from $N_{\rm H}{}^{XMM}_{part.cov.} = 1.55^{+0.12}_{-0.13} \times 10^{23}$cm^{-2} to $N_{\rm H}{}^{Suzaku}_{part.cov.} = 8.72^{+0.69}_{-0.75} \times 10^{22}$cm^{-2} for the partial covering absorber, and from $N_{\rm H}{}^{XMM}_{ful.cov.} = 1.16^{+0.05}_{-0.05} \times 10^{23}$cm^{-2} to $N_{\rm H}{}^{Suzaku}_{ful.cov.} = 6.93^{+0.36}_{-0.31} \times 10^{22}$cm^{-2} for the full covered component.

Then the *Suzaku* best-fit model was adopted, where the presence of a reflector plus a Fe Kα and Fe Kβ emission lines was consistently modelled by the PEXMON component. Given the observed variation of the Fe Kα emission line intensity it is expected that, when applying the best-fit model simultaneously to *Suzaku* and XMM-*Newton* data, different reflection scaling factors of PEXMON are needed.

Now I will consider as starting point the best-fit model found for *Suzaku* (thus the model including the ionised absorbers). The analysis was done in the following steps:

1. If I allow as free parameters between the two observations only the $N_{\rm H}$ of the neutral absorber together with the reflection R factor of PEXMON as well as the soft emission and absorption lines the result is $\chi^2/d.o.f. = 589.8/409$. The neutral absorber column density varies from $N_{\rm H}{}^{Suzaku}_{\rm neutral} = 4.27^{+0.50}_{-0.47} \times 10^{22}$cm^{-2} to $N_{\rm H}{}^{XMM}_{\rm neutral} = 1.23^{+0.06}_{-0.06} \times 10^{23}$cm^{-2}.

2. Since there are some residuals in the 6–8 keV region, also the column densities of the ionized absorbers were allowed to vary as free parameters. This yields $\chi^2/d.o.f. = 568.7/407$ ($\Delta\chi^2$=21.1 for 2 d.o.f.); the parameters changing more significantly are the $N_{\rm H}$ of the neutral absorber and the $N_{\rm H}$ of the mildly ionised absorber, implying that the source, when observed with XMM-*Newton*, is generally more absorbed than when observed with *Suzaku*.

3. Finally also the ionization parameters were allowed to vary between *Suzaku* and

XMM-*Newton*, obtaining $\chi^2/d.o.f. = 551.6/407$. The ionisation parameter of the mildly ionised absorber change from $\log\xi_1^{Suzaku} = 1.67^{+0.11}_{-0.10}$erg cm s^{-1} to $\log\xi_1^{XMM} = 2.04^{+0.19}_{-0.18}$erg cm s^{-1}. This will be considered as the best–fit model and all the relative best-fit parameters are listed in table 4.3.

I note that if the outflow velocity of XMM-*Newton* ionised absorbers is untied with respect to *Suzaku* then $\Delta\chi^2 = 17$ with respect to the best fit model; the outflow velocity of the first ionised absorber is statistically unchanged, while for the second ionised absorber it is slightly lower ($z = -0.020^{+0.006}_{-0.006}$, corresponding to a velocity of $0.034c$).
When attempting to fix the $N_{\rm Hneutral}$ of XMM-*Newton* to the *Suzaku* best fit value, the fit gets worse by a factor $\Delta\chi^2$=20.
I conclude that the difference in the observed X-ray spectra between *Suzaku* and XMM-*Newton* can be accounted for through a variation in absorbing column density of both the neutral absorber and one of the ionised absorbers, together with a change in the ionisation parameter of the same ionised absorber.

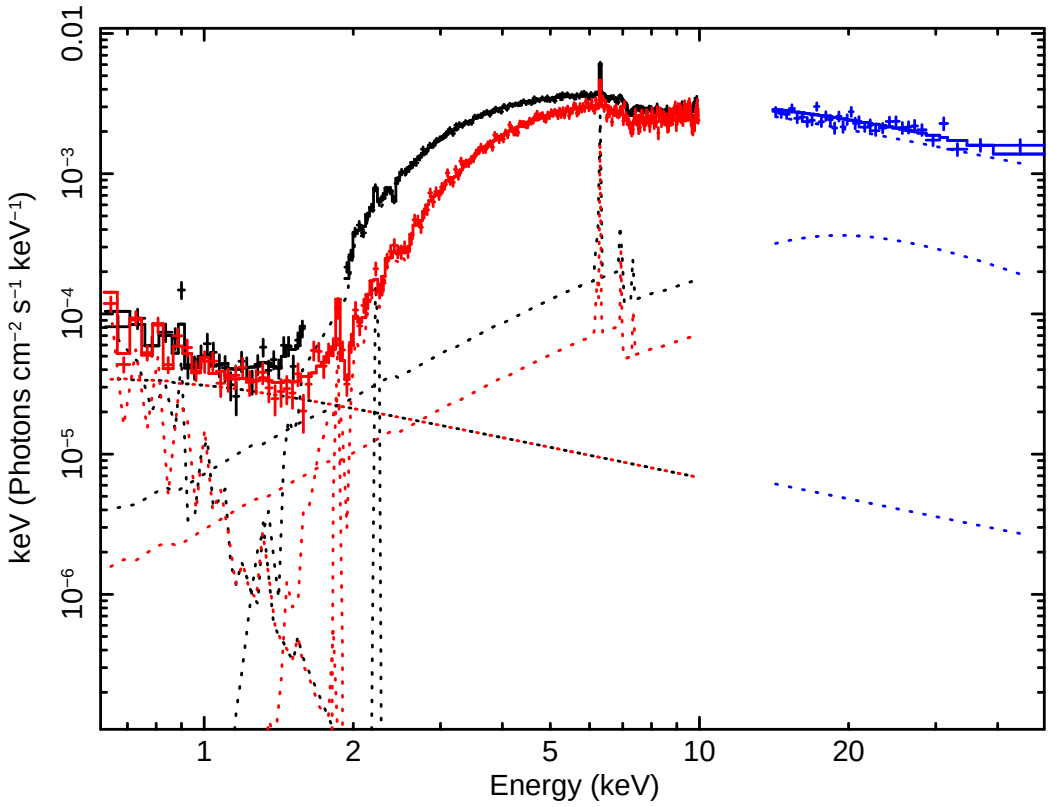

Figure 4.9: *Comparison between the X-ray emission measured with* Suzaku *in 2008 (black data points) and XMM-*Newton *(red data points) in 2002. The continuum model is the best fit model composed of a primary power-law component transmitted trough a neutral absorber, a scattered power-law component, a Compton reflected component (modelled with* PEXMON*), and two ionized absorbers.*

4.3.1 Reflection scenarios

As discussed in Section 4.3, when fitting *Suzaku* and XMM-*Newton* data I assumed that different reflection scaling factors of PEXMON are needed, due to the observed variation in the Fe Kα emission line intensity. The validity of this hypothesis can be tested by comparing the two following scenarios (summarised in Table 4.2):

1. a variable continuum and a constant reflection component, i.e. a scenario in which the reflecting matter is quite far and does not respond immediately to the continuum variability. In terms of fitting parameters this is represented by

   - a free normalization of the primary power law between XMM-*Newton* and *Suzaku*;
   - the reflection parameters of XMM-*Newton* (reflection fraction R and normalization) tied to those of *Suzaku*.

   The resulting fit yielded $\chi^2 = 567.7$ for 407 d.o.f., and the assumption of constant reflection leaves residuals in the Fe Kα region.

2. a scenario where both the primary continuum and the reflection component were allowed to vary between *Suzaku* and XMM-*Newton* observations, i.e. a situation where, by the time the second observation is performed, a variability in the continuum reverberates in the reflecting material, meaning that the reflector would be located closer in. Thus the fit was characterised by

   - a free normalization of the primary power law between XMM-*Newton* and *Suzaku*;
   - a free reflection fraction R_{XMM} with respect to R_{Suzaku};
   - The normalization of PEXMON tied to the normalization of the primary power law, for XMM-*Newton* and *Suzaku* independently.

   This representation lead to a better fit ($\chi^2 = 551.1$ for 406 d.o.f.), where the continuum is unchanged (variations within the errors) while the reflection fraction does change, as expected.

Thus, it is possible to conclude that *Suzaku* and XMM-*Newton* observations do not show continuum variability, but the Fe Kα emission line does show signs of variation between the two spectra. For this reason I can consider that a good description of the *Suzaku* and XMM-*Newton* data is obtained by fixing the continuum and the PEXMON normalizations, while allowing the reflection fraction R free to vary between the two observations. This confirms the validity of the assumption made in the best-fit obtained at the end of Section 4.3.

Table 4.2: Model parameters of the two possible scenarios (described in Sec. 4.3 to explain the variation of the Fe Kα emission line intensity between *Suzaku* and XMM-*Newton* observations.

Scenario	Model Component	Parameter	*Suzaku*	XMM-*Newton*
Constant Reflection	Power Law	Normalisation[a]	$1.61^{-0.08}_{+0.08} \times 10^{-2}$	$1.70^{-0.08}_{+0.08} \times 10^{-2}$
	Reflection	Normalisation[a]	$1.61^{fixed} \times 10^{-2}$	$1.61^{fixed} \times 10^{-2}$
		R	$0.22^{-0.03}_{-0.03}$	0.22^{fixed}
				χ^2/d.o.f=567.7/407
Variable Reflection	Power Law	Normalisation[a]	$1.60^{-0.08}_{+0.08} \times 10^{-2}$	$1.66^{-0.19}_{+0.31} \times 10^{-2}$
	Reflection	Normalisation[a]	$1.60^{fixed} \times 10^{-2}$	$1.66^{fixed} \times 10^{-2}$
		R	$0.28^{-0.05}_{-0.04}$	$0.12^{+0.05}_{-0.05}$
				χ^2/d.o.f=551.1/406

[a] units of photons keV^{-1} cm^{-2} s^{-1}.

4.3.2 $N_{\rm H}$ past observations

The measured values of $N_{\rm H}$ found here are within the range of the column densities measured in past observations (*Ginga*, *Asca* and *RXTE*), as shown and summarised in Fig. 4.10, where I reported the measured values of $N_{\rm H}$ of previous observations together with XMM-*Newton* and *Suzaku* observations. In particular the results of the previous observations are:

- *Ginga* (1987): the measured column density was $N_{\rm H} \sim 10^{23}$ cm^{-2}.
- *ASCA* (August 1996): as published by Awaki et al. (2000) the column density was $N_{\rm H} \sim 1.6 \times 10^{23}$ cm^{-2}. I remark that during this observation the observed 2–10 keV flux was $\sim 5 \times 10^{-12}$erg cm^{-2} s^{-1}, that is respectively a factor 5 and a factor 7 lower than what we observed with XMM-*Newton* and *Suzaku*. If I hypothesize a scenario where there is a delay in Fe Kα response with respect to continum variations, this intrinsic variability in the continuum could be responsible for the different Fe Kα intensities discussed at the beginning of Section 4.3. In fact, the lower intensity Fe Kα line observed with XMM-*Newton* could be responding with a time delay to a different past continum (in this case a weaker continum) in a scenario where the reflector producing this emission line is far from the central variable X-ray source.
- *RXTE* (from mid 1996 to mid 1997, and in 2011): $N_{\rm H}$ took values in the range 0.9 – 3.2×10^{23}cm^{-2}during 14 months between mid 1996 and mid 1997 (Akylas et al.

2002; Smith et al. 2001) and in the range $14 - 17 \times 10^{22}$ cm^{-2}during the observation in 2011 (Markowitz, Krumpe, & Nikutta 2013).

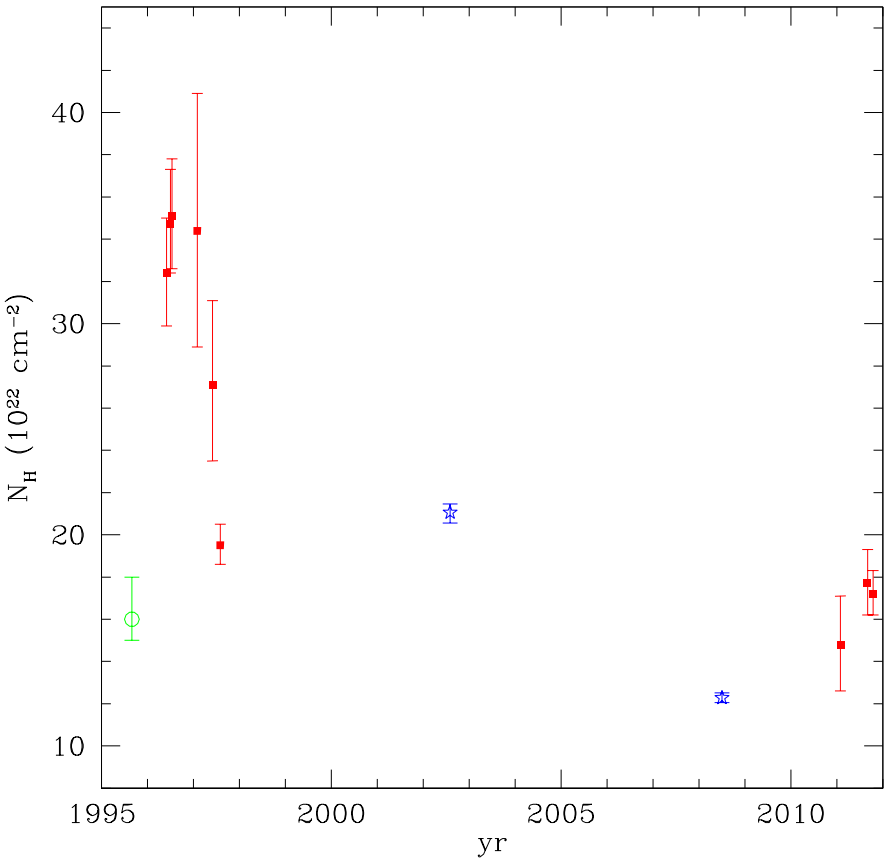

Figure 4.10: *Comparison of the measured values of* N_H *in* ASCA *observation (Awaki et al. 2000, green empty circles), in* RXTE *observation (red squares) during the time lag from 1997 to 2011 (Akylas et al. 2002 and A. Markowitz in prep. for the 2011 data) and the* N_H *measured from* Suzaku *and XMM-*Newton *observations (blue stars, this work). The* N_H*values of this work and of* RXTE *observations are based on the abundances relative to Solar reported in Wilms et al. (2000).*

Table 4.3: Summary of the *Suzaku* and XMM-*Newton* parameters for the best-fit models described in section 4.2.1.2, and 4.3.

Model Component	Parameter	*Suzaku* 2008-June	XMM-*Newton* 2002-July
Power law	Γ	$1.72^{+0.02}_{-0.02}$	fixed to Γ_{Suzaku}
	Normalisation[a]	$1.60^{-0.08}_{+0.08} \times 10^{-2}$	fixed to $norm_{Suzaku}$
Scattered Component	Normalisation[a]	$3.66^{+0.41}_{-0.42} \times 10^{-5}$	fixed to $norm_{Suzaku}$
MEKAL	Normalisation[a]	$4.34^{+0.71}_{-0.70} \times 10^{-5}$	fixed to $norm_{Suzaku}$
	k_BT	$0.24^{+0.02}_{-0.02}$ keV	fixed to kT_{Suzaku}
Neutral Absorber	N_H	$4.50^{+0.56}_{-0.51} \times 10^{22}$ cm^{-2}	$9.99^{-1.39}_{+1.32} \times 10^{22}$ cm^{-2}
Reflection	R	$0.29^{+0.04}_{-0.04}$	$0.12^{+0.05}_{-0.05}$
Ionised Absorber 1	N_H	$1.44^{+0.10}_{-0.10} \times 10^{23}$cm^{-2}	$2.11^{+0.19}_{-0.18} \times 10^{23}$cm^{-2}
	logξ	$1.67^{+0.11}_{-0.10}$erg cm s^{-1}	$2.04^{+0.03}_{-0.01}$erg cm s^{-1}
	z	fixed to z of Ionised Absorber 2	fixed to z of Ionised Absorber 2
	v_{turb}	5000 km s^{-1}	5000 km s^{-1}
Ionised Absorber 2	N_H	$1.31^{+1.22}_{-0.88} \times 10^{23}$cm^{-2}	$9.94^{+29.6}_{-0.57} \times 10^{22}$cm^{-2}
	logξ	$3.87^{+0.11}_{-0.39}$erg cm s^{-1}	$3.73^{+0.52}_{-0.27}$erg cm s^{-1}
	z	$-0.044^{+0.007}_{-0.006}$	fixed to z_{Suzaku}
	v_{turb}	5000 km s^{-1}	5000 km s^{-1}
	F $_{(0.5-2)keV}$	$\sim 3.3 \times 10^{-13}$erg cm^{-2} s^{-1}	$\sim 3.4 \times 10^{-13}$erg cm^{-2} s^{-1}
	F $_{(0.5-2)^{mekal}keV}$	$\sim 3.4 \times 10^{-14}$erg cm^{-2} s^{-1}	$\sim 4.04 \times 10^{-14}$erg cm^{-2} s^{-1}
	F$_{(2-10)keV}$	$\sim 3.6 \times 10^{-11}$erg cm^{-2} s^{-1}	$\sim 4.2 \times 10^{-11}$erg cm^{-2} s^{-1}
	F $_{(14-150)keV}$	$\sim 7.6 \times 10^{-12}$erg cm^{-2} s^{-1}	$\sim 7.04 \times 10^{-12}$erg cm^{-2} s^{-1}
	L $_{(0.5-2)keV}$	$\sim 1.72 \times 10^{43}$erg s^{-1}	$\sim 1.73 \times 10^{43}$erg s^{-1}
	L $_{(0.5-2)^{mekal}keV}$	$\sim 2.15 \times 10^{40}$erg s^{-1}	$\sim 2.11 \times 10^{40}$erg s^{-1}
	L$_{(2-10)keV}$	$\sim 3.26 \times 10^{43}$erg s^{-1}	$\sim 3.17 \times 10^{43}$erg s^{-1}
	L$_{(14-150)keV}$	$\sim 4.51 \times 10^{42}$erg s^{-1}	$\sim 4.20 \times 10^{42}$erg s^{-1}

[a] units of photons keV^{-1} cm^{-2} s^{-1}.

4.4 Discussion

As already done for NGC454 it is now interesting to make a first order estimate of the maximum distance of this ionised absorber from the central black hole by means of the equation

$$R_{ion} = \frac{L_{\rm ion}\Delta R}{N_{\rm H}\xi R} \tag{4.2}$$

relating the ionisation parameter, the density of the absorber and the continuum luminosity $L_{\rm ion}$. In this case the estimate of $L_{\rm ion}$ (in the energy range between 13.6 eV and 13.6 keV) from the best fit model is of the order of $L_{\rm ion} \sim 7{\times}10^{43}$ erg s^{-1}. Assuming that the thickness of the absorber, $\Delta R{=}N_{\rm H}/n$, is smaller than the distance R_{ion} ($\Delta R/R_{ion} < 1$), we can set an upper limit to the distances of each ionised absorber, using *Suzaku* observations:

$$R_{ion} < \frac{L_{\rm ion}}{N_{\rm H}\xi} \tag{4.3}$$

These upper limits are 0.026 pc and 2.72 pc for the highly and the mildly ionised absorber respectively. Despite being upper limits, they suggest that the likely location of these absorbers does not corresponds to the same radius with respect to the central source. The distance of the first ionised absorber is consistent in being a wind launched from a region located within the Broad Line Region.

The higher distance inferred for the mildly ionised absorber is due to the lower ionisation parameter, with respect to the highly ionised absorber. Its location could correspond to the region of the molecular torus, at a parsec-scale distance from the central source. However as this is an upper limit, we should not exclude the possibility that we are observing across this wind, thus we are not viewing directly the inner radius, which could be located at sub-parsec scales.

Another method to put a constraint on the possible location of these absorbers is to estimate a lower limit on the radial distance by determining the escape radius at which the material will be able to leave the system. This can be determined once we have an estimate of the outflow velocity. Assuming spherical geometry, this radius is:

$$R_{esc} \geq \frac{2GM}{v_{out}^2} \simeq \frac{2c^2 R_g}{v_{out}^2} \tag{4.4}$$

where R_g is the gravitational radius (R_g=GM/c^2). Since the measured outflow velocity is ∼0.055 c, I obtain that $R_{esc} \geq 660R_g$. From the literature we have estimates of the mass of the central black hole, ranging from $M_{BH} \sim 1.6 \times 10^7 M_{\odot}$ (Woo & Urry 2002) to $M_{BH} \sim 7.5 \times 10^7 M_{\odot}$ (Nikolajuk, Papadakis, & Czerny 2004), so I can infer that $R_g \sim 2.5 - 11.1 \times 10^{12}$cm, thus $R_{esc} \geq 1.6 - 7.3 \times 10^{15}$cm $\sim 0.0005 - 0.002$ pc. This means that the wind may have been launched at least from a distance of the order of $10^{-4} - 10^{-3}$pc from the central black hole in order for it to escape, so an origin in the accretion disk or the Broad Line Region is plausible. In particular, this estimate suggests that the range of location of the first highly ionised absorber is between 5×10^{-4} pc and 0.026 pc (*Suzaku* observation). However, it is worth noting that another possibility could be that the wind is part of some aborted outflow, i.e. a wind with outflow velocity lower

than the escape velocity and thus unable to leave the system; in that case we would only have an estimate of the maximum distance of the ionised absorber but not the minimum distance from which it was launched.

This analysis highlights the complexity and possible stratifications of the absorbers intercepting our line of sight. Indeed the observed spectrum could be explained with physically different scenarios: a unique and multi-phase absorber, where higher density (and lower ionisation) clouds are confined by lower density (higher ionisation) clouds, implying that the location of the two absorbers are actually the same; or a configuration where there are effectively two winds at different physical states and distances, intercepting the line of sight. Neither of these two explanations can be ruled out at the moment, since higher spectral resolution observations are needed.

I conclude that the comparison between *Suzaku* and XMM-*Newton* observations of Mrk 348 does not show extreme variability, such as the transition from a Compton-thick to a Compton-thin state characterizing "changing look" AGN. However I cannot exclude that, given the long time elapsed between observations, I was not able to observe the source during an obscured Compton-thick phase. In this work I do not observe a variation of the primary continuum, despite past RXTE observations which showed brightness variations on time scales down to 1 day (Smith et al. 2001). The satellite ASCA also observed the source (13 years earlier) in a state with flux 7 times lower than the flux observed with *Suzaku*.
Mrk 348 can be placed among the large number of AGN where a non uniform distribution of the circumnuclear absorbing matter determines $N_{\rm H}$variations in different epochs. This is consistent with recent theoretical models (Nenkova et al. 2008a,b) and works (Elitzur 2008, 2012) supported by mid-IR observations, that indicate the possible clumpy nature of the torus, suggesting that the unified model of AGN is a too simplified scheme. The unified scheme is based on the assumption of a uniform torus, with the same opening angle for all AGN, implying that the viewing angle is the unique factor determining the classification into Type 1 and Type 2 AGN. This is clearly in conflict with both the $N_{\rm H}$ variability and infrared observations (Lutz et al. 2004; Horst et al. 2006) showing that there is no significant difference in the mid-IR emission, normalized to the X-ray flux, of Type 1 and Type 2 AGN, contrary to the expectation of strong anisotropy of the unified model. The results presented here for Mrk 348 agree with the model a "soft-edged" clumpy torus (Elitzur 2012)

4.5 Conclusions

I presented the analysis of the X-ray spectrum of Mrk 348 obtained by *Suzaku* and compared it to the spectrum observed by XMM-*Newton*.
The main results can be summarised in this way:

- The best-fit model representing the observed X-ray emission is composed of a primary continuum intercepting three absorbers with different densities and ionisations

(including one neutral absorber). I suggest that the location of the neutral absorber and of the mildly ionised absorber are at a parsec scale distance, thus consistent with the location of the putative torus. Instead, the highly ionised absorber appears to be located within ∼ 0.03 pc from the central source, likely in the Broad Line Region.

- The comparison with the XMM-*Newton* observation leads to the conclusions that: 1) the normalization and photon index of the primary and scattered power law do not vary between the two observations, despite such variations were observed in past observations (Smith et al. 2001, Awaki et al. 2000); 2) the observed spectral variation requires a change in $N_{\rm H}$ of the neutral ($\Delta {\rm N_H} \sim 5.5 \times 10^{22} {\rm cm}^{-2}$) and one of the ionised absorbers ($\Delta {\rm N_H} \sim 6.7 \times 10^{22} {\rm cm}^{-2}$).

- I find the presence of the Fe Kα emission line, with equivalent width EW ∼81 eV during the *Suzaku* observation, in agreement with a fairly weak reflection contribution. During the XMM-*Newton* observation the equivalent width is lower ($EW \sim 47$ eV), and it could be responding to a past weaker continuum, as was observed during earlier *ASCA* observations (Awaki et al. 2000). I do not observe any broadening of the Fe Kα line as expected for lines produced in the inner regions of the accretion disk, in agreement with the results of Smith et al. (2001) and Netzer, Turner, & George (1998).

- I detect a weak absorption line with an energy centroid at E ∼7.4 keV, consistent with a possible blueshifted 1s→2p transition of Fexxvı (at 6.95 keV). I infer that the ionised absorber responsible for this feature has an observed outflow velocity of v_{out} ∼0.05 c. Higher resolution observations are needed in order to improve the significance of this detection.

- The long time elapsed between the two observations does not allow us to infer the time scale of the variability, so I can only determine upper limits on the distances of the ionised absorbers. However, as the mass of the central black hole is known from previous works, it is possible to estimate the minimum escape radius of the outflowing material. The ionisation parameters inferred for the two ionised absorbers suggest that one of them must be located at sub-parsec scales, and thus in the region ranging from the accretion disk to the BLR, while the second absorber is likely located at a parsec-scale distance.

CHAPTER 5

Conclusions and Future prospects

In this PhD thesis I studied two sources belonging to the Swift BAT-70 months catalogue, displaying promising features for the understanding of the structure and condition of the matter in the inner regions of AGNs, in the context of the validity of the Unified Model. The sources considered for this study are

- NGC 454E, a Seyfert galaxy belonging to the interacting system NGC454, at redshift z=0.0122. The high variability in column density of the neutral absorber allowed me to include it in the class of "changing look" AGN, where still only few sources have been found up to now.
- Mrk 348 (NGC 262), a bright Compton-thin Seyfert 2 galaxy at z=0.015, with a complex X-spectrum, showing the presence of multiple absorbers, some of which featuring variability.

In this conclusive chapter I will go through the common characteristics found for the two sources, together with the differences.

Variability of absorption column density of the neutral absorber For both sources I found a variation in the absorbing column density, leading to a different spectral shape of the observed X-ray spectra relative to different epochs. For NGC 454E the $N_{\rm H}$ of the neutral absorber undergoes an extreme variation, from $\sim 1 \times 10^{24}$cm^{-2}(*Suzaku*) to $\sim 1 \times 10^{23}$cm^{-2}(XMM-*Newton*) in 6 months, which is rarely observed. Mrk 348 has a more moderate variation of the $N_{\rm H}$ of the neutral absorber (ΔN$_{\rm H} \sim 5.5 \times 10^{22}$cm^{-2}). However, even if Mrk 348 does not show a variability as extreme as the one characterizing NGC 454E, it is not possible to exclude that this source went through an unobserved obscured Compton-thick phase, given the long time elapsed between observations.

Variability of the ionised absorbers In both sources the X-ray spectrum reveals that the primary emitted radiation intercepts ionised absorbing media, besides the neutral one. In the case of NGC 454E, during XMM-*Newton* observation I found a ionised absorber with ionisation parameter logξ = 3.55 erg cm s^{-1} and column density $N_{\rm H} = 5.31 \times 10^{23}$ cm^{-2}. This absorber was not observed during *Suzaku* observation, despite its detectability, indicating that it may have varied or moved away from the line of sight in the 6 months between the two observations.
For Mrk 348 I found features revealing the presence of two ionised absorbers, one highly ionised ($log\xi \sim 3.8$ erg cm s^{-1}) and one mildly ionised ($log\xi \sim 2$ erg cm s^{-1}), both having

an outflow velocity of ~ 0.03c. When comparing *Suzaku* and XMM-*Newton* spectra I found that the mildly ionised absorber changes both in column density ($\Delta N_H \sim 6.7 \times 10^{22} cm^{-2}$) and ionization state (from $\log\xi = 1.67^{+0.11}_{-0.10}$erg cm s^{-1} to $\log\xi = 2.04^{+0.03}_{-0.01}$erg cm s^{-1}).

Variability of the reflected emission While in the observations of NGC 454E I did not detect a change of the reflected emission between *Suzaku* and XMM-*Newton* spectra, for Mrk 348 such variability is present. In fact the EW of the FeKα emission line changes from 82^{+9}_{-8} eV during *Suzaku* observation to 47^{+13}_{-12} eV during XMM-*Newton* observations. This suggests that the reflected emission observed by *Suzaku* was responding to a past weaker emission (as confirmed by a previous *ASCA* observations, Awaki et al. 2000).

Distances of the ionised absorbers Unfortunately, none of these sources was observed in monitoring campaigns, thus the comparison between different observations, typically performed at intervals of months to years (as those discussed here), provides only upper limits to the intrinsic time scales of N_H variations and thus on the possible location of the thicker obscuring material (obscuring “torus" vs. Broad Line Region clouds).
Concerning the ionised absorbers, I derived a first order estimate of their distance from the central BH for the two sources. The ionised absorber found in NGC 454 is estimated to have a location within 10^{-3} pc, consistent with being inside the BLR. For Mrk 348, besides estimating an upper limit to the distance of the ionised absorbers (0.026 pc and 2.72 pc for the highly and the mildly ionised absorber respectively), I could also infer a lower limit, thanks to the outflow velocity derived in the X-ray spectral analysis and being the mass of the SMBH known from previous studies. Thus I concluded that range of location of the highly ionised absorber is between 5×10^{-4} pc and 0.026 pc (*Suzaku* observation), consistently with an origin of the wind either in the accretion disk or the BLR. The moderately ionised absorber is instead likely located at a parsec-scale distance, consistent with a location on a scale typical of the putative obscuring torus.
In Fig. 5.1 and 5.2 I report in graphical schemes the scenarios described for NGC454 and Mrk348 respectively, with the indication of the main components causing the X-ray spectral variability.

As highlighted by the studies performed in the last years, and confirmed in this thesis, X-ray spectra of AGN show higher complexity than what foreseen by the standard unified model. Among the factors influencing the shape of the spectrum, there is the presence of clumpy neutral or ionized absorbers and multiphase outflows, located at different distances and having different physical states. The clumpiness of the absorbing media is a scenario shared by most of the recent alternative models (as discussed in Section 1.5), suggesting that the clouds responsible for the variable absorption on short time scales may be located closer-in than the putative torus and, in some cases, are consistent in being the same clouds that produce the broad emission lines in the BLR, as I showed for NGC 454.
The observed spectrum of Mrk 348 can be explained by different scenarios, all contradicting the uniformity of the molecular torus depicted in the “basic” Unified Model. Indeed a possible configuration is an absorbing medium composed by unique and multi-phase absorber, where higher density (and lower ionisation) clouds are confined by lower

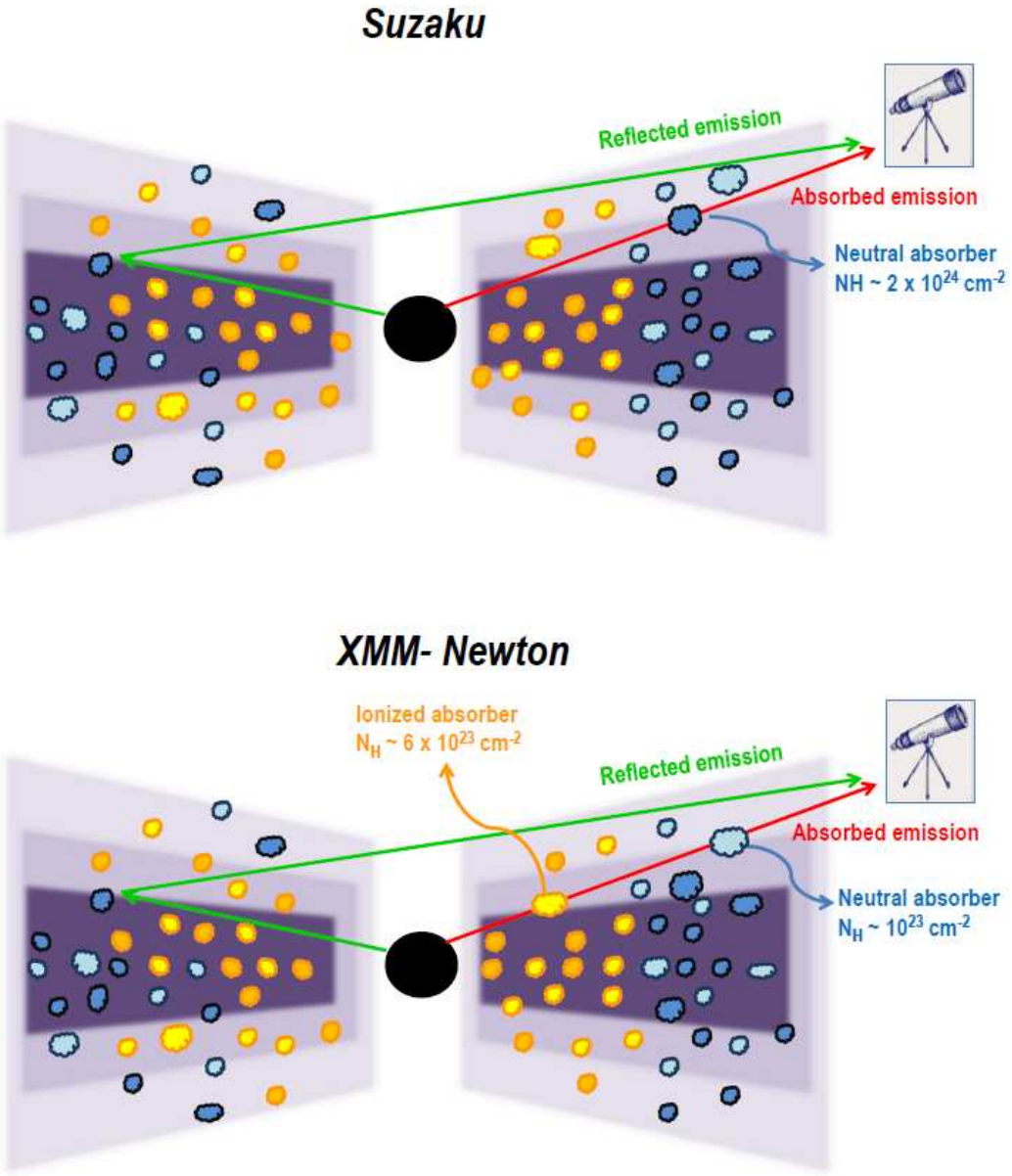

Figure 5.1: *Possible absorption scenario for the* Suzaku *(upper panel) and XMM-*Newton *(lower panel) observations of NGC 454.*

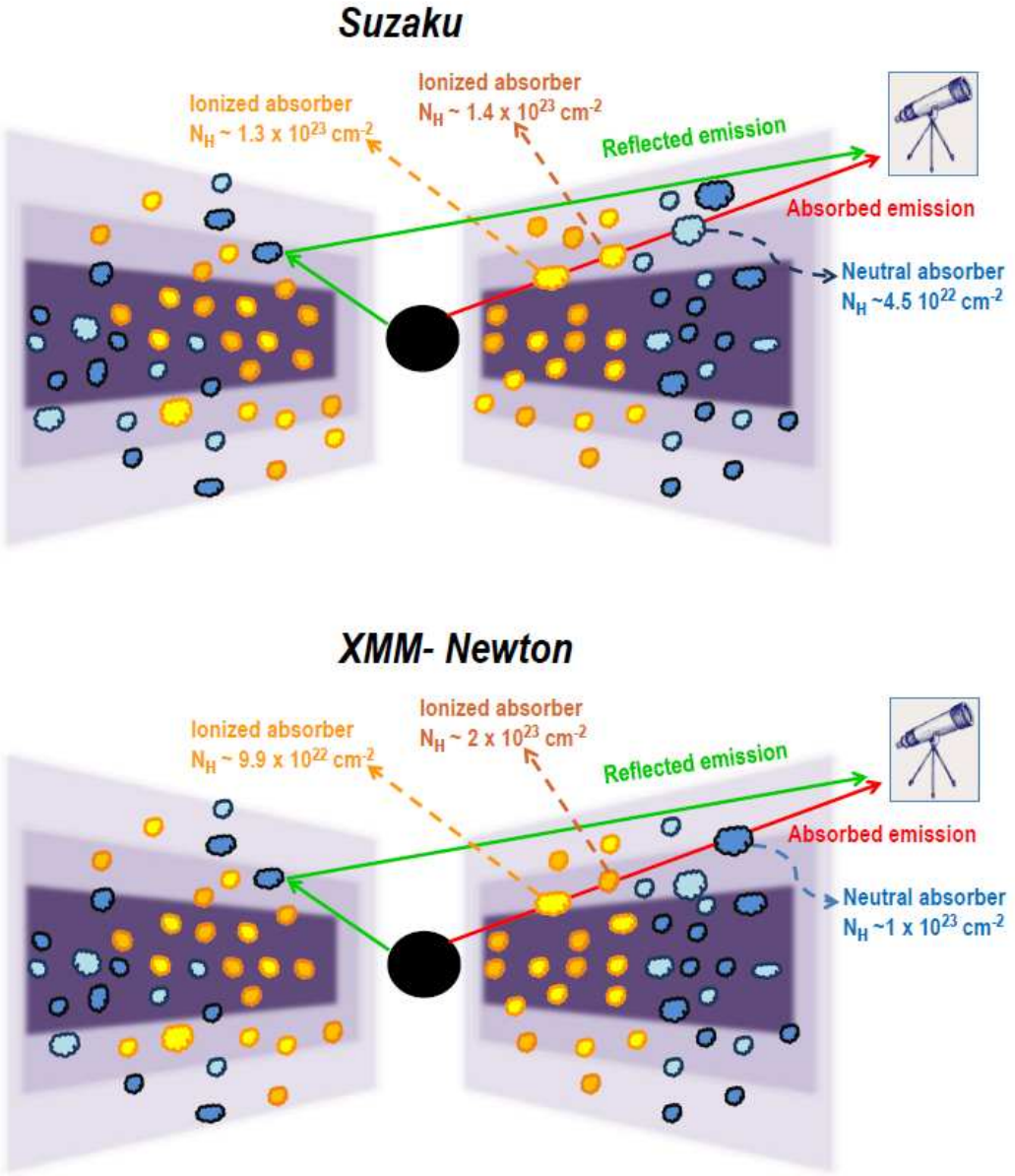

Figure 5.2: *Possible absorption scenario for the* Suzaku *(upper panel) and XMM-*Newton *(lower panel) observations of Mrk 348.*

density (higher ionisation) clouds, implying that the location of the two absorbers are actually the same. An alternative scenario foresees the presence of two wind located at different physical states and distances, intercepting the line of sight. Neither of these two explanations can be ruled out at the moment, since higher spectral resolution observations are needed.

As remarked in this study, the long times elapsed during the observations is a strong limitation in placing stronger constraints on the location, dimensions and origin of the different absorbers, thus a more precise monitoring program would be needed. An alternative approach in the study of X-ray variability in AGN is the systematic analysis of the variations in X-ray column densities in samples of local AGN. Such studies are currently being performed by different research groups. Among these, the first statistical survey with the goal of modelling the circumnuclear material around SMBH was recently performed by Markowitz, Krumpe, & Nikutta (2014). In this work, thanks to *RXTE* observations, they disposed of a multi time-scale (from days to years) X-ray spectral monitoring of a selected sample of 55 Seyfert galaxies (37 Seyfert 1s and 18 Compton-thin Seyfert 2s). They found 12 eclipse events in 8 sources, and distances of the clouds in the range $0.3 - 140\ R_g$, thus in the outer regions of the BLR or factors up to 10 the BLR. The average diameter of the clouds was estimated to be $\sim 6.5 \times 10^{14}$cm. They concluded that the probability of detecting an absorption event in a source, with a duration between 0.2 days and 16 years is $0.006^{+0.160}_{-0.003}$ for Sy1s and $0.110^{+0.461}_{-0.071}$ for Sy2s, thus it is higher for Sy2s, for which in most cases there is also detection of X-ray absorption due to a likely homogeneous absorber. The observation of eclipse events both in Type 1 and Type 2 AGN is in support of a smooth-edged cloud distribution, rather than a sharp-edged one.
Another very recent statistical work on X-ray occultation was published by Torricelli-Ciamponi et al. (2014), where a representative sample of $\sim$ 40 X-ray bright AGN with XMM-*Newton* and *Suzaku* observations have been analysed. About 64% of these sources are in common with the study of Markowitz, Krumpe, & Nikutta (2014). The result of this study, besides suggesting a new faster method to identify occultation (based on the hardness ratio curve), is that eclipse events due to the passage of BLR clouds are very common in AGN (with rate of occurrence of $\sim$ 54% in their sample). They also provide an estimate on the lower limit of the size of the clouds of $R_{cloud} \geq R_X$, where R_X is the X-ray source radius.

A future mission that can provide X-ray monitoring similar to the one obtained thanks to *RXTE* is *Röntgen Survey with an Imaging Telescope* (*eROSITA*, Predehl et al. 2011). Indeed, an intensive monitoring on time scales higher than a few year and in a large range of luminosities, is of great importance in order to test the current alternative models to the Unified Scheme. Further X-ray missions are ASTRO-H and *Athena*. The launch of ASTRO-H[1] (2015), carrying on board an X-ray calorimeter spectrometer, will allow to perform high resolution X-ray spectroscopy in the Fe-K band, with an extremely high signal-to-noise ratio. This will give an improved view of the X-ray reflection signatures, in particular of the fluorescent iron emission line, whose profile contains a wealth of information on the

[1] http://astro-h.isas.jaxa.jp/en/

dynamics and the geometry of the emitting material. A further improvement will concern the study of UFOs, since ASTRO-H will be able to detect absorption features at higher ionisation states with respect to current satellites. *Athena*[2] mission (launch in 2028) will provide improved angular resolution, spectral resolution, detection sensitivity and a larger throughput. Among the key issues that will be treated thanks to *Athena* are the physics of accretion onto black holes, the launch of winds and outflows from accretion disks around black holes and the physical conditions characterizing the growth of SMBH at redshifts $z\sim 1-4$. In particular, for nearby and bright sources, its high throughput and spectral resolution will allow to determine the physical parameters of outfows, on a short dynamical time scales, comparable to the time scales of variability of the central X-ray source, therefore it will be able to resolve changes in the wind structure of bright AGN.
To conclude, the present and "near future" X-ray missions will make the next years fruitful for the study of the structure and evolution of AGN, arising new open questions but especially allowing to put constraints on our knowledge on what happens inside these fascinating and complex objects.

[2] http://www.the-athena-x-ray-observatory.eu/

APPENDIX A

XMM-*Newton* and *Suzaku*

In this appendix I will review the X-ray missions whose observations were of biggest importance in this thesis: XMM-*Newton* and *Suzaku*.

A.1 The XMM-*Newton* Observatory

The X-ray Multi Mirror Mission Newton (XMM-*Newton*, Jansen et al. (2001)) is an orbiting X-ray mission launched in December 1999, whose original lifetime was designed to be 10 years, but thanks to the excellent performances of the instruments it is estimated to be operational until the end of 2019. Its orbit has an apogee of ~115,000 km and a perigee of ~ 6000 km. The satellite weights 3.8 tons and has a total length of 10 metres, which becomes 16 metres when the solar arrays are deployed. The disposal of the telescopes and the instruments onboard the XMM-*Newton* spacecraft is shown in Fig. A.1. XMM-*Newton* carries on board three Wolter-type 1 X-ray telescopes, each of them containing 58 concentric mirror shells, with a combined effective area of 4650 cm^2 at 1.5 keV and ~3000 cm^2 at 6 keV (Fig. A.2). Each of the X-ray telescopes has at its focus a CCD camera (EPIC-MOS1, EPIC-MOS2 and EPIC-pn). Besides, two of the three telescopes (those focussing on the MOS cameras) are equipped with a Reflection Grating Spectrometer (RGS), allowing high resolution spectroscopy.

In more detail, on XMM-*Newton* there are:

- three European Photon Imaging Cameras (EPIC-MOS1, EPIC-MOS2 and EPIC-pn) working in the band 0.15-15 keV, for imaging and spectroscopy;

- the Reflection Grating Spectrometer (RGS) for high resolution spectroscopy, sensitive below 2 keV, placed along the converging beam of each of the two telescopes having EPIC MOS cameras at their focus. It consists of an array of reflection gratings that intercepts half of the light coming from the X-ray telescope and deflects it to a CCD detector (Fig. A.5), while the undeflected X-rays are detected by the EPIC-MOS cameras;

- a 30 cm diameter Ritchey Chretien optical/UV telescope (OM, Mason et al. 2001), sensitive in the band 180-600 mm and with a field of view of 17 arcmin. It allows multi-wavelength observations of the same target both in the X-rays and optical-UV bands. In my thesis I did not make use of the data available from the OM, thus it will not be discussed further.

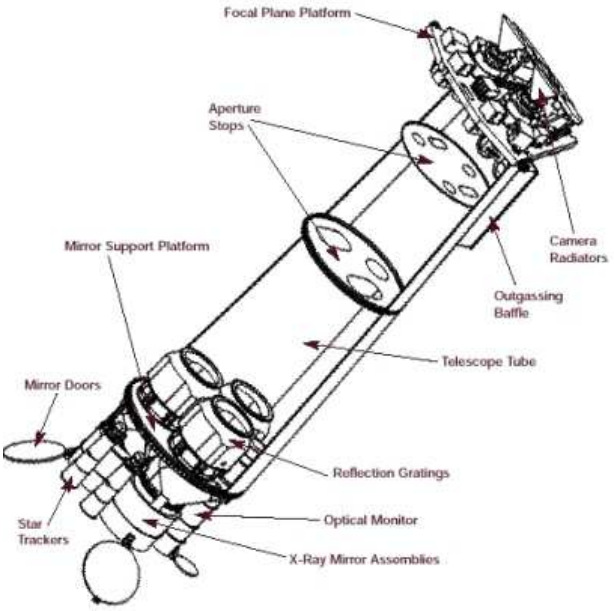

Figure A.1: *Diagram of the XMM-*Newton *spacecraft (adapted from the ESA website).*

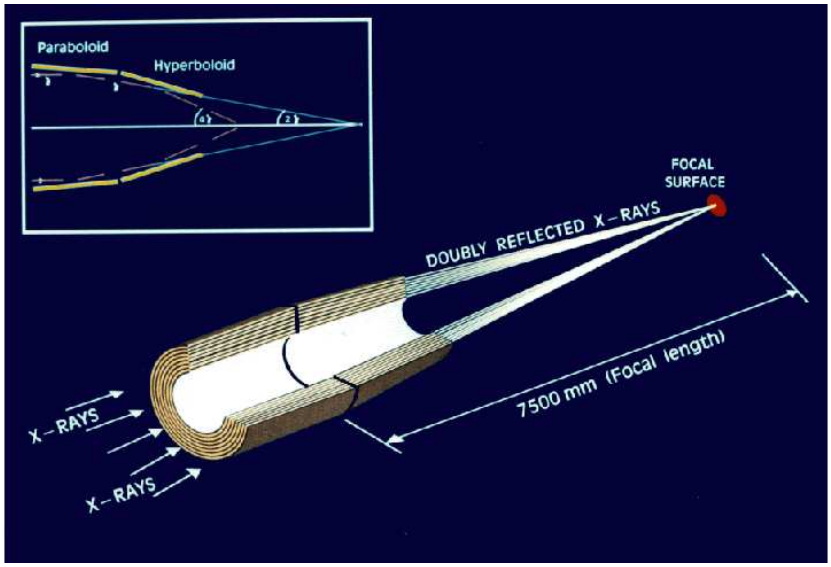

Figure A.2: *Representation of the path followed by radiation incident on the XMM-*Newton *X-ray telescope mirrors, with the pn camera in focus (image not to scale: adapted from the XMM-Newton User's Handbook).*

A.1.1 EPIC

Each of the three EPIC cameras have $\sim$ 30 arcmin FOV, an angular resolution of $\sim 6''$ FWHM and a spectral resolution of $E/\Delta E \sim 20 - 50$. All the EPIC detectors are charge-coupled devices (CCDs), with the EPIC-MOS cameras adopting metal oxide semi-conductors (MOS) CCDs, and the EPIC-pn using a new type of CCD (pn). They operate in photon counting mode, registering for each photon its position, arrival time and energy.
The two EPIC-MOS detectors (Turner et al. 2001) are front illuminated CCD cameras, each of them consisting of on array of seven silicon chips, made up of a matrix of 600×600, 40 micron square pixels. Each pixel covers 1.1 × 1.1 arcsec on the FOV. Since the depth of silicon is only 40 μm, the EPIC-MOS are less responsive to high energy X-ray photons, with respect to EPIC-pn.
The EPIC-pn detector is a back illuminated CCD camera, composed of a single chip, with thickness of 300 μm that allows a more efficient detection of high energy. The pn detector has 400×400 pixel matrix of 6 cm× 6 cm. The pixel size is 150 × 150 micron (4.1 arcsec). The 36 cm^2 sensitive area made it the largest X-ray CCD detector built at that time, and it remained like this for many years.

The X-ray images produced by the EPIC cameras are stored in a temporary data collecting area. Depending on the speed at which the data are acquired from this area, there is a different number of images. Thus there are several modes of data reading.
For the MOS cameras they are:

- "Full Frame" mode: all pixels are read out and the whole FOV is covered, thus the number of images taken per second is rather limited. In this mode the observer receives a full 600×600 pixels image every 2.6 s;
- "Partial Window": in this mode only part of the CCD of the MOS is read out. The possible modes are the Large Window Mode (a 300×300 pixels image every 0.9 s) or the Small Window Mode (a 100×100 pixels image every 0.3 s);
- "Timing Mode": a one dimensional 100×600 pixels image is produced at high speed (1.75 ms). As the 2 MOS cameras are oriented at an angle of 90 from each other, the resulting imaging directions are perpendicular to each other.

For the pn camera the readout modes are:

- "Full Frame": a 376×384 pixels image every 73.5 ms;
- "Extended Full Frame': a 376×384 pixels image every 199.1 ms;
- "Partial Window": it includes the Large Window Mode and the Small Window Mode. In the Large Window Mode half of the area of the 12 CCDs is read out and a 198×384 pixels image is produced every 47.7 ms. In the Small Window Mode only a part of CCD number 4 is used, and a 63×64 pixels image is produced every 5.7 ms;

- "Timing Mode": a one dimensional 64×200 pixels image is produced at a speed of 0.03 ms;
- "Burst Mode": this mode allows very high time resolution (7μs).

The choice of the frame mode is also dependent on the source that is being observed. Indeed a source could be too faint to be detected within a single frame, or on the contrary it could be so bright to cause a *pile up* effect, when more than one X-ray photon arrive at the same pixel, in a time less than the reading time of the CCD, preventing the measurement of the right photon energy, since the single photon information cannot be disentangled.

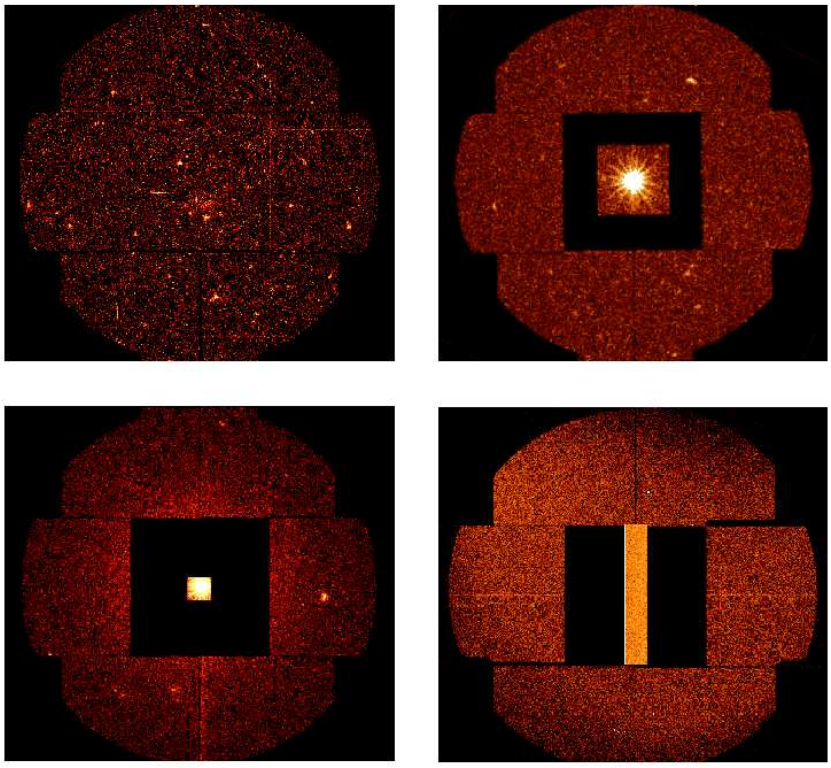

Figure A.3: *Operating modes of the MOS-CCD cameras: On the top left the Full frame mode, on top right the Large window mode, on bottom left the Small window mode and on bottom right the Timing mode.*

A.1.1.1 The EPIC Point Spread Function

The Point Spread Function (PSF) measures the response of the imaging system to a point source, i.e. the spatial distribution of the light received from the point source. The shape of the PSFs of the three X-ray telescopes of XMM-*Newton* is different among each other,

as shown in Fig. A.4, in particular the FWHM of the PSFs varies from 12.5 arcsec (HEW 15.2 arcsec) for the pn to ∼ 4 arcsec (HEW ∼ 13 arcsec) for the MOS cameras at on-axis position. The PSF can be affected by pile-up, because when many photons arrive within the same readout frame in the core of the PSF, they create a multi-pixel photon patterns. This means that we are not able to understand if several photons were detected in the time frame or if only one photon was detected, with an equivalent higher energy. The latter scenario is which is what is registered by the system electronics, resulting in a artificially higher X-ray spectrum. Generally pile-up occurs more frequently for the MOS camera with respect to the pn, for a source with the same flux. It is possible to minimize or correct for the pile-up through the Science Analysis System (SAS, [1]). However this is necessary only for the pn, since for the MOS camera these patterns are already automatically rejected by the on board event reconstruction softare. In presence of pile up, the PSF shows artificial "holes".

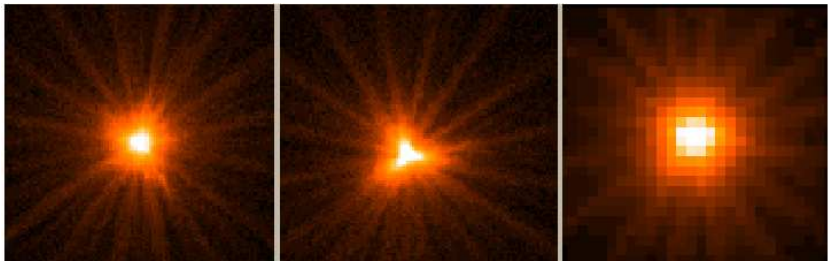

Figure A.4: *PSFs for the MOS1 (left panel), MOS2 (central panel) and the pn (right panel) X-ray telescopes, for the same source. It is visible the different shapes of the PSFs, in particular for the MOS2, which shows a triangular shape. Figure adapted from the ESA website.*

A.1.1.2 The EPIC background

The background in the EPIC cameras can be divided into 3 classes: cosmic X-ray background, particle background and instrumental background. The cosmic X-ray background is produced by astrophysical sources, and it is constituted by thermal emission at low energies (< 1 keV, produced by Galactic emission, in particular by the hot gas in the local bubble) and by a power law at higher energies (produced by unresolved AGN).
The particle X-ray background be distinguished into 2 components. The first one is an external "flaring" and variable component. It is produced by soft proton flares (energies below a few 100 keV) from the Sun, which are thought to be located in clouds in the Earth magnetosphere, and that can be encountered by the satellite with a frequency dependent on its position and on the solar activity. The second component is an internal and stable background, produced by high energy particles (E higher than some MeV) interacting with the structure around the detectors or even with the CCDs themselves. The background spectra resulting from these interactions is flat with the presence of spectral fluorescence features

[1] http://xmm.esac.esa.int/external/xmm_data_analysis/

from the detectors: Al-Kα and Si-Kα lines are observable in the MOS spectrum. For the pn Al-Kα and a complex due to Cu-Kα, Ni-Kα and Z-Kα lines around 8 keV are visible. Finally, the instrumental background, which can be important at energies below 0.2 keV, is the electronic noise produced by the detectors themselves, like bright pixels or readout noise.

A.1.2 RGS

The two MOS-focusing telescopes have a grating structure on their mirror, reflecting ~ 40 per cent of the radiation to a secondary focus, with its own CCD camera, while 44 percent of the radiation is directed to the EPIC MOS cameras at the primary focus of the telescope. The Reflection Grating Spectrometer (RGS, den Herder et al. 2001), allows high resolution spectroscopy. The two reflection grating arrays on XMM-Newton are each composed of 182 grating plates, each of them with about 645 grooves per mm. The RGS works in an energy range of $\sim 0.35 - 1.8$ keV.

The back-illuminated CCDs of the RGS operate in single photon counting and they can measure accurately position and energy of the incoming photon, achieving a spectral resolution of $E/\Delta E \sim 200 - 800$.

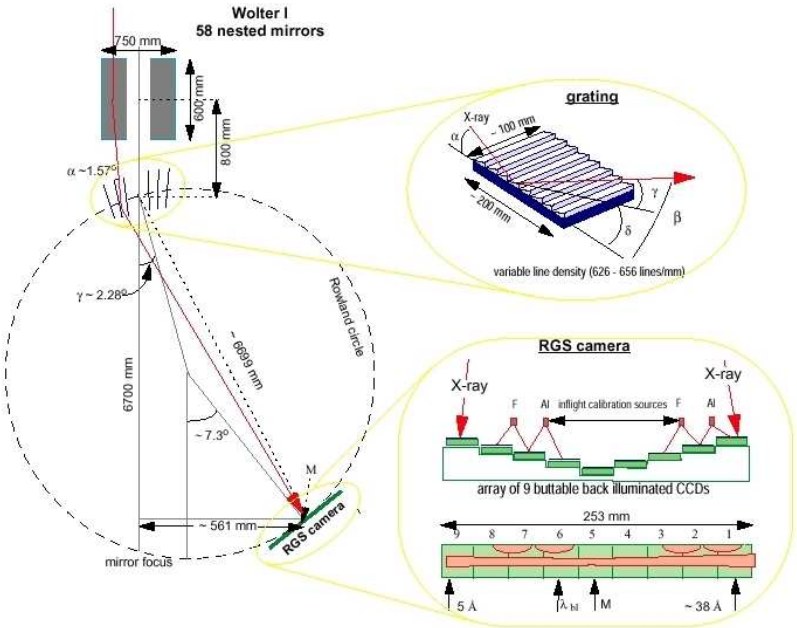

Figure A.5: *Design of the RGS (Brinkman et al. 1998)*

A.1.2.1 XMM-*Newton* prominent features

To conclude this section, I will now discuss what are the main characteristics of XMM-*Newton* with respect to other X-ray missions. For this reason, a small digression on the *Chandra* X-ray mission is worth.

Chandra The *Chandra X-ray Observatory* was launched on July 23, 1999 and its X-ray telescope is composed by 4 Wolter type I mirrors, called the High Resolution Mirror Assembly (HRMA), with an effective area of 800 cm^2 at 0.25 keV, 400 cm^2 at 5 keV and 100 cm^2 at 8 keV (therefore a lower effective area with respect to XMM-*Newton*). The on axis Point Spread Function of *Chandra* is $\sim 0.5''$. The X-rays focussed by the mirrors converge to two focal plane science instruments:

- the Advanced CCD Imaging Spectrometer (ACIS), working in the energy range 0.2-10 keV
- the High Resolution Camera (HRC), composed by two microchannel plates. It has a FOV OF $30' \times 30'$, it works in the energy range 0.08-10 keV.

Two other instruments on board of *Chandra* are the Low energy Transmission Grating Spectrometer (LETGS, energy range of 0.08-2.00 keV) and the High Energy Transmission Grating Spectrometer (HETG, energy range 0.4-10 keV). The strengths of *Chandra* are the excellent angular resolution (on axis FWHM $\sim$ 0.5 arcsec) and the low background, which makes it sensitive to faint sources and implies a high signal-to-noise ratio.

In Table A.1 I report what are the main characteristics of XMM-*Newton* with respect to other X-ray past and present missions, of which the most important ones are:

- the high Earth orbit, allowing longer uninterrupted observations of up to 40 hours (while a lower orbit would have more frequent Earth occultations);
- the simultaneous activity of all the scientific instruments, in particular of the optical/UV observations, allowing an optical identification of the X-ray sources;
- the large effective area (4650 cm^2 at 1 keV, as compared to Chandra's 555 cm^2, only NuStar has a higher one) which implies a large photon counting statistics;
- the large FOV of the EPIC-MOS camera is good for performing sky surveys, even if the PSF not as good as *Chandra*;
- the good energy resolution (4 eV at 1 keV), similar to *Chandra* (1 eV at 1 keV);
- the relatively good angular resolution (the PSF has a FWHM of $6''$, as compared to the $\sim 0.5''$ of *Chandra*);
- high and unstable background with respect to *Chandra* (faint sources are more difficult to detect).

Table A.1: Main characteristics of XMM-*Newton* (see The XMM-*Newton* Users' Handbook for further details).

Instrument	**EPIC MOS**	**EPIC pn**	**RGS**	**OM**
Bandpass	0.15-12 keV	0.15-15 keV	0.35-2.5 keV	180-600 nm
Orbital target vis.[(1)]	5-135 ks	5-135 ks	5-145 ks	5-145 ks
Sensitivity[(2)]	∼10 -14[(3)]	∼10 -14[(3)]	∼8×10-5[(4)]	20.7 mag [(5)]
Field of view (FOV)	30'	30'	∼5'	17'
PSF (FWHM/HEW)	5"/14"	6"/15"	N/A	1.4"-1.9"
Pixel size	40 μm (1.1")	150 μm (4.1")	81 μm (9×10-3 Å)	0.47"
Timing resolution[(6)]	1.5 ms	0.03 ms	16 ms	0.5 s
Spectral resolution[(7)]	∼70 eV	∼80 eV	0.04/0.025 Å	350[(8)]

[(1)] Total time available for science per orbit.
[(2)] After 10 ks.
[(3)] In the energy range 0.15-15.0 keV, in units of erg $s^{-1}cm^{-2}$.
[(4)] OVII 0.57 keV line flux in photons $s^{-1}cm^{-2}$, for an integration time of 10 ks and a background of 10^{-4} photons $s^{-1}cm^{-2}keV^{-1}$.
[(5)] 5-σ detection of an A0 star in 1000 s.
[(6)] In fast data acquisition mode (i.e., fast mode for OM and timing mode for EPIC, high time resolution mode for RGS).
[(7)] At 1 keV. At the energy of Fe Kα (6.4 keV), the energy resolution of both EPIC cameras ∼150 eV.
[(8)] Resolving power ($\lambda/\Delta\lambda$) with UV and optical grism.

Table A.2: Comparison of the main XMM-*Newton* properties with the other X-ray missions

Satellite	Mirror PSF FWHM [″]	Mirror PSF HEW [″]	E range [keV]	A_e at 1 keV [cm^2][a]	Orbital target visibility [hr]	Energy resolution
XMM-Newton	6	15	0.15 - 12	4650	36.7[b]	4 eV at 1 keV (RGS)
Chandra	0.2	0.5	0.1 - 10	555 (ACIS-S)	44.4[b]	1 eV at 1 keV (HETG)
ROSAT	3.5	7	0.1 - 2.4	400	1.3[c]	500 eV at 1 keV
ASCA	73	174	0.5 - 10	350	0.9[c]	100 eV at 1 keV
Suzaku	n.av.[e]	120	0.2 - 600	1760 (XIS)	0.72[c]	130 eV at 6 keV
RXTE	n.a.[e]	n.a.[e]	2-250	n.a.[e]	1[c]	n.a.[e]
Swift	8.8	18[d]	0.2-10 (XRT)	133.5	~0.8[c]	70 eV at 1 keV
NuSTAR	18	n.av.[e]	3-79	n.a.[e]	~0.8[c]	0.4 keV at 6 keV, 0.9 keV at 60 keV

[a] Mirror effective area.

[b] Orbital visibility outside the particle-radiation dominated zone.

[c] Low orbit with Earth occultation.

[d] At 1.5 keV.

[e] n.av.: not available, n.a.: not applicable.

A.2 *Suzaku*

The Japanese X-ray mission *Suzaku* (Mitsuda et al. 2007) was launched on July 10,2005 by a Japanese M-V 6 rocket from the Uchinoura Space Center (USC), and was put into a low circular orbit at an altitude of ∼ 570 km, with an orbital period of ∼ 96 minutes. The spacecraft is long 6.5 m and weights ∼1700 kg.
Suzaku covers the energy range 0.2-600 keV, and it carries on board the following instruments: an X-ray micro-calorimeter (X-ray Spectrometer, or XRS, no longer operative), four X-ray CCDs (the X-ray Imaging Spectrometers, or XISs, Koyama et al. 2007), and a hard X-ray detector (HXD, Takahashi et al. 2007). All these instruments operate simultaneously.

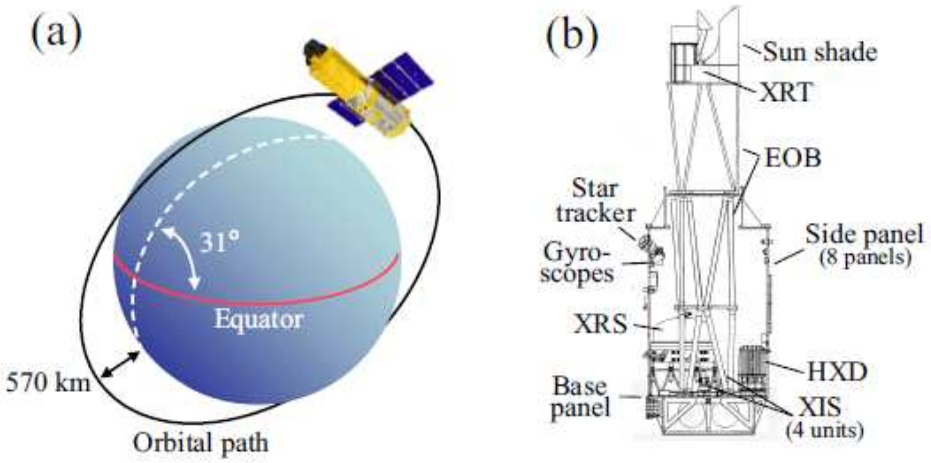

Figure A.6: *(a) Schematic image of the Suzaku satellite in orbit (b) Side view of Suzaku with the internal structures (Mitsuda et al. 2007).*

A.2.1 XIS

Each of the XISs is located at the focus of an X-ray telescope (XRT, Serlemitsos et al. 2007). The XRTs are Wolter-1 X-ray reflection mirrors, with a focal length of 4.5 m each. They are composed by closely nested conical reflectors, reflecting X-ray photons having small grazing incident angles ($\lesssim 0.7^\circ$). Each XRT module is composed by 175 thin foil layers. The angular resolution (expressed as Half-Power Diameter) of each X-ray mirror is of $\sim 2'$.

Each XIS CCD camera, at the focal plane of an XRT, has a single chip, with an imaging area of 1024×1024 pixels and a field of view of $\sim 18' \times 18'$. Each chip is composed by four segments (named A,B,C and D), each with its own readout node (see Fig. A.7).

Three of the XIS CCDs (XIS0, XIS2, XIS3) are front-illuminated (FI) and detect X-rays that penetrate the gate structure with a thickness of ∼0.7 μm, while the XIS1 is a back-illuminated (BI) CCD, where the thickness of the surface dead layer is ∼ 10 μm.

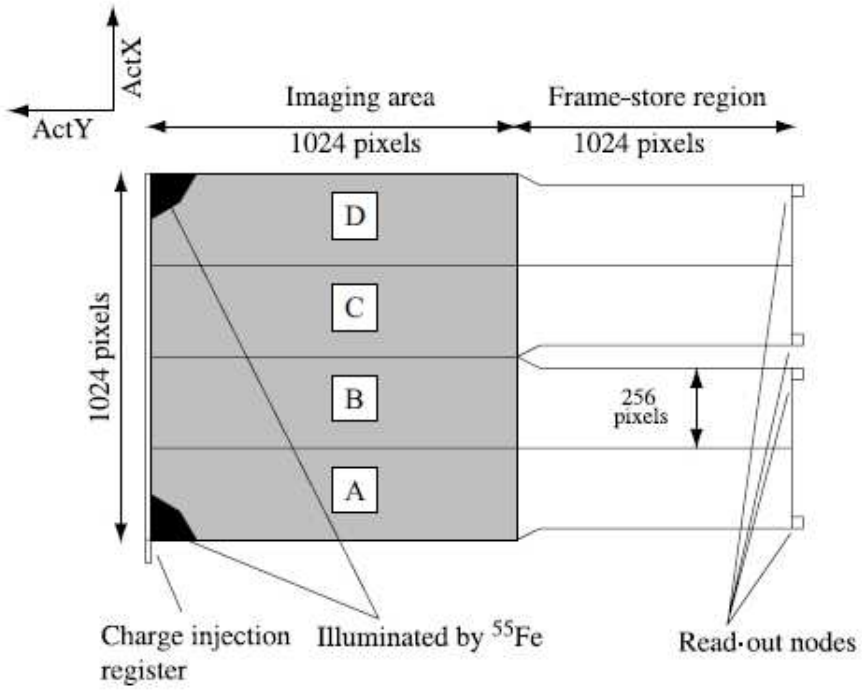

Figure A.7: *Scheme of the XIS CCD (Koyama et al. 2007).*

The BI CCD reach a high quantum efficiency (which measures the capability of incident photons to be absorbed in the depletion region of the detector) even at low energies (below $\sim$ 1 keV), since the gate structure is not present. However, since the depletion layer of the FI CCDs is thicker ($\sim$ 76 μm) than the one of the BI CCD ($\sim$ 42 μm), they have a higher quantum efficiency for high energy photons. In particular, the FI CCDs cover the energy range 0.6-10 keV, with a resolution of FWHM $\simeq$ 120 – 150 eV at 6 keV and the XIS1 and has a better sensitivity at energies below 2 keV (down to 0.2 keV).
The XISs can work in a normal two-dimensional mode or the P-sum mode, that produces a one dimensional image and provides a better time resolution. The normal mode includes two further options: the window option, that uses a smaller selected area of the CCD, and the burst option, that uses a smaller exposure time in the readout intervals.

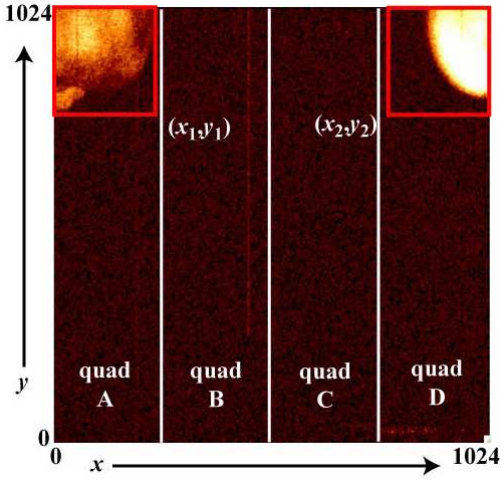

Figure A.8: *XIS2 field, showing the calibration sources that illuminate the upper corners, with their extraction regions identified. Figure adapted from http://space.mit.edu/XIS/monitor/ccdperf/ .*

Calibration Sources In order to perform on-orbit calibration, each XIS unit is is equipped with two radioactive calibration sources (^{55}Fe). ^{55}Fe decays leaving ^{55}Mn via electron capture (in 88.5% of the cases) from the K-shell. As a consequence strong fluorescence lines are emitted at 5.9 keV (Mn Kα) and 6.5 keV (Mn Kβ). As shown in Fig. A.7 and Fig. A.8 these sources illuminate the two far corners of the segments A and D, on the opposite side of the readout nodes, for each detector.

A.2.2 Hard X-ray Detector (HXD)

The HXD is a non-imaging collimated detector, with an effective area of $\sim$ 260 cm^2, sensitive in the energy range 12-600 keV, thus allowing broad band studies of astrophysical sources. It consisting of 16 well-counter units, each of them composed by two types of

detectors: four (2×2) silicon PIN diodes located in front of Gadolinium Silicate crystal (GSO) scintillators. The PIN diodes are sensitive in the energy range 12-70 keV and become gradually transparent to higher energy photons; their energy resolution is ∼ 4.0 keV. The GSO phoswich counter is sensitive to the photons that pass through the PIN in the energy range 50-600 keV and it has an energy resolution of $7.6/\sqrt{E_{MeV}}$%. The HXD field of view is collimated to $4.5^\circ \times 4.5^\circ$ for energies $\gtrsim$ 100 keV, and it is further collimated to a field of view of $34' \times 34'$ at energies $\lesssim$ 100 keV.

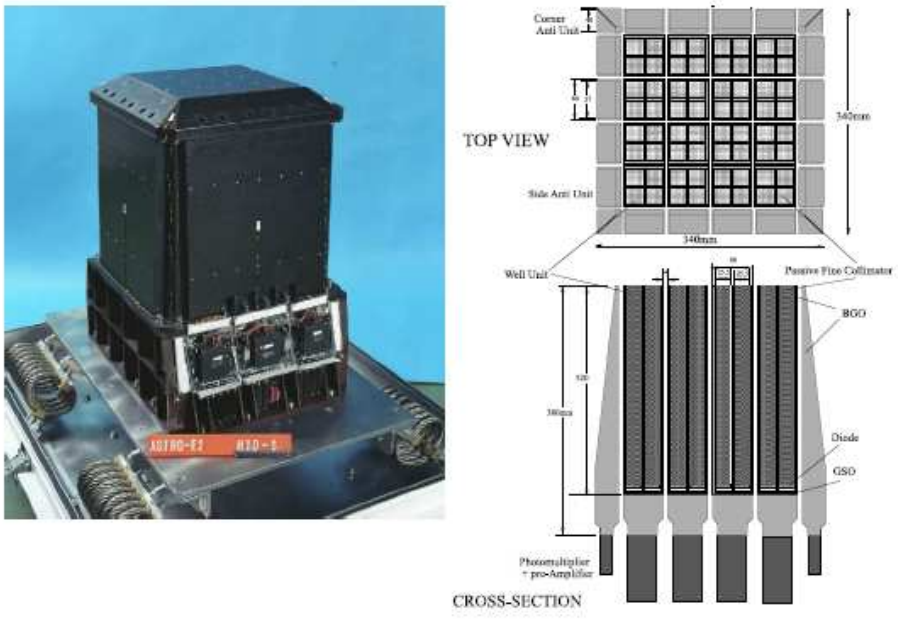

Figure A.9: *Picture and scheme of the HXD (Kokubun et al. 2007).*

In table A.3 I summarise the main characteristics of the *Suzaku* satellite and its instruments.

A.2.3 Background

Suzaku low Earth orbit has the advantage of providing protection from most of the cosmic ray particles that in XMM-*Newton* and *Chandra* observations (both in higher orbits) induce stronger background contamination. Since the event data include both particle background events (the Non X-Ray Background, NXB) and X-ray background events, their contribution must be estimated and subtracted to the observed data. For the XIS event data, this can be done by measuring the background in an extraction region far away from the target source, in the same XIS CCD. When this is not feasible, like for the case of extended sources, then the NXB can be estimated from observations taken during the "night Earth", i.e. when *Suzaku* observes the night side of the Earth and the X-ray emission is obscured. For the HXD event files it is not possible to obtain background data from the observations,

Table A.3: Main features of the *Suzaku* spacecraft and instruments

Spacecraft	Altitude	$\sim$ 570 km
	Orbital Inclination	31°
	Orbital Period	31°
	Weight	1706 kg
	Length	6.5 m
XRT	Focal Length	4.75 m
	Effective area	440 cm^2 at 1.5 keV, 250 cm^2 at 8 keV
	Angular Resolution	2' (half power diameter)
XIS	Energy Coverage	0.2-12 keV
	Field of View	17'.8$\times$ 17'.8
	Energy resolution	$\sim$130 eV at 6 keV (FWHM)
	Effective Area	330 cm^2 (FI), 370 cm^2 (BI) at 1.5 keV
	Time resolution	8 s (normal mode), 7.8 s (P-sum mode)
HXD	Energy Coverage	12-70 keV (PIN), 50-600 keV (GSO)
	Field of View	$34' \times 34'$ ($\lesssim$ 100 keV), 4°.5$\times$ 4°.5 ($\gtrsim$ 100 keV)
	Energy Resolution	PIN : $\sim$ 3keV (FWHM)
		GSO : 7.6/ $\sqrt{E_{MeV}}$% (FWHM)
	Effective Area	$\sim$160 cm^2 at 20 keV, $\sim$260 cm^2 at 100 keV
	Time resolution	61 μm

being PIN a collimated instrument. Therefore, for the NXB, models of particle background are provided by the HXD team. These background event files don't include the cosmic X-ray background, that needs to be estimated (performing simulations) and subtracted after the NXB.

A source of background is also due to the passage of *Suzaku* through the South Atlantic Anomaly (a region of high particle flux, due to the locally weaker Earth magnetic field), given the low-Earth orbit. Indeed during this passage, occurring in one third of the revolutions, the instrumental performances are highly impacted, therefore the events registered during this phase must be excluded.

To conclude, I will go through the main features of *Suzaku* with respect to other missions:

- it has a low and stable background, thanks to the low Earth orbit. This is good to observe X-ray sources with low surface brightness;
- it allows a simultaneous wide-band X-ray spectral covering, thanks to the contemporaneous observations of the XISs and the HXD;
- its effective area is better than *Chandra*, but smaller than XMM-*Newton*;
- it has a large PSF, meaning that it is not as good as *Chandra* and XMM-*Newton* for studies where high spatial resolution is required (e.g. for surveys).

A.3 *Swift Gamma-ray burst observatory*

Even if I didn't analyse the X-ray spectra from *Swift* I will briefly describe the features of this satellite. The *Swift Gamma-ray burst observatory* (Gehrels et al. 2004) was launched on 20th November 2004, and was dedicated to the observation and study of gamma-ray bursts (GRBs). The satellite was put in a low Earth orbit at an altitude of ~ 600 km with a low inclination of 22 degrees (to minimize the time spent in the South Atlantic Anomaly), it has a diameter of ~ 2.7 m and a length of ~ 5.7 m. The main objectives of the mission concern the determination of the origin and evolution of gamma ray bursts, and to use them to study the early Universe. Besides that, *Swift* was designed to perform the first sensitive survey of the the sky in the hard X-ray band.
Swift carries on board 3 co-aligned telescopes, the X-ray Telescope (XRT), the Ultraviolet/Optical Telescope (UVOT) and the Burst Alert Telescope (BAT), thus any source can be observed simultaneously in different wavebands. Up to February 2015 *Swift* has detected 942 bursts.

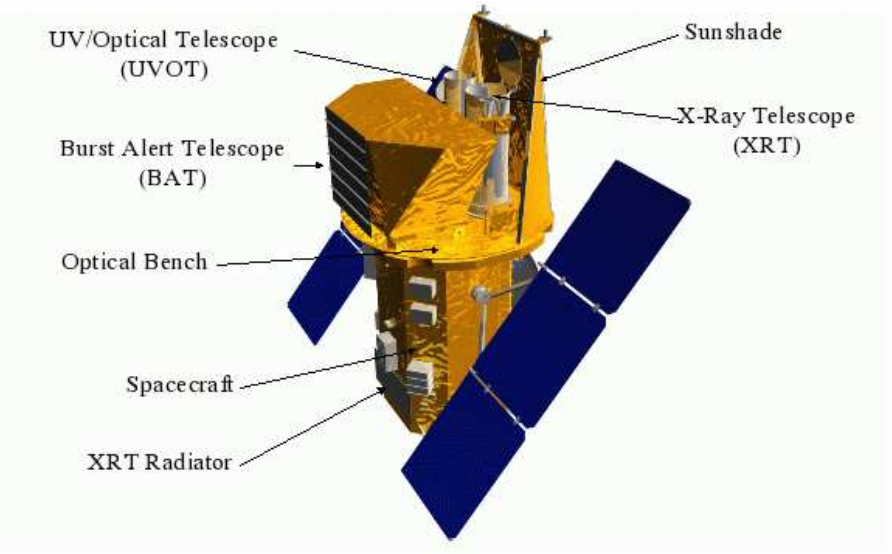

Figure A.10: *Scheme of the* Swift *observatory (Gehrels et al. 2004).*

A.3.1 Burst Alert Telescope (BAT)

The Burst Alert Telescope (BAT) (Fig. A.11, Barthelmy et al. 2005), is a large coded-mask telescope sensitive in the energy band 15-150 keV, with ~ 7 keV energy resolution, and a sensitivity of $\sim 10^{-8}$erg cm^{-2} s^{-1}. BAT was designed to detect transient GRBs: it has a large field of view of 60×100 degrees, much larger than the other instruments on board, allowing it to detect GRBs from a large fraction of sky, at any time. In fact BAT is the first of the *Swift* instruments to detect a GRB shortly after it occurs. The general strategy of

observation is to target predefined sources with the narrow field of the XRT, until a GRB is detected by BAT. BAT calculates on board the burst position, with an accuracy of 1-4 arcminutes, within ~20 sec after the event starts. The position is transmitted to the XRT and UVOT, that within 20-70 sec are re-pointed to target the GRB, and follow it until the X-ray afterglow fade off below the detection limit. Besides observing bursts, BAT automatically performs an all-sky hard X-ray survey.
BAT is composed by 52,000 pieces of lead ($5 \times 5 \times 1mm$) with a separation of 1 m between mask and detector plane. The BAT can operate in two modes: burst mode, producing burst positions, and survey mode, to perform hard X-ray survey (that collect count rate data in five-minute time bins for 80 energy intervals). A table with the main features of BAT is reported in Fig. A.12.

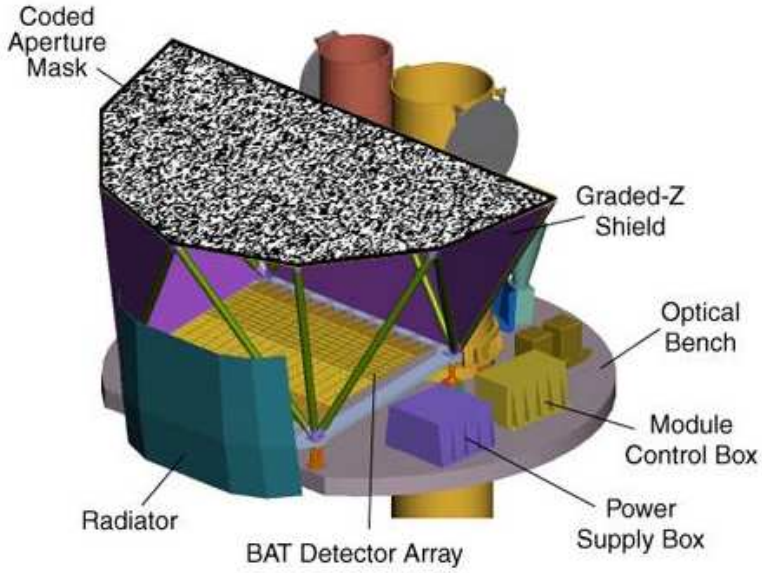

Figure A.11: *Scheme of the* Burst Alert Telescope *(BAT) (Gehrels et al. 2004)*

Parameter	Value
Energy Range	15-150 keV
Energy Resolution	~7 keV
Aperture	Coded mask, random pattern, 50% open
Detecting Area	5240 cm^2
Detector Material	CdZnTe (CZT)
Detector Operation	Photon counting
Field of View	1.4 sr (half-coded)
Detector Elements	256 Modules of 128 elements/Module
Detector Element Size	4.00 x 4.00 x 2.00 mm^3
Coded Mask Cell Size	5.00 x 5.00 x 1.00 mm^3 Pb tiles
Instrument Dimensions	2.4m x 1.2m x 1.2 m
Telescope PSF	17 arcmin
Source Position Accuracy	1-4 arcmin

Figure A.12: *Table reporting the main features of the BAT instrument (Barthelmy et al. 2005).*

A.3.2 X-Ray Telescope (XRT)

The XRT (Fig. A.13) is a X-ray CCD imaging spectrometer at the focal plane of a 3.5 m focal length grazing Wolter 1 telescope, with an effective area 110 cm^2, field of view 23.6'×23.6', a resolution of 18″ (half power diameter). The CCD detector is sensitive in the energy band 0.2-10 keV, to a flux of 2×10^{-14}erg cm^{-2} s^{-1} in 104 seconds, and it has an image area of 600×602 pixels. The energy resolution is ~ 190 eV at 10 keV and ~ 50 eV at 0.1 keV. Two read-out modes are supported: the Imaging Mode, that measures the total energy received in each pixel and does not allow spectroscopy, and the Photon Counting Mode, that permits to obtain full spectral and spatial information. A table with the main features of the *XRT* is reported in Fig. A.4.

A.3.3 Ultraviolet and Optical Telescope (UVOT)

UVOT is a 30 cm diameter modified Ritchey-Chrétien telescope, with a field of view of ~ 17′, sensitive to magnitude 22.3 in 1000 s. The light received by the telescope is then directed by a 45 degree mirror to two dectectors, constituted by micro-channel plate intensified charged-coupled devices (MICs), lying behind 6 bandpass filters that cover the range of 170-650 nm, and two Optical/UV grisms. The MICs operate in a photon counting mode. The good sensitivity achieved despite the modest dimensions, comparable to a 4 m ground-based telescope on Earth, is due to the absence of the Earth atmosphere and to the low sky background permitted by the low Earth orbit occupied by the satellite. In Fig. A.14 I report a table with the main parameters of the *UVOT* instrument (Roming et al. 2005).

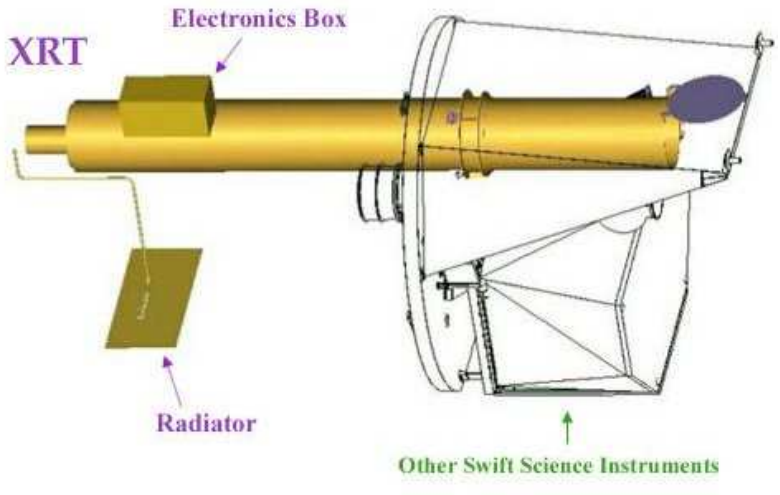

Figure A.13: *Scheme of the* Swift X-ray Telescope *(XRT, Burrows et al. 2005).*

Table A.4: Table with the main features of the *Swift X-ray Telescope* (XRT, Burrows et al. 2005).

Telescope:	Wolter I (3.5 m focal length)
Detector:	e2v CCD-22
Detector Format:	600×600 pixels
Pixel Size:	$40\ \mu$m $\times$ $40\ \mu$m
Readout Modes:	Image (IM) mode
	Photodiode (PD) mode
	Windowed Timing (WT) mode
	Photon-Counting (PC) mode
Pixel Scale:	2.36 arcseconds/pixel
Field of View:	23.6×23.6 arcminutes
PSF:	18 arcseconds HPD @ 1.5 keV
	22 arcseconds HPD @ 8.1 keV
Position Accuracy:	3 arcseconds
Time Resolution:	0.14 ms, 1.8 ms, or 2.5 s
Energy Range:	0.2 - 10 keV
Energy Resolution:	140 eV @ 5.9 keV (at launch)
Effective Area:	~ 125 cm^2 @ 1.5 keV
	~ 20 cm^2 @ 8.1 keV
Sensitivity:	2×10^{-14} erg cm^{-2} s^{-1}in 10^4 seconds
Operation:	Autonomous

Telescope	Modified Ritchey-Chrétien
Aperture	30 cm diameter
f-number	12.7
Filters	11
Wavelength Range	170-600 nm
Detector	MCP Intensified CCD
Detector Operation	Photon Counting
Sensitivity	m_B=24.0 in white light in 1000s
Field of View	17 x 17 arcmin^2
Detection Element	256 x 256 pixels
Sampling Element	2048 x 2048 after centroiding
Telescope PSF	0.9 arcsec FWHM @ 350nm
Pixel Scale	0.5 arcsec

Figure A.14: *Table reporting the main parameter of* UVOT *(Roming et al. 2005).*

The *Swift* mission received the contribution of Italy, thanks to the financing of the Italian Space Agency (ASI) and the Istituto Nazionale di Astrofisica (INAF), for the mirrors of the XRT and part of the X-ray data analysis software. Besides, *Swift* uses antennas of the Malindi (Kenya) ASI station to receive data and transmit commands, about twelve times per day.

Appendix B

Modelling AGN X-ray spectra

The XSPEC software (Arnaud 1996) is an X-ray spectral fitting program including a wide range of models to fit X-ray spectra. Throughout this thesis I used XSPEC in order to infer the physical parameters of the best-fit models describing the observed X-ray spectra. In this section I will discuss what are the most common models included in XSPEC and adopted to describe the different components of a typical AGN X-ray spectrum.

- The simplest starting model to describe the AGN spectra is a power law, which represents the primary X-ray emission due to inverse Compton-scattering of the optical-UV photons emitted by the accretion disk, without any obscuration. The corresponding model will be referred as POWERLAW, and takes as input parameters the normalization at 1 keV (in units of photons $\mathrm{keV}^{-1}\mathrm{cm}^{-2}\mathrm{s}^{-1}$) and the photon index Γ.

- Photo-electric absorption of the intrinsic power law can be modelled through different multiplicative models, depending on the photoelectric cross sections and relative abundances. I will go through the most used ones and indicate the main differences. All the models have the form:

$$M(E) = e^{-N_{\mathrm{H}}\sigma(E)} \tag{B.1}$$

  where $\sigma(E)$ is the photoelectric cross section. A model that used to describe Galactic absorption, is WABS model, where the cross sections are those computed by Morrison & McCammon 1983, and that do not include Thomson scattering.
  Another model that I used to describe photo-electric absorption is PHABS, which is similar to WABS, but it leaves as free parameters the photo-electric cross section and the relative abundance. In this work I used the cross sections computed by Balucinska-Church & McCammon 1992 with a new He cross-section based on Yan, Sadeghpour, & Dalgarno (1998). To describe absorption by a partial covering absorber, the PCFABS model can be used. It is defined as:

$$M(E) = f \times e^{-N_{\mathrm{H}}\sigma(E)} + (1 - f) \tag{B.2}$$

  where f, is the covering factor, defined in the range $0 < f < 1$, thus a fully covering absorber corresponds to $f = 1$. Since Compton scattering is not included in these models, WABS, PHABS and PCFABS best describe a structure with low column density ($N_{\mathrm{H}} < 5\times 10^{23}\mathrm{cm}^{-2}$) along the line of sight, where no scattering occurs. Therefore the loss of high energy photons that occurs at higher column densities must be described with some other model.

- A model that describe *non-relativistic optically-thin Compton scattering* is the CABS model, that accounts for the photons that are Compton-scattered away from the line of sight, in an optically-thin medium. Geometrically it represents a sphere of material that intercepts the primary radiation. Its expression is always of the form described in Eq. B.1, but σ is the Thomson cross-section with Klein-Nishina corrections at high energies. Combining the CABS with the PHABS model allow us to describe the attenuation due both to Compton scattering and to photoelectric absorption. However, since this model is a good description only for optically-thin medium, it does not account for the "forward scattering", i.e. the downshifting in energy of the photons coming from other directions and scattered into the line of sight, but it accounts only for the attenuation of the primary radiation due to photons scattered out of the line of sight. For high column densities the fraction of primary X-ray continuum that can be suppressed by Compton down-scattering is not negligible.
  Thus, a more realistic model is PLCABS (Yaqoob 1997), describing a cut-off power law observed through dense, cold matter. It accounts both for the transmitted and the scattered radiation into the line of sight, produced by fully covering matter spherically distributed around the X-ray source (thus a different geometry than the CABS model), correctly taking into account also Compton down-scattering. However this model can be considered valid only up to column densities of $N_{\rm H} = 5 \times 10^{24} {\rm cm}^{-2}$, and in a range of energies between 10 and 18.5 keV in the rest frame, depending on the column density (Yaqoob 1997). One point of attention when using the CABS and PLCABS models to describe scattering is that they can give different constraint on luminosity, at the same N_H. In fact, since CABS only subtracts photons to the continuum and does not consider the addition of photons scattered into the line of sight from other directions, the intrinsic luminosity obtained from this model can only be considered as an upper limit. Instead, the intrinsic luminosity inferred from the PLCABS model can be considered as a lower limit, since in this case there is also the contribution from the photons scattered into the line of sight from other directions, almost compensating the photons scattered out of the line of sight.

- As we discussed in Section 2.2.1, either the putative torus or the accretion disk, produce a reflection spectrum characterized by a hump in the range $\sim 10 - 30$ keV, as well as fluorescent emission lines and “Compton shoulders” for the emission lines produced by elements, such as Fe, which have high abundance. The X-ray continuum reflected out of the line of sight by a semi-infinite slab of cold material can be modelled by the PEXRAV model (Magdziarz & Zdziarski 1995), representing an exponentially cut off power law spectrum reflected from neutral material. The main parameters of this model are the photon index, the high energy cut-off (in keV units), the abundances relative to the solar ones, the cosine of inclination angle and the reflection scaling factor R which is a measure of the solid angle subtended by the reflecting material as seen from the source emitting the primary continuum, $R=\Omega/2\pi$, so it is equal to 1 for for point source isotropically illuminating infinite optically thick

slab. R is < 0 if there is only the reflection component and no direct emission. Since PEXRAV describes only the reflected continuum, in order to account also for the contribution of the Fe Kα and Fe Kβ emission lines it is possible to use simple gaussian profiles (modelled through the GAUSS component). Alternatively, the PEXMON model (Nandra et al. 2007) can be used, which combines PEXRAV consistently with Fe Kα, Fe Kβ, Ni Kα and the Fe Kα Compton shoulder. The parameters of the model are the same as for PEXRAV.

When X-ray irradiation is intense and matter get ionised, the reflection spectrum changes, as described in Section 2.3.1. One of the models that can describe such ionised reflected spectrum is REFLIONX (Ross & Fabian (2005)). This model assumes that the primary radiation illuminates a constant density partially ionised semi-infinite slab of optically thick gas (such as the surface of the accretion disk) and gets reflected by this ionized slab. The illuminating radiation has a high-energy exponential cut-off fixed at 300 keV and a low energy cut-off at 0.1 keV. The model include lines and edges from Fe, O, Si, Mg, N and C, as well as other elements. The input parameters of the REFLIONX model are the iron abundance, the ionization parameter of the reflecting matter (in the range 30 to 10^4 erg cm/s, so this model cannot be used for neutral absorbers), the photon index of the illuminating radiation and the normalization.

- We saw that the photoelectric absorption by neutral matter can be modelled through the WABS, PHABS, CABS models. However when the absorbing matter is ionised, the presence of several narrow absorption lines and edges, depending on the material ionisation state, is evident in the spectrum. XSPEC includes some built in models to represent ionised absorbers (such as ABSORI) but they are a first order approximation of a more complex scenario. For this reason the complexity of these absorbers can be modelled through the use of numerical codes making assumptions on atomic data, numerical algorithms and physical processes. In this thesis I used pre-created grids, obtained through the XSTAR photoionization code (Kallman et al. 2004), that calculates the physical state and the emission/absorption spectra produced by photoionised gas. The physical scenario it describes is essentially a spherical shell of gas surrounding a source of ionizing radiation, absorbing a fraction of it and re-emitting the radiation at different wavelengths. The result of the code calculation is a multiplicative grid (in FITS format) that can be used in XSPEC to fit the spectral data, with three free parameters: the ionisation parameter, the column density and the redshift of the absorber.

Aknowledgements

Un ringraziamento speciale va ai miei relatori, Valentina Braito, Roberto Della Ceca e Monica Colpi. Valentina, grazie per la pazienza, i consigli, la disponibilità, i sabati e le domeniche che mi hai dedicato a Merate, per l'esperienza che mi hai consentito di fare a Leicester, per tutto quello che mi hai insegnato e per la passione che metti in quello che fai, che non è da tutti. Grazie per avermi dato una grossissima mano a raggiungere questo obiettivo! Grazie Roberto, perchè sei stato sempre presente durante questo percorso, per il tuo ottimismo e il tuo sostegno continuo dai tempi della tesi di laurea ad oggi, grazie infinite!

Grazie Monica, perchè sei stata sempre comprensiva, disponibile e presente quando ne ho avuto bisogno, e grazie anche a tutti i ricercatori dell'osservatorio di Brera, in particolare Paola, Alessandro, Lucia, Anna per tutti i vostri suggerimenti, e il tempo che mi avete dedicato!

Vorrei anche ringraziare le mie amiche Ilaria Perrino, Martina Cimmarrusto, Silvia Sguinzo e Ilaria Biganzoli, per la vostra vicinanza, comprensione, amicizia e affetto incondizionato, soprattutto negli ultimi due anni! Un abbraccio va a tutta la mia famiglia, mio padre, mio fratello Claudio, le mie fantastiche zie e zii, e le mie nonne Angela e Bianca. Dedico a te, papà, questa tesi, perchè sei la persona che nella mia vita mi ha sempre appoggiato con lo spirito, la pazienza e il sostegno pratico. Senza il tuo aiuto niente di tutto ciò sarebbe stato possibile. Grazie per gli stimoli continui, per la passione e la determinazione che mi hai sempre trasmesso. Grazie per credere sempre in me e in quello che faccio, e per esserti sorbito tutte le mie preoccupazioni, soprattutto quando ho iniziato a lavorare. Grazie anche a te mamma, che mi accompagni sempre in ogni piccolo o grande passo che faccio, perchè la tua presenza nel mio cuore non mi ha mai abbandonato.

L'ultimo e più importante ringraziamento vorrei dedicarlo alla persona che più mi è stata vicina, mi ha dato forza e mi ha sopportato (e sopporterà ancora!) in questo percorso, Luca Zeni, e alla sua famiglia. Grazie per aver compreso l'importanza che riveste per me questa mia passione, e per avermi sostenuto e incoraggiato anche nei momenti in cui mi sembrava di non potercela fare, per tutto quello che hai fatto per aiutarmi a trovare il tempo da dedicare a questo lavoro di tesi.

Bibliography

Aharonian F., et al., 2007, ApJ, 664, L71 (Cited on page 8.)

Anders E., Grevesse N., 1989, GeCoA, 53, 197 (Cited on page 78.)

Antón S., Thean A., Browne I., Pedlar A., 2002, ASPC, 284, 289 (Cited on pages 83, 84 and 92.)

Akylas, A., Georgantopoulos, I., Griffiths, R. G., Papadakis, I. E., Mastichiadis, A., Warwick, R. S., Nandra, K., & Smith, D. A. 2002, MNRAS, 332, L23 (Cited on pages 4, 86, 100, 104 and 105.)

Aleksić J., et al., 2014, Sci, 346, 1080 (Cited on page 8.)

Alonso-Herrero A., Quillen A. C., Simpson C., Efstathiou A., Ward M. J., 2001, AJ, 121, 1369 (Cited on page 35.)

Anders E., Ebihara M., 1982, GeCoA, 46, 2363 (Not cited.)

Antón S., Thean A. H. C., Pedlar A., Browne I. W. A., 2002, MNRAS, 336, 319 (Cited on pages 83, 84 and 92.)

Antonucci, R. 1993, ARA&A, 31, 473 (Cited on pages 1, 25 and 44.)

Arnaud K. A., et al., 1985, MNRAS, 217, 105 (Cited on page 40.)

Arnaud, K. A. 1996, Astronomical Data Analysis Software and Systems V, 101, 17 (Cited on pages 90 and 137.)

Arp, H. C., & Madore, B. F. 1987, A Catalogue of Southern Peculiar Galaxies and Associations (Cambridge: Cambridge Univ. Press) (Cited on page 60.)

Awaki H., Ueno S., Taniguchi Y., Weaver K. A., 2000, ApJ, 542, 175 (Cited on pages 4, 104, 105, 109 and 112.)

Baldwin J. A., Phillips M. M., Terlevich R., 1981, PASP, 93, 5 (Cited on page 12.)

Ballantyne D. R., et al., 2014, ApJ, 794, 62 (Cited on page 43.)

Ballo L., et al., 2015, arXiv, arXiv:1505.02593 (Cited on page 3.)

Baloković M., et al., 2015, ApJ, 800, 62 (Cited on page 43.)

Balucinska-Church M., McCammon D., 1992, ApJ, 400, 699 (Cited on page 137.)

Barthelmy S. D., et al., 2005, SSRv, 120, 143 (Cited on pages 5, 131 and 133.)

Barvainis R., 1987, ApJ, 320, 537 (Cited on page 35.)

Baumgartner W. H., Tueller J., Markwardt C. B., Skinner G. K., Barthelmy S., Mushotzky R. F., Evans P. A., Gehrels N., 2013, ApJS, 207, 19 (Cited on pages 65, 83 and 89.)

Beckmann V., et al., 2009, A&A, 505, 417 (Cited on pages 16 and 43.)

Beckmann V., Shrader C. R., 2012, agn..book, (Not cited.)

Behar, E., Kaspi, S., Reeves, J., et al. 2010, ApJ, 712, 26 (Not cited.)

Bianchi, S., Guainazzi, M., Mattm, G., et al. 2005, A&A, 442, 185 (Cited on pages 3, 27 and 59.)

Bianchi, S., Piconcelli, E., Chiaberge, M., Bailòn, E. J., Matt, G., & Fiore, F. 2009, ApJ, 695, 781 (Cited on pages 3, 27, 29 and 59.)

Bicknell G. V., 1995, ApJS, 101, 29 (Cited on page 15.)

Blandford R. D., Znajek R. L., 1977, MNRAS, 179, 433 (Cited on page 9.)

Blandford R. D., 1993, AIPC, 280, 533 (Cited on page 25.)

Blustin A. J., Page M. J., Fuerst S. V., Branduardi-Raymont G., Ashton C. E., 2005, A&A, 431, 111 (Cited on pages 2, 40, 53, 54 and 55.)

Böhringer H., Matsushita K., Churazov E., Ikebe Y., Chen Y., 2002, A&A, 382, 804 (Cited on page 9.)

Boldt, E. 1987, Phys. Rep., 146, 215 (Cited on pages 65 and 88.)

Brightman, M. & Nandra, K. 2011, MNRAS, 413, 1206 (Cited on page 44.)

Braito, V., Reeves, J. N., Dewangan, G. C., George, I., Griffiths, R. E., Markowitz, A., Nandra, K., Porquet, D., Ptak, A., Turner, T. J., Yaqoob, T., & Weaver, K., 2007, ApJ, 670, 978 (Cited on pages 2, 55 and 77.)

Braito V., Ballo L., Reeves J. N., Risaliti G., Ptak A., Turner T. J., 2013, MNRAS, 428, 2516 (Cited on pages 27 and 28.)

Brenneman L. W., et al., 2014, ApJ, 788, 61 (Cited on page 43.)

Brinkman A., et al., 1998, sxmm.conf, 2 (Cited on pages 5 and 122.)

Brusa M., et al., 2003, A&A, 409, 65 (Cited on page 18.)

Burrows D. N., et al., 2005, SSRv, 120, 165 (Cited on pages 5, i and 134.)

Burtscher L., et al., 2013, A&A, 558, A149 (Cited on page 25.)

Caccianiga A., Marchã M. J. M., 2004, MNRAS, 348, 937 (Cited on page 18.)

Caccianiga A., Severgnini P., Della Ceca R., Maccacaro T., Carrera F. J., Page M. J., 2007, A&A, 470, 557 (Cited on page 16.)

Caccianiga A., et al., 2008, A&A, 477, 735 (Cited on page 5.)

Caccianiga A., Fanali R., Severgnini P., Della Ceca R., Marchese E., Mateos S., 2013, A&A, 549, A119

Cappi, M., Tombesi, F., Bianchi, S., et al. 2009, A&A, 504, 401 (Cited on page 5.)

Chartas G., Brandt W. N., Gallagher S. C., Garmire G. P., 2002, ApJ, 579, 169 (Cited on page 77.)

Chartas G., Brandt W. N., Gallagher S. C., 2003, ApJ, 595, 85 (Cited on pages 2 and 55.)

Chiaberge M., Capetti A., Celotti A., 2000, A&A, 355, 873 (Cited on pages 2 and 55.) (Not cited.)

Comastri A., Fiore F., Vignali C., Matt G., Perola G. C., La Franca F., 2001, MNRAS, 327, 781 (Cited on page 18.)

Corral A., Barcons X., Carrera F. J., Ceballos M. T., Mateos S., 2005, A&A, 431, 97 (Cited on page 18.)

Cusumano G., La Parola V., Segreto A., Ferrigno C., Maselli A., Sbarufatti B., Romano P., Chincarini G.,Giommi P., Masetti N., Moretti A., Parisi P., Tagliaferri G., 2010, A&A, 524, A64 (Cited on pages 65 and 68.)

Crenshaw D. M., Kraemer S. B., 1999, ASPC, 175, 341 (Not cited.)

Crenshaw D. M., Kraemer S. B., 2012, ApJ, 753, 75 (Cited on page 55.)

Dadina, M., Cappi, M., Malaguti, G., Ponti, G., & de Rosa, A. 2005, A&A, 442, 461 (Cited on page 77.)

Dadina, M. 2008, A&A, 485, 417 (Cited on pages 43, 71 and 92.)

Dauser T., et al., 2012, MNRAS, 422, 1914 (Cited on pages 2 and 55.)

Davis T. A., Bureau M., Cappellari M., Sarzi M., Blitz L., 2013, Natur, 494, 328 (Cited on page 8.)

Della Ceca, R., Ballo, L., Tavecchio, F., et al. 2002, ApJ, 581, L9 (Cited on page 68.)

Della Ceca R., et al., 2004, A&A, 428, 383 (Cited on page 5.)

Della Ceca R., et al., 2008, A&A, 487, 119 (Cited on pages 16 and 36.)

den Herder, J. W., et al. 2001, A&A, 365, L7 (Cited on page 122.)

de Vaucouleurs, G., de Vaucouleurs, A., Corwin, H., Buta, R. J., Paturel, G., & Fouqu, P. 1991, Third Reference Catalogue of Bright Galaxies (Berlin: Springer) (Cited on page 83.)

Dickey, J. M., & Lockman, F. J. 1990, ARA&A, 28, 215 (Cited on page 69.)

Di Matteo T., Springel V., Hernquist L., 2005, Natur, 433, 604 (Cited on page 9.)

Done C., 2010, arXiv, arXiv:1008.2287 (Not cited.)

Dunlop J. S., McLure R. J., Kukula M. J., Baum S. A., O'Dea C. P., Hughes D. H., 2003, MNRAS, 340, 1095 (Cited on page 16.)

Ehle, M., et al. 2001, XMM-*Newton* Users' Handbook (Cited on page 66.)

Elitzur M., 2007, ASPC, 373, 415 (Cited on pages 2 and 36.)

Elitzur M., 2008, NewAR, 52, 274 (Cited on pages 36 and 108.)

Elitzur M., Ho L. C., 2009, ApJ, 701, L91 (Cited on page 37.)

Elitzur M., 2012, ApJ, 747, L33 (Cited on pages 36, 37 and 108.)

Elvis M., 2000, ApJ, 545, 63 (Cited on pages 3, 2, 31, 32, 34 and 58.)

Elvis, M., Risaliti, G., Nicastro, F., Miller, J. M., Fiore, F., & Puccetti, S. 2004, ApJ, 615, L25 (Cited on pages 3, 27, 38 and 59.)

Elvis M., 2004, ASPC, 311, 109 (Cited on page 31.)

Fabian A. C., 1999, MNRAS, 308, L39 (Cited on pages 9 and 40.)

Fabian A. C., Iwasawa K., Reynolds C. S., Young A. J., 2000, PASP, 112, 1145 (Cited on pages 46, 48, 49, 50 and 51.)

Fabian A. C., Wilman R. J., Crawford C. S., 2002, MNRAS, 329, L18 (Cited on page 9.)

Fabian A. C., 2006, ESASP, 604, 463 (Cited on page 41.)

Fabian A. C., 2012, ARA&A, 50, 455 (Cited on page 9.)

Fanali R., Caccianiga A., Severgnini P., Della Ceca R., Marchese E., Carrera F. J., Corral A., Mateos S., 2013, MNRAS, 433, 648 (Cited on page 5.)

Fanali R., Caccianiga A., Severgnini P., Della Ceca R., Dotti M., Marchese E., 2013, MmSAI, 84, 717 (Cited on page 5.)

Fanaroff B. L., Riley J. M., 1974, MNRAS, 167, 31P (Cited on page 15.)

Fath E. A., 1909, LicOB, 5, 71 (Cited on page 10.)

Ferrarese L., Merritt D., 2000, ApJ, 539, L9 (Cited on pages 1, 8 and 9.)

Feruglio C., et al., 2015, arXiv, arXiv:1503.01481 (Cited on page 57.)

Francis P. J., Hewett P. C., Foltz C. B., Chaffee F. H., Weymann R. J., Morris S. L., 1991, ApJ, 373, 465 Symposium, 267, 341 (Cited on pages 11 and 81.)

Fukazawa Y., et al., 2009, PASJ, 61, 17 (Cited on page 88.)

Garcet O., et al., 2007, A&A, 474, 473 (Cited on pages 16 and 18.)

Gaskell C. M., 2009, NewAR, 53, 140 (Cited on page 38.)

Gebhardt K., et al., 2000, ApJ, 539, L13 (Cited on pages 1 and 9.)

Genzel R., Eisenhauer F., Gillessen S., 2010, RvMP, 82, 3121 (Cited on page 8.)

Gruber, D. E., Matteson, J. L., Peterson, L. E., & Jung, G. V. 1999, ApJ, 520, 124 (Cited on pages 65 and 88.)

Gehrels, N., Chincarini, G., Giommi, P., et al. 2004, ApJ, 611, 1005 (Cited on pages 5, 65, 89, 131 and 132.)

George I. M., Fabian A. C., 1991, MNRAS, 249, 352 (Cited on page 39.)

George I. M., Turner T. J., Yaqoob T., Netzer H., Laor A., Mushotzky R. F., Nandra K., Takahashi T., 2000, ApJ, 531, 52 (Cited on page 40.)

Ghisellini G., Haardt F., Matt G., 1994, MNRAS, 267, 743 (Cited on page 92.)

Ghisellini G., Celotti A., 2001, A&A, 379, L1 (Cited on pages 15 and 27.)

Ghisellini, G., Haardt, F., & Matt, G. 2004, A&A, 413, 535 (Cited on pages 76 and 77.)

Giacconi R., et al., 1979, ApJ, 230, 540 (Cited on page 42.)

Gierliński M., Done C., 2004, MNRAS, 349, L7 (Cited on page 40.)

Lobban A. P., Reeves J. N., Miller L., Turner T. J., Braito V., Kraemer S. B., Crenshaw D. M., 2011, MNRAS, 414, 1965 (Cited on pages 2 and 55.)

Gofford J., et al., 2011, MNRAS, 414, 3307 (Cited on pages 2 and 55.)

Gofford J., Reeves J. N., Tombesi F., Braito V., Turner T. J., Miller L., Cappi M., 2013, MNRAS, 430, 60 (Cited on pages 2 and 55.)

Gruber, D. E., Matteson, J. L., Peterson, L. E., & Jung, G. V. 1999, ApJ, 520, 124 (Cited on pages 65 and 88.)

Grupe D., 1996, PhDT (Cited on page 19.)

Grupe D., Mathur S., 2004, ApJ, 606, L41 (Cited on page 19.)

Grupe D., 2004, AJ, 127, 1799 (Cited on page 19.)

Guainazzi M., Bianchi S., de La Calle Pérez I., Dovčiak M., Longinotti A. L., 2011, A&A, 531, A131 (Cited on page 90.)

Guilbert P. W., Rees M. J., 1988, MNRAS, 233, 475 (Cited on page 39.)

Haardt F., Maraschi L., 1991, ApJ, 380, L51 (Cited on page 43.)

Haardt F., Maraschi L., 1993, ApJ, 413, 507 (Cited on page 43.)

Halpern J. P., 1984, ApJ, 281, 90 (Cited on pages 40, 42 and 53.)

Harrison F. A., et al., 2013, ApJ, 770, 103 (Cited on pages 30 and 43.)

Herrnstein J. R., 1999, AAS, 31, 921 (Cited on page 8.)

Holt S. S., Mushotzky R. F., Boldt E. A., Serlemitsos P. J., Becker R. H., Szymkowiak A. E., White N. E., 1980, ApJ, 241, L13 (Cited on page 40.)

Horst H., Smette A., Gandhi P., Duschl W. J., 2006, A&A, 457, L17 (Cited on pages 2, 35 and 108.)

Hopkins P. F., Elvis M., 2010, MNRAS, 401, 7 (Cited on page 55.)

Ishibashi W., Fabian A. C., 2012, MNRAS, 427, 2998 (Cited on page 9.)

Jaffe W., et al., 2004, Natur, 429, 47 (Cited on page 25.)

Jansen, F., et al. 2001, A&A, 365, L1 (Cited on page 117.)

Jefremov P. I., Tsupko O. Y., Bisnovatyi-Kogan G. S., 2015, arXiv, arXiv:1503.07060 (Cited on page 23.)

Johansson, L. 1988, A&A, 191, 29 (Cited on pages 60, 61, 63, 64 and 67.)

Junkkarinen V. T., Burbidge E. M., Smith H. E., 1983, ApJ, 265, 51 (Cited on page 31.)

Kaastra, J. S., Mewe, R., Liedahl, D. A., Komossa, S., and Brinkman, A. C. 2000, A&A 354, L83 (Cited on pages 2 and 53.)

Kaastra J. S., et al., 2014, Sci, 345, 64 (Cited on page 53.)

Kalberla P. M. W., Burton W. B., Hartmann D., Arnal E. M., Bajaja E., Morras R., Pöppel W. G. L., 2005, A&A, 440, 775 (Cited on page 90.)

Kallman T. R., Palmeri P., Bautista M. A., Mendoza C., Krolik J. H., 2004, ApJS, 155, 675 (Cited on pages 77, 95 and 139.)

Kaspi S., Brandt W. N., Netzer H., Sambruna R., Chartas G., Garmire G. P., Nousek J. A., 2000, ApJ, 535, L17 (Cited on pages 2 and 53.)

Kaspi, S., Brandt, W. N., Netzer, H., et al. 2001, ApJ, 554, 216 (Cited on page 53.)

Kaspi, S., Brandt, W. N., George, I. M., et al. 2002, ApJ, 574, 643 (Cited on page 53.)

Kaspi, S., Maoz, D., Netzer, H., et al. 2005, ApJ, 629, 61 (Cited on page 81.)

Kazanas D., Fukumura K., Behar E., Contopoulos I., 2012, ASPC, 460, 181 (Cited on page 58.)

Kellermann K. I., Sramek R., Schmidt M., Shaffer D. B., Green R., 1989, AJ, 98, 1195 (Cited on page 15.)

Kennicutt R. C., Jr., 1983, ApJ, 272, 54 (Cited on page 67.)

Khachikian, E. Y., & Weedman, D. W. 1974, ApJ, 192, 581 (Cited on pages 12 and 83.)

King A., 2003, ApJ, 596, L27 (Cited on page 9.)

King A., 2005, ApJ, 635, L121 (Cited on page 9.)

King A., Pounds K., 2015, arXiv, arXiv:1503.05206 (Cited on page 9.)

Kokubun, M., et al. 2007, PASJ, 59, 53 (Cited on pages 5, 65, 88 and 129.)

Kollatschny W., 2003, PYunO, 95, 32 (Cited on page 24.)

Kormendy J., Richstone D., 1995, ARA&A, 33, 581 (Cited on pages 1 and 8.)

Koyama, K., Tsunemi, H., Dotani, T., et al. 2007, PASJ, 59, 23 (Cited on pages 61, 126 and 127.)

Krolik J. H., Kriss G. A., 2001, ApJ, 561, 684 (Cited on page 54.)

Krolik, J. H. & Begelman, M. C. 1988, ApJ, 329, 702 97, 146 (Cited on page 35.)

Krongold,Y., Nicastro, F., Brickhouse,N. S., et al. 2003, ApJ, 597, 832 (Cited on page 53.)

Laha S., Guainazzi M., Dewangan G. C., Chakravorty S., Kembhavi A. K., 2014, MNRAS, 441, 2613 (Cited on page 58.)

Laing R. A., Bridle A. H., 1987, MNRAS, 228, 557 (Cited on page 17.)

Laor A., 1991, ApJ, 376, 90 (Cited on page 95.)

Laor A., Fiore F., Elvis M., Wilkes B. J., McDowell J. C., 1997, ApJ, 477, 93 (Cited on page 40.)

Laor A., 2003, ApJ, 590, 86 (Cited on pages 19, 37 and 38.)

Lawrence, A. 1991, MNRAS, 252, 586 33, 59, 146 (Cited on pages 2, 36 and 37.)

Levenson N. A., Heckman T. M., Krolik J. H., Weaver K. A., Zycki P. T., 2006, ApJ, 648, 111 (Cited on page 46.)

Lightman A. P., White T. R., 1988, ApJ, 335, 57 (Cited on page 39.)

Lutz D., Maiolino R., Spoon H. W. W., Moorwood A. F. M., 2004, A&A, 418, 465 (Cited on pages 2, 35 and 108.)

Lobban, A. P., Reeves, J. N., Miller, L., et al. 2011, MNRAS, 414, 1965 (Cited on pages 3, 27 and 59.)

Lusso E., et al., 2013, ApJ, 777, 86 (Cited on pages 2 and 36.)

Magdziarz, P., & Zdziarski, A. A. 1995, MNRAS, 273, 837 (Cited on pages 44, 71, 86, 92 and 138.)

Magdziarz P., Blaes O. M., Zdziarski A. A., Johnson W. N., Smith D. A., 1998, MNRAS, 301, 179 (Cited on page 40.)

Magorrian J., et al., 1998, AJ, 115, 2285 (Cited on page 8.)

Maiolino R., Risaliti G., 2007, ASPC, 373, 447 (Cited on page 36.)

Malizia A., Stephen J. B., Bassani L., Bird A. J., Panessa F., Ubertini P., 2010, arXiv, arXiv:1002.4712 (Cited on page 16.)

Malizia A., Molina M., Bassani L., Stephen J. B., Bazzano A., Ubertini P., Bird A. J., 2014, ApJ, 782, L25 (Cited on page 43.)

Marcha M. J. M., Browne I. W. A., Impey C. D., Smith P. S., 1996, MNRAS, 281, 425 (Cited on pages 4, 83 and 85.)

Marchese E., Della Ceca R., Caccianiga A., Corral A., Severgnini P., 2010, AIPC, 1248, 467 (Cited on pages 5 and 43.)

Marchese E., Braito V., Della Ceca R., Caccianiga A., Severgnini P., 2012, MNRAS, 421, 1803 (Cited on page 60.)

Marchese E., et al., 2014, MNRAS, 437, 2806 (Cited on pages 5, 60 and 87.)

Marconi A., Hunt L. K., 2003, ApJ, 589, L21 (Cited on pages 1 and 9.)

Marinucci A., et al., 2014, MNRAS, 440, 2347 (Cited on page 43.)

Marinucci A., et al., 2015, MNRAS, 447, 160 (Cited on page 43.)

Markowitz A., Krumpe M., Nikutta R., 2013, HEAD, 13, #108.10 (Cited on page 105.)

Markowitz A. G., Krumpe M., Nikutta R., 2014, MNRAS, 439, 1403 (Cited on pages 3 and 115.)

Mason K. O., et al., 2001, A&A, 365, L36 (Cited on page 117.)

Masetti N., et al., 2006, A&A, 448, 547 (Not cited.)

Masetti N., et al., 2008, A&A, 482, 113 (Cited on page 13.)

Mateos S. et al., 2008, A&A, 492, 51 (Cited on page 68.)

Matt G., Fabian A. C., Ross R. R., 1993, MNRAS, 264, 839 (Cited on page 50.)

Matt G., Brandt W. N., Fabian A. C., 1996, MNRAS, 280, 823 (Cited on pages 16, 50 and 92.)

Matt G., Guainazzi M., Maiolino R., 2003, MNRAS, 342, 422 (Cited on page 18.)

Matt G., et al., 2014, MNRAS, 439, 3016 (Cited on page 43.)

Matt G., et al., 2015, MNRAS, 447, 3029 (Cited on page 43.)

McKernan B., Yaqoob T., Reynolds C. S., 2007, MNRAS, 379, 1359 (Cited on page 55.)

Meier D. L., 1999, ApJ, 522, 753 (Cited on page 15.)

Mewe, R., Gronenschild, E.H.B.M., and van den Oord, G.H.J. 1985,A&AS, 62, 197 (Cited on pages 69 and 92.)

Miller, J. S. & Goodrich, R. W. 1990, ApJ, 355, 456 (Cited on page 83.)

Miniutti G., et al., 2007, PASJ, 59, 315 (Cited on page 53.)

Mitsuda, K., et al. 2007, PASJ, 59, 1 (Cited on pages 5, 61, 88 and 126.)

Molina M., et al., 2009, MNRAS, 399, 1293 (Cited on page 43.)

Morrison, R. & McCammon, D. 1983, ApJ, 270, 119 (Cited on page 137.)

Murphy, K. D., Yaqoob, T., & Terashima, Y. 2007, ApJ, 666, 96 (Cited on page 59.)

Murphy, K. D., & Yaqoob, T. 2009, MNRAS, 397, 1549 (Cited on pages 44, 46, 47, 78 and 81.)

Murphy K. D., Yaqoob T., 2011, MNRAS, 415, 3962 (Cited on page 92.)

Murray N., Quataert E., Thompson T. A., 2005, ApJ, 618, 569 (Cited on page 9.)

Nandra K., George I. M., Mushotzky R. F., Turner T. J., Yaqoob T., 1997a, ApJ, 477, 602 (Cited on page 46.)

Nandra K., George I. M., Mushotzky R. F., Turner T. J., Yaqoob T., 1997b, ApJ, 488, L91 (Cited on page 46.)

Nandra K., O'Neill P. M., George I. M., Reeves J. N., 2007, MNRAS, 382, 194 (Cited on pages 92 and 139.)

Nardini E., et al., 2015, Sci, 347, 860 (Cited on page 57.)

Narayan R., Yi I., 1995, ApJ, 452, 710 (Cited on page 16.)

Netzer H., 1990, agn..conf, 57 (Cited on pages 7, 24 and 25.)

Netzer H., Laor A., 1993, ApJ, 404, L51 (Cited on page 37.)

Netzer H., Turner T. J., George I. M., 1998, ApJ, 504, 680 (Cited on page 109.)

Netzer, H., Kaspi, S., Behar, E., et al. 2003, ApJ, 599, 933 (Cited on page 53.)

Neff S. G., de Bruyn A. G., 1984, IAUS, 110, 263 (Cited on page 86.)

Nenkova M., Ivezić Ž., Elitzur M., 2002, ApJ, 570, L9 (Cited on page 36.)

Nenkova M., Sirocky M. M., Nikutta R., Ivezić Ž., Elitzur M., 2008, ApJ, 685, 160 (Cited on pages 35, 36 and 108.)

Nenkova M., Sirocky M. M., Ivezić Ž., Elitzur M., 2008, ApJ, 685, 147 (Cited on pages 35, 36 and 108.)

Nicastro F., 2000, ApJ, 530, L65 (Cited on pages 37 and 38.)

Nikolajuk M., Papadakis I. E., Czerny B., 2004, MNRAS, 350, L26 (Cited on page 107.)

Noguchi K., Terashima Y., Ishino Y., Hashimoto Y., Koss M., Ueda Y., Awaki H., 2010, ApJ, 711, 144 (Cited on page 71.)

Oliva E., Origlia L., Maiolino R., Moorwood A. F. M., 1999, A&A, 350, 9 (Cited on page 35.)

Osterbrock D. E., Ferland G. J., 2006, agna.book, (Cited on page 10.)

Page M. J., et al., 2006, MNRAS, 369, 156 (Cited on page 16.)

Palmeri, P., Mendoza, C., Kallman, T. R., Bautista, M. A., & Meléndez, M. 2003, A&A, 410, 359 (Cited on pages 71, 92 and 98.)

Persic M., Rephaeli Y., 2007, A&A, 463, 481 (Cited on page 67.)

Peterson B. M., 1997, iagn.book, (Cited on page 14.)

Peterson B. M., 1998, AdSpR, 21, 57 (Cited on page 24.)

Peterson B. M., et al., 2000, ApJ, 542, 161 (Cited on page 19.)

Petrucci P. O., et al., 2001, ASPC, 234, 445 (Cited on page 43.)

Piconcelli E., Jimenez-Bailón E., Guainazzi M., Schartel N., Rodríguez-Pascual P. M., Santos-Lleó M., 2005, A&A, 432, 15 (Cited on page 53.)

Pounds K. A., Reeves J. N., King A. R., Page K. L., O'Brien P. T., Turner M. J. L., 2003, MNRAS, 345, 705 (Cited on pages 2 and 55.)

Pounds, K. A., Reeves, J. N., Page, K. L., & O'Brien, P. T. 2004, ApJ, 616, 696 (Cited on pages 3, 27 and 59.)

Ponti G., et al., 2010, MNRAS, 406, 2591 (Cited on page 40.)

Ponti G., Morris M. R., Terrier R., Goldwurm A., 2013, ASSP, 34, 331 (Cited on page 47.)

Pravdo S. H., Nugent J. J., Nousek J. A., Jensen K., Wilson A. S., Becker R. H., 1981, ApJ, 251, 501 (Cited on page 40.)

Predehl P., Schmidt J., 1995, A&A, 293, 889 (Cited on page 115.)

Proga, D., & Kallman, T. R. 2004, ApJ, 616, 688 (Cited on pages 54, 76 and 77.)

Puccetti, S., Fiore, F., Risaliti, G., Capalbi, M., Elvis, M., & Nicastro, F. 2007, MNRAS, 377, 607 (Cited on pages 3, 27 and 59.)

Ranalli P., Comastri A., Setti G., 2003, A&A, 399, 39 (Cited on page 67.)

Reeves J. N., 2003, in Collin S., Combes F., Shlosman I., eds, ASP Conf. Ser. Vol. 290, Active Galactic Nuclei: from Central Engine to Host Galaxy. Astron. Soc. Pac., San Francisco, p. 35 (Cited on page 46.)

Reeves J. N., Sambruna R. M., Braito V., Eracleous M., 2009, ApJ, 702, L187 (Cited on pages 2 and 55.)

Reeves J. N., Porquet D., Braito V., Gofford J., Nardini E., Turner T. J., Crenshaw D. M., Kraemer S. B., 2013, ApJ, 776, 99 (Cited on pages 53 and 56.)

Reynolds C. S., 1997, ASPC, 128, 173 (Cited on page 40.)

Risaliti, G., Elvis, M., & Nicastro, F. 2002, ApJ, 571, 234 (Cited on pages 3, 2, 27, 34, 35, 37 and 59.)

Risaliti G., Elvis M., 2004, ASSL, 308, 187 (Cited on page 19.)

Risaliti, G., Elvis, M., Fabbiano, G., Baldi, A., & Zezas, A. 2005, ApJ, 623, L93 (Cited on pages 3, 27, 28, 59 and 77.)

Risaliti, G., Elvis, M., Fabbiano, G., Baldi, A., Zezas, A., & Salvati, M. 2007, ApJ, 659, L111 (Cited on pages 3, 27, 28 and 59.)

Risaliti, G., et al. 2009, ApJ, 696, 160 (Cited on pages 3, 27 and 59.)

Risaliti G., et al., 2009, MNRAS, 393, L1 (Cited on pages 3, 27, 28 and 59.)

Risaliti, G. 2010, in American Institute of Physics Conference Series, Vol. 1248, American Institute of Physics Conference Series, ed. A. Comastri, L. Angelini, & M. Cappi, 351-354 (Not cited.)

Risaliti G., Elvis M., Bianchi S., Matt G., 2010, MNRAS, 406, L20 (Cited on pages 3, 27 and 59.)

Roming P. W. A., et al., 2005, SSRv, 120, 95 (Cited on pages 5, 133 and 135.)

Ross R. R., Fabian A. C., 2005, MNRAS, 358, 211 (Cited on page 139.)

Ryan R. E., Jr., Cohen S. H., Windhorst R. A., Silk J., 2008, ApJ, 678, 751 (Cited on page 3.)

Sbarufatti B., Ciprini S., Kotilainen J., Decarli R., Treves A., Veronesi A., Falomo R., 2009, AJ, 137, 337 (Cited on page 21.)

Schmidt M., 1963, Natur, 197, 1040 (Cited on page 11.)

Schmidt M., Green R. F., 1983, ApJ, 269, 352 (Cited on pages 10 and 11.)

Seyfert C. K., 1943, ApJ, 97, 28 (Cited on page 10.)

Serlemitsos P. J., et al., 2007, PASJ, 59, 9 (Cited on page 126.)

Shakura N. I., Sunyaev R. A., 1973, A&A, 24, 337 (Cited on pages 23 and 43.)

Shuder J. M., Osterbrock D. E., 1981, ApJ, 250, 55 (Cited on page 19.)

Sim, S. A., Proga, D., Miller, L., Long, K. S., & Turner, T. J. 2010, MNRAS, 408, 1396 (Cited on pages 76 and 77.)

Simkin S. M., van Gorkom J., Hibbard J., Su H.-J., 1987, Sci, 235, 1367 (Cited on page 83.)

Simpson, C. 2005, MNRAS, 360, 565 147, 204 (Cited on pages 2, 36 and 37.)

Singh K. P., Garmire G. P., Nousek J., 1985, ApJ, 297, 633 (Cited on page 40.)

Singh V., Shastri P., Risaliti G., 2011, A&A, 532, A84 (Cited on pages 86, 90, 95 and 100.)

Smith, D. A., Georgantopoulos , I., Warwick, R. S., 2001, ApJ, 550, 635 (Cited on pages 86, 100, 105, 108 and 109.)

Smith E. P., Heckman T. M., 1990, ApJ, 348, 38 (Cited on page 15.)

Springel V., Di Matteo T., Hernquist L., 2005, MNRAS, 361, 776 (Cited on page 9.)

Stiavelli, M., Panagia, N., Carollo, M.C., Romaniello, M., Heyer, I., Gonzaga, S. 1998, ApJ 492, L135 (Cited on page 60.)

Storchi-Bergmann T., Mulchaey J. S., Wilson A. S., 1992, ApJ, 395, L73 (Cited on page 35.)

Strüder, L., et al. 2001, A&A, 365, L5 (Cited on page 66.)

Suganuma M., et al., 2006, ApJ, 639, 46 (Cited on page 37.)

Takahashi, T., et al. 2007, PASJ, 59, 35 (Cited on pages 61 and 126.)

Tombesi F., Cappi M., Reeves J. N., Palumbo G. G. C., Yaqoob T., Braito V., Dadina M., 2010, A&A, 521, 57 (Cited on pages 2, 55, 58, 76 and 77.)

Tombesi F., Cappi M., Reeves J. N., Palumbo G. G. C., Braito V., Dadina M., 2011, ApJ accepted (Cited on pages 76 and 77.)

Tombesi F., Cappi M., Reeves J. N., Nemmen R. S., Braito V., Gaspari M., Reynolds C. S., 2012, arXiv, arXiv:1212.4851 (Cited on page 58.)

Tombesi F., Cappi M., Reeves J. N., Nemmen R. S., Braito V., Gaspari M., Reynolds C. S., 2013, MNRAS, 430, 1102 (Cited on pages 55 and 57.)

Tombesi F., Cappi M., 2014, MNRAS, 443, L104 (Cited on page 58.)

Tombesi F., Meléndez M., Veilleux S., Reeves J. N., González-Alfonso E., Reynolds C. S., 2015, Natur, 519, 436 (Cited on page 57.)

Tremaine S., et al., 2002, ApJ, 574, 740 (Cited on pages 1 and 9.)

Turner, M., et al. 2001, A&A, 365, L27 (Cited on pages 66 and 119.)

Turnshek D. A., 1998, semi.conf, 263 (Cited on page 31.)

Torricelli-Ciamponi G., Pietrini P., Risaliti G., Salvati M., 2014, MNRAS, 442, 2116 (Cited on pages 3 and 115.)

Trump J. R., et al., 2006, ApJS, 165, 1 (Cited on page 31.)

Unger S. W., Pedlar A., Neff S. G., de Bruyn A. G., 1984, MNRAS, 209, 15P (Cited on page 83.)

Urry, C. M., & Padovani, P. 1995, PASP, 107, 803 (Cited on pages 15 and 26.)

Uttley, P., Taylor, R. D., McHardy, I. M., et al. 2004, MNRAS, 347, 1345 (Cited on pages 3, 27 and 59.)

Vasudevan R. V., Mushotzky R. F., Reynolds C. S., Fabian A. C., Lohfink A. M., Zoghbi A., Gallo L. C., Walton D., 2014, ApJ, 785, 30 (Cited on page 40.)

Véron-Cetty M.-P., Véron P., 2001, A&A, 374, 92 (Cited on page 60.)

Walsh J. L., van den Bosch R. C. E., Barth A. J., Sarzi M., 2012, ApJ, 753, 79 (Cited on page 8.)

Walton D., Risaliti G., Harrison F., NuSTAR Team, 2014, xru..conf, 203 (Cited on page 30.)

Warwick, R. S., Koyama, K., Inoue, H., Takano, S., Awaki, H., & Hoshi, R. 1989, PASJ, 41, 739 (Cited on page 86.)

Weaver, K. A., Nousek, J., Yaqoob, T., et al. 1996, ApJ, 458, 160 (Cited on page 59.)

Weedman D. W., 1977, ARA&A, 15, 69 (Cited on page 10.)

Weymann R. J., Morris S. L., Foltz C. B., Hewett P. C., 1991, ApJ, 373, 23 (Cited on page 31.)

Williams R. J., Mathur S., Pogge R. W., 2004, ApJ, 610, 737 (Cited on page 19.)

Wilms, J., Allen, A., & McCray, R. 2000, ApJ, 542, 914 (Cited on page 105.)

Woo J.-H., Urry C. M., 2002, ApJ, 579, 530 (Cited on page 107.)

Xu C., Livio M., Baum S., 1999, AJ, 118, 1169 (Cited on page 86.)

Yan M., Sadeghpour H. R., Dalgarno A., 1998, ApJ, 496, 1044 (Cited on page 137.)

Yaqoob, T. 1997, ApJ, 479, 184 (Cited on page 138.)

Yaqoob T., Padmanabhan U., 2004, ApJ, 604, 63 (Cited on page 46.)

Young A. J., Lee J. C., Fabian A. C., Reynolds C. S., Gibson R. R., Canizares C. R., 2005, ApJ, 631, 733 (Cited on page 53.)

A&A 549, A119 (2013)
DOI: 10.1051/0004-6361/201220343
© ESO 2013

Astronomy & Astrophysics

Black-hole masses of type 1 AGN in the *XMM-Newton* bright serendipitous survey⋆,⋆⋆

A. Caccianiga[1], R. Fanali[1,2], P. Severgnini[1], R. Della Ceca[1], E. Marchese[1], and S. Mateos[3,4]

[1] INAF - Osservatorio Astronomico di Brera, via Brera 28, 20121 Milan, Italy
e-mail: alessandro.caccianiga@brera.inaf.it
[2] Dipartimento di Fisica, Universitá degli Studi di Milano-Bicocca, Piazza Della Scienza 3, 20126 Milano, Italy
[3] Instituto de Física de Cantabria (CSIC-UC), Avenida de los Castros, 39005 Santander, Spain
[4] X-ray & Observational Astronomy Group, Department of Physics and Astronomy, Leicester University, Leicester LE1 7RH, UK

Received 6 September 2012 / Accepted 15 November 2012

ABSTRACT

Aims. We derive masses of the central supermassive black hole (SMBH) and accretion rates for 154 type 1 AGN belonging to a well-defined X-ray-selected sample, the *XMM-Newton* serendipitous sample (XBS).
Methods. We used the most recent "single-epoch" relations, based on Hβ and MgIIλ2798 Å emission lines, to derive the SMBH masses. We then used the bolometric luminosities, computed on the basis of an SED-fitting procedure, to calculate the accretion rates, both absolute and normalized to the Eddington luminosity (Eddington ratio).
Results. The selected AGNs cover a range of masses from 10^7 to 10^{10} $M_\odot$ with a peak around 8×10^8 $M_\odot$ and a range of accretion rates from 0.01 to ∼50 $M_\odot$/year (assuming an efficiency of 0.1), with a peak at ∼1 $M_\odot$/year. The values of Eddington ratio range from 0.001 to ∼0.5 and peak at 0.1.

Key words. galaxies: active – galaxies: nuclei – X-rays: galaxies – surveys

1. introduction

The nuclear activity of an active galactic nucleus (AGN) is powered by the accretion of matter into the gravitational well of the central supermassive black hole (SMBH). It has now become clear that the majority of galaxies host an SMBH and that they must have experienced an activity phase during their lifetime (see Merloni & Heinz 2012 for a review). Much observational evidence, like the SMBH mass-bulge relations (e.g. Magorrian et al. 1998; Gültekin et al. 2009), strongly suggest that this activity phase must have played a critical role in galaxy evolution. For these reasons, a better understanding of the accretion mechanism represents a fundamental step not only in improving our knowledge of the AGN physics, but also for general comprehension of the galaxy formation and evolution.

X-rays offer a direct probe of the accretion mechanism since they are produced in the very inner part of the nucleus through a (still poorly understood) mechanism that probably involves the electrons in a "hot" corona and the UV photons produced within the accretion disk (e.g. Haardt & Maraschi 1991, 1993), thus carrying direct information on the physics very close to the SMBH. The highly penetrating capability of X-rays often makes them the only tool for gathering direct information on the nuclear activity when the disk emission, peaked in the UV part of the spectrum, is absorbed and unobservable.

While X-ray observations of single sources can shed light on the complexity of the emission at these energies, a statistical approach based on large samples offers the unique opportunity of studying the link between hot corona and the phenomenon of accretion on the central SMBH (e.g. see Young et al. 2010; Vasudevan & Fabian 2009; Grupe et al. 2010; Lusso et al. 2012, and references therein). To this end, statistically complete and well-defined samples of AGNs equipped with X-ray spectral data and with a reliable estimate of the accretion parameters (SMBH mass, the absolute accretion rate, the accretion rate normalized to the Eddington limit) are required.

The recent availability of statistical relations (see Vestergaard 2009 for a review) that allow the systematic computation of the black-hole mass on large numbers of AGN has made it possible to estimate black-hole masses for very large samples of AGNs (usually optically selected): for instance, the last release of the SDSS QSO catalogue contains a mass estimate for more than 100 000 AGNs (Shen et al. 2011). In spite of these large numbers, the samples that contain information on both black-hole masses and X-ray spectra are significantly smaller. In particular, if we restrict attention to the hard X-ray energies (above 2 keV), where the primary X-ray emission is best observed and studied, the largest samples available for this kind of study contain a few hundred objects at most. The largest samples are often built using X-ray data from the *XMM-Newton* archive combined with optical data that come from SDSS (Risaliti et al. 2009; Vagnetti et al. 2010), from the literature (Bianchi et al. 2009) or from dedicated observations (Lusso et al. 2012; Grupe et al. 2010). A major problem affecting many samples is that they are often just a collection of sources available in both an X-ray and an optical

⋆ Based on observations collected at the Telescopio Nazionale Galileo (TNG) and at the European Southern Observatory (ESO), La Silla, Chile and on observations obtained with *XMM-Newton*, an ESA science mission with instruments and contributions directly funded by ESA Member States and the USA (NASA).
⋆⋆ Table 1 is available in electronic form at http://www.aanda.org

catalogue so they do not necessarily represent a statistically complete and representative sample of AGNs.

To limit the possible biases deriving from this kind of selection, we present here a new data set containing black-hole masses and accretion rates (both absolute and normalized to the Eddington limit) for a well-defined flux-limited sample of X-ray sources selected from *XMM-Newton*, the Bright Serendipitous Survey (XBS[1], Della Ceca et al. 2004; Caccianiga et al. 2008). The XBS is now almost completely identified (>98%) after ten years of dedicated spectroscopic observations, and it contains, by definition, *XMM-Newton* data of medium/good quality (from 100 to 10^4 net counts) that has allowed systematic X-ray spectral analysis for all the selected AGN (Corral et al. 2011). For most of the type 1 AGN contained in this sample, the optical/UV spectral energy distribution has been studied and a reliable estimate (i.e. not based on a bolometric correction) of the bolometric luminosity has already been published (Marchese et al. 2012). In this paper we present the estimate of the black-hole masses, using the single-epoch method. In a companion paper we will use these values, combined with the results of the X-ray analysis, to study the statistical relationship between X-ray properties and the accretion rate on the central SMBH (Fanali et al., in prep.).

The structure of the paper is the following. In Sect. 2 we briefly describe the XBS sample while in Sects. 3 and 4 we present the derivation of black-hole masses and accretion rates, respectively. In Sect. 5 we discuss how the presence of the radiation pressure can change the derived quantities, and in Sect. 6 we summarize results and conclusions.

We assume a flat ΛCDM cosmology with $H_0 = 65$, $\Omega_\Lambda = 0.7$ and $\Omega_M = 0.3$.

2. The XBS sample of type 1 AGN

The XBS (Della Ceca et al. 2004; Caccianiga et al. 2008) is a wide-angle (28 sq. deg), high Galactic latitude ($|b| > 20$ deg) survey based on the *XMM-Newton* archival data. It is composed of two samples that are both flux-limited ($\sim 7 \times 10^{-14}$ erg s^{-1} cm^{-2}) in two separate energy bands: the 0.5−4.5 keV band (the BSS sample) and the 4.5−7.5 keV band (the "hard" HBSS sample). A total of 400 sources have been selected, 389 belonging to the BSS sample and 67 to the HBSS sample (56 sources are in common). Selection criteria and the general properties of the 400 objects are discussed in Della Ceca et al. (2004).

To date, the spectroscopic identification has nearly been completed, and 98% of the 400 sources have been spectroscopicaly observed and classified. The details of the classification process are presented in Caccianiga et al. (2007, 2008). In this paper we want to derive the mass of the central SMBH for the type 1 AGNs. In total, the XBS contains 276 type 1 AGN but we have computed the M_{BH} only for the sub-sample of sources that was studied by Marchese et al. (2012) in order to have a reliable estimate of the bolometric luminosity. The sub-sample considered by Marchese et al. contains the type 1 AGN that fall in the area of sky surveyed by GALEX (Martin et al. 2005; Morrissey et al. 2007), therefore it can be considered as representative of the entire XBS sample of type 1 AGN. We have then excluded a few sources whose optical spectrum is either not available or without broad emission lines required to compute the BH mass, leaving us with a total of 154 AGNs. In Fig. 1, we compare the redshift distribution of the 154 type 1 AGN studied here and of the total XBS sample of 276 type 1 AGN. The two distributions are similar, as demonstrated by a KS test (KS probability of 98.6%).

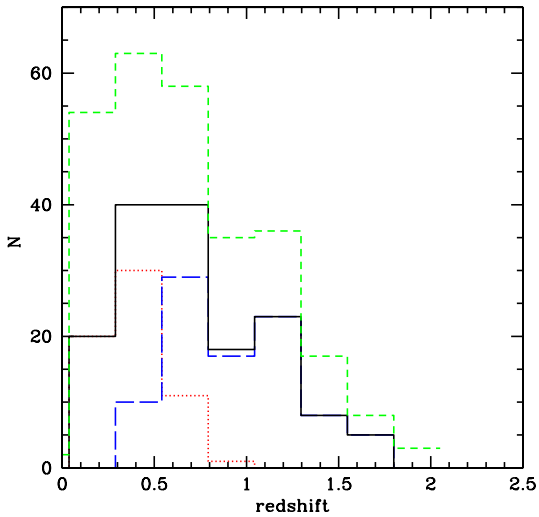

Fig. 1. Redshift distribution for the 154 XBS AGN1 discussed in this paper (continuous black line) compared to the distribution of the total sample of 276 AGN1 (green short-dashed line). Dotted (red) and long-dashed (blue) histograms indicate the objects whose black-hole mass has been derived using the Hβ and MgIIλ2798 Å lines, respectively.

3. Black-hole mass

To estimate the black-hole masses of the XBS type 1 AGN, we used the "single epoch" (SE) spectral method, which is based on measuring the broad line widths and the continuum emission in a single spectrum (e.g. see Peterson 2010 and Marziani & Sulentic 2012, and references therein). The method assumes both that the BLR traces the gravitational potential due to the presence of the central SMBH and that the virial theorem can be applied. The two input quantities, the velocity dispersion and the size of the system (R_{BLR}), can be inferred directly from the optical/UV spectrum: the line width yields direct information on the velocity dispersion, while the continuum luminosity can be used to estimate the system size through the R_{BLR}/L "scaling relations" (e.g. Kaspi et al. 2000; Bentz et al. 2009). The unknown geometry of the BLR is one fundamental source of uncertainty for this method and, in general, for all methods based on the BLR kinematics (including the reverberation mapping method, Vestergaard 2009). The average value of the "virial factor" that takes the particular geometry of the system into account can be assumed "a priori" (e.g. McLure & Jarvis 2002) or it can be estimated through a comparison with the M_{BH}-σ empirical relation observed in non-active galaxies (Onken et al. 2004; Woo et al. 2010; Graham et al. 2011). That the BLR geometry is probably different from object to object creates an intrinsic dispersion on the "virial factor", which is one of the most important sources of uncertainty associated to these methods. Besides this "zero point" uncertainty, the SE method has an additional source of uncertainty due to the scatter on the size-luminosity relation. All considered, the total uncertainty on the SE method has been recently estimated to be between 0.35 and 0.46 dex (Park et al. 2012).

[1] The XBS is one of the research programmes conducted by the *XMM-Newton* Survey Science Center (SSC, see http://xmmssc-www.star.le.ac.uk), a consortium of 10 international institutions, appointed by the European Space Agency (ESA) to help the *XMM-Newton* Science Operations Centre (SOC) in developing the software analysis system, to pipeline process all the *XMM-Newton* data, and to exploit the *XMM-Newton* serendipitous detections. The Osservatorio Astronomico di Brera is one of the Consortium Institutes.

The emission lines used for the $M_{\rm BH}$ measurement depend on the redshift of the source. For the XBS sample, the type 1 AGNs cover a redshift range between 0.02 and 2, therefore, the emission lines that can be used for the mass estimate are the Hβ (up to $z \sim 0.8$) and the MgIIλ2798 Å (from $z \sim 0.3$). In a number of cases both lines are included in the observed spectral range.

In this paper we adopt the relationships that are anchored to the virial factor estimated by Onken et al. (2004). For the Hβ, we used the relation discussed in Vestergaard & Peterson (2006):

$$\mathrm{Log}\ M_{\rm BH} = 6.91 + 2\,\mathrm{Log}\ \frac{FWHM(H\beta)}{1000\ \mathrm{km\,s^{-1}}} + 0.50\,\mathrm{Log}\ \frac{\lambda L_{5100\ \text{Å}}}{10^{44}\ \mathrm{erg}}. \quad (1)$$

For the MgIIλ2798 Å line we used the relation presented in Shen et al. (2011):

$$\mathrm{Log}\ M_{\rm BH} = 6.74 + 2\,\mathrm{Log}\ \frac{FWHM(MgII)}{1000\ \mathrm{km\,s^{-1}}} + 0.62\,\mathrm{Log}\ \frac{\lambda L_{3000\ \text{Å}}}{10^{44}\ \mathrm{erg}} \quad (2)$$

this equation has been obtained by Shen et al. (2011) in such a way that the zero-order point (i.e. the virial factor) is the same as in the Hβ relation presented above (Eq. (1)) so that the masses are consistently derived from these two equations. In both relations, the line widths refer to the broad component, and it is assumed that a narrow component has been subtracted during the fitting procedure.

In the following sections we describe in detail the methods adopted to compute the two critical input quantities of the equations reported above, i.e. the line widths and the continuum luminosity.

3.1. Line width measurements

The different dependence of $M_{\rm BH}$ on line width and luminosity (see Eqs. (1) and (2)) means that the statistical (i.e. not including the intrinsic dispersion of the relation and the uncertainty on the virial factor) uncertainty of the final $M_{\rm BH}$ estimate will mostly come from the uncertainty on the line width. The line width measurement is then particularly difficult owing to the presence of different spectral components and considering the average quality of our spectra (average $S/N \sim 10-11$ in the spectral regions close to Hβ and MgIIλ2798 Å emission lines, with ~25% of objects having S/N below 5).

In particular, the correct determination of the width of the broad component of the emission line is hampered by a narrow component (which is particularly important for the Hβ line) and by the iron pseudo-continuum (which is critical for the MgIIλ2798 Å line). A simple component fit, not considering the possible presence of a narrow component, would lead to a systematic under-estimate of the broad line width (Denney et al. 2009). At the same time, not considering the existence of the iron pseudo-continuum may lead to an over-estimate of the line width. A common practice for taking this spectral complexity into account is to subtract a FeII template from the spectrum and, then, fit the subtracted spectrum with a number of narrow and broad components (usually with a Gaussian profile, e.g. see Shen et al. 2011, for details on the method). In the following, we discuss separately the methods used to derive the width of the broad components of the Hβ and MgII.

3.1.1. Hβ

For the fit of the Hβ line we use the method usually adopted in the literature i.e. we subtract an iron template to the spectra and then fit the residuals. To this end, we use the iron template presented in Véron-Cetty et al. (2004) and consider the 3500–6000 Å (rest-frame) spectral region. In this procedure there are three independent parameters that need to be determined: the normalization of the iron template ($N_{\rm Fe}$), the line broadening ($\sigma_{\rm Fe}$), and velocity offset ($V_{\rm Fe}$) of the iron lines. Constraining the lattest two parameters is usually difficult even for good quality spectra. In medium quality spectra (like the one of the SDSS spectra considered by Shen et al. 2011, where $S/N \sim 10$) these parameters are poorly constrained (e.g. see discussion in Shen et al. 2011). The quality of our spectra is, on average, similar to the ones of the SDSS spectra (and in some cases even lower), so we decided to fix both parameters. After subtracting of the iron template, we fit the resulting spectrum around the Hβ line using a model composed by three components: a PL continuum plus four Gaussians representing, respectively, the narrow and the broad components of the Hβ and the two [OIII] narrow lines. The width of the component describing the narrow Hβ is constrained to be equal to the width of two [OIII] lines. We run the fit in two steps: first we freeze the positions of the Gaussians to the expected wavelengths. In a second step, we leave the positions of the Gaussians describing the emission lines free to vary (with the maximum possible variation in the position of the iron components fixed to ~30 Å to avoid problems with the fitting procedure). The broad and the narrow Hβ components do not necessarily peak at the same wavelength to account for possible velocity offsets between the BLR and the NLR. We show an example of this fitting procedure in Fig. 2.

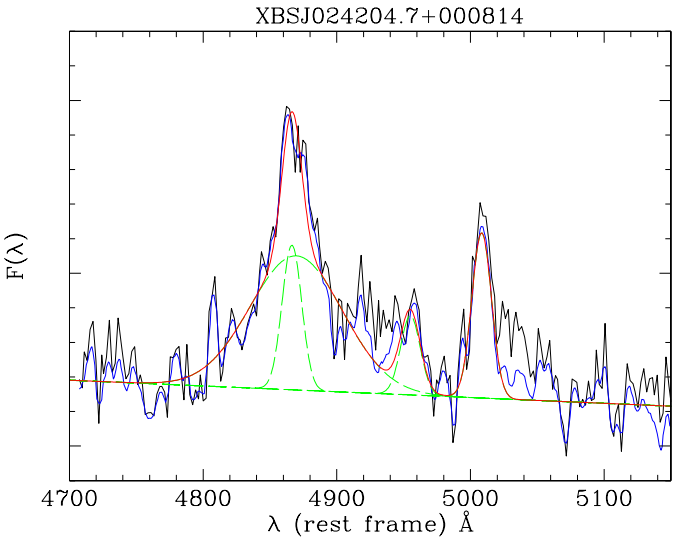

Fig. 2. Example of a spectral model used to fit the region around the Hβ line. As described in the text, we first subtract an iron template from the spectrum (black line) and then we fit the residual (blue line) with a power-law continuum plus 3 Gaussians describing the narrow Hβ and the two [OIII] lines, plus an additional Gaussian to describe the broad component of the Hβ line. These components are represented by the dashed green lines while the total fit is represented by the red continuous line.

We note that keeping the iron line width and position fixed during the fitting procedure may introduce a certain degeree of uncertainity (even systematic) in the computation of the broad Hβ width. The possibity that the iron lines could be systematically shifted with respect to the Hβ line has been investigated by several authors, and although there have been some claims of systematic large velocity offsets (up to 2000 km s^{-1}) in the spectra of SDSS quasars (Hu et al. 2008), the analysis of good

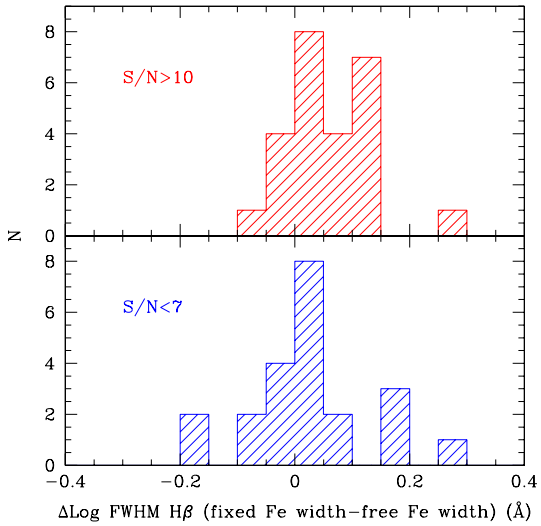

Fig. 3. Difference between the logarithms of the broad Hβ emission line width derived with two different methods, one based on the subtraction of an iron template where the line widths are fixed and a second method that, instead, leaves the iron line widths free to vary (see text for details). The data are split on the basis of the signal-to-noise around the Hβ line.

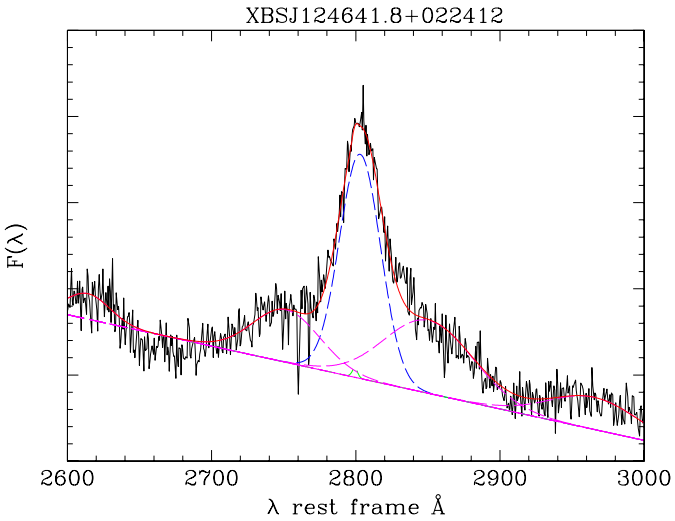

Fig. 4. Example of a spectral model to fit the region around the MgIIλ2798 Å line. This method includes the iron lines directly in the fitting procedure rather than subtracting an iron template from the spectrum, as typically done in the literature. The total fit is represented by the solid red line while the different components (the power-law continuum, the narrow and the broad components of the line and the iron humps) are represented by the dashed lines.

signal-to-noise ratio (S/N) spectra has recently demonstrated that the actual offsets are much smaller (<300 km s^{-1}, Sulentic et al. 2012), if present. The impact of such small offsets on our fitting procedure is not going to be relevant. On the contrary, keeping the iron line width fixed can have a more significant impact on our mass estimates. To quantitatively evaluate this effect, we applied a second fitting method, not based on subtraction of an iron template, using an approach similar to the one used for fitting the MgIIλ2798 Å line (see below). In this method, we adopted a model composed of six Gaussians plus a power-law continuum. Two Gaussians are used to model the Hβ (for the narrow and the broad components), while two Gaussians are used to fit the two [OIII] narrow emission lines. The remaining two Gaussians are used to account for the two strongest FeII components usually observed at 4924 Å and 5023 Å. The widths of these two lines are left free to vary. Then we ran the fitting procedure following the two steps described above and found the best-fit width of the broad Hβ component. The resulting widths were finally compared to those obtained by subtracting the iron template. We carried out this comparison by splitting the sample into two sets: a first data set containing only the low S/N (in the Hβ region) spectra ($S/N < 7$) and a second data set containing the best spectra we have ($S/N > 10$). In Fig. 3 we show the distribution of the difference in the widths (in Log) computed using the two procedures, for both data sets. In the case of low S/N spectra there is no systematic difference between the two estimates. This is expected since, in case of very poor quality spectra, it is very difficult to detect any real difference in the iron line width, and all the differences are probably due just to random fluctuations in the fitting procedure. In contrast, for relatively good spectra ($S/N > 10$), we do observe a significant ($\sim 3\sigma$) systematic offset between the line widths, the Hβ being typically larger in the iron template subtraction method (where the iron lines are fixed), when compared to the method where the iron lines are left free to vary. This is probably because, in the first method, part of the iron emission may be included in the broad Hβ component thus producing larger widths. We stress, however, that even in the $S/N > 10$ data set, the average quality of the spectra (S/N between 10 and 30) is certainly not comparable to the one typically required for a proper spectral deconvolution (>50) and, therefore, there is a high degree of degeneracy in the fitting process. We cannot exclude, for instance, that part of the observed offset is related to an underestimate of the broad Hβ component in the method where the iron widths are left free to vary. For this reason, it is difficult to establish which one of the two methods gives better results. However, the observed offset can be used as an estimate of the possible effect on the broad Hβ width because we have fixed the iron width when subtracting the iron template. The observed offset is 0.057 dex, which translates into an expected offset in the mass computed using the Hβ line of ~0.11. This offset is within the average statistical uncertainty on the masses computed from the Hβ line (~0.18 dex).

We finally note that fitting the Hβ broad line using only one Gaussian is certainly a simplification. The analysis of high S/N spectra of local Seyfert galaxies has revealed a complex phenomenology (e.g. see Sulentic et al. 2000, for a review). Given the typical S/N of our spectra, however, any attempt to provide a more complex fit to the broad Hβ profile would lead to very uncertain results, except for very few cases. Indeed, this is a general problem connected with the systematic application of the SE relation to large samples of spectra whose quality is typically much lower than that of the brightest and best-studied local Seyferts.

3.1.2. MgII

For the MgII we did not follow the same procedure as adopted for the Hβ line due to the difficulty of obtaining a reliable iron template at these wavelengths. We thus decided to include the iron components in the fitting procedure. Specifically, we adopted a model including two Gaussians for the narrow and broad components of MgIIλ2798 Å plus four additional Gaussians to reproduce the iron humps at 2630 Å, 2740 Å, 2886 Å and 2950 Å plus a power-law continuum (see Fig. 4).

Since, in the case of MgII, we do not have the two [OIII] line as a reference for the narrow line widths, we set the MgII narrow component to be equal to the instrumental resolution, for the spectra with a resolution worse than 500 km s^{-1}. For the

very few spectra with better resolution, the width of the narrow component is fixed to 500 km s^{-1}. Again, as a first step we fix the positions of the components to the expected values and, then, we left them free to vary (with a maximum possible variation of 30 Å for the iron components). In fitting the MgII line we have thus assumed that a narrow component is present. It should be noted, however, that for the MgIIλ2798 Å line, the actual presence of a narrow component is less obvious than for the Hβ line. In their work, Vestergaard & Osmer (2009) did not subtract a narrow component during the fitting procedure of the MgII profile (which was modelled with two Gaussians both attributed to the broad component), while other authors (e.g. Mc Lure & Dunlop 2004) have considered a narrow plus a broad component for the MgIIλ298 Å line as in the analysis presented here. The choice of including the narrow component of the MgIIλ2798 Å is somewhat arbitrary. In our analysis, including the narrow MgIIλ2798 Å component gives a slightly better consistency between the masses computed using MgIIλ2798 Å and those computed using Hβ, so we decided to adopt this type of model.

3.1.3. Instrumental resolution

Finally, given the moderate resolution of the spectroscopic observations (~650−1200 km s^{-1}), we applied a correction to the widths of the broad components of both Hβ and MgIIλ2798 Å, resulting from the fitting procedures described above, to account for the instrumental broadening, i.e.,

$$\Delta\lambda = \sqrt{\Delta\lambda_{\rm o}^2 - \Delta\lambda_{\rm inst}^2}$$

where $\Delta\lambda$, $\Delta\lambda_o$ and $\Delta\lambda_{\rm inst}$ are the intrinsic, the observed, and the instrumental line width, respectively.

3.2. Monochromatic luminosities

Determination of the monochromatic luminosities at 5100 Å and 3000 Å also requires some caution. In principle we can use the fluxes derived directly from the spectra. This procedure, however, is not accurate for several reasons:

- the absolute spectro-photometric calibration of our spectra is not always accurate since most of the data have been collected during non-photometric nights;
- the spectra are often contaminated by the host galaxy light (the slit width used was often relatively large, from 1 to 2 arcsecs, depending to the seeing conditions);
- the spectra must be corrected for the extinction, both Galactic and at the source. This is a particularly critical point since, given the relatively hard X-ray selection band, the XBS sample contains many type 1 AGNs with moderate levels of absorption (A_V up to 1−2 mag, see Caccianiga et al. 2008).

To account for these points, we used the result of a systematic study of the optical/UV spectral energy distribution (SED) of the type 1 AGN of the XBS survey, described in Marchese et al. (2012). In this work we have collected photometric points, both in the optical (most from the SDSS) and in the UV band (from GALEX) and built the SED for each source. In the derivation of the SED we carefully took the presence of the host galaxy into account, on the basis of the strength of the 4000 Å contrast, and excluded it from the final SEDs. We also corrected the photometric points for the extinction, both due to our Galaxy and at the source, using the values of $N_{\rm H}$ derived from the X-ray analysis (Corral et al. 2011) and assuming a Galactic gas-to-dust ratio. This is certainly an approximation since there are well-known examples of AGN where the dust-to-gas ratio is significantly different from what is observed in our Galaxy. However, in the XBS survey we have found generally good agreement between the optical classification (type1/type2 AGN) and the measured levels of $N_{\rm H}$ (lower or greater than 4×10^{21} cm^{-2}), with only a few (<10%) exceptions (Caccianiga et al. 2004; Corral et al. 2011). Therefore, we expect that this problem is not going to have a strong impact on our results, at least from a statistical point of view.

These SEDs have been then fitted with a multi-colour blackbody accretion disk model, which includes corrections for temperature distribution near the black hole (for details see DISKPN in the XSPEC 12 software package, Arnaud et al. 1996). From this fit, we computed the rest frame 5100 Å and 3000 Å luminosities to be used in Eqs. (1) and (2) for the mass estimate.

3.3. Computing the BH masses

Using the methods described in the previous sections, we computed the black-hole masses for all the 154 type 1 AGNs of the XBS for which we analysed the SED, as described in Marchese et al. (2012) and for which we acquired an optical spectrum. For 32 objects we only covered the Hβ emission line while for 70 objects we have covered only the MgIIλ2798 Å line. In 52 cases we have detected both lines in the spectrum. In these cases we chose the mass estimate that is considered more accurate, i.e. the one based on the line with the best S/N and/or with the smallest error in the measured width (quite often, one of the two lines is at the edge of the observed spectrum). Overall, the black-hole masses were derived from the Hβ, in 62 cases, and from MgIIλ2798 Å line, in 92 cases.

The masses for the 154 type 1 AGN are reported in Table 1, together with the (statistical) errors. In Table 1 we also report the full width at half maximum (FWHM) of the lines and the values of the monochromatic luminosities used for the mass estimate. The distribution of the masses obtained for the 154 AGN1 of the XBS sample are reported in Fig. 5.

3.4. Uncertainties on BH masses

Statistical uncertainities on the BH masses were estimated by combining the statistical errors on both line width and monochromatic luminosity, assuming that the two errors are independent:

$$\sigma^{+,-}_{{\rm Log}M} = \sqrt{(A\sigma^{+,-}_{{\rm Log}\,FWHM})^2 + (B\sigma^{+,-}_{{\rm Log}\,L})^2}$$

where $A = 2$ and B is equal to 0.5 for the Hβ while it is 0.62 for MgIIλ2798 Å. $\sigma^{+,-}$ are the asymmetric errors (at the 68% confidence level) to the logarithm of the FWHM and luminosities, respectively.

The errors on the Hβ and MgIIλ2798 Å broad components are derived from the fitting precedure described above, by imposing $\Delta\chi^2 = \pm 1$. Similarly, the errors on the monochromatic luminosities are computed from the SED fitting procedure by again imposing $\Delta\chi^2 = \pm 1$ from the best-fit value. As described in Marchese et al. (2012), the SED fitting procedure takes the

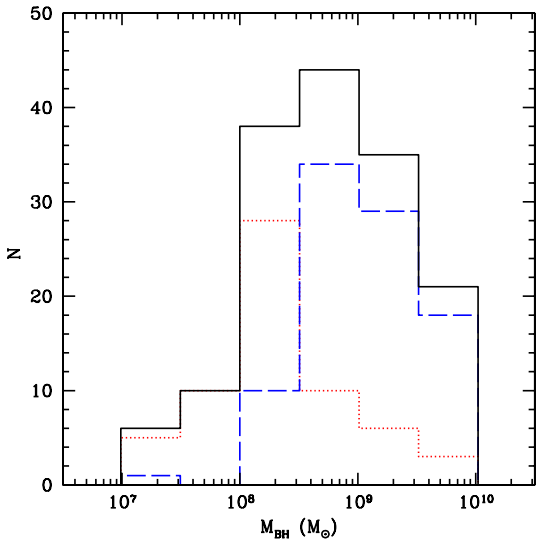

Fig. 5. Distribution of the black-hole masses for the 154 XBS AGN1. Dotted (red) and dashed (blue) histograms show masses derived from Hβ and MgIIλ2798 Å lines respectively.

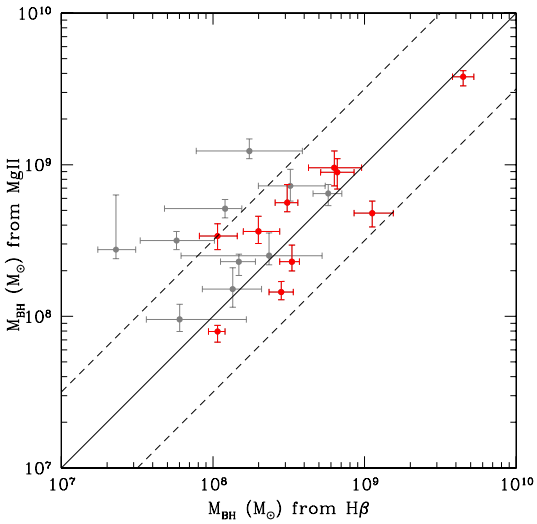

Fig. 6. Comparison between black-hole masses computed on the basis of the MgIIλ2798 Å and the Hβ lines for the XBS AGNs where both lines are included in the spectrum. Red points represent sources with a relatively high S/N (>5) around the line of interest and with lower statistical error bars (<0.2 dex) while grey points are objects with lower S/N spectra and/or larger error bars. As reference we plot the relation 1:1 (solid line), while the two dashed lines represent a scatter of 0.5 dex.

errors on the photometric points into account. These 1σ uncertainities include both the errors on photometry and additional sources of error due to the correction for the intrinsic extinction and the long term variability (since the used photometric data are not simultaneous). The uncertainty due to the correction for the host galaxy, based on the 4000 Å break, is not folded into these errors. However, in Marchese et al. (2012) we evaluated that by changing the starting value of the 4000 Å break within a reasonable range of values (from 45% to 55%), the variations in the photometric points only produce a negligible (≤14%) change in the best fit luminosity.

The statistical 1-σ errors on the broad line widths, monochromatic luminosities, and on the final black-hole masses are reported in Table 1. We stress that the errors on black-hole masses do not include the uncertainity on the SE method that, as already explained, is expected to be between 0.35 dex and 0.46 dex (Park et al. 2012) i.e. dominant when compared to the average statistical errors (~0.14 dex).

3.5. Comparison of the black-hole mass estimates

With the derived line widths and monochromatic luminosities we computed the $M_{\rm BH}$ for all the AGN1 for which either the Hβ or the MgIIλ2798 Å lines have been observed. For the 52 sources where both Hβ and MgIIλ2798 Å are included in the spectrum it is possible to compare the two $M_{\rm BH}$ estimates. To evaluate the presence systematic offsets better, we first considered the objects with a relatively good spectrum ($S/N > 5$) and excluded the sources with large statistical errors on the final mass estimate (>0.2 dex). The comparison (Fig. 6) shows generally good agreement, without significant offsets and with a spread of ~0.28 dex. Considering all the objects, including those with less accurate determination of the mass the spread increases to ~0.38 dex, and there seems to be a systematic shift probably related to the difficulty of properly accounting for all the components during the spectral fit (in particular the iron lines around the MgIIλ2798 Å line and the narrow component of the Hβ line). In Table 1 we have flagged the masses derived from a problematic fit and those resulting from the analysis of poor S/N (<5) spectra.

As a further test of the reliability of our mass estimate we compared the black-hole masses derived in our work with those computed in Shen et al. (2011) for the few sources in common. Since Shen et al. (2011) presents masses computed using different formulae, we used the ones computed in the same way for the comparison, i.e. the VP06 for Hβ, and the S10 for MgIIλ2798 Å. The result of the comparison is presented in Fig. 7. In some cases, we used the same SDSS spectrum to derive the BH masses while in other cases we acquired an independent spectrum. As before, we first excluded from the test the sources with low S/N (<5) spectra (used in our analysis) and large errors (>0.2 dex) in either our estimate or in the Shen et al. estimate. The comparison shows a spread of ~0.2−0.3 dex and a marginal systematic offset between the two masses, with the ones computed in this work being larger on average by a factor ~0.17 dex. The offset is mainly present in the masses computed from MgIIλ2798 Å. By comparing separately the line widths and the monochromatic luminosities we have established that this offset is mainly attributed to an offset in luminosity rather than in line width. This offset is probably due to the method we used to compute the monochromatic luminosities that corrects for the extinction (both Galactic and at the source), as explained in the previous sections, thus yelding, on average, to higher corrected luminosities, in particular in the blue/UV spectral region. Considering all the sources in common between the two samples the spread increases to ~0.4 dex.

4. Eddington ratio and $\dot{M}$

An important parameter that is suspected of regulating a number of observational properties of AGNs is the "normalized" bolometric luminosity, i.e. the so-called Eddington ratio, which is defined as

$$\lambda = L_{\rm bol}/L_{\rm Edd} \quad (3)$$

where:

$$L_{\rm Edd} = 1.26 \times 10^{38} \frac{M_{\rm BH}}{M_\odot} \ {\rm erg\ s^{-1}} \quad (4)$$

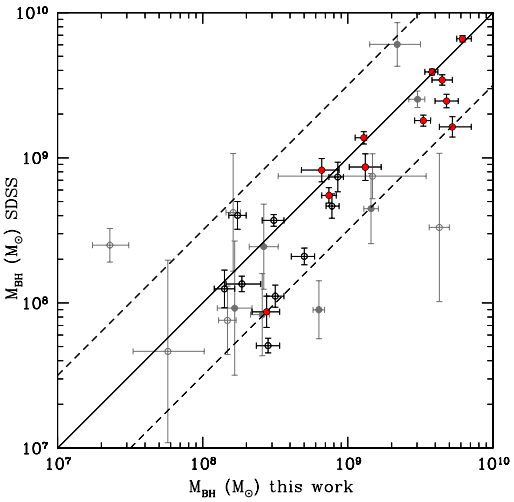

Fig. 7. Comparison between black-hole masses computed in this paper and those computed by Shen et al. (2011), for the XBS AGNs included in the SDSS sample. Red and black points represent the objects with higher signal-to-noise ratio (>5) and smaller uncertainties on the mass derivation (<0.2 dex). Grey points, instead, represent the data with lower S/N and/or larger error bars. Filled (and red, in electronic version) points are sources for which we have used the SDSS spectrum to derive the BH mass, while open points indicate sources for which we used an optical spectrum taken in our own observations. As reference we plot the relation 1:1 (solid line), while the two dashed lines represent a scatter of 0.5 dex.

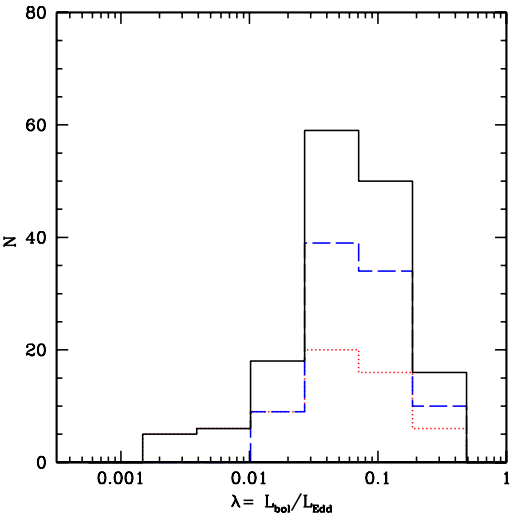

Fig. 8. Distribution of the values of Eddington ratio for the 154 XBS AGN1. Dotted (red) and dashed (blue) histograms show the values based on masses derived from Hβ and MgIIλ2798 Å lines respectively.

We compute the values of Eddington ratio using the bolometric luminosities taken from Marchese et al. (2012) which was computed, as explained above, by fitting the optical/UV data with a disk model. The photometric points, and therefore the bolometric luminosity, were corrected for reddening as detailed in Marchese et al. (2012). The distribution of Eddington ratios is reported in Fig. 8.

From the bolometric luminosity we can also derive an estimate of the absolute (i.e. not normalized to the Eddington limit) accretion rate:

$$\dot{M} = \frac{L_{\rm bol}}{\eta c^2} \sim 1.8 \times 10^{-3} \frac{L_{44}}{\eta}\ M_\odot\ {\rm yr}^{-1} \quad (5)$$

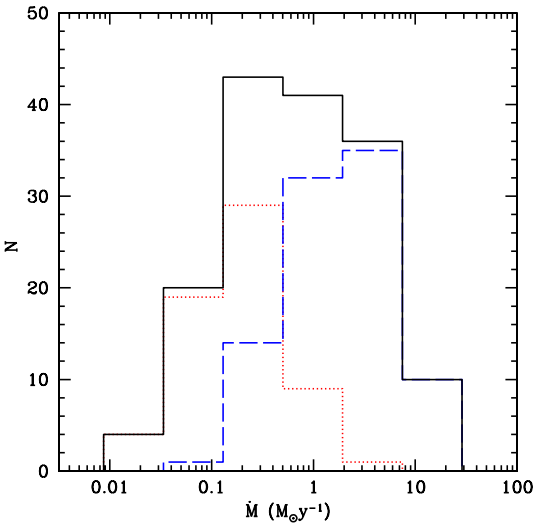

Fig. 9. Distribution of the values of $\dot{M}$ for the 154 XBS AGN1. Line styles as in Fig. 5.

where L_{44} is the bolometric luminosity in units of 10^{44} erg s^{-1} and η is the efficiency of the mass-to-energy conversion. We assume here an efficiency of 0.1 (Marconi et al. 2004). We note that the bolometric luminosities used to compute $\dot{M}$ also include the X-ray emission (in addition to the disk component) as described in Marchese et al. (2012). Therefore, by using these bolometric luminosities to compute $\dot{M}$ we are implicitly assuming that the energy budget carried by the X-ray emission is directly related to the accretion process. This is, of course, not an obvious assumption, since the origin of the X-ray emission is still an open issue. In any case, we stress that the contribution of the X-ray emission to the bolometric luminosity is, in general, relatively low (~25% on average in our sample) and, therefore, the values of $\dot{M}$ are not going to change significantly (on average) if we use only the disk emission in Eq. (5).

The distribution of $\dot{M}$ is reported in Fig. 9. To facilitate the comparison with previous figures we also show the $\dot{M}$ separately for Hβ and MgIIλ2798 Å mass-derived sources, although in this case, the value of $\dot{M}$ does not depend on the derived BH mass.

5. The effect of radiation pressure

It has been suggested (Marconi et al. 2008; Marconi et al. 2009) that the black-hole masses derived from the virial theorem can be severely underestimated due to the effect of the radiation pressure. This effect, not considered in the usual SE relations, is expected to be important for accretion rates close to the Eddington limit according to the following equation (Marconi et al. 2008):

$$M_{\rm BH} = M_{\rm BH,0}\left[1 + \lambda_0\left(1 - a + \frac{a}{\sigma_T N_{\rm H}}\right)\right] \quad (6)$$

where $M_{\rm BH}$ is the "real" black-hole mass, $M_{\rm BH,0}$ is the black-hole virial mass computed by neglecting the radiation pressure, λ_0 is the Eddington ratio computed using $M_{\rm BH,0}$, $a = L_{\rm ion}/L$ (i.e. the ratio between the ionizing continuum luminosity and the bolometric luminosity), $\sigma_{\rm T}$ is the Thomson cross-section, and $N_{\rm H}$ the column density of each BLR cloud along the line of sight. As noted by Marconi et al. (2008), for reasonable assumptions on the BLR density (~10^{23} cm^{-2}) if the accretion is close to the Eddington limit, the correction could be as high as a factor 10. The actual importance of the radiation pressure, however, has

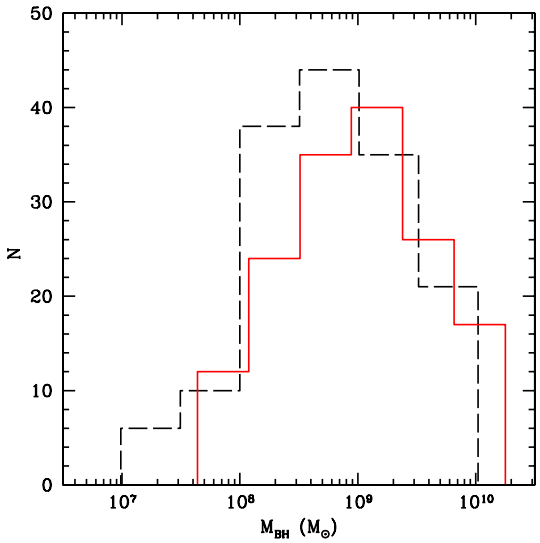

Fig. 10. Distribution of the black-hole masses corrected for the radiation pressure (red continuous line), as described in the text. For comparison we show the distribution of uncorrected masses (black dashed line).

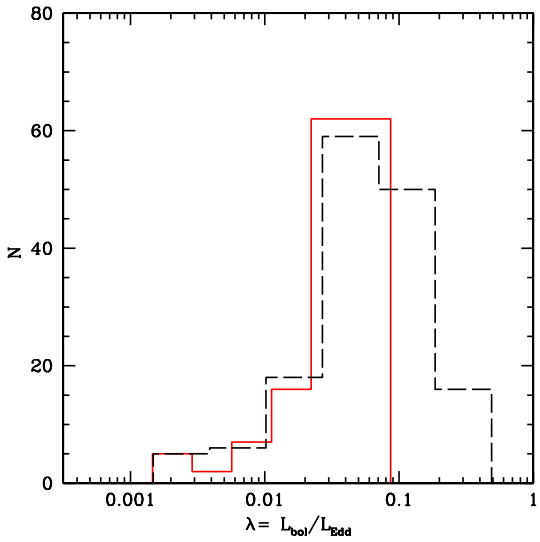

Fig. 11. Distribution of the Eddington ratios corrected for the radiation pressure (red continuous line), as described in the text. For comparison we show the distribution of uncorrected masses (black dashed line).

been debated in the recent literature. Netzer (2009), for instance, notes that the Eddington ratios of a sample of type 1 AGN from the SDSS (whose black-hole masses were computed using the virial method), when corrected for the radiation pressure, turnes out to be significantly lower when compared to the Eddington ratio distribution of an SDSS sample of type 2 AGN for which the black-hole masses have been computed using a different technique (M-σ relation). In contrast, if no correction is applied, the two distributions are similar.

Given the difficulty of assessing the actual importance of the radiation pressure, we decided to present both the corrected and the uncorrected masses and Eddington ratios in this paper. The corrected masses, in particular, were computed using the equation above and assuming $a = 0.6$ and $N_{\rm H} = 10^{23}$ cm^{-2} (the values assumed in Marconi et al. 2008).

In Fig. 10 we show the black-hole mass and in Fig. 11 the Eddington ratio distributions corrected for the radiation pressure and compared with the uncorrected quantities. As expected, the corrected masses are shifted towards the higher values, while the Eddington ratio presents a sharp cut off at 0.1 (see discussion in Marconi et al. 2008).

The values of masses and Eddington ratios corrected for the radiation pressure are included in Table 1.

6. Summary and conclusions

We have presented black-hole masses and accretion rates (both absolute and relative to the Eddington limit) for 154 type 1 AGNs belonging to the XBS sample. The masses were derived using the single-epoch method and adopting the most recent scaling relations involving the Hβ and the MgIIλ2798 Å emission lines. The selected sources cover a range of masses from 10^7 to 10^{10} $M_\odot$ with a peak around 8×10^8 $M_\odot$ and a range of accretion rates from 0.01 to ~50 $M_\odot$/y (assuming an efficiency of 0.1), with a peak at around 1 $M_\odot$/y. The values of the Eddington ratio range from 0.001 to ~0.5 and peak at 0.1.

We have verified that the computed masses are in broad agreement with the ones presented in Shen et al. (2011) although we found a systematic offset of ~0.17 dex (with our masses being higher) probably because of the different methods adopted in the two works to estimate the continuum luminosity.

We stress that the 154 type 1 AGN presented here constitute a well-defined flux-limited sample of type 1 AGN and not just a collection of data from the literature or from public archives. This characteristic, combined with the systematic availability for all these objects of crucial X-ray information (based on X-ray spectral analysis) and on the optical/UV SED, makes this sample instrumental for statistical studies. In a companion paper (Fanali et al., in prep.), we will use the results presented here to study the link between the hot-corona, responsible for the X-ray emission, and the accretion process onto the central black hole.

Acknowledgements. We thank the referee for useful comments that significantly improved the paper and Tommaso Maccacaro for his initial involvement in the XBS project. The authors acknowledge financial support from ASI (grants No. I/088/06/0 and I/009/10/0). S.M. acknowledges financial support by the Spanish Ministry of Economy and Competitiveness, through grant AYA2010-21490-C02-01.

References

Arnaud, K. A. 1996, Astronomical Data Analysis Software and Systems V, eds. G. Jacoby, & J. Barnes, ASP Conf. Ser., 101, 17
Bentz, M. C., Peterson, B. M., Netzer, H., Pogge, R. W., & Vestergaard, M. 2009, ApJ, 697, 160
Bianchi, S., Bonilla, N. F., Guainazzi, M., Matt, G., & Ponti, G. 2009, A&A, 501, 915
Caccianiga, A., Severgnini, P., Braito, V., et al. 2004, A&A, 416, 901
Caccianiga, A., Severgnini, P., Della Ceca, R., et al. 2007, A&A, 470, 557
Caccianiga, A., Severgnini, P., Della Ceca, R., et al. 2008, A&A, 477, 735
Corral, A., Della Ceca, R., Caccianiga, A., et al. 2011, A&A, 530, A42
Della Ceca, R., Maccacaro, T., Caccianiga, A., et al. 2004, A&A, 428, 383
Denney, K. D., Peterson, B. M., Dietrich, M., Vestergaard, M., & Bentz, M. C. 2009, ApJ, 692, 246
Graham, A. W., Onken, C. A., Athanassoula, E., & Combes, F. 2011, MNRAS, 412, 2211
Grupe, D., Komossa, S., Leighly, K. M., & Page, K. L. 2010, ApJS, 187, 64
Gültekin, K., Richstone, D. O., Gebhardt, K., et al. 2009, ApJ, 698, 198
Haardt, F., & Maraschi, L. 1991, ApJ, 380, L51
Haardt, F., & Maraschi, L. 1993, ApJ, 413, 507
Hu, C., Wang, J.-M., Ho, L. C., et al. 2008, ApJ, 687, 78
Kaspi, S., Smith, P. S., Netzer, H., et al. 2000, ApJ, 533, 631
Lusso, E., Comastri, A., Simmons, B. D., et al. 2012, MNRAS, 425, 623
McLure, R. J., & Dunlop, J. S. 2004, MNRAS, 352, 1390

McLure, R. J., & Jarvis, M. J. 2002, MNRAS, 337, 109
Magorrian, J., Tremaine, S., Richstone, D., et al. 1998, AJ, 115, 2285
Marchese, E., Della Ceca, R., Caccianiga, A., et al. 2012, A&A, 539, A48
Marconi, A., Risaliti, G., Gilli, R., et al. 2004, MNRAS, 351, 169
Marconi, A., Axon, D. J., Maiolino, R., et al. 2008, ApJ, 678, 693
Marconi, A., Axon, D. J., Maiolino, R., et al. 2009, ApJ, 698, L103
Martin, D. C., Fanson, J., Schiminovich, D., et al. 2005, ApJ, 619, L1
Marziani, P., & Sulentic, J. W. 2012, New Astron. Rev., 56, 49
Merloni, A., & Heinz, S. 2012 [arXiv:1204.4265]
Morrissey, P., Conrow, T., Barlow, T. A., et al. 2007, ApJS, 173, 682
Netzer, H. 2009, ApJ, 695, 793
Onken, C. A., Ferrarese, L., Merritt, D., et al. 2004, ApJ, 615, 645
Park, D., Woo, J.-H., Treu, T., et al. 2012, ApJ, 747, 30
Peterson, B. M. 2010, IAU Symp., 267, 151
Risaliti, G., Young, M., & Elvis, M. 2009, ApJ, 700, L6
Shen, Y., Richards, G. T., Strauss, M. A., et al. 2011, ApJS, 194, 45
Sulentic, J. W., Marziani, P., & Dultzin-Hacyan, D. 2000, ARA&A, 38, 521
Sulentic, J. W., Marziani, P., Zamfir, S., & Meadows, Z. A. 2012, ApJ, 752, L7
Vagnetti, F., Turriziani, S., Trevese, D., & Antonucci, M. 2010, A&A, 519, A17
Vasudevan, R. V., & Fabian, A. C. 2009, MNRAS, 392, 1124
Vestergaard, M. 2009 [arXiv:0904.2615]
Vestergaard, M., & Peterson, B. M. 2006, ApJ, 641, 689
Véron-Cetty, M.-P., Joly, M., & Véron, P. 2004, A&A, 417, 515
Vestergaard, M., & Osmer, P. S. 2009, ApJ, 699, 800
Woo, J.-H., Treu, T., Barth, A. J., et al. 2010, ApJ, 716, 269
Young, M., Elvis, M., & Risaliti, G. 2010, ApJ, 708, 1388

Pages 10 to 14 are available in the electronic edition of the journal at http://www.aanda.org

Table 1. Black-hole masses of the XBS AGN1.

Name	z	Log $FWHM$ Hβ	Log $FWHM$ MgIIλ2798 Å	Log λL_λ 5100 Å	Log λL_λ 3000 Å	Log M_{BH} Hβ	Log M_{BH} MgIIλ2798 Å	Log M_{BH} best	Log M_{BH} p_{rad}	Log $\dot{M}$	Log L/L_{Edd}	Log L/L_{Edd} p_{rad}	Flag
(1)	(2)	(3)	(4)	(5)	(6)	(7)	(8)	(9)	(10)	(11)	(12)	(13)	(14)
XBSJ000027.7−250442	0.336	$3.81^{+0.045}_{-0.043}$	$3.72^{+0.018}_{-0.019}$	$44.21^{+0.11}_{-0.16}$	$44.34^{+0.11}_{-0.16}$	$8.63^{+0.10}_{-0.12}$	$8.39^{+0.07}_{-0.09}$	$8.63^{+0.10}_{-0.12}$	8.68	$-0.94^{+0.09}_{-0.12}$	$-1.93^{+0.13}_{-0.17}$	−1.98	
XBSJ000031.7−245502	0.284	$3.48^{+0.664}_{-0.042}$	–	$44.28^{+0.12}_{-0.48}$	$44.17^{+0.13}_{-0.48}$	$8.02^{+1.32}_{-0.25}$	–	$8.02^{+1.32}_{-0.25}$	8.15	$-1.05^{+0.11}_{-0.33}$	$-1.43^{+1.32}_{-0.41}$	−1.56	2
XBSJ000102.4−245850	0.433	$3.73^{+0.067}_{-0.062}$	$3.66^{+0.033}_{-0.017}$	$43.57^{+0.14}_{-0.16}$	$43.79^{+0.15}_{-0.15}$	$8.16^{+0.15}_{-0.14}$	$7.93^{+0.09}_{-0.09}$	$8.16^{+0.15}_{-0.14}$	8.26	$-1.06^{+0.07}_{-0.06}$	$-1.58^{+0.17}_{-0.15}$	−1.68	
XBSJ001831.6+162925	0.553	–	$3.50^{+0.007}_{-0.007}$	$45.09^{+0.12}_{-0.09}$	$45.29^{+0.12}_{-0.09}$	–	$8.54^{+0.06}_{-0.05}$	$8.54^{+0.06}_{-0.05}$	8.92	$0.06^{+0.10}_{-0.09}$	$-0.84^{+0.12}_{-0.10}$	−1.22	2
XBSJ002618.5+105019	0.473	$3.75^{+0.045}_{-0.064}$	$3.48^{+0.036}_{-0.040}$	$45.23^{+0.11}_{-0.10}$	$45.43^{+0.11}_{-0.10}$	$9.03^{+0.10}_{-0.14}$	$8.59^{+0.09}_{-0.09}$	$9.03^{+0.10}_{-0.14}$	9.24	$0.20^{+0.10}_{-0.08}$	$-1.19^{+0.14}_{-0.16}$	−1.40	
XBSJ002637.4+165953	0.554	$3.42^{+0.050}_{-0.238}$	$3.72^{+0.019}_{-0.020}$	$44.92^{+0.12}_{-0.15}$	$45.06^{+0.11}_{-0.16}$	$8.21^{+0.11}_{-0.41}$	$8.83^{+0.07}_{-0.09}$	$8.21^{+0.11}_{-0.41}$	8.63	$-0.20^{+0.08}_{-0.11}$	$-0.77^{+0.14}_{-0.42}$	−1.19	2
XBSJ003315.5−120700	1.206	–	$3.94^{+0.030}_{-0.033}$	$45.32^{+0.28}_{-0.34}$	$45.52^{+0.28}_{-0.34}$	–	$9.56^{+0.16}_{-0.18}$	$9.56^{+0.16}_{-0.18}$	9.67	$0.40^{+0.21}_{-0.19}$	$-1.52^{+0.26}_{-0.26}$	−1.63	
XBSJ003316.0−120456	0.660	–	$3.62^{+0.031}_{-0.033}$	$45.01^{+0.18}_{-0.15}$	$45.25^{+0.18}_{-0.15}$	–	$8.76^{+0.11}_{-0.10}$	$8.76^{+0.11}_{-0.10}$	9.09	$0.19^{+0.16}_{-0.14}$	$-0.93^{+0.19}_{-0.17}$	−1.26	
XBSJ003418.9−115940	0.850	–	$3.76^{+0.034}_{-0.037}$	$44.70^{+0.17}_{-0.23}$	$44.94^{+0.18}_{-0.22}$	–	$8.84^{+0.11}_{-0.13}$	$8.84^{+0.11}_{-0.13}$	9.03	$-0.05^{+0.14}_{-0.16}$	$-1.25^{+0.18}_{-0.21}$	−1.44	
XBSJ005009.9−515934	0.610	$3.66^{+0.172}_{-0.299}$	$3.67^{+0.075}_{-0.172}$	$44.44^{+0.11}_{-0.10}$	$44.63^{+0.12}_{-0.09}$	$8.45^{+0.35}_{-0.58}$	$8.47^{+0.16}_{-0.34}$	$8.45^{+0.35}_{-0.58}$	8.62	$-0.48^{+0.08}_{-0.06}$	$-1.29^{+0.36}_{-0.58}$	−1.46	2
XBSJ005031.1−520012	0.463	$3.60^{+0.110}_{-0.097}$	$3.75^{+0.028}_{-0.030}$	$44.85^{+0.19}_{-0.26}$	$45.05^{+0.19}_{-0.27}$	$8.53^{+0.23}_{-0.22}$	$8.89^{+0.11}_{-0.15}$	$8.53^{+0.23}_{-0.22}$	8.78	$-0.19^{+0.17}_{-0.22}$	$-1.08^{+0.29}_{-0.31}$	−1.33	
XBSJ005032.3−521543	1.216	–	$3.86^{+0.023}_{-0.024}$	$45.33^{+0.21}_{-0.30}$	$45.53^{+0.20}_{-0.30}$	–	$9.42^{+0.11}_{-0.16}$	$9.42^{+0.11}_{-0.16}$	9.55	$0.36^{+0.16}_{-0.20}$	$-1.42^{+0.19}_{-0.26}$	−1.55	
XBSJ010421.4−061418	0.520	–	$3.48^{+0.061}_{-0.072}$	$43.40^{+0.15}_{-0.22}$	$43.67^{+0.14}_{-0.23}$	–	$7.49^{+0.13}_{-0.18}$	$7.49^{+0.13}_{-0.18}$	7.93	$-0.89^{+0.07}_{-0.09}$	$-0.74^{+0.15}_{-0.20}$	−1.18	2
XBSJ010432.8−583712	1.640	–	$4.03^{+0.020}_{-0.021}$	$45.62^{+0.14}_{-0.16}$	$45.85^{+0.14}_{-0.16}$	–	$9.94^{+0.08}_{-0.09}$	$9.94^{+0.08}_{-0.09}$	10.06	$0.82^{+0.10}_{-0.09}$	$-1.48^{+0.13}_{-0.13}$	−1.60	2
XBSJ010701.5−172748	0.890	–	$3.58^{+0.038}_{-0.042}$	$45.16^{+0.17}_{-0.16}$	$45.42^{+0.18}_{-0.15}$	–	$8.78^{+0.11}_{-0.11}$	$8.78^{+0.11}_{-0.11}$	9.35	$0.60^{+0.15}_{-0.13}$	$-0.54^{+0.19}_{-0.17}$	−1.11	
XBSJ010747.2−172044	0.980	–	$3.67^{+0.011}_{-0.011}$	$45.91^{+0.11}_{-0.16}$	$46.14^{+0.11}_{-0.16}$	–	$9.41^{+0.06}_{-0.09}$	$9.41^{+0.06}_{-0.09}$	9.81	$0.97^{+0.11}_{-0.14}$	$-0.80^{+0.13}_{-0.17}$	−1.20	
XBSJ012000.0−110429	0.351	$3.21^{+0.060}_{-0.073}$	–	$43.67^{+0.21}_{-0.34}$	$43.93^{+0.22}_{-0.34}$	$7.16^{+0.14}_{-0.20}$	–	$7.16^{+0.14}_{-0.20}$	7.87	$-0.84^{+0.17}_{-0.22}$	$-0.36^{+0.22}_{-0.30}$	−1.07	2
XBSJ012025.2−105441	1.338	–	$3.77^{+0.015}_{-0.016}$	$46.05^{+0.14}_{-0.16}$	$46.28^{+0.14}_{-0.16}$	–	$9.68^{+0.08}_{-0.08}$	$9.68^{+0.08}_{-0.08}$	10.01	$1.11^{+0.14}_{-0.14}$	$-0.93^{+0.16}_{-0.16}$	−1.26	
XBSJ012119.9−110418	0.204	$3.57^{+0.020}_{-0.021}$	–	$44.15^{+0.14}_{-0.16}$	$44.37^{+0.15}_{-0.15}$	$8.13^{+0.08}_{-0.09}$	–	$8.13^{+0.08}_{-0.09}$	8.33	$-0.72^{+0.12}_{-0.12}$	$-1.21^{+0.14}_{-0.15}$	−1.41	
XBSJ013204.9−400050	0.445	$3.43^{+0.057}_{-0.049}$	$3.67^{+0.013}_{-0.007}$	$44.56^{+0.14}_{-0.16}$	$44.75^{+0.15}_{-0.15}$	$8.05^{+0.13}_{-0.12}$	$8.55^{+0.08}_{-0.07}$	$8.05^{+0.13}_{-0.12}$	8.40	$-0.47^{+0.13}_{-0.13}$	$-0.88^{+0.18}_{-0.18}$	−1.23	
XBSJ014251.5+133352	1.071	–	$3.90^{+0.022}_{-0.023}$	$45.52^{+0.12}_{-0.09}$	$45.75^{+0.12}_{-0.10}$	–	$9.63^{+0.07}_{-0.07}$	$9.63^{+0.07}_{-0.07}$	9.77	$0.61^{+0.10}_{-0.09}$	$-1.38^{+0.12}_{-0.11}$	−1.53	
XBSJ015957.5+003309	0.310	$3.21^{+0.071}_{-0.074}$	$3.79^{+0.181}_{-0.181}$	$44.06^{+0.11}_{-0.10}$	$44.19^{+0.11}_{-0.10}$	$7.36^{+0.13}_{-0.12}$	$8.44^{+0.36}_{-0.36}$	$7.36^{+0.13}_{-0.12}$	7.95	$-0.80^{+0.05}_{-0.03}$	$-0.52^{+0.14}_{-0.12}$	−1.11	2
XBSJ020029.0+002846	0.174	$3.53^{+0.084}_{-0.106}$	–	$43.35^{+0.12}_{-0.09}$	$43.48^{+0.12}_{-0.09}$	$7.65^{+0.17}_{-0.20}$	–	$7.65^{+0.17}_{-0.20}$	7.74	$-1.61^{+0.06}_{-0.05}$	$-1.62^{+0.18}_{-0.21}$	−1.71	1
XBSJ021808.3−045845	0.712	$3.56^{+0.057}_{-0.067}$	$3.82^{+0.011}_{-0.011}$	$45.55^{+0.11}_{-0.10}$	$45.74^{+0.12}_{-0.09}$	$8.81^{+0.11}_{-0.12}$	$9.45^{+0.06}_{-0.05}$	$9.45^{+0.06}_{-0.05}$	9.63	$0.53^{+0.09}_{-0.08}$	$-1.28^{+0.11}_{-0.09}$	−1.46	
XBSJ021817.4−045113	1.080	–	$3.82^{+0.014}_{-0.014}$	$45.19^{+0.12}_{-0.18}$	$45.38^{+0.13}_{-0.17}$	–	$9.23^{+0.07}_{-0.09}$	$9.23^{+0.07}_{-0.09}$	9.46	$0.46^{+0.05}_{-0.07}$	$-1.13^{+0.09}_{-0.11}$	−1.36	
XBSJ021820.6−050427	0.646	$3.31^{+0.079}_{-0.100}$	$3.68^{+0.026}_{-0.027}$	$44.87^{+0.08}_{-0.15}$	$45.07^{+0.08}_{-0.15}$	$7.96^{+0.14}_{-0.18}$	$8.76^{+0.06}_{-0.10}$	$8.76^{+0.06}_{-0.10}$	8.95	$-0.12^{+0.06}_{-0.12}$	$-1.24^{+0.08}_{-0.16}$	−1.43	2
XBSJ021923.2−045148	0.632	$3.76^{+0.016}_{-0.017}$	$3.69^{+0.018}_{-0.019}$	$44.92^{+0.11}_{-0.10}$	$45.11^{+0.12}_{-0.09}$	$8.88^{+0.07}_{-0.06}$	$8.81^{+0.07}_{-0.05}$	$8.81^{+0.07}_{-0.05}$	8.99	$-0.11^{+0.10}_{-0.08}$	$-1.28^{+0.12}_{-0.09}$	−1.46	
XBSJ023459.7−294436	0.446	$3.67^{+0.025}_{-0.016}$	$3.68^{+0.003}_{-0.003}$	$45.19^{+0.21}_{-0.22}$	$45.42^{+0.21}_{-0.22}$	$8.84^{+0.12}_{-0.11}$	$8.98^{+0.10}_{-0.11}$	$8.84^{+0.12}_{-0.11}$	9.14	$0.23^{+0.20}_{-0.22}$	$-0.97^{+0.23}_{-0.25}$	−1.28	
XBSJ024200.9+000020	1.112	–	$3.95^{+0.017}_{-0.018}$	$45.74^{+0.09}_{-0.05}$	$45.87^{+0.09}_{-0.05}$	–	$9.79^{+0.06}_{-0.04}$	$9.79^{+0.06}_{-0.04}$	9.89	$0.57^{+0.07}_{-0.04}$	$-1.58^{+0.09}_{-0.06}$	−1.68	
XBSJ024204.7+000814	0.383	$3.69^{+0.031}_{-0.032}$	$3.53^{+0.016}_{-0.016}$	$44.31^{+0.11}_{-0.10}$	$44.58^{+0.11}_{-0.10}$	$8.45^{+0.08}_{-0.08}$	$8.17^{+0.06}_{-0.06}$	$8.45^{+0.08}_{-0.08}$	8.69	$-0.31^{+0.11}_{-0.09}$	$-1.12^{+0.14}_{-0.12}$	−1.36	
XBSJ024207.3+000037	0.385	$3.74^{+0.047}_{-0.041}$	–	$44.07^{+0.08}_{-0.10}$	$44.29^{+0.08}_{-0.09}$	$8.42^{+0.10}_{-0.10}$	–	$8.42^{+0.10}_{-0.10}$	8.52	$-0.79^{+0.06}_{-0.07}$	$-1.57^{+0.12}_{-0.12}$	−1.67	

Notes. Column 1: source name; Col. 2: redshift; Col. 3: logarithm of the FWHM of the broad component of the Hβ (in km s^{-1}); Col. 4: logarithm of the FWHM of the broad component of the MgIIλ2798 Å (in km s^{-1}); Col. 5: logarithm of the monochormatic luminosity at 5100 Å (taken from the SED fitting presented in Marchese et al. (2012); Col. 6: logarithm of the monochormatic luminosity at 3000 Å (taken from the SED fitting presented in Marchese et al. (2012); Col. 7: logarithm of the black-hole mass derived from Hβ (in solar mass units); Col. 8: logarithm of the black-hole mass derived from MgIIλ2798 Å (in solar mass units); Col. 9: logarithm of the black-hole mass considered as best estimate (in solar mass units); Col. 10: logarithm of the best estimate black-hole mass corrected for the effect of radiation pressure (in solar mass units); Col. 11: logarithm of the absolute accretion rate (in units of solar masses per year); Col. 12: logarithm of the Eddington ratio; Col. 13: logarithm of the Eddington ratio corrected for the effects of radiation pressure; Col. 14: flag indicating uncertainity in the best estimate mass (1 = problems during the spectral fitting procedure, 2 = low S/N (<5) in the spectral region of the line used for the mass estimate) (errors are at 68% confidence level).

Table 1. continued.

Name	z	Log $FWHM$ Hβ	Log $FWHM$ MgIIλ2798 Å	Log λL_λ 5100 Å	Log λL_λ 3000 Å	Log M_{BH} Hβ	Log M_{BH} MgIIλ2798 Å	Log M_{BH} best	Log M_{BH} p_{rad}	Log $\dot{M}$	Log L/L_{Edd}	Log L/L_{Edd} p_{rad}	Flag
(1)	(2)	(3)	(4)	(5)	(6)	(7)	(8)	(9)	(10)	(11)	(12)	(13)	(14)
XBSJ025606.1+001635	0.629	$3.26^{+0.143}_{-0.153}$	$3.62^{+0.014}_{-0.015}$	$44.65^{+0.11}_{-0.10}$	$44.85^{+0.11}_{-0.10}$	$7.76^{+0.25}_{-0.24}$	$8.50^{+0.06}_{-0.06}$	$7.76^{+0.25}_{-0.24}$	8.39	$-0.34^{+0.09}_{-0.07}$	$-0.46^{+0.27}_{-0.25}$	−1.09	2
XBSJ031015.5−765131	1.187	–	$3.98^{+0.026}_{-0.028}$	$45.94^{+0.13}_{-0.18}$	$46.14^{+0.12}_{-0.18}$	–	$10.02^{+0.08}_{-0.10}$	$10.02^{+0.08}_{-0.10}$	10.16	$0.99^{+0.09}_{-0.12}$	$-1.39^{+0.12}_{-0.16}$	−1.53	
XBSJ031311.7−765428	1.274	–	$3.78^{+0.033}_{-0.035}$	$45.66^{+0.20}_{-0.23}$	$45.88^{+0.21}_{-0.22}$	–	$9.47^{+0.13}_{-0.13}$	$9.47^{+0.13}_{-0.13}$	9.74	$0.78^{+0.17}_{-0.16}$	$-1.05^{+0.21}_{-0.21}$	−1.32	
XBSJ033208.7−274735	0.544	$4.17^{+0.030}_{-0.029}$	–	$44.72^{+0.08}_{-0.18}$	$44.85^{+0.09}_{-0.18}$	$9.60^{+0.07}_{-0.11}$	–	$9.60^{+0.07}_{-0.11}$	9.62	$-0.45^{+0.07}_{-0.13}$	$-2.41^{+0.10}_{-0.17}$	−2.43	
XBSJ033506.0−255619	1.430	–	$3.77^{+0.019}_{-0.020}$	$46.32^{+0.18}_{-0.22}$	$46.52^{+0.17}_{-0.23}$	–	$9.83^{+0.10}_{-0.12}$	$9.83^{+0.10}_{-0.12}$	10.15	$1.25^{+0.17}_{-0.20}$	$-0.94^{+0.20}_{-0.23}$	−1.26	
XBSJ033851.4−352646	1.070	–	$3.87^{+0.037}_{-0.040}$	$45.88^{+0.21}_{-0.22}$	$46.02^{+0.20}_{-0.22}$	–	$9.74^{+0.12}_{-0.13}$	$9.74^{+0.12}_{-0.13}$	9.87	$0.66^{+0.19}_{-0.20}$	$-1.44^{+0.22}_{-0.24}$	−1.57	
XBSJ033912.1−352813	0.466	$3.70^{+0.037}_{-0.036}$	$3.89^{+0.010}_{-0.010}$	$44.16^{+0.17}_{-0.16}$	$44.29^{+0.17}_{-0.16}$	$8.38^{+0.11}_{-0.11}$	$8.70^{+0.08}_{-0.09}$	$8.70^{+0.08}_{-0.09}$	8.75	$-0.85^{+0.11}_{-0.07}$	$-1.91^{+0.14}_{-0.11}$	−1.96	
XBSJ041108.1−711341	0.923	–	$3.75^{+0.066}_{-0.078}$	$45.07^{+0.23}_{-0.31}$	$45.29^{+0.24}_{-0.30}$	–	$9.04^{+0.18}_{-0.21}$	$9.04^{+0.18}_{-0.21}$	9.24	$0.20^{+0.19}_{-0.21}$	$-1.20^{+0.26}_{-0.30}$	−1.40	2
XBSJ050446.3−283821	0.840	$3.56^{+0.171}_{-0.179}$	$4.01^{+0.007}_{-0.007}$	$44.34^{+0.15}_{-0.16}$	$44.54^{+0.14}_{-0.16}$	$8.20^{+0.35}_{-0.36}$	$9.09^{+0.07}_{-0.08}$	$8.20^{+0.35}_{-0.36}$	8.49	$-0.44^{+0.08}_{-0.06}$	$-1.00^{+0.36}_{-0.36}$	−1.29	
XBSJ050501.8−284149	0.257	$3.36^{+0.029}_{-0.029}$	–	$43.64^{+0.18}_{-0.15}$	$43.84^{+0.17}_{-0.16}$	$7.44^{+0.11}_{-0.09}$	–	$7.44^{+0.11}_{-0.09}$	7.67	$-1.33^{+0.14}_{-0.11}$	$-1.13^{+0.18}_{-0.14}$	−1.36	
XBSJ051651.9+794314	0.557	$3.50^{+0.070}_{-0.085}$	$3.63^{+0.030}_{-0.033}$	$45.42^{+0.23}_{-0.22}$	$45.65^{+0.23}_{-0.22}$	$8.63^{+0.17}_{-0.19}$	$9.01^{+0.13}_{-0.12}$	$9.01^{+0.13}_{-0.12}$	9.37	$0.50^{+0.21}_{-0.20}$	$-0.87^{+0.25}_{-0.23}$	−1.23	
XBSJ051955.5−455727	0.562	$3.61^{+0.041}_{-0.045}$	$3.63^{+0.021}_{-0.022}$	$44.95^{+0.11}_{-0.16}$	$44.84^{+0.11}_{-0.15}$	$8.60^{+0.10}_{-0.11}$	$8.51^{+0.07}_{-0.08}$	$8.51^{+0.07}_{-0.08}$	8.72	$-0.31^{+0.08}_{-0.11}$	$-1.18^{+0.11}_{-0.14}$	−1.39	
XBSJ052022.0−252309	0.745	$4.31^{+0.083}_{-0.065}$	–	$44.90^{+0.22}_{-0.43}$	$45.03^{+0.22}_{-0.44}$	$9.97^{+0.20}_{-0.25}$	–	$9.97^{+0.20}_{-0.25}$	9.98	$-0.20^{+0.16}_{-0.25}$	$-2.53^{+0.26}_{-0.35}$	−2.54	
XBSJ052144.1−251518	0.321	$3.73^{+0.070}_{-0.068}$	–	$43.90^{+0.11}_{-0.16}$	$44.09^{+0.12}_{-0.15}$	$8.32^{+0.15}_{-0.15}$	–	$8.32^{+0.15}_{-0.15}$	8.39	$-1.08^{+0.09}_{-0.11}$	$-1.76^{+0.17}_{-0.19}$	−1.83	2
XBSJ052543.6−334856	0.735	$3.75^{+0.067}_{-0.065}$	$3.82^{+0.008}_{-0.008}$	$44.86^{+0.23}_{-0.22}$	$45.06^{+0.23}_{-0.22}$	$8.84^{+0.18}_{-0.17}$	$9.03^{+0.11}_{-0.11}$	$8.84^{+0.18}_{-0.17}$	9.01	$-0.10^{+0.18}_{-0.15}$	$-1.30^{+0.25}_{-0.23}$	−1.47	
XBSJ065214.1+743230	0.620	$3.51^{+0.051}_{-0.058}$	$3.86^{+0.054}_{-0.039}$	$45.25^{+0.20}_{-0.22}$	$45.48^{+0.20}_{-0.22}$	$8.55^{+0.14}_{-0.15}$	$9.39^{+0.14}_{-0.14}$	$9.39^{+0.14}_{-0.14}$	9.52	$0.33^{+0.18}_{-0.19}$	$-1.42^{+0.23}_{-0.24}$	−1.55	
XBSJ065400.0+742045	0.362	$3.56^{+0.036}_{-0.032}$	$3.27^{+0.042}_{-0.047}$	$44.41^{+0.15}_{-0.15}$	$44.61^{+0.15}_{-0.15}$	$8.24^{+0.10}_{-0.10}$	$7.67^{+0.10}_{-0.11}$	$8.24^{+0.10}_{-0.10}$	8.44	$-0.61^{+0.12}_{-0.13}$	$-1.21^{+0.16}_{-0.16}$	−1.41	1
XBSJ074202.7+742625	0.599	$3.72^{+0.062}_{-0.073}$	$3.76^{+0.011}_{-0.011}$	$44.16^{+0.14}_{-0.16}$	$44.40^{+0.15}_{-0.15}$	$8.42^{+0.14}_{-0.16}$	$8.51^{+0.08}_{-0.08}$	$8.51^{+0.08}_{-0.08}$	8.71	$-0.35^{+0.07}_{-0.06}$	$-1.22^{+0.11}_{-0.10}$	−1.42	2
XBSJ074352.0+744258	0.800	–	$3.72^{+0.027}_{-0.028}$	$45.22^{+0.11}_{-0.16}$	$45.41^{+0.12}_{-0.15}$	–	$9.06^{+0.08}_{-0.09}$	$9.06^{+0.08}_{-0.09}$	9.26	$0.21^{+0.10}_{-0.12}$	$-1.21^{+0.13}_{-0.15}$	−1.41	
XBSJ080504.6+245156	0.980	–	$3.63^{+0.073}_{-0.089}$	$44.43^{+0.08}_{-0.10}$	$44.63^{+0.08}_{-0.10}$	–	$8.39^{+0.14}_{-0.17}$	$8.39^{+0.14}_{-0.17}$	8.64	$-0.33^{+0.03}_{-0.05}$	$-1.08^{+0.14}_{-0.18}$	−1.33	2
XBSJ080608.1+244420	0.357	$3.47^{+0.028}_{-0.027}$	$3.47^{+0.017}_{-0.007}$	$44.62^{+0.08}_{-0.10}$	$44.84^{+0.08}_{-0.09}$	$8.15^{+0.07}_{-0.07}$	$8.21^{+0.05}_{-0.05}$	$8.15^{+0.07}_{-0.07}$	8.57	$-0.25^{+0.06}_{-0.07}$	$-0.76^{+0.09}_{-0.10}$	−1.18	
XBSJ083049.8+524908	1.200	–	$3.63^{+0.048}_{-0.055}$	$44.80^{+0.08}_{-0.09}$	$45.00^{+0.08}_{-0.09}$	–	$8.62^{+0.10}_{-0.11}$	$8.62^{+0.10}_{-0.11}$	9.01	$0.16^{+0.03}_{-0.03}$	$-0.82^{+0.10}_{-0.11}$	−1.21	2
XBSJ083737.1+254751	0.080	$4.20^{+0.149}_{-0.031}$	–	$43.53^{+0.11}_{-0.10}$	$43.76^{+0.11}_{-0.10}$	$9.07^{+0.30}_{-0.08}$	–	$9.07^{+0.30}_{-0.08}$	9.08	$-1.34^{+0.09}_{-0.07}$	$-2.77^{+0.31}_{-0.11}$	−2.78	
XBSJ083838.6+253616	0.601	–	$3.75^{+0.042}_{-0.047}$	$44.92^{+0.12}_{-0.09}$	$45.15^{+0.11}_{-0.10}$	–	$8.96^{+0.10}_{-0.11}$	$8.96^{+0.10}_{-0.11}$	9.12	$-0.02^{+0.11}_{-0.09}$	$-1.34^{+0.15}_{-0.14}$	−1.50	2
XBSJ083905.9+255010	0.250	$3.86^{+0.096}_{-0.106}$	–	$43.23^{+0.14}_{-0.16}$	$43.45^{+0.15}_{-0.15}$	$8.24^{+0.20}_{-0.22}$	–	$8.24^{+0.20}_{-0.22}$	8.27	$-1.55^{+0.10}_{-0.09}$	$-2.15^{+0.22}_{-0.24}$	−2.18	
XBSJ085530.7+585129	0.905	–	$3.66^{+0.034}_{-0.037}$	$44.41^{+0.08}_{-0.15}$	$44.64^{+0.08}_{-0.16}$	–	$8.46^{+0.07}_{-0.11}$	$8.46^{+0.07}_{-0.11}$	8.77	$-0.14^{+0.03}_{-0.05}$	$-0.96^{+0.08}_{-0.12}$	−1.27	2
XBSJ094548.3−084824	1.748	–	$3.72^{+0.010}_{-0.010}$	$46.31^{+0.19}_{-0.34}$	$46.55^{+0.19}_{-0.34}$	–	$9.77^{+0.09}_{-0.17}$	$9.77^{+0.09}_{-0.17}$	10.25	$1.46^{+0.19}_{-0.31}$	$-0.67^{+0.21}_{-0.35}$	−1.15	
XBSJ095054.5+393924	1.299	–	$3.58^{+0.047}_{-0.053}$	$45.41^{+0.11}_{-0.10}$	$45.65^{+0.12}_{-0.09}$	–	$8.93^{+0.11}_{-0.11}$	$8.93^{+0.11}_{-0.11}$	9.40	$0.61^{+0.10}_{-0.08}$	$-0.68^{+0.15}_{-0.14}$	−1.16	
XBSJ095309.7+013558	0.477	$3.87^{+0.138}_{-0.206}$	$3.61^{+0.038}_{-0.042}$	$43.94^{+0.11}_{-0.16}$	$44.21^{+0.11}_{-0.16}$	$8.63^{+0.28}_{-0.41}$	$8.08^{+0.10}_{-0.11}$	$8.08^{+0.10}_{-0.11}$	8.37	$-0.57^{+0.09}_{-0.12}$	$-1.01^{+0.13}_{-0.16}$	−1.30	
XBSJ095509.6+174124	1.290	–	$3.75^{+0.053}_{-0.060}$	$45.13^{+0.08}_{-0.10}$	$45.40^{+0.08}_{-0.10}$	–	$9.12^{+0.11}_{-0.13}$	$9.12^{+0.11}_{-0.13}$	9.47	$0.59^{+0.07}_{-0.07}$	$-0.89^{+0.13}_{-0.15}$	−1.24	2
XBSJ100100.0+252103	0.794	–	$3.68^{+0.010}_{-0.011}$	$44.96^{+0.11}_{-0.10}$	$45.09^{+0.12}_{-0.09}$	–	$8.78^{+0.06}_{-0.05}$	$8.78^{+0.06}_{-0.05}$	8.95	$-0.15^{+0.08}_{-0.07}$	$-1.29^{+0.10}_{-0.09}$	−1.46	
XBSJ100309.4+554135	0.673	$3.88^{+0.050}_{-0.051}$	$3.71^{+0.010}_{-0.010}$	$44.91^{+0.08}_{-0.10}$	$45.14^{+0.08}_{-0.10}$	$9.12^{+0.11}_{-0.11}$	$8.87^{+0.05}_{-0.05}$	$8.87^{+0.05}_{-0.05}$	9.06	$-0.01^{+0.08}_{-0.08}$	$-1.23^{+0.09}_{-0.09}$	−1.42	
XBSJ100828.8+535408	0.384	$3.56^{+0.033}_{-0.033}$	$3.85^{+0.149}_{-0.123}$	$44.37^{+0.08}_{-0.09}$	$44.51^{+0.08}_{-0.10}$	$8.21^{+0.07}_{-0.08}$	$8.75^{+0.30}_{-0.24}$	$8.75^{+0.30}_{-0.24}$	8.80	$-0.82^{+0.07}_{-0.08}$	$-1.93^{+0.31}_{-0.25}$	−1.98	
XBSJ100921.7+534926	0.387	$3.63^{+0.049}_{-0.046}$	$3.74^{+0.007}_{-0.007}$	$44.10^{+0.12}_{-0.15}$	$44.30^{+0.11}_{-0.15}$	$8.22^{+0.12}_{-0.12}$	$8.41^{+0.05}_{-0.08}$	$8.22^{+0.12}_{-0.12}$	8.36	$-0.83^{+0.08}_{-0.10}$	$-1.41^{+0.14}_{-0.16}$	−1.55	
XBSJ100926.5+533426	1.718	–	$3.68^{+0.075}_{-0.091}$	$45.80^{+0.11}_{-0.10}$	$45.99^{+0.12}_{-0.10}$	–	$9.34^{+0.16}_{-0.19}$	$9.34^{+0.16}_{-0.19}$	9.68	$0.80^{+0.09}_{-0.07}$	$-0.90^{+0.18}_{-0.20}$	−1.24	2
XBSJ101506.0+520157	0.610	$3.40^{+0.050}_{-0.058}$	$3.79^{+0.028}_{-0.003}$	$44.73^{+0.11}_{-0.10}$	$44.97^{+0.12}_{-0.09}$	$8.07^{+0.10}_{-0.11}$	$8.92^{+0.08}_{-0.04}$	$8.92^{+0.08}_{-0.04}$	9.07	$-0.09^{+0.11}_{-0.08}$	$-1.37^{+0.14}_{-0.09}$	−1.52	2
XBSJ101838.0+411635	0.577	$3.48^{+0.132}_{-0.341}$	$3.82^{+0.014}_{-0.014}$	$44.43^{+0.08}_{-0.10}$	$44.67^{+0.08}_{-0.09}$	$8.09^{+0.25}_{-0.54}$	$8.79^{+0.05}_{-0.06}$	$8.79^{+0.05}_{-0.06}$	8.91	$-0.33^{+0.07}_{-0.07}$	$-1.48^{+0.09}_{-0.09}$	−1.60	
XBSJ101850.5+411506	0.577	$3.87^{+0.186}_{-0.335}$	$3.69^{+0.005}_{-0.005}$	$45.06^{+0.07}_{-0.10}$	$45.25^{+0.08}_{-0.09}$	$9.17^{+0.37}_{-0.65}$	$8.89^{+0.05}_{-0.04}$	$8.89^{+0.05}_{-0.04}$	9.10	$0.07^{+0.07}_{-0.08}$	$-1.18^{+0.09}_{-0.08}$	−1.39	

Table 1. continued.

Name	z	Log $FWHM$ Hβ	Log $FWHM$ MgIIλ2798 Å	Log λL_λ 5100 Å	Log λL_λ 3000 Å	Log M_{BH} Hβ	Log M_{BH} MgIIλ2798 Å	Log M_{BH} best	Log M_{BH} p_{rad}	Log $\dot{M}$	Log L/L_{Edd}	Log L/L_{Edd} p_{rad}	Flag
(1)	(2)	(3)	(4)	(5)	(6)	(7)	(8)	(9)	(10)	(11)	(12)	(13)	(14)
XBSJ101922.6+412049	0.239	$4.04^{+0.033}_{-0.378}$	–	$43.83^{+0.11}_{-0.10}$	$43.96^{+0.11}_{-0.10}$	$8.90^{+0.08}_{-0.75}$	–	$8.90^{+0.08}_{-0.75}$	8.92	$-1.05^{+0.05}_{-0.04}$	$-2.31^{+0.09}_{-0.75}$	−2.33	
XBSJ102412.3+042023	1.458	–	$3.68^{+0.130}_{-0.189}$	$45.54^{+0.11}_{-0.10}$	$45.77^{+0.11}_{-0.10}$	–	$9.19^{+0.26}_{-0.37}$	$9.19^{+0.26}_{-0.37}$	9.53	$0.64^{+0.10}_{-0.07}$	$-0.91^{+0.28}_{-0.38}$	−1.25	
XBSJ103120.0+311404	1.190	–	$3.86^{+0.020}_{-0.021}$	$45.08^{+0.15}_{-0.10}$	$45.31^{+0.15}_{-0.10}$	–	$9.27^{+0.09}_{-0.06}$	$9.27^{+0.09}_{-0.06}$	9.45	$0.35^{+0.09}_{-0.05}$	$-1.28^{+0.13}_{-0.08}$	−1.46	2
XBSJ103154.1+310732	0.299	$4.20^{+0.132}_{-0.093}$	–	$43.89^{+0.08}_{-0.09}$	$44.03^{+0.07}_{-0.10}$	$9.25^{+0.26}_{-0.19}$	–	$9.25^{+0.26}_{-0.19}$	9.26	$-1.22^{+0.06}_{-0.06}$	$-2.83^{+0.27}_{-0.20}$	−2.84	1
XBSJ103909.4+205222	0.980	–	$3.71^{+0.016}_{-0.017}$	$45.16^{+0.11}_{-0.10}$	$45.36^{+0.11}_{-0.10}$	–	$9.00^{+0.07}_{-0.05}$	$9.00^{+0.07}_{-0.05}$	9.24	$0.24^{+0.08}_{-0.06}$	$-1.12^{+0.11}_{-0.08}$	−1.36	
XBSJ103932.7+205426	0.237	$3.64^{+0.082}_{-0.066}$	–	$43.66^{+0.12}_{-0.09}$	$43.80^{+0.11}_{-0.10}$	$8.02^{+0.17}_{-0.13}$	–	$8.02^{+0.17}_{-0.13}$	8.09	$-1.36^{+0.07}_{-0.05}$	$-1.74^{+0.18}_{-0.14}$	−1.81	2
XBSJ103935.8+533036	0.229	$3.82^{+0.023}_{-0.024}$	–	$44.32^{+0.11}_{-0.15}$	$44.21^{+0.12}_{-0.15}$	$8.70^{+0.07}_{-0.09}$	–	$8.70^{+0.07}_{-0.09}$	8.74	$-0.99^{+0.09}_{-0.12}$	$-2.05^{+0.11}_{-0.15}$	−2.09	
XBSJ104026.9+204542	0.465	$3.73^{+0.014}_{-0.032}$	$3.63^{+0.055}_{-0.063}$	$44.32^{+0.08}_{-0.10}$	$44.58^{+0.08}_{-0.09}$	$8.52^{+0.05}_{-0.08}$	$8.36^{+0.11}_{-0.13}$	$8.52^{+0.05}_{-0.08}$	8.87	$-0.01^{+0.04}_{-0.04}$	$-0.89^{+0.06}_{-0.09}$	−1.24	
XBSJ104034.3+205110	0.670	–	$3.74^{+0.029}_{-0.032}$	$45.04^{+0.15}_{-0.16}$	$45.28^{+0.15}_{-0.15}$	–	$9.02^{+0.09}_{-0.10}$	$9.02^{+0.09}_{-0.10}$	9.24	$0.21^{+0.13}_{-0.15}$	$-1.17^{+0.16}_{-0.18}$	−1.39	2
XBSJ104509.3−012442	0.472	$3.53^{+0.020}_{-0.019}$	$3.48^{+0.011}_{-0.011}$	$44.08^{+0.08}_{-0.09}$	$44.28^{+0.08}_{-0.10}$	$8.00^{+0.06}_{-0.05}$	$7.86^{+0.05}_{-0.05}$	$8.00^{+0.06}_{-0.05}$	8.20	$-0.85^{+0.05}_{-0.06}$	$-1.21^{+0.08}_{-0.08}$	−1.41	
XBSJ104912.8+330459	0.226	$3.98^{+0.105}_{-0.083}$	–	$43.17^{+0.11}_{-0.15}$	$43.30^{+0.11}_{-0.15}$	$8.46^{+0.21}_{-0.18}$	–	$8.46^{+0.21}_{-0.18}$	8.48	$-1.40^{+0.02}_{-0.03}$	$-2.22^{+0.21}_{-0.18}$	−2.24	1
XBSJ105014.9+331013	1.012	–	$3.88^{+0.058}_{-0.024}$	$45.78^{+0.11}_{-0.14}$	$45.98^{+0.11}_{-0.14}$	–	$9.72^{+0.13}_{-0.09}$	$9.72^{+0.13}_{-0.09}$	9.87	$0.71^{+0.10}_{-0.13}$	$-1.37^{+0.16}_{-0.16}$	−1.52	
XBSJ105239.7+572431	1.113	–	$3.73^{+0.014}_{-0.015}$	$45.87^{+0.08}_{-0.10}$	$46.07^{+0.08}_{-0.10}$	–	$9.48^{+0.05}_{-0.06}$	$9.48^{+0.05}_{-0.06}$	9.76	$0.82^{+0.07}_{-0.09}$	$-1.02^{+0.09}_{-0.11}$	−1.30	2
XBSJ105316.9+573551	1.204	–	$3.55^{+0.056}_{-0.064}$	$45.38^{+0.08}_{-0.09}$	$45.58^{+0.08}_{-0.10}$	–	$8.82^{+0.12}_{-0.14}$	$8.82^{+0.12}_{-0.14}$	9.31	$0.53^{+0.05}_{-0.05}$	$-0.65^{+0.13}_{-0.15}$	−1.15	
XBSJ105624.2−033522	0.635	–	$3.69^{+0.012}_{-0.012}$	$44.82^{+0.07}_{-0.10}$	$45.01^{+0.08}_{-0.09}$	–	$8.75^{+0.05}_{-0.05}$	$8.75^{+0.05}_{-0.05}$	8.92	$-0.20^{+0.07}_{-0.08}$	$-1.31^{+0.09}_{-0.09}$	−1.48	
XBSJ110652.0−182738	1.435	–	$3.73^{+0.096}_{-0.125}$	$45.29^{+0.34}_{-0.40}$	$45.52^{+0.34}_{-0.40}$	–	$9.15^{+0.25}_{-0.31}$	$9.15^{+0.25}_{-0.31}$	9.47	$0.57^{+0.22}_{-0.18}$	$-0.94^{+0.33}_{-0.36}$	−1.26	2
XBSJ112022.3+125252	0.406	$3.46^{+0.041}_{-0.042}$	$3.61^{+0.021}_{-0.023}$	$44.26^{+0.08}_{-0.09}$	$44.49^{+0.08}_{-0.10}$	$7.96^{+0.08}_{-0.08}$	$8.26^{+0.06}_{-0.06}$	$8.26^{+0.06}_{-0.06}$	8.47	$-0.57^{+0.06}_{-0.06}$	$-1.19^{+0.08}_{-0.08}$	−1.40	
XBSJ112046.7+125429	0.382	$3.82^{+0.037}_{-0.041}$	$3.71^{+0.035}_{-0.038}$	$44.25^{+0.08}_{-0.09}$	$44.48^{+0.08}_{-0.10}$	$8.67^{+0.08}_{-0.09}$	$8.45^{+0.08}_{-0.09}$	$8.67^{+0.08}_{-0.09}$	8.76	$-0.59^{+0.06}_{-0.07}$	$-1.62^{+0.10}_{-0.11}$	−1.71	1 2
XBSJ113106.9+312518	1.482	–	$3.59^{+0.019}_{-0.020}$	$45.71^{+0.14}_{-0.16}$	$45.94^{+0.14}_{-0.16}$	–	$9.13^{+0.08}_{-0.09}$	$9.13^{+0.08}_{-0.09}$	9.63	$0.85^{+0.11}_{-0.12}$	$-0.64^{+0.14}_{-0.15}$	−1.14	
XBSJ115317.9+364712	0.725	–	$3.53^{+0.024}_{-0.026}$	$44.53^{+0.15}_{-0.15}$	$44.80^{+0.14}_{-0.16}$	–	$8.30^{+0.08}_{-0.09}$	$8.30^{+0.08}_{-0.09}$	8.75	$-0.05^{+0.13}_{-0.14}$	$-0.71^{+0.15}_{-0.17}$	−1.17	
XBSJ120359.1+443715	0.641	–	$3.72^{+0.014}_{-0.015}$	$44.76^{+0.11}_{-0.10}$	$44.95^{+0.12}_{-0.09}$	–	$8.77^{+0.06}_{-0.06}$	$8.77^{+0.06}_{-0.06}$	8.89	$-0.34^{+0.11}_{-0.10}$	$-1.47^{+0.13}_{-0.12}$	−1.59	
XBSJ120413.7+443149	0.492	–	$3.67^{+0.013}_{-0.014}$	$43.93^{+0.08}_{-0.09}$	$44.20^{+0.08}_{-0.10}$	–	$8.21^{+0.04}_{-0.06}$	$8.21^{+0.04}_{-0.06}$	8.39	$-0.70^{+0.08}_{-0.09}$	$-1.27^{+0.09}_{-0.11}$	−1.45	
XBSJ123036.2+642531	0.744	–	$3.56^{+0.036}_{-0.039}$	$44.67^{+0.12}_{-0.09}$	$44.80^{+0.12}_{-0.09}$	–	$8.36^{+0.09}_{-0.08}$	$8.36^{+0.09}_{-0.08}$	8.58	$-0.44^{+0.08}_{-0.07}$	$-1.16^{+0.12}_{-0.11}$	−1.38	2
XBSJ123116.5+641115	0.454	$4.18^{+0.086}_{-0.062}$	–	$43.89^{+0.08}_{-0.10}$	$44.03^{+0.07}_{-0.10}$	$9.21^{+0.18}_{-0.13}$	–	$9.21^{+0.18}_{-0.13}$	9.22	$-1.07^{+0.05}_{-0.04}$	$-2.64^{+0.19}_{-0.14}$	−2.65	1 2
XBSJ123218.5+640311	1.013	–	$3.51^{+0.130}_{-0.198}$	$44.79^{+0.14}_{-0.16}$	$44.98^{+0.15}_{-0.15}$	–	$8.36^{+0.25}_{-0.34}$	$8.36^{+0.25}_{-0.34}$	8.78	$-0.04^{+0.08}_{-0.07}$	$-0.76^{+0.26}_{-0.35}$	−1.18	2
XBSJ123759.6+621102	0.910	–	$3.71^{+0.007}_{-0.007}$	$45.41^{+0.08}_{-0.09}$	$45.61^{+0.08}_{-0.10}$	–	$9.16^{+0.05}_{-0.05}$	$9.16^{+0.05}_{-0.05}$	9.40	$0.40^{+0.06}_{-0.08}$	$-1.12^{+0.08}_{-0.09}$	−1.36	
XBSJ123800.9+621338	0.440	$3.62^{+0.044}_{-0.044}$	$3.79^{+0.002}_{-0.002}$	$44.57^{+0.08}_{-0.09}$	$44.77^{+0.08}_{-0.09}$	$8.44^{+0.09}_{-0.10}$	$8.80^{+0.04}_{-0.04}$	$8.44^{+0.09}_{-0.10}$	8.62	$-0.48^{+0.07}_{-0.08}$	$-1.28^{+0.11}_{-0.13}$	−1.46	
XBSJ124214.1−112512	0.820	–	$3.65^{+0.014}_{-0.014}$	$45.25^{+0.13}_{-0.11}$	$45.38^{+0.13}_{-0.11}$	–	$8.89^{+0.07}_{-0.06}$	$8.89^{+0.07}_{-0.06}$	9.12	$0.12^{+0.09}_{-0.08}$	$-1.13^{+0.11}_{-0.10}$	−1.36	
XBSJ124557.6+022659	0.708	$3.58^{+0.075}_{-0.075}$	$3.69^{+0.028}_{-0.029}$	$44.70^{+0.15}_{-0.15}$	$44.97^{+0.15}_{-0.16}$	$8.41^{+0.17}_{-0.16}$	$8.71^{+0.09}_{-0.10}$	$8.71^{+0.09}_{-0.10}$	9.04	$0.15^{+0.12}_{-0.13}$	$-0.92^{+0.15}_{-0.16}$	−1.25	
XBSJ124607.6+022153	0.491	$3.64^{+0.048}_{-0.047}$	$3.58^{+0.011}_{-0.012}$	$44.41^{+0.08}_{-0.09}$	$44.64^{+0.08}_{-0.10}$	$8.40^{+0.10}_{-0.10}$	$8.30^{+0.04}_{-0.06}$	$8.40^{+0.10}_{-0.10}$	8.61	$-0.42^{+0.06}_{-0.07}$	$-1.18^{+0.12}_{-0.12}$	−1.39	1
XBSJ124641.8+022412	0.934	–	$3.55^{+0.005}_{-0.005}$	$45.89^{+0.04}_{-0.10}$	$46.03^{+0.04}_{-0.10}$	–	$9.11^{+0.02}_{-0.06}$	$9.11^{+0.02}_{-0.06}$	9.53	$0.70^{+0.03}_{-0.08}$	$-0.77^{+0.04}_{-0.10}$	−1.19	
XBSJ124647.9+020955	1.074	–	$3.81^{+0.046}_{-0.052}$	$45.12^{+0.15}_{-0.15}$	$45.35^{+0.15}_{-0.15}$	–	$9.20^{+0.12}_{-0.13}$	$9.20^{+0.12}_{-0.13}$	9.36	$0.22^{+0.13}_{-0.12}$	$-1.34^{+0.18}_{-0.18}$	−1.50	
XBSJ124914.6−060910	1.627	–	$3.75^{+0.025}_{-0.027}$	$45.74^{+0.08}_{-0.09}$	$45.97^{+0.08}_{-0.10}$	–	$9.46^{+0.06}_{-0.07}$	$9.46^{+0.06}_{-0.07}$	9.75	$0.83^{+0.07}_{-0.09}$	$-0.99^{+0.09}_{-0.11}$	−1.29	2
XBSJ124949.4−060722	1.053	–	$3.42^{+0.017}_{-0.017}$	$45.35^{+0.08}_{-0.10}$	$45.55^{+0.08}_{-0.10}$	–	$8.53^{+0.05}_{-0.06}$	$8.53^{+0.05}_{-0.06}$	9.10	$0.34^{+0.06}_{-0.08}$	$-0.55^{+0.08}_{-0.10}$	−1.12	
XBSJ130619.7−233857	0.351	$3.86^{+0.035}_{-0.033}$	–	$44.49^{+0.15}_{-0.15}$	$44.72^{+0.15}_{-0.15}$	$8.87^{+0.11}_{-0.10}$	–	$8.87^{+0.11}_{-0.10}$	8.96	$-0.39^{+0.12}_{-0.12}$	$-1.62^{+0.16}_{-0.16}$	−1.71	
XBSJ130658.1−234849	0.375	$3.63^{+0.039}_{-0.038}$	–	$44.44^{+0.17}_{-0.23}$	$44.57^{+0.17}_{-0.22}$	$8.39^{+0.12}_{-0.13}$	–	$8.39^{+0.12}_{-0.13}$	8.51	$-0.73^{+0.15}_{-0.17}$	$-1.48^{+0.19}_{-0.21}$	−1.60	

Table 1. continued.

Name	z	Log $FWHM$ Hβ	Log $FWHM$ MgIIλ2798 Å	Log λL_λ 5100 Å	Log λL_λ 3000 Å	Log M_{BH} Hβ	Log M_{BH} MgIIλ2798 Å	Log M_{BH} best	Log M_{BH} p_{rad}	Log $\dot{M}$	Log L/L_{Edd}	Log L/L_{Edd} p_{rad}	Flag
(1)	(2)	(3)	(4)	(5)	(6)	(7)	(8)	(9)	(10)	(11)	(12)	(13)	(14)
XBSJ132038.0+341124	0.065	$3.56^{+0.042}_{-0.041}$	–	$43.41^{+0.12}_{-0.09}$	$43.55^{+0.11}_{-0.10}$	$7.73^{+0.10}_{-0.08}$	–	$7.73^{+0.10}_{-0.08}$	7.78	$-1.77^{+0.09}_{-0.08}$	$-1.86^{+0.13}_{-0.11}$	−1.91	
XBSJ132101.6+340656	0.335	$3.75^{+0.028}_{-0.030}$	$3.87^{+0.059}_{-0.113}$	$44.17^{+0.08}_{-0.10}$	$44.43^{+0.08}_{-0.09}$	$8.49^{+0.07}_{-0.08}$	$8.75^{+0.12}_{-0.23}$	$8.49^{+0.07}_{-0.08}$	8.68	$-0.39^{+0.06}_{-0.09}$	$-1.24^{+0.09}_{-0.12}$	−1.43	
XBSJ133807.5+242411	0.631	$3.36^{+0.023}_{-0.024}$	$3.65^{+0.010}_{-0.010}$	$45.24^{+0.08}_{-0.09}$	$45.44^{+0.08}_{-0.10}$	$8.24^{+0.06}_{-0.06}$	$8.93^{+0.04}_{-0.06}$	$8.93^{+0.04}_{-0.06}$	9.17	$0.18^{+0.07}_{-0.09}$	$-1.11^{+0.08}_{-0.11}$	−1.35	
XBSJ134749.9+582111	0.646	$3.94^{+0.030}_{-0.028}$	$3.81^{+0.004}_{-0.004}$	$45.74^{+0.08}_{-0.10}$	$45.96^{+0.08}_{-0.09}$	$9.65^{+0.07}_{-0.07}$	$9.58^{+0.04}_{-0.05}$	$9.65^{+0.07}_{-0.07}$	9.87	$0.84^{+0.06}_{-0.08}$	$-1.17^{+0.09}_{-0.11}$	−1.39	
XBSJ140102.0−111224	0.037	$3.58^{+0.489}_{-0.418}$	–	$43.26^{+0.09}_{-0.11}$	$43.16^{+0.09}_{-0.11}$	$7.71^{+0.96}_{-0.82}$	–	$7.71^{+0.96}_{-0.82}$	7.74	$-2.06^{+0.07}_{-0.09}$	$-2.13^{+0.96}_{-0.82}$	−2.16	
XBSJ140113.4+024016	0.631	$3.54^{+0.220}_{-0.111}$	$3.66^{+0.038}_{-0.011}$	$43.58^{+0.12}_{-0.15}$	$43.85^{+0.11}_{-0.16}$	$7.77^{+0.44}_{-0.22}$	$7.97^{+0.09}_{-0.08}$	$7.77^{+0.44}_{-0.22}$	8.08	$-0.82^{+0.07}_{-0.09}$	$-0.95^{+0.45}_{-0.24}$	−1.27	2
XBSJ140127.7+025605	0.265	$3.51^{+0.017}_{-0.016}$	–	$44.30^{+0.08}_{-0.16}$	$44.43^{+0.08}_{-0.16}$	$8.08^{+0.05}_{-0.09}$	–	$8.08^{+0.05}_{-0.09}$	8.36	$-0.59^{+0.03}_{-0.06}$	$-1.03^{+0.06}_{-0.11}$	−1.31	
XBSJ140921.1+261336	1.100	–	$3.62^{+0.035}_{-0.039}$	$45.56^{+0.17}_{-0.16}$	$45.82^{+0.18}_{-0.15}$	–	$9.10^{+0.12}_{-0.10}$	$9.10^{+0.12}_{-0.10}$	9.74	$1.01^{+0.15}_{-0.12}$	$-0.45^{+0.19}_{-0.16}$	−1.09	2
XBSJ141531.5+113156	0.257	$4.09^{+0.081}_{-0.074}$	–	$44.08^{+0.08}_{-0.10}$	$43.97^{+0.08}_{-0.09}$	$9.13^{+0.17}_{-0.15}$	–	$9.13^{+0.17}_{-0.15}$	9.14	$-1.06^{+0.05}_{-0.05}$	$-2.55^{+0.18}_{-0.16}$	−2.56	
XBSJ144937.5+090826	1.260	–	$3.86^{+0.017}_{-0.017}$	$45.47^{+0.11}_{-0.10}$	$45.66^{+0.12}_{-0.09}$	–	$9.50^{+0.07}_{-0.06}$	$9.50^{+0.07}_{-0.06}$	9.67	$0.56^{+0.08}_{-0.06}$	$-1.30^{+0.11}_{-0.08}$	−1.47	
XBSJ150428.3+101856	1.010	–	$3.73^{+0.006}_{-0.007}$	$45.90^{+0.11}_{-0.10}$	$46.13^{+0.11}_{-0.10}$	–	$9.52^{+0.05}_{-0.06}$	$9.52^{+0.05}_{-0.06}$	9.85	$0.95^{+0.11}_{-0.09}$	$-0.93^{+0.12}_{-0.11}$	−1.26	
XBSJ151815.0+060851	1.294	–	$3.96^{+0.011}_{-0.011}$	$45.42^{+0.13}_{-0.20}$	$45.65^{+0.13}_{-0.20}$	–	$9.68^{+0.07}_{-0.10}$	$9.68^{+0.07}_{-0.10}$	9.80	$0.55^{+0.11}_{-0.15}$	$-1.49^{+0.13}_{-0.18}$	−1.61	
XBSJ153205.7−082952	1.239	–	$3.78^{+0.049}_{-0.055}$	$45.42^{+0.15}_{-0.15}$	$45.69^{+0.14}_{-0.16}$	–	$9.36^{+0.11}_{-0.14}$	$9.36^{+0.11}_{-0.14}$	9.71	$0.83^{+0.13}_{-0.14}$	$-0.89^{+0.17}_{-0.20}$	−1.24	
XBSJ153419.0+011808	1.283	–	$3.87^{+0.020}_{-0.021}$	$45.55^{+0.15}_{-0.15}$	$45.82^{+0.14}_{-0.16}$	–	$9.61^{+0.08}_{-0.09}$	$9.61^{+0.08}_{-0.09}$	9.90	$0.97^{+0.13}_{-0.14}$	$-1.00^{+0.15}_{-0.17}$	−1.29	
XBSJ153456.1+013033	0.310	$3.51^{+0.037}_{-0.041}$	$3.79^{+0.013}_{-0.014}$	$44.70^{+0.21}_{-0.15}$	$44.95^{+0.20}_{-0.16}$	$8.27^{+0.13}_{-0.11}$	$8.90^{+0.10}_{-0.08}$	$8.90^{+0.10}_{-0.08}$	9.04	$-0.13^{+0.19}_{-0.15}$	$-1.39^{+0.21}_{-0.17}$	−1.53	
XBSJ160706.6+075709	0.233	$3.42^{+0.055}_{-0.059}$	–	$43.88^{+0.08}_{-0.09}$	$44.02^{+0.08}_{-0.10}$	$7.70^{+0.10}_{-0.11}$	–	$7.70^{+0.10}_{-0.11}$	7.87	$-1.24^{+0.06}_{-0.07}$	$-1.30^{+0.12}_{-0.13}$	−1.47	
XBSJ160731.5+081202	0.226	$3.18^{+0.059}_{-0.079}$	–	$43.44^{+0.12}_{-0.09}$	$43.71^{+0.11}_{-0.10}$	$6.99^{+0.09}_{-0.11}$	–	$6.99^{+0.09}_{-0.11}$	7.64	$-1.09^{+0.09}_{-0.08}$	$-0.44^{+0.13}_{-0.14}$	−1.09	
XBSJ161615.1+121353	0.843	–	$3.90^{+0.091}_{-0.104}$	$44.35^{+0.08}_{-0.16}$	$44.48^{+0.08}_{-0.16}$	–	$8.84^{+0.19}_{-0.22}$	$8.84^{+0.19}_{-0.22}$	8.92	$-0.49^{+0.03}_{-0.05}$	$-1.69^{+0.19}_{-0.23}$	−1.77	2
XBSJ161825.4+124145	0.396	$3.53^{+0.125}_{-0.127}$	–	$44.22^{+0.15}_{-0.09}$	$44.42^{+0.15}_{-0.10}$	$8.08^{+0.25}_{-0.24}$	–	$8.08^{+0.25}_{-0.24}$	8.28	$-0.78^{+0.12}_{-0.08}$	$-1.22^{+0.28}_{-0.25}$	−1.42	
XBSJ165406.6+142123	0.641	–	$3.68^{+0.030}_{-0.032}$	$45.40^{+0.15}_{-0.16}$	$45.29^{+0.15}_{-0.15}$	–	$8.90^{+0.09}_{-0.10}$	$8.90^{+0.09}_{-0.10}$	9.10	$0.04^{+0.13}_{-0.13}$	$-1.22^{+0.16}_{-0.16}$	−1.42	
XBSJ165425.3+142159	0.178	$3.39^{+0.141}_{-0.228}$	–	$43.83^{+0.12}_{-0.09}$	$43.97^{+0.11}_{-0.10}$	$7.61^{+0.26}_{-0.36}$	–	$7.61^{+0.26}_{-0.36}$	7.90	$-1.02^{+0.04}_{-0.04}$	$-0.99^{+0.26}_{-0.36}$	−1.29	2
XBSJ165448.5+141311	0.320	–	$4.01^{+0.014}_{-0.014}$	$43.77^{+0.08}_{-0.10}$	$43.97^{+0.08}_{-0.10}$	–	$8.75^{+0.05}_{-0.06}$	$8.75^{+0.05}_{-0.06}$	8.81	$-0.68^{+0.02}_{-0.02}$	$-1.79^{+0.05}_{-0.06}$	−1.85	2
XBSJ185518.7−462504	0.788	–	$3.66^{+0.021}_{-0.023}$	$45.83^{+0.17}_{-0.23}$	$45.96^{+0.18}_{-0.22}$	–	$9.28^{+0.10}_{-0.12}$	$9.28^{+0.10}_{-0.12}$	9.57	$0.63^{+0.16}_{-0.18}$	$-1.01^{+0.19}_{-0.22}$	−1.30	
XBSJ185613.7−462239	0.768	–	$3.63^{+0.074}_{-0.091}$	$44.87^{+0.15}_{-0.16}$	$45.07^{+0.14}_{-0.16}$	–	$8.67^{+0.16}_{-0.19}$	$8.67^{+0.16}_{-0.19}$	8.96	$0.02^{+0.09}_{-0.08}$	$-1.01^{+0.18}_{-0.21}$	−1.30	
XBSJ204159.2−321439	0.738	$3.47^{+0.105}_{-0.142}$	$3.60^{+0.018}_{-0.019}$	$44.79^{+0.15}_{-0.15}$	$44.99^{+0.15}_{-0.16}$	$8.25^{+0.21}_{-0.26}$	$8.55^{+0.09}_{-0.08}$	$8.55^{+0.09}_{-0.08}$	8.83	$-0.11^{+0.10}_{-0.10}$	$-1.02^{+0.13}_{-0.13}$	−1.30	
XBSJ204204.1−321601	0.384	$3.87^{+0.073}_{-0.088}$	$3.85^{+0.047}_{-0.052}$	$43.82^{+0.17}_{-0.16}$	$44.08^{+0.18}_{-0.16}$	$8.56^{+0.16}_{-0.19}$	$8.48^{+0.13}_{-0.13}$	$8.48^{+0.13}_{-0.13}$	8.57	$-0.77^{+0.16}_{-0.13}$	$-1.61^{+0.21}_{-0.18}$	−1.70	
XBSJ204208.2−323523	1.184	–	$3.75^{+0.021}_{-0.028}$	$44.88^{+0.17}_{-0.30}$	$45.12^{+0.18}_{-0.30}$	–	$8.93^{+0.09}_{-0.16}$	$8.93^{+0.09}_{-0.16}$	9.15	$0.13^{+0.14}_{-0.21}$	$-1.16^{+0.17}_{-0.26}$	−1.38	2
XBSJ205635.7−044717	0.217	$3.39^{+0.030}_{-0.030}$	–	$43.84^{+0.15}_{-0.15}$	$44.07^{+0.15}_{-0.15}$	$7.60^{+0.10}_{-0.09}$	–	$7.60^{+0.10}_{-0.09}$	7.90	$-1.01^{+0.11}_{-0.11}$	$-0.97^{+0.15}_{-0.14}$	−1.28	
XBSJ205829.9−423634	0.232	$3.62^{+0.045}_{-0.046}$	–	$43.44^{+0.18}_{-0.22}$	$43.64^{+0.17}_{-0.22}$	$7.88^{+0.12}_{-0.15}$	–	$7.88^{+0.12}_{-0.15}$	8.02	$-1.15^{+0.06}_{-0.06}$	$-1.39^{+0.13}_{-0.16}$	−1.53	1
XBSJ210325.4−112011	0.720	–	$4.00^{+0.011}_{-0.011}$	$45.48^{+0.56}_{-0.44}$	$45.70^{+0.56}_{-0.44}$	–	$9.79^{+0.28}_{-0.22}$	$9.79^{+0.28}_{-0.22}$	9.88	$0.53^{+0.54}_{-0.40}$	$-1.62^{+0.61}_{-0.46}$	−1.71	2
XBSJ210355.3−121858	0.792	–	$3.94^{+0.021}_{-0.022}$	$44.97^{+0.15}_{-0.22}$	$45.10^{+0.15}_{-0.22}$	–	$9.30^{+0.09}_{-0.12}$	$9.30^{+0.09}_{-0.12}$	9.36	$-0.14^{+0.11}_{-0.15}$	$-1.80^{+0.14}_{-0.19}$	−1.86	
XBSJ213002.3−153414	0.562	$3.36^{+0.067}_{-0.089}$	$3.36^{+0.011}_{-0.011}$	$45.61^{+0.15}_{-0.16}$	$45.74^{+0.15}_{-0.15}$	$8.44^{+0.14}_{-0.17}$	$8.53^{+0.08}_{-0.07}$	$8.53^{+0.08}_{-0.07}$	9.13	$0.39^{+0.14}_{-0.13}$	$-0.50^{+0.16}_{-0.15}$	−1.10	
XBSJ213729.7−423601	0.664	$3.56^{+0.059}_{-0.033}$	$3.68^{+0.014}_{-0.014}$	$44.77^{+0.18}_{-0.15}$	$44.90^{+0.18}_{-0.15}$	$8.41^{+0.14}_{-0.10}$	$8.66^{+0.09}_{-0.08}$	$8.41^{+0.14}_{-0.10}$	8.66	$-0.32^{+0.13}_{-0.10}$	$-1.09^{+0.19}_{-0.14}$	−1.34	
XBSJ213733.2−434800	0.427	$3.56^{+0.084}_{-0.089}$	$3.60^{+0.047}_{-0.053}$	$44.23^{+0.20}_{-0.22}$	$44.42^{+0.21}_{-0.22}$	$8.15^{+0.19}_{-0.20}$	$8.21^{+0.14}_{-0.15}$	$8.15^{+0.19}_{-0.20}$	8.33	$-0.76^{+0.16}_{-0.17}$	$-1.27^{+0.25}_{-0.26}$	−1.45	2
XBSJ214041.4−234720	0.490	$4.36^{+0.083}_{-0.070}$	$3.93^{+0.015}_{-0.016}$	$44.90^{+0.12}_{-0.09}$	$45.13^{+0.11}_{-0.10}$	$10.08^{+0.18}_{-0.14}$	$9.31^{+0.06}_{-0.06}$	$9.31^{+0.06}_{-0.06}$	9.39	$0.01^{+0.10}_{-0.08}$	$-1.66^{+0.12}_{-0.10}$	−1.74	

Table 1. continued.

Name	z	Log $FWHM$ Hβ	Log $FWHM$ MgIIλ2798 Å	Log λL_λ 5100 Å	Log λL_λ 3000 Å	Log $M_{\rm BH}$ Hβ	Log $M_{\rm BH}$ MgIIλ2798 Å	Log $M_{\rm BH}$ best	Log $M_{\rm BH}$ $p_{\rm rad}$	Log $\dot{M}$	Log $L/L_{\rm Edd}$	Log $L/L_{\rm Edd}$ $p_{\rm rad}$	Flag
(1)	(2)	(3)	(4)	(5)	(6)	(7)	(8)	(9)	(10)	(11)	(12)	(13)	(14)
XBSJ220446.8−014535	0.540	$3.73^{+0.148}_{-0.162}$	$3.99^{+0.074}_{-0.089}$	$44.12^{+0.20}_{-0.30}$	$44.38^{+0.21}_{-0.30}$	$8.42^{+0.31}_{-0.34}$	$8.96^{+0.18}_{-0.23}$	$8.42^{+0.31}_{-0.34}$	8.64	$-0.38^{+0.16}_{-0.20}$	$-1.16^{+0.35}_{-0.39}$	−1.38	2
XBSJ221623.3−174317	0.754	–	$3.39^{+0.069}_{-0.083}$	$44.70^{+0.16}_{-0.26}$	$44.90^{+0.16}_{-0.27}$	–	$8.08^{+0.16}_{-0.20}$	$8.08^{+0.16}_{-0.20}$	8.55	$-0.24^{+0.12}_{-0.16}$	$-0.68^{+0.20}_{-0.26}$	−1.16	
XBSJ223547.9−255836	0.304	$3.61^{+0.034}_{-0.034}$	$3.39^{+0.124}_{-0.138}$	$43.92^{+0.15}_{-0.15}$	$44.15^{+0.15}_{-0.15}$	$8.09^{+0.09}_{-0.10}$	$7.61^{+0.23}_{-0.25}$	$8.09^{+0.09}_{-0.10}$	8.23	$-0.95^{+0.12}_{-0.11}$	$-1.40^{+0.15}_{-0.15}$	−1.54	
XBSJ223555.0−255833	1.800	–	$3.71^{+0.028}_{-0.030}$	$46.23^{+0.21}_{-0.22}$	$46.43^{+0.20}_{-0.22}$	–	$9.66^{+0.11}_{-0.13}$	$9.66^{+0.11}_{-0.13}$	10.03	$1.17^{+0.19}_{-0.20}$	$-0.85^{+0.22}_{-0.24}$	−1.22	
XBSJ223949.8+080926	1.406	–	$3.73^{+0.037}_{-0.041}$	$46.01^{+0.23}_{-0.40}$	$46.20^{+0.23}_{-0.39}$	–	$9.57^{+0.14}_{-0.21}$	$9.57^{+0.14}_{-0.21}$	9.87	$0.95^{+0.21}_{-0.35}$	$-0.98^{+0.25}_{-0.41}$	−1.28	
XBSJ224756.6−642721	0.598	$3.68^{+0.035}_{-0.031}$	$3.67^{+0.004}_{-0.004}$	$45.00^{+0.11}_{-0.16}$	$45.23^{+0.11}_{-0.16}$	$8.78^{+0.09}_{-0.10}$	$8.84^{+0.06}_{-0.08}$	$8.78^{+0.09}_{-0.10}$	9.03	$0.06^{+0.11}_{-0.14}$	$-1.08^{+0.14}_{-0.17}$	−1.33	2
XBSJ225025.1−643225	1.206	–	$3.76^{+0.066}_{-0.078}$	$45.28^{+0.18}_{-0.15}$	$45.48^{+0.18}_{-0.16}$	–	$9.17^{+0.16}_{-0.17}$	$9.17^{+0.16}_{-0.17}$	9.36	$0.28^{+0.15}_{-0.11}$	$-1.25^{+0.22}_{-0.20}$	−1.44	
XBSJ225050.2−642900	1.251	–	$3.88^{+0.036}_{-0.020}$	$45.82^{+0.15}_{-0.16}$	$45.95^{+0.15}_{-0.15}$	–	$9.71^{+0.11}_{-0.08}$	$9.71^{+0.11}_{-0.08}$	9.85	$0.69^{+0.11}_{-0.10}$	$-1.38^{+0.16}_{-0.13}$	−1.53	
XBSJ225118.0−175951	0.172	$3.40^{+0.028}_{-0.030}$	–	$44.29^{+0.54}_{-0.34}$	$44.55^{+0.54}_{-0.34}$	$7.86^{+0.27}_{-0.18}$	–	$7.86^{+0.27}_{-0.18}$	8.43	$-0.33^{+0.53}_{-0.34}$	$-0.55^{+0.59}_{-0.38}$	−1.12	
XBSJ230400.4−083755	0.411	$3.95^{+0.053}_{-0.048}$	$3.74^{+0.013}_{-0.014}$	$44.50^{+0.18}_{-0.15}$	$44.75^{+0.17}_{-0.16}$	$9.05^{+0.14}_{-0.12}$	$8.68^{+0.08}_{-0.09}$	$9.05^{+0.14}_{-0.12}$	9.12	$-0.33^{+0.16}_{-0.15}$	$-1.74^{+0.21}_{-0.19}$	−1.81	
XBSJ230443.8+121636	1.405	–	$3.89^{+0.049}_{-0.056}$	$45.71^{+0.32}_{-0.44}$	$45.90^{+0.32}_{-0.44}$	–	$9.70^{+0.18}_{-0.25}$	$9.70^{+0.18}_{-0.25}$	9.85	$0.70^{+0.28}_{-0.30}$	$-1.36^{+0.33}_{-0.39}$	−1.51	2
XBSJ230459.6+121205	0.560	$3.21^{+0.063}_{-0.077}$	–	$44.16^{+0.19}_{-0.27}$	$44.29^{+0.19}_{-0.27}$	$7.41^{+0.14}_{-0.18}$	–	$7.41^{+0.14}_{-0.18}$	8.16	$-0.54^{+0.06}_{-0.06}$	$-0.31^{+0.15}_{-0.19}$	−1.06	1 2
XBSJ231342.5−423210	0.973	–	$3.74^{+0.046}_{-0.052}$	$45.24^{+0.12}_{-0.10}$	$45.44^{+0.11}_{-0.10}$	–	$9.12^{+0.11}_{-0.11}$	$9.12^{+0.11}_{-0.11}$	9.33	$0.30^{+0.08}_{-0.06}$	$-1.18^{+0.14}_{-0.13}$	−1.39	
XBSJ231601.7−424038	0.383	$3.66^{+0.033}_{-0.057}$	–	$44.05^{+0.11}_{-0.16}$	$44.32^{+0.11}_{-0.16}$	$8.25^{+0.09}_{-0.14}$	–	$8.25^{+0.09}_{-0.14}$	8.48	$-0.52^{+0.10}_{-0.13}$	$-1.13^{+0.13}_{-0.19}$	−1.36	

Monthly Notices
of the
ROYAL ASTRONOMICAL SOCIETY

MNRAS **433,** 648–658 (2013)
Advance Access publication 2013 May 21

doi:10.1093/mnras/stt757

Studying the relationship between X-ray emission and accretion in AGN using the *XMM–Newton* Bright Serendipitous Survey

R. Fanali,[1,2]★ A. Caccianiga,[1] P. Severgnini,[1] R. Della Ceca,[1] E. Marchese,[2] F. J. Carrera,[3] A. Corral[4] and S. Mateos[3]

[1]*INAF – Osservatorio Astronomico di Brera, via Brera 28, I-20121 Milan, Italy*
[2]*Universitá degli Studi di Milano Bicocca, Piazza Della Scienza 3, I-20126 Milan, Italy*
[3]*Instituto de Fisica de Cantabria (CSIC-UC), Avenida de los Castros, 39005 Santander, Spain*
[4]*National Observatory of Athens (NOA), Palaia Penteli, 15236 Athens, Greece*

Accepted 2013 April 29. Received 2013 April 29; in original form 2013 February 18

ABSTRACT

We study the link between the X-ray emission in radio-quiet active galactic nuclei (AGN) and the accretion rate on the central supermassive black hole using a statistically well-defined and representative sample of 71 type 1 AGN extracted from the *XMM–Newton* Bright Serendipitous Survey. We search and quantify the statistical correlations between some fundamental parameters that characterize the X-ray emission, i.e. the X-ray spectral slope, Γ, and the X-ray 'loudness', and the accretion rate, both absolute ($\dot{M}$) and normalized to the Eddington luminosity (Eddington ratio, λ). We parametrize the X-ray loudness using three different quantities: the bolometric correction $K_{\rm bol}$, the two-point spectral index $\alpha_{\rm OX}$ and the disc/corona luminosity ratio. We find that the X-ray spectral index depends on the normalized accretion rate while the 'X-ray loudness' depends on both the normalized and the absolute accretion rate. The dependence on the Eddington ratio, in particular, is probably induced by the $\Gamma - \lambda$ correlation. The two proxies usually adopted in the literature to quantify the X-ray loudness of an AGN, i.e. $K_{\rm bol}$ and $\alpha_{\rm OX}$, behave differently, with $K_{\rm bol}$ being more sensitive to the Eddington ratio and $\alpha_{\rm OX}$ having a stronger dependence with the absolute accretion. The explanation of this result is likely related to the different sensitivity of the two parameters to the X-ray spectral index.

Key words: galaxies: active – galaxies: nuclei – quasars: general – X-rays: galaxies.

1 INTRODUCTION

The engine of active galactic nuclei (AGN) is powered by the accretion of matter on to the supermassive black hole (SMBH), placed in the centre of the host galaxy: the matter is heated (10^5–10^6 K) through viscous and magnetic processes and forms an accretion disc around the SMBH emitting in the ultraviolet (UV)–optical region. A fraction of energy is also emitted in the X-ray band with a spectrum that can be represented, at first order, by a power law from 0.1 to 100 keV at rest frame. In the now accepted disc–corona model (Haardt & Maraschi 1991), the X-rays are produced in a hot ($T = 10^8$–10^9 K) corona, reprocessing the primary UV–optical emission of the disc via inverse-Compton mechanism. X-rays are a probe of accretion since they are produced in the very inner part of the nucleus and carry direct information on the physics very close to the SMBH. For instance, the hard X-ray spectral index (Γ) gives direct information about the energy distribution of the electrons in the corona, while the intensity of the X-ray emission with respect to the UV–optical emission quantifies the relative importance between disc and corona. This latter quantity is often parametrized with the X-ray bolometric correction $K_{\rm bol}$ (e.g. Vasudevan & Fabian 2009), defined as the ratio between bolometric luminosity and 2–10 keV luminosity, or with the two-point spectral index $\alpha_{\rm OX}$ (e.g. Vignali, Brandt & Schneider 2003), defined between 2500 Å and 2 keV. The different values of X-ray spectral index and of the disc/corona luminosity ratio observed from source to source are likely a consequence of fundamental differences in the physical parameters of the central engine.

First studies, essentially based on *ROSAT* data, suggested correlations between the 'soft' spectral index $\Gamma_{(0.5–2.4)\,\rm keV}$ and the full width at half-maximum (FWHM) of Hβ emission line coming from the broad line region (BLR; Wang, Brinkmann & Bergeron 1996; Laor et al. 1997; Sulentic, Marziani & Dultzin-Hacyan 2000; Grupe et al. 2004). Assuming that BLR dynamics is directly dependent on the black hole (BH) mass, this correlation was suggesting a direct link between $\Gamma_{(0.5–2.4)\,\rm keV}$ and some physical parameters like the BH mass or accretion rate. In particular, it was suggested that the main

★ E-mail: r.fanali@campus.unimib.it

© 2013 The Authors
Published by Oxford University Press on behalf of the Royal Astronomical Society

Downloaded from http://mnras.oxfordjournals.org/ at INAF Brera Milano (Osservatorio Astronomico di Brera) on May 7, 2015

physical driver of this correlation is the accretion rate normalized to the Eddington luminosity[1] (Eddington ratio): sources accreting close to the Eddington limit produce the steepest values of $\Gamma_{(0.5\text{–}2.4)\,\mathrm{keV}}$ (Laor et al. 1997; Sulentic et al. 2000; Grupe et al. 2004; Wang, Watarai & Mineshige 2004). However, since the measured value of $\Gamma_{0.5\text{–}2.4\,\mathrm{keV}}$ can be significantly contaminated by the presence of a spectral component called 'soft excess',[2] it was difficult to establish on a firm ground whether it was the slope of the primary emission that correlates with the accretion rate or, instead, it was the intensity of the soft excess.

Using *ASCA* observations, Brandt, Mathur & Elvis (1997) and Wang et al. (2004) have found that also the 'hard' spectral slope ($\Gamma_{(2\text{–}10)\,\mathrm{keV}}$) has a strong dependence with the FWHM(Hβ). Since the 2–10 keV energy range is not affected by the 'soft excess', this result was considered as a compelling indication that the slope of the primary component of the X-ray emission actually correlates with FWHM(Hβ). First studies made with *XMM–Newton*, *Chandra* and *Swift*-X-Ray Telescope (XRT) have further suggested the possible presence of a second trend, i.e. an anticorrelation between $\Gamma_{(2\text{–}10)\,\mathrm{keV}}$ and the BH mass M_{BH} (Porquet et al. 2004; Piconcelli et al. 2005). The availability of hard X-ray data from *XMM–Newton* and *Chandra* and of statistical relations that allow the systematic computation of M_{BH} on large numbers of AGN have produced in the very recent years a big leap forward on this kind of study, extending the analysis on significantly larger samples, including up to a few hundreds of sources (Kelly et al. 2008; Shemmer et al. 2008; Gu & Cao 2009; Risaliti, Young & Elvis 2009; Grupe et al. 2010; Zhou & Zhang 2010). These studies seem to confirm the presence of a correlation between the hard Γ and the Eddington ratio (Risaliti et al. 2009; Grupe et al. 2010) with some exceptions (Bianchi et al. 2009). Shemmer et al. (2008) have also demonstrated that the observed strong anticorrelation usually observed between Γ and FWHM(Hβ) is a secondary correlation induced by the dependence between Γ and the Eddington ratio.

Also the bolometric correction is expected to be related to the physical parameters that regulate the accretion mechanism. A possible dependence of the K_{bol} with the luminosity has been suggested (Marconi et al. 2004; Hopkins, Richards & Herquist 2007), but more recent observations seem to point out that the principal dependence is between K_{bol} and the Eddington ratio (Vasudevan & Fabian 2007, 2009; Kelly et al. 2008; Lusso et al. 2012). An alternative way to study the relative intensity between disc and corona is through the α_{OX}, defined as the slope between 2500 Å and 2 keV. Past studies generally found a strong correlation between α_{OX} and L_{UV} (e.g. Vignali et al. 2003; Marchese et al. 2012) or L_{bol} (Kelly et al. 2008; Shemmer et al. 2008) while a dependence of α_{OX} with the Eddington ratio is usually weak or absent (Young, Elvis & Risaliti 2010), contrary to what has been found for K_{bol}. This is quite surprising since K_{bol} and α_{OX} are both supposed to be proxies of the disc/corona relative intensity and, therefore, they are somehow expected to behave in a similar way.

In this paper we investigate the link between X-ray properties and the accretion rate by analysing a well-defined sample of type 1 AGN selected from the *XMM–Newton* Bright Serendipitous Survey (XBS). In particular, we study the spectral index Γ estimated in the energy range 0.5–10 and 2–10 keV and three different parameters that quantify the 'X-ray loudness', i.e. the bolometric correction K_{bol}, the α_{OX} and the disc/corona luminosity ratio (i.e. the ratio between the accretion disc luminosity and the 0.1–100 keV X-ray luminosity). The approach followed in this study is to search for statistically significant correlations between these parameters and the value of accretion rate, both absolute and normalized to Eddington luminosity.

The structure of the paper is the following. In Section 2 we describe the survey, the sample selection and the parameters used for our work. In Section 3 we describe the statistical analysis used to find the correlations between the parameters, taking into account a number of potential biases. In Section 4 we present our results. Finally, in Section 5 we report the summary and conclusions.

We assume here a flat Λ cold dark matter (ΛCDM) cosmology with $H_0 = 65$ km s^{-1} Mpc^{-1}, $\Omega_\Lambda = 0.7$ and $\Omega_{\mathrm{M}} = 0.3$.

2 *XMM–NEWTON* BRIGHT SERENDIPITOUS SURVEY

The XBS is a wide-angle ($\sim$28 deg^2) high Galactic latitude ($|b| > 20^\circ$) survey based on the *XMM–Newton* archival data. It is composed of two flux-limited samples: the *XMM* Bright Source Sample (BSS; 0.5–4.5 keV band, 389 sources) and the *XMM* Hard Bright Source Sample (HBSS; 4.5–7.5 keV band, 67 sources, with 56 sources in common with the BSS sample), having a flux limit of $\sim 7 \times 10^{-14}$ erg cm^{-2} s^{-1} in both energy selection bands. Selection criteria and properties of these samples are described in Della Ceca et al. (2004). The XBS is composed of sources that are detected serendipitously in the field-of-view of the *XMM–Newton* pointing, thus excluding the targets of the observations. For this reason the XBS can be considered as representative of the X-ray sky down to its flux limit.

To date, the spectroscopic identification level has reached 98 and 100 per cent in the BSS and the HBSS samples, respectively. Most of the spectroscopic identifications are presented and discussed in Caccianiga et al. (2007, 2008).

The availability of good *XMM–Newton* data for the sources in the XBS sample, spanning the energy range between $\sim$0.3 and $\sim$10 keV, allowed us to perform a reliable X-ray spectral analysis for almost every AGN of the sample (Corral et al. 2011).

2.1 The sample

Since the goal of this paper is the study of the possible dependence of Γ, K_{bol}, α_{OX} and the disc/corona luminosity ratio on the accretion rate, we restrict the analysis to the subsample of radio-quiet 154 type 1 AGN for which all these parameters have been already derived by fitting the UV–optical spectral energy distribution (SEDs) of the sources (Marchese et al. 2012) and by studying the X-ray and optical spectra. The radio-loud AGN of the sample (see Galbiati et al. 2005) were not considered to avoid possible contamination from the relativistic jet to the SED. The analysis of the SEDs was carried out on a subset of objects for which optical and UV data are available (either a detection or an upper limit) from existing catalogues [Sloan Digital Sky Survey (SDSS) and *Galaxy Evolution Explorer* (*GALEX*)]. Since the availability of these data depends mainly on the position of the source in the sky and not on its intrinsic properties, this subset can be confidently considered as a representative

[1] The Eddington luminosity is a theoretical limit beyond which the accretion process stops for effect of radiation pressure.

[2] The 'soft excess' is an excess of counts, at energies below 2 keV, with respect to the power-law component fitted at higher energies (typically between 2 and 10 keV).

Downloaded from http://mnras.oxfordjournals.org/ at INAF Brera Milano (Osservatorio Astronomico di Brera) on May 7, 2015

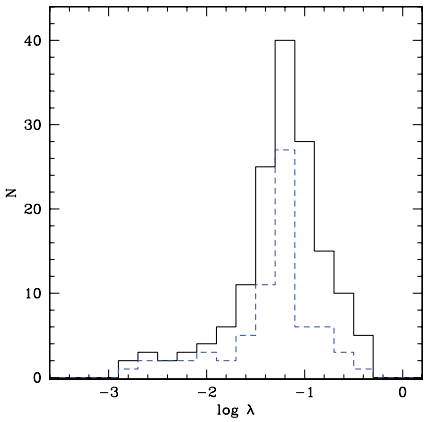

Figure 1. Eddington ratio distribution for the total sample presented in Marchese et al. (2012) (solid black line, 154 AGN) and for the subsample used here (dashed blue line, 71 AGN). The K–S test gives a probability for the null hypothesis (i.e. the two distributions are drawn from the same parent population) of 0.12.

subsample of the original one (see Marchese et al. 2012). In addition, in order to minimize the uncertainties on the values of $L_{\rm bol}$, we have further restricted the analysis on a subsample of objects for which the possible effects of absorption are negligible, i.e. type 1 AGN with an intrinsic absorbing column density, measured from the X-ray spectra, below 5×10^{20} cm^{-2}. Finally, we have excluded from the analysis the small fraction (∼8 per cent) of 'elusive' type 1 AGN, i.e. those sources whose optical spectrum is dominated by the host galaxy (see Severgnini 2003; Caccianiga et al. 2007), due to the impossibility of computing the BH mass through the single epoch (SE) spectral method (e.g. see Peterson 2010; Marziani & Sulentic 2012). In total, the final sample contains 71 objects. A Kolmogorov–Smirvov (K–S) test indicates that this subsample is not statistically different (at 95 per cent confidence level) from the original one from what concerns the Eddington ratio (Fig. 1) and the redshift (Fig. 2) distributions. We have also evaluated the possible impact of the exclusion of 'elusive' AGN from the analysis (see Section 3). The final sample used in this work consists of type 1 AGN with rest frame 2–10 keV luminosities ranging from 6×10^{41} to 9×10^{46} erg s^{-1} and redshift from 0.04 to 2.

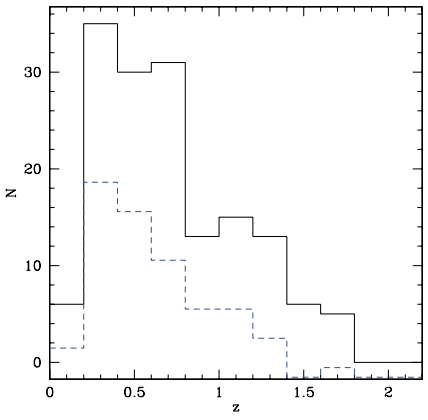

Figure 2. Redshift distribution for the total sample presented in Marchese et al. (2012) (solid black line, 154 AGN) and for the subsample used here (dashed blue line, 71 AGN). The K–S test gives a probability for the null hypothesis (i.e. the two distributions are drawn from the same parent population) of 0.35.

2.2 Parameters

In this section, we describe the methods adopted to determine the parameters of interest (all reported in Table C1).

(i) $L_{\rm bol}$ and $\dot{M}$. Bolometric luminosities were obtained as the sum of the accretion disc luminosity ($L_{\rm disc}$) and the 0.1–100 keV X-ray luminosity. $L_{\rm disc}$ was obtained by fitting the optical–UV data with a disc model (Marchese et al. 2012), while $L_{\rm X}$ was obtained by extrapolating the results obtained in the 2–10 keV energy range analysing the *XMM–Newton* data (Corral et al. 2011). As described in Marchese et al. (2012), the uncertainties on the bolometric luminosities take into account both the statistical errors on photometry and additional sources of error due to the correction for the intrinsic extinction and the long-term variability (since the used photometric data are not simultaneous).

From bolometric luminosities we estimate the absolute accretion rate, defined as

$$\dot{M} = \frac{L_{\rm bol}}{\eta c^2}, \tag{1}$$

where η is the efficiency of the mass to energy conversion, assumed to be 0.1. The uncertainties associated with the values of $\dot{M}$ in Table C1 are those related to the bolometric luminosity, i.e. we do not assume any error on η. The uncertainty on this value is difficult to assess. Marconi et al. (2004) estimate a range of values for η between 0.04 and 0.16 and, therefore, an additional uncertainty on $\dot{M}$ up to a factor of ∼2 could be expected, besides that reported in Table C1. We note that, as explained above, the bolometric luminosities include the X-ray emission. Therefore, by using these bolometric luminosities to compute $\dot{M}$ we are implicitly assuming that the energy budget carried by the X-ray emission is directly related to the accretion process.

(ii) $M_{\rm BH}$ and Eddington ratio λ. Black hole masses of the XBS type 1 AGN are computed in Caccianiga et al. (2013) using the SE method (Peterson 2010; Marziani & Sulentic 2012). This method assumes that the BLR is gravitationally influenced by the SMBH, so the virial theorem can be applied. The velocity dispersion is derived from the broad emission line widths while the BLR size is estimated from the continuum luminosity. The choice of emission lines used for $M_{\rm BH}$ estimate depends on the redshift of the source. In this sample we used Hβ (for $0 < z \leq 0.8$) and Mg II at 2798 Å lines (for $0.8 < z \leq 2$). In particular, we adopted the relation discussed in Vestergaard & Peterson (2006) for the Hβ:

$$\mathrm{Log}M_{\rm BH} = 6.91 + 2\,\mathrm{Log}\frac{\mathrm{FWHM(H}\beta)}{1000\,\mathrm{km\,s^{-1}}} + 0.50\,\mathrm{Log}\frac{\lambda L_{5100\,\text{Å}}}{10^{44}\,\mathrm{erg\,s^{-1}}}, \tag{2}$$

and the relation presented in Shen et al. (2011) for the Mg II λ2798 Å line:

$$\mathrm{Log}M_{\rm BH} = 6.74 + 2\,\mathrm{Log}\frac{\mathrm{FWHM(Mg\,II)}}{1000\,\mathrm{km\,s^{-1}}} + 0.62\,\mathrm{Log}\frac{\lambda L_{3000\,\text{Å}}}{10^{44}\,\mathrm{erg\,s^{-1}}}, \tag{3}$$

the latter equation has been obtained by Shen et al. (2011) in such a way that the zero-order point (the virial factor) is the same as in the Hβ relation presented above so that the masses are consistently derived from these two equations (see the discussion in Shen et al. 2011). In both relations, the line widths refer to the broad component, and it is assumed that a narrow component has been

Downloaded from http://mnras.oxfordjournals.org/ at INAF Brera Milano (Osservatorio Astronomico di Brera) on May 7, 2015

Table 1. Spearman 'rank' correlation coefficients and probabilities for the null hypothesis for the relations discussed in the text.

	Γ $r^a_{\rm obs}$, P $r^b_{\rm i}$	$\Gamma_{(2-10)\,\rm keV}$ $r_{\rm obs}$, P $r^b_{\rm i}$	$K_{\rm bol}$ $r_{\rm obs}$, P $r^b_{\rm i}$	$\alpha_{\rm OX}$ $r_{\rm obs}$, P $r^b_{\rm i}$	Disc/corona $r_{\rm obs}$, P $r^b_{\rm i}$
z	−0.27, 1.64 per cent	−0.13, 28.92 per cent	0.03, 80.26 per cent	−0.22, 6.29 per cent	0.18, 11.41 per cent
λ	0.36, 0.10 per cent 0.60	0.24, 4.14 per cent 0.51	0.33, 0.42 per cent 0.52	−0.25, 3.32 per cent −0.39	0.28, 1.64 per cent 0.44
$\dot{M}$	0.17, 15.86 per cent 0.19		0.27, 2.14 per cent 0.24	−0.41, <0.10 per cent −0.41	0.37, <0.10 per cent 0.37

[a]These values of $r_{\rm obs}$ are computed by excluding the dependence on redshift via partial correlation.
[b]These values of r are an estimate of the 'intrinsic' correlation coefficients computed by taking into account the role of errors (see text for details).

subtracted during the fitting procedure and that the iron emission has been taken into account. All the details on how the FWHM of the emission lines have been computed are given in Caccianiga et al. (2013). The monochromatic luminosities at 5100 Å ($L_{5100\,\text{Å}}$) and 3000 Å ($L_{3000\,\text{Å}}$), respectively, are derived from the SED fitting presented in Marchese et al. (2012).

The SE method is intrinsically affected by a large uncertainty, usually estimated between 0.35 and 0.46 dex (Park et al. 2012), essentially due to the unknown geometry of the BLR. Since the presence of large uncertainties can reduce significantly the strength of the correlations involving BH masses (and the derived quantities) we have estimated the impact of these errors on the analysis presented here (see Section 3.2).

From the BH masses we can estimate the accretion rate normalized to Eddington luminosity, defined as

$$\lambda = \frac{L_{\rm bol}}{L_{\rm Edd}}, \tag{4}$$

where $L_{\rm Edd}$ is the Eddington luminosity:

$$L_{\rm Edd} = \frac{4\pi G c M_{\rm BH} m_{\rm p}}{\sigma_{\rm e}} = 1.26 \times 10^{38} \left(\frac{M_{\rm BH}}{\rm M_\odot}\right) \ {\rm erg\ s^{-1}}. \tag{5}$$

(iii) Γ, $L_{(2-10)\,\rm keV}$, $K_{\rm bol}$, $\alpha_{\rm OX}$ and disc/corona luminosity ratio. The values of $\Gamma_{(0.5-10)\,\rm keV}$ and $L_{(2-10)\,\rm keV}$ are taken from the spectral X-ray analysis presented in Corral et al. (2011). The bolometric corrections and the values of $\alpha_{\rm OX}$ are available from Marchese et al. (2012). In particular, the bolometric correction is defined as

$$K_{\rm bol} = \frac{L_{\rm bol}}{L_{(2-10)\,\rm keV}}, \tag{6}$$

while $\alpha_{\rm OX}$ is defined as

$$\alpha_{\rm OX} = \frac{\rm Log(\it f_{\rm o}/\it f_{\rm x})}{\rm Log(\nu_{\rm o}/\nu_{\rm x})}, \tag{7}$$

where $f_{\rm o}$ and $f_{\rm x}$ are, respectively, the rest-frame monochromatic fluxes at $\nu_{\rm o} = 1.20 \times 10^{15}$ Hz (corresponding to $\lambda_{\rm o} = 2500$ Å) and $\nu_{\rm x} = 4.84 \times 10^{17}$ Hz (corresponding to $E = 2$ keV).

Finally, the disc/corona luminosity ratios, defined as the ratio between the accretion disc luminosity, $L_{\rm disc}$, and the 0.1–100 keV X-ray luminosity ($L_{\rm X}$), are computed on the basis of the luminosities presented, again, in the Marchese et al. (2012) work.

3 STATISTICAL ANALYSIS

We perform a non parametric Spearman rank test on each correlation between X-ray properties (spectral index Γ, $K_{\rm bol}$, $\alpha_{\rm OX}$, disc/corona luminosity ratio) and accretion rate (absolute $\dot{M}$ and normalized to Eddington luminosity, λ). When the correlation is statistically significant, we perform a fit to the data [using both the ordinary least-squares (OLS) and the bisector methods; Isobe et al. 1990 to derive the functional dependence. We define a *very significant correlation* if the probability of null hypothesis (the two quantities are not correlated) is $P \leq 0.10$ per cent, a *significant correlation* if $P \leq 1.00$ per cent and a *marginal correlation* if $P \leq 5.00$ per cent. For convenience, the main correlation coefficients and probabilities computed in this paper are summarized in Table 1. During the analysis, we evaluate the impact of some possible biases that we detail in the following subsections.

3.1 Flux limited nature of the sample

The XBS is a flux-limited sample. The strong L–z correlation, induced by the presence of a flux limit, may create spurious correlations or cancel real ones. This is not a problem for the correlations involving the X-ray loudness ($K_{\rm bol}$, $\alpha_{\rm OX}$ and disc/corona luminosity ratio) since we find that these parameters are not dependent on z (see Table 1). On the contrary, the values of Γ turned out to be marginally dependent on z (see Section 4.1) and, therefore, the correlations involving this quantity are potentially affected by the aforementioned problem. To exclude this possible effect, we use the partial correlation analysis (Kendall & Stuart 1979, see also Appendix) which allows us to evaluate the correlation between two parameters excluding a third variable on which both parameters depend (in this case, the redshift). As further check of the effect of z on the correlations, we analyse the correlations involving Γ in a relatively narrow bin of z ($0 \leq z < 0.4$).

3.2 Error impact on correlation coefficient

As explained above, some parameters like the BH mass and λ are characterized by uncertainties comparable with their variance. This clearly reduces the strength of a correlation by decreasing the values of the correlation parameters. Under the hypothesis of independent errors, and if the average error on the quantities is known, it is possible to have an estimate of the intrinsic correlation parameter using the following relation:

$$r_{\rm i} = r_{\rm obs} \sqrt{\left(1 + \frac{\epsilon_x^2}{\sigma_x^2}\right)\left(1 + \frac{\epsilon_y^2}{\sigma_y^2}\right)}, \tag{8}$$

where ϵ_x, ϵ_y are the average errors on the two variables, σ_x^2 and σ_y^2 are the intrinsic variances on the two variables, $r_{\rm obs}$ is the observed coefficient and the term under square root is the correction

Downloaded from http://mnras.oxfordjournals.org/ at INAF Brera Milano (Osservatorio Astronomico di Brera) on May 7, 2015

factor. The intrinsic variances can be obtained from the observed variances, $\sigma^2_{x,o}$ and $\sigma^2_{y,o}$, by subtracting quadratically the errors, i.e. $\sigma^2_x = \sigma^2_{x,o} - \epsilon^2_x$ and $\sigma^2_y = \sigma^2_{y,o} - \epsilon^2_y$.

The relation (8) can be derived from linear correlation coefficient, assuming independent errors on variables. Using Monte Carlo simulations we have verified that it can be also applied to Spearman coefficients in the case of a non-linear relation (Appendix A).

The correction presented above is particularly important for the correlations involving the Eddington ratio, since its computation is based on the highly uncertain BH mass estimate. In this work we assume an intrinsic uncertainty on the BH mass of 0.40 dex which corresponds to a correction factor for the Eddington ratio of about ∼1.57.

We note that the correction discussed above can be used only to have an estimate of the intrinsic strength of the correlation under study. The probability associated with the correlation coefficient (to assess the actual presence of a correlation), instead, is still the one associated with the value of r_{obs}. Therefore, we will apply this correction only to the correlations that have been established to be statistically significant on the basis of the probabilities associated with the values of r_{obs}.

3.3 Induced correlations

$\dot{M}$ and λ are interrelated quantities since they both depend on bolometric luminosity. A possible correlation, e.g. between Γ and λ, can create an unreal correlation between Γ and $\dot{M}$. To verify this situation, we use partial correlation analysis which allows us to calculate the correlation degree between the parameters of X-ray emission and λ, excluding the dependence on $\dot{M}$ and vice versa. If the correlation disappears by excluding the dependence on the other variable, it is possible that the observed correlation is just induced by the other variable. Conversely, if the correlation remains, then both the observed correlations are likely to be real and not induced by the other variable.

3.4 Elusive AGN

As already mentioned, we have excluded from the analysis a number of type 1 AGN whose optical spectrum is dominated by the light from the host galaxy. As discussed in Severgnini (2003) and Caccianiga et al. (2007) these sources appear in the optical band as 'normal' (i.e. non-active galaxies) because the nuclear light is diluted by the light coming from the host galaxy. The spectrum shows no emission lines (the so-called XBONG sources) or few emission lines that do not allow the clear recognition of the AGN and to derive the correct spectral classification. In Caccianiga et al. (2007) we have used the X-ray spectral analysis to assess the actual presence of the AGN and to characterize it as 'type 2' (absorbed, $N_H > 4 \times 10^{21}$ cm^{-2}) or 'type 1' (unabsorbed, $N_H < 4 \times 10^{21}$ cm^{-2}) AGN. As expected, the frequency of 'elusive' AGN is higher in type 2 AGN, since the absorption makes the dilution more effective to hide the AGN. However, also a fraction (∼8 per cent; see Caccianiga et al. 2007) of type 1 AGN is affected by this problem and this fraction increases rapidly when we consider type 1 AGN of lower and lower X-ray luminosity, becoming very high (>50 per cent) for $L_{(2-10)\,keV}$ lower than 10^{43} erg s^{-1}. In the sample considered here, i.e. the XBS type 1 AGN from Marchese et al. (2012) with low values of N_H, there are seven elusive AGN that we have excluded from the analysis. Even if few, these objects could in principle change the results of the statistical analysis if they are not randomly distributed. We know, for instance, that these objects typically have the lowest values of the optical-to-X-ray flux ratio, i.e. the lowest values of K_{bol} and the 'flattest' values of α_{OX} (all but one have log $K_{bol} < 1.3$ and $\alpha_{OX} > -1.4$). In order to evaluate the impact of the exclusion of these objects from the analysis, we have derived a rough estimate of the BH mass using the absolute magnitude in the K band and adopted the relation discussed in Graham (2007):

$$\log M_{BH} = -0.37(K + 24) + 8.29, \quad (9)$$

where M_{BH} is given in units of solar masses and K is the absolute K-band magnitude. We have then estimated the values of Eddington ratio and $\dot{M}$. As expected, these objects have low accretion rates with respect to the rest of the sample (log λ < −1.7 and log $\dot{M}$ < −1.3). We found that the elusive AGN in general follow the trends observed in the total sample, so their impact on the analysis is not important. However, during the analysis presented in the following sections we will discuss, case by case, the effect of introducing the elusive AGN on the correlation parameters.

4 RESULTS

4.1 Spectral index Γ

The spectral index Γ is found to marginally correlate with the Eddington ratio ($r_{obs} = 0.27$, $P = 1.64$ per cent, Fig. 3) while the correlation between Γ and $\dot{M}$ is not significant ($r_{obs} = 0.17$, $P = 15.86$ per cent). Since Γ marginally depends also on z ($r_{obs} = -0.27$, $P = 1.64$ per cent) it is important to verify whether the observed Γ – λ correlation is in some way influenced by the luminosity–z correlation induced by the flux-limited nature of the sample (see discussion in Section 3.1). In Fig. 4 we present the Γ – λ correlation for sources in the range $0 \le z < 0.4$. This is the range that contains the greatest number of object and offers the widest coverage of Γ – λ plane at the same time. The correlation in this bin of z is highly significant ($r_{obs} = 0.71$, $P < 0.10$ per cent).

To further check this correlation, we have used the partial correlation method to exclude the dependence on z from the analysis on the total sample of 71 AGN. Again, we find a significant correlation with $r_{obs} = 0.36$ ($P = 0.10$ per cent). We conclude that the Γ – λ correlation is not induced by z. Rather, the effect of z is to weaken the correlation (see Fig. 3).

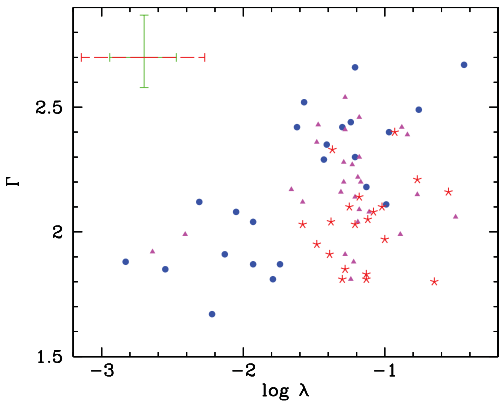

Figure 3. Plot of Γ against λ. A typical error is shown in the upper left-hand corner: the green solid error bar is the statistical error, the red dashed one corresponds to the total error on λ (which includes the uncertainty related to the virial method used to estimate the BH masses). The filled points (blue in the colour version) are sources with $0 \le z < 0.4$, triangles (magenta in the colour version) are sources with $0.4 \le z < 0.8$ and the stars (red in the colour version) are sources with $0.8 \le z < 2$.

Downloaded from http://mnras.oxfordjournals.org/ at INAF Brera Milano (Osservatorio Astronomico di Brera) on May 7, 2015

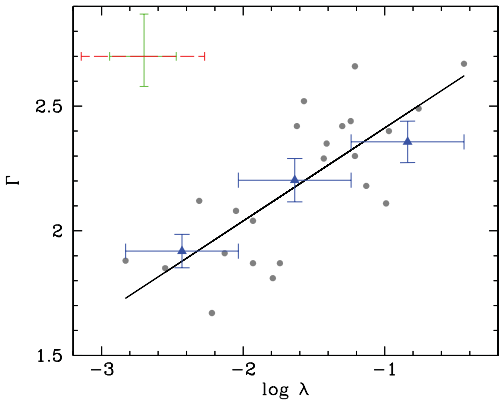

Figure 4. Plot of Γ against λ in the range $0 \leq z < 0.4$. A typical error is shown in the upper left-hand corner: the green solid error bar is the statistical error, the red dashed one corresponds to the total error on λ (which includes the uncertainty related to the virial method used to estimate the BH masses). The solid line represents the OLS best-fitting relation. Blue triangles are the binned data.

It is interesting to establish the origin of the Γ – z dependence. The spectral index Γ was computed using data in the range between 0.5 and 10 keV at rest frame. In this energy range the X-ray spectrum could be contaminated by the presence of the soft excess component. The origin of this component is still unclear. The classical interpretation of the soft excess is represented by the high-energy tail of blackbody emission of the disc accretion (Czerny & Elvis 1987; Grupe et al. 2010). However, this interpretation was questioned when several studies showed that the observed temperature of resulting blackbody is remarkably constant across orders of magnitude of luminosities and BH masses (Gierliński & Done 2004; Crummy et al. 2006). In the spectral analysis discussed in Corral et al. (2011) the soft excess component has been included in the model only if statistically required by the fit. This means that, if the number of counts is not large enough, the presence of the soft excess could be undetected and, thus, not included as additional component in the fitting procedure. In these cases the fit is expected to produce a steeper value of Γ. Notably, the influence of this component depends on z: with increasing z, the soft excess is confined to lower energies and it becomes negligible for $z > 1$ – 2 (Mateos et al. 2010; Scott et al. 2011). Therefore, the presence of the soft excess can produce a spurious anticorrelation between Γ and z making steeper values of Γ at low redshifts. In order to test whether the soft excess is at the origin of the observed Γ – z dependence, we have re-computed the values of Γ by restricting the data to energies above 2 keV (rest frame) in order to exclude the possible contamination due to the soft excess. The resulting values of $\Gamma_{(2-10)\,\mathrm{keV}}$ are poorly determined due to the low statistics in the hard part of the spectrum. Nevertheless, they can be used as an independent test of our conclusions. We find that the values of $\Gamma_{(2-10)\,\mathrm{keV}}$ do not depend on z ($\boldsymbol{r}_{\mathrm{obs}} = -0.13$, $P = 28.92$ per cent), while they depend on λ, although with a lower significance ($\boldsymbol{r}_{\mathrm{obs}} = 0.24$, $P =$ 4.14 per cent) when compared to Γ. In principle, given the larger errors on $\Gamma_{(2-10)\,\mathrm{keV}}$ if compared to Γ, we do expect any correlation to be weaker when considering this parameter. Using equation (8) discussed in Section 3.2, it is possible to have an estimate of the impact of the larger errors on the correlations. Since the average error on $\Gamma_{(2-10)\,\mathrm{keV}}$ ($\epsilon \sim 0.20$) is a factor ∼2.5 larger than the average error on Γ ($\epsilon \sim 0.08$) we expect a decrease by a factor of ∼1.3 of the correlation coefficient just due to the increased errors. Thus, if $\Gamma_{(2-10)\,\mathrm{keV}}$ had the same dependence on z and λ as Γ ($r_{\mathrm{obs}} = -0.27$ and 0.36, respectively) we should expect to observe correlation coefficients reduced by a factor of 1.3, i.e. $r_{\mathrm{obs}} = -0.21$ and 0.28, respectively. While the observed coefficient for the $\Gamma_{(2-10)\,\mathrm{keV}}$ – λ correlation (0.24) is quite close to the expected one (0.28), the $\Gamma_{(2-10)\,\mathrm{keV}}$ – z correlation coefficient (−0.13) is nearly half than the expected one (−0.21). We consider this as an indication that the $\Gamma_{(0.5-10\,\mathrm{keV})}$ – λ and Γ – λ correlation has probably a similar strength while the dependence of the hard spectral index with redshift is much weaker (if any). These results support both the idea that the dependence between Γ and z is (mainly) induced by the presence of the soft excess and the idea that it is the spectral index of the primary X-ray component, and not the soft excess intensity, that correlates with the Eddington ratio. Clearly, better quality spectra, in particular at energies above 2 keV, are required to put these conclusions on a firmer ground.

Both Γ and, in particular, λ are characterized by uncertainties that are on average large with respect to the variance of the parameters. As explained in Section 3.2, the presence of such large errors reduces significantly the measured strength of the correlation, i.e. the value of r. In order to have a better estimate of the actual level of correlation between Γ and λ, we have thus applied the corrections described in Section 3.2 finding a *corrected* value of $\boldsymbol{r}_{\mathrm{i}}$ of 0.6. In the case of linear correlation, the square of $\boldsymbol{r}_{\mathrm{i}}$ gives an indication of how much of the observed variance on Γ is regulated by the value of λ. We thus conclude that about 40 per cent of the variance on the spectral index is explained by λ. This is the strongest correlation found in the sample. We have evaluated the impact of the elusive AGN (Section 3.4) by adding these objects to the sample. We find that their addition improves the Γ – λ correlation while the Γ–$\dot{M}$ correlation remains not significant. We conclude that the observed Γ – λ correlation is not due to the exclusion of the elusive AGN.

We compute the OLS fit for the correlation Γ – λ and we obtain

$$\log \Gamma = 0.25 \log \lambda + 2.48 \tag{10}$$

with an error of ±0.05 on the slope, and the bisector from which

$$\log \Gamma = 0.75 \log \lambda - 2.77 \tag{11}$$

with an error of ±0.04 on the slope.

4.2 Bolometric correction K_{bol}

We find a significant correlation between K_{bol} and λ ($\boldsymbol{r}_{\mathrm{obs}} = 0.33$, $P = 0.42$ per cent, Fig. 5), while the correlation between K_{bol} and $\dot{M}$ is only marginally significant ($\boldsymbol{r}_{\mathrm{obs}} = 0.27$, $P = 2.14$ per cent).

By using the equation (8) to correct the correlation coefficient of K_{bol} – λ correlation, we obtain $\boldsymbol{r}_{\mathrm{i}} = 0.52$ which suggests that ∼25 per cent of the variance on K_{bol} is explained by λ. We compute the OLS fit for the correlation K_{bol} – λ and we obtain

$$\log K_{\mathrm{bol}} = 0.18 \log \lambda + 1.61 \tag{12}$$

with an error of ±0.06 on the slope, and the bisector from which

$$\log K_{\mathrm{bol}} = 0.72 \log \lambda - 2.32 \tag{13}$$

with an error of ±0.05 on the slope.

The slope obtained using the bisector method (0.72 ± 0.05) is in good agreement with that presented in Lusso et al. (2012) (0.75 ± 0.04) while the OLS slope is significantly (∼2.5σ) flatter (0.18 versus 0.39). The discrepancy is slightly reduced if we fit the data on the same range of K_{bol} observed in Lusso et al. (2012) (we find 0.24 ± 0.11). Again, we have verified that the observed correlations are not due to the exclusion of the elusive AGN.

Downloaded from http://mnras.oxfordjournals.org/ at INAF Brera Milano (Osservatorio Astronomico di Brera) on May 7, 2015

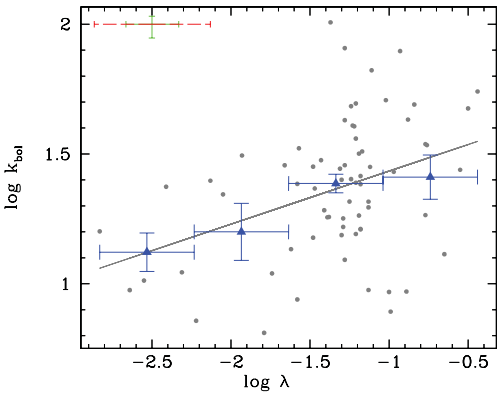

Figure 5. Plot of K_{bol} against λ. A typical error is shown in the upper left-hand corner: the green solid error bar is the statistical error, the red dashed one corresponds to the total error on λ (which includes the uncertainty related to the virial method used to estimate the BH masses). The solid line represents the OLS best-fitting relation. Blue triangles are the binned data.

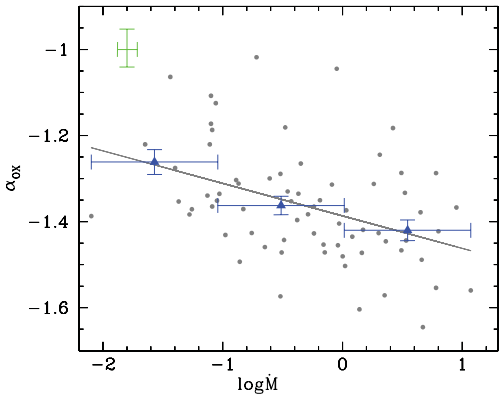

Figure 7. Plot of α_{OX} against $\dot{M}$. A typical error is shown in the upper left-hand corner and it is the average statistical error on α_{OX} and $\dot{M}$. The solid line represents the OLS best-fitting relation. Blue triangles are the binned data.

In conclusion, the results show that both the spectral index Γ and the bolometric correction K_{bol} depend significantly on λ: steep Γ (∼2.5) and high K_{bol} (∼30–60) values correspond to higher λ (∼1), flat Γ (∼1.7) and low K_{bol} values (∼10) correspond to lower λ ($\sim 10^{-2}$). Since K_{bol} depends also on Γ it is possible that the K_{bol} – λ correlation is induced by the (stronger) Γ – λ correlation. Again, we have verified this hypothesis using the partial correlation analysis and found that the dependence between K_{bol} and λ can indeed be explained as induced to the Γ – λ correlation.

In order to visualize these dependences we show in Fig. 6 two theoretical SEDs representing two extreme cases of low ($\lambda \sim 10^{-3}$, left-hand panel) and high (λ ∼ 1, right-hand panel) accretion rate. We have built these SEDs using a Shakura–Sunyaev disc model with a maximum temperature of 3 eV (corresponding to the average temperature of the sample sources) and a power law in the range between ∼0.01 and 100 keV with a cut-off at 0.1 keV. The values of the spectral index of the X-ray power law and the relative normalizations between the disc and the X-ray component are obtained from our Γ – λ and K_{bol} – λ fits, i.e. from (10) and (12). In this way the two SEDs of Fig. 6 can be considered as a visual representation of the correlation analysis discussed in the previous sections. To simplify the comparison between the two SEDs, we assumed the same disc emission in both cases. It is clear from the comparison of the two SEDs that the variation of K_{bol} with λ can be simply explained as due to a change of Γ, as suggested by the partial correlation analysis. We stress that the point where the disc emission intersects the corona emission is not fixed 'a priori' but it comes from the values of Γ and K_{bol} obtained from the fits.

4.3 α_{OX}

Contrary to what is observed for the K_{bol}, we find a marginally significant anticorrelation between α_{OX} and λ ($r_{obs} = -0.25$, $P = 3.32$ per cent) while we find a significant anticorrelation between α_{OX} and $\dot{M}$ ($r_{obs} = -0.41$, $P < 0.10$ per cent, Fig. 7). Even if we weight the correlation coefficients for the errors the dependence between α_{OX} and $\dot{M}$ remains the strongest one ($r_i = -0.41$ versus −0.39). This result confirms what is usually found in the literature, i.e. that the value of α_{OX} anticorrelates with the bolometric/UV luminosity while it has weaker dependence with the Eddington ratio. The inclusion of the elusive AGN improves the significance of both α_{OX} – λ and $\alpha_{OX} - \dot{M}$ correlations.

Since both K_{bol} and α_{OX} are expected to be in some way proxies of the disc/corona relative intensity, the fact of finding two different dependences for these two quantities, one (K_{bol}) on the relative accretion rate and the other (α_{OX}) on the absolute accretion, seems difficult to reconcile. However, these two observational parameters are clearly related but not identical. The major difference is the fact that α_{OX} is defined at given monochromatic frequencies while K_{bol} is the ratio of two integrated quantities. For a fixed value of K_{bol}

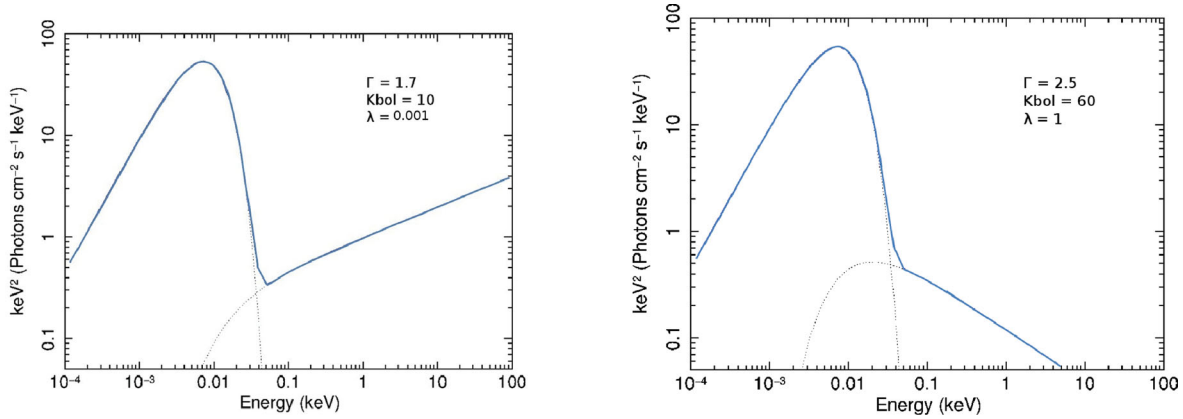

Figure 6. SEDs obtained using the results of the Γ – λ and K_{bol} – λ best fits. The SED on the left represents the case of low accretion ($\lambda \sim 10^{-3}$): the K_{bol} value is low and Γ is flat. The SED on the right represents instead the case of high accretion rate (λ ∼ 1): in this case K_{bol} is high and Γ is steep.

Downloaded from http://mnras.oxfordjournals.org/ at INAF Brera Milano (Osservatorio Astronomico di Brera) on May 7, 2015

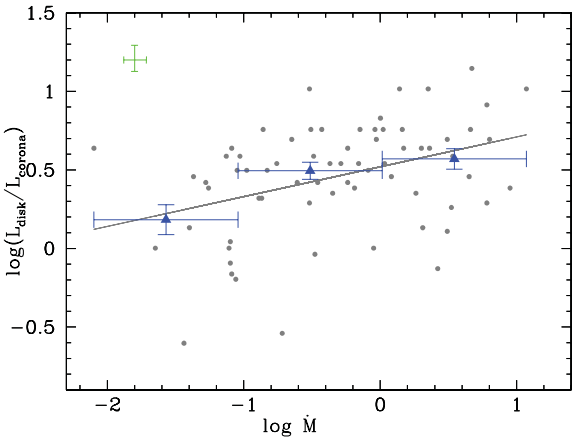

Figure 8. Plot of disc–corona luminosity ratio against $\dot{M}$. A typical error is shown in the upper left-hand corner and it is the average statistical error on disc–corona luminosity ratio and $\dot{M}$. The solid line represents the OLS best-fitting relation. Blue triangles are the binned data.

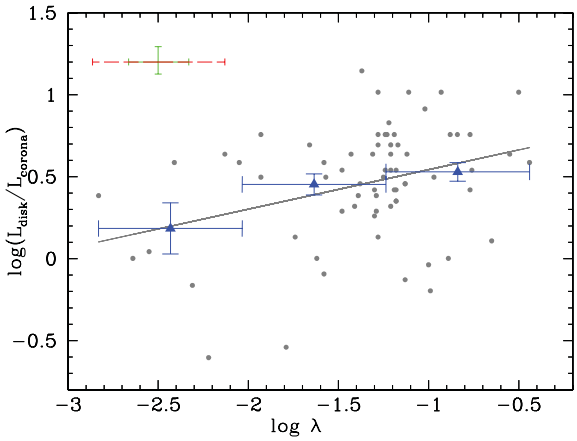

Figure 9. Plot of disc–corona ratio against λ. A typical error is shown in the upper left-hand corner: the green solid error bar is the statistical error, the red dashed one corresponds to the total error on λ (which includes the uncertainty related to the virial method used to estimate the BH masses). The solid line represents the OLS best-fitting relation. Blue triangles are the binned data.

we can measure different values of α_{OX} depending on the actual spectral shape and vice versa. In particular, the value of α_{OX} is less sensitive to the slope of the X-ray emission if compared to K_{bol} ($\boldsymbol{r}_{obs} = -0.24$, $P = 4.04$ per cent for $\alpha_{OX} - \Gamma$, and $\boldsymbol{r}_{obs} = 0.53$, $P < 0.1$ per cent for $K_{bol} - \Gamma$). As shown in the previous section, the dependence of K_{bol} to the Eddington ratio is probably induced by a change of Γ so it is probable that the weaker dependence of α_{OX} on λ is a consequence of the weaker dependence of α_{OX} on Γ.

On the other hand, the significant dependence of α_{OX} with $\dot{M}$ suggests that the disc/corona relative intensity depends also on the absolute accretion rate. We test this hypothesis in the next section by studying directly the disc/corona luminosity ratio.

4.4 Disc–corona luminosity ratio

The dependences of K_{bol} and α_{OX} discussed in the previous sections seem to suggest a complex relationship between the disc/corona luminosity ratio and the accretion. From the one hand, there is a significant dependence on the Eddington ratio, probably related to a change of X-ray slope with λ. On the other hand, there could be also a dependence of the disc/corona luminosity ratio on the absolute level of accretion rate. We now want to study directly the dependence of the disc/corona luminosity ratio with accretion. As expected, the situation in this case is more complex than the K_{bol} and α_{OX} case. We find significant correlation with $\dot{M}$ ($\boldsymbol{r}_{obs} = 0.37$, $P < 0.10$ per cent, Fig. 8) and a marginally significant correlation with λ ($\boldsymbol{r}_{obs} = 0.28$, $P = 1.64$ per cent, Fig. 9). We find a similar result if we add the elusive AGN into the analysis. The strength of the two correlations, once corrected for the errors, is quite similar ($\boldsymbol{r}_i \sim 0.4$) so it is difficult to establish if there is a dominant correlation that explains also the other one. It is thus possible that both correlations are in fact present, i.e. that the disc/corona relative intensity depends both on λ and $\dot{M}$, as expected from the combination of the results obtained for K_{bol} and α_{OX}.

5 DISCUSSION AND CONCLUSIONS

In this paper we studied the link between X-ray emission and accretion rate in a statistically well-defined and complete sample of 71 type 1 AGN extracted from the XBS. The X-ray properties analysed here are the spectral index Γ in the range 0.5–10 and 2–10 keV band and the X-ray 'loudness' parametrized with both the bolometric correction K_{bol} (defined as the ratio between bolometric luminosity and 2–10 keV luminosity) and the two-points spectral index α_{OX}. We have also directly analysed the disc/corona luminosity ratio. The spectral index gives direct information about the energy distribution of the electrons in the corona, while the other three parameters quantify, in different ways, the relative importance between disc and corona.

We have considered different possible biases which can influence final results, such as

(i) soft excess contamination;
(ii) redshift-induced correlations (important in flux-limited samples);
(iii) impact of errors on correlation coefficients (especially on M_{BH} estimate);
(iv) interconnected dependences due to the fact that the parameters considered in the analysis are not all independent;
(v) the impact of the exclusion of 'elusive' AGN from the analysis on the final results.

The results can be summarized as follows.

(i) The spectral index Γ depends significantly on accretion rate normalized to Eddington luminosity; in particular, ∼40 per cent of Γ variance could be explained by λ. This correlation is not due to the soft excess contamination, but it probably reflects a true dependence of the slope of the primary X-emission with λ. The Γ – λ dependence can be speculatively attributed to the effect of cooling of the electrons in the corona: for high values of λ, a large number of photons comes from the accretion disc and cools corona electrons rapidly, thus producing steep X-ray spectra while for low values of λ, less photons are available and this makes electron cooling inefficient, thus producing flat X-ray spectra (see for instance Cao 2009).

(ii) The 'X-ray loudness' depends both on λ and $\dot{M}$ but the dependence with λ is probably just the consequence of the (stronger) Γ – λ dependence.

(iii) The strength of the dependence between the 'X-ray loudness' and λ or $\dot{M}$ is different depending on whether we parametrize the X-ray loudness using the K_{bol} or the α_{OX}: while K_{bol} seems to depend mainly on λ, the values of α_{OX} show a stronger dependence with

Downloaded from http://mnras.oxfordjournals.org/ at INAF Brera Milano (Osservatorio Astronomico di Brera) on May 7, 2015

$\dot{M}$. The explanation is likely connected to the different sensitivity of these two parameters to the X-ray spectral index.

ACKNOWLEDGEMENTS

We thank the referee for useful comments that improved the paper. We acknowledge Massimo Dotti, Francesco Haardt, Monica Colpi and Valentina Braito for useful discussions and Laura Maraschi and Tommaso Maccacaro for the precious comments. The authors acknowledge financial support from ASI (grant n. I/088/06/0), from the Italian Ministry of Education, Universities and Research (PRIN2010-2011, grant n. 2010NHBSBE) and from the Spanish Ministry of Economy and Competitiveness through grant AYA2012-31447.

REFERENCES

Bianchi S., Bonilla N. F., Guainazzi M., Matt G., Ponti G., 2009, A&A, 501, 915
Brandt W. N., Mathur S., Elvis M., 1997, MNRAS, 285, L25
Caccianiga A., Severgnini P., Della Ceca R., Maccacaro T., Carrera F. J., Page M. J., 2007, A&A, 470, 557
Caccianiga A. et al., 2008, A&A, 477, 735
Caccianiga A., Fanali R., Severgnini P., Della Ceca R., Marchese E., Mateos S., 2013, A&A, 549, A119
Cao X., 2009, MNRAS, 394, 207
Corral A., Della Ceca R., Caccianiga A., Severgnini P., Brunner H., Carrera F. J., Page M. J., Schwope A. D., 2011, A&A, 530, A42
Crummy J., Fabian A. C., Gallo L., Ross R. R., 2006, MNRAS, 365, 1067
Czerny B., Elvis M., 1987, ApJ, 321, 305
Della Ceca R. et al., 2004, A&A, 428, 383
Galbiati E. et al., 2005, A&A, 430, 927
Gierliński M., Done C., 2004, MNRAS, 349, L7
Graham A. W., 2007, MNRAS, 379, 711
Grupe D., Leighly K. M., Burwitx V., Predehl P., Mathur S., 2004, AJ, 128, 1524
Grupe D., Komossa S., Leighly K. M., Page K. L., 2010, ApJS, 187, 64
Gu M., Cao X., 2009, MNRAS, 399, 349
Haardt F., Maraschi L., 1991, ApJ, 380, L51
Hopkins P. F., Richards G. T., Herquist L., 2007, ApJ, 654, 731
Isobe T., Feigelson E. D., Akritas M. G., Babu G. J., 1990, ApJ, 364, 104
Kelly B. C., Bechtold J., Trump J. R., Vestergaard M., Siemiginowska A., 2008, ApJS, 176, 355
Kendall M., Stuart A., 1979, The Advanced Theory of Statistics. MacMillan, New York
Laor A., Fiore F., Elvis M., Wilkes B. J., McDowell J. C., 1997, ApJ, 477, 93
Lusso E. et al., 2012, MNRAS, 425, 623
Marchese E., Della Ceca R., Caccianiga A., Severgnini P., Corral A., Fanali R., 2012, A&A, 539, 48
Marconi A., Risaliti G., Gilli R., Hunt L. K., Maiolino R., Salvati M., 2004, MNRAS, 351, 169
Marziani P., Sulentic J. W., 2012, New Astron. Rev., 56, 49
Mateos S. et al., 2010, A&A, 510, A35
Park S.*et al.*, 2012, ApJ, 743, 30
Peterson B. M., 2010, in Peterson B., Somerville R., Storchi-Bergmann T., eds, Proc. IAU Symp. 267, Co-Evolution of Central Black Holes and Galaxies. Cambridge Univ. Press, Cambridge, p. 151
Piconcelli E., Jimenez-Bailón E., Guainazzi M., Schartel N., Rodriguez-Pascual P. M., Santos-Lleo M., 2005, A&A, 432, 15
Porquet D., Reeves J. N., O'Brien P., Brinkmann W., 2004, A&A, 422, 85
Risaliti G., Yourng M., Elvis M., 2009, ApJ, 700, L6
Scott A. E., Steward G. C., Mateos S., Alexander D., Hutton S., Ward M. J., 2011, MNRAS, 417, 992
Severgnini P., 2003, A&A, 406, 483
Shemmer O., Brandt W. N., Netzer H., Maiolino R., Kaspi S., 2008, ApJ, 682, 81
Shen Y. et al., 2011, ApJ, 194, A45
Sulentic J. W., Marziani P., Dultzin-Hacyan D., 2000, A&AR, 38, 521
Vasudevan R. V., Fabian A. C., 2007, MNRAS, 381, 1235
Vaudevan R. V., Fabian A. C., 2009, MNRAS, 392, 1124
Vestergaard M., Peterson B. M., 2006, ApJ, 641, 689
Vignali C., Brandt W. N., Schneider D. P., 2003, AJ, 125, 433
Wang T., Brinkmann W., Bergeron J., 1996, A&A, 309, 81
Wang J. M., Watarai K. Y., Mineshige S., 2004, ApJ, 607, L107
Young M., Elvis M., Risaliti G., 2010, ApJ, 708, 1388
Zhou X. L., Zhang S. N., 2010, ApJ, 713, L11

APPENDIX A: ERROR IMPACT ON CORRELATION COEFFICIENT

Some parameters used in this analysis (like the BH mass and the Eddington ratio) are characterized by very large errors, principally related to the method adopted to estimate the BH masses. If the error is comparable to the variance of a variable, this can reduce the strength of a correlation by decreasing the values of the correlation coefficients. We estimate the intrinsic correlation parameter by using the relation:

$$r_{\rm i} = r_{\rm obs}\sqrt{\left(1+\frac{\epsilon_x^2}{\sigma_x^2}\right)\left(1+\frac{\epsilon_y^2}{\sigma_y^2}\right)}, \qquad \text{(A1)}$$

where ϵ_x, ϵ_y are the average errors on the two variables, σ_x^2 and σ_y^2 are the intrinsic (i.e. not folded with the errors) variances on the two variables, $r_{\rm obs}$ is the observed coefficient and the term under square root of this variable is the correction factor. This relation can be derived from linear correlation coefficient, assuming independent errors on variables. Using Monte Carlo simulations we have verified that it can be also applied to Spearman coefficients in the case of a non-linear relation. Fig. A1 represents a Monte Carlo simulation where we show the case of a cubic correlation between two variables, X and Y, with an intrinsic correlation coefficient $r \sim 0.87$ (lower panel in Fig. A1). If we add an error on Y comparable to the variance on this variable, the coefficient correlation is reduced to $r \sim 0.62$ (upper panel in Fig. A1).

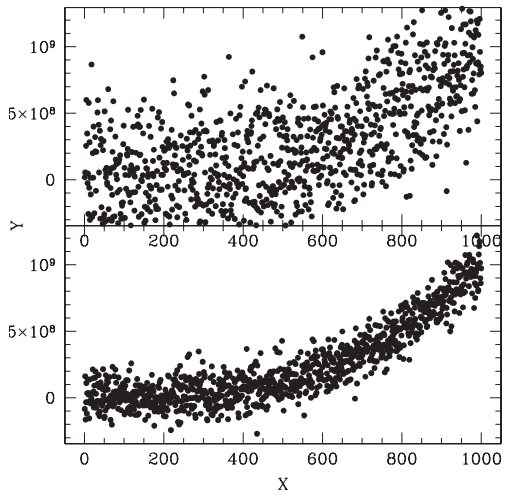

Figure A1. Numerical simulation (∼1000 points) that shows the impact of a big error (comparable with the variance of the variable, in this example Y) on the $Y-X$ correlation. In this example we assume a correlation coefficient $r \sim 0.87$ (lower panel) and we add an error on Y comparable with the intrinsic variance on Y. The resulting correlation (upper panel) is significantly reduced ($r \sim 0.62$).

Downloaded from http://mnras.oxfordjournals.org/ at INAF Brera Milano (Osservatorio Astronomico di Brera) on May 7, 2015

We repeated these simulations for different values of errors and the trend of the observed r_{obs} is shown in Fig. A2 (blue stars). In Fig. A2 we also report the values of r_i estimated according to equation (A1) (red points). The starting value of $r_i \sim 0.9$ is reasonably recovered.

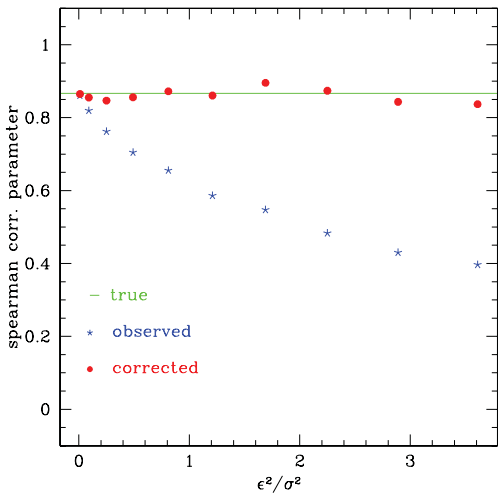

Figure A2. Results of numerical simulations that show the variation of the observed correlation coefficient (blue stars) with respect to the error^2/variance ratio, assuming a starting value of $r \sim 0.87$. The red points represent corrected r values.

APPENDIX B: PARTIAL CORRELATIONS

As explained in Section 3.1, in a flux-limited sample like the XBS the luminosity is strongly correlated with redshift. This relation could give rise to spurious correlations. A way of dealing with the problem is to examine the correlations between luminosities excluding the dependence on redshift via partial correlation analysis. If r_{12} is the correlation coefficient between x_1 and x_2 and r_{13} and r_{23} are the correlation coefficients of the two variables with z, the correlation coefficient between x_1 and x_2, excluding the effect of z, is

$$r_{12,3} = \frac{r_{12} - r_{13}r_{23}}{\sqrt{(1 - r_{13}^2)(1 - r_{23}^2)}}. \quad \text{(B1)}$$

This equation can be generalized to more than three variables. For example, in the case of four variables it becomes

$$r_{12,34} = \frac{r_{12,4} - r_{13,4}r_{23,4}}{\sqrt{(1 - r_{13,4}^2)(1 - r_{23,4}^2)}}. \quad \text{(B2)}$$

APPENDIX C: THE SAMPLE

In this section we present the table (Table C1) including all the quantities used in the analysis discussed in the text.

Table C1. Main properties of the sample of 70 type 1 AGN analysed in this work.

Name	z	Γ	Γ_{2-10}	Log K_{bol}	Log M_{BH}	Log $\dot{M}$	Log λ	α_{OX}	Log(L_{disc}/L_{corona})
XBS J000027.7−250442	0.336	$1.87^{+0.06}_{-0.05}$	$1.57^{+0.27}_{-0.25}$	$1.32^{+0.09}_{-0.11}$	$8.63^{+0.10}_{-0.12}$	$-0.94^{+0.09}_{-0.12}$	$-1.93^{+0.13}_{-0.17}$	−1.430	0.497
XBS J000031.7−245502	0.284	$2.29^{+0.08}_{-0.08}$	$1.86^{+0.42}_{-0.52}$	$1.48^{+0.10}_{-0.34}$	$8.02^{+1.32}_{-0.25}$	$-1.05^{+0.11}_{-0.33}$	$-1.43^{+1.32}_{-0.41}$	−1.362	0.638
XBS J000102.4−245850	0.433	$2.12^{+0.08}_{-0.07}$	$1.89^{+0.28}_{-0.34}$	$0.94^{+0.07}_{-0.06}$	$8.16^{+0.15}_{-0.14}$	$-1.06^{+0.07}_{-0.06}$	$-1.58^{+0.17}_{-0.15}$	−1.106	−0.093
XBS J001831.6+162925	0.553	$2.39^{+0.04}_{-0.04}$	$2.11^{+0.14}_{-0.17}$	$1.69^{+0.10}_{-0.08}$	$8.54^{+0.06}_{-0.05}$	$0.06^{+0.10}_{-0.09}$	$-0.84^{+0.12}_{-0.10}$	−1.501	0.757
XBS J002618.5+105019	0.473	$2.04^{+0.04}_{-0.04}$	$1.95^{+0.16}_{-0.15}$	$1.50^{+0.10}_{-0.08}$	$9.03^{+0.10}_{-0.14}$	$0.20^{+0.10}_{-0.08}$	$-1.19^{+0.14}_{-0.16}$	−1.469	0.757
XBS J002637.4+165953	0.554	$2.15^{+0.04}_{-0.03}$	$2.07^{+0.13}_{-0.13}$	$1.26^{+0.09}_{-0.11}$	$8.21^{+0.11}_{-0.41}$	$-0.20^{+0.08}_{-0.11}$	$-0.77^{+0.14}_{-0.42}$	−1.363	0.420
XBS J003418.9−115940	0.850	$2.10^{+0.27}_{-0.16}$	$2.03^{+0.43}_{-0.51}$	$1.32^{+0.14}_{-0.16}$	$8.84^{+0.11}_{-0.13}$	$-0.05^{+0.14}_{-0.16}$	$-1.25^{+0.18}_{-0.21}$	−1.310	0.497
XBS J005009.9−515934	0.610	$2.28^{+0.09}_{-0.08}$	$2.11^{+0.44}_{-0.42}$	$1.22^{+0.08}_{-0.06}$	$8.45^{+0.35}_{-0.58}$	$-0.48^{+0.08}_{-0.06}$	$-1.29^{+0.36}_{-0.58}$	−1.287	0.289
XBS J010432.8−583712	1.640	$1.95^{+0.05}_{-0.04}$	$1.76^{n.d.}_{n.d.}$	$1.18^{+0.10}_{-0.10}$	$9.94^{+0.08}_{-0.09}$	$0.82^{+0.10}_{-0.09}$	$-1.48^{+0.13}_{-0.13}$	−1.285	0.289
XBS J012025.2−105441	1.338	$2.40^{+0.21}_{-0.18}$	$2.32^{+0.36}_{-0.31}$	$1.90^{+0.14}_{-0.14}$	$9.68^{+0.08}_{-0.08}$	$1.11^{+0.14}_{-0.14}$	$-0.93^{+0.16}_{-0.16}$	−1.558	1.016
XBS J012119.9−110418	0.204	$2.66^{+0.23}_{-0.14}$	$3.56^{+1.54}_{-1.16}$	$1.69^{+0.12}_{-0.12}$	$8.13^{+0.08}_{-0.09}$	$-0.72^{+0.12}_{-0.12}$	$-1.21^{+0.14}_{-0.15}$	−1.424	0.540
XBS J013204.9−400050	0.445	$2.42^{+0.17}_{-0.14}$	$2.48^{+0.52}_{-0.43}$	$1.63^{+0.13}_{-0.13}$	$8.05^{+0.13}_{-0.12}$	$-0.47^{+0.13}_{-0.13}$	$-0.88^{+0.18}_{-0.18}$	−1.470	0.757
XBS J020029.0+002846	0.174	$2.42^{+0.10}_{-0.10}$	$2.22^{+0.66}_{-0.80}$	$1.13^{+0.06}_{-0.05}$	$7.65^{+0.17}_{-0.20}$	$-1.61^{+0.06}_{-0.05}$	$-1.62^{+0.18}_{-0.21}$	−1.218	0.002
XBS J021808.3−045845	0.712	$1.91^{+0.04}_{-0.03}$	n.d.	$1.46^{+0.10}_{-0.08}$	$9.45^{+0.06}_{-0.05}$	$0.53^{+0.09}_{-0.08}$	$-1.28^{+0.11}_{-0.09}$	−1.465	0.694
XBS J021817.4−045113	1.080	$1.83^{+0.04}_{-0.03}$	$1.78^{+0.08}_{-0.07}$	$0.98^{+0.06}_{-0.07}$	$9.23^{+0.07}_{-0.09}$	$0.46^{+0.05}_{-0.07}$	$-1.13^{+0.09}_{-0.11}$	−1.181	−0.128
XBS J021820.6−050427	0.646	$1.81^{+0.04}_{-0.04}$	$1.70^{+0.14}_{-0.13}$	$1.40^{+0.06}_{-0.12}$	$8.76^{+0.06}_{-0.10}$	$-0.12^{+0.06}_{-0.12}$	$-1.24^{+0.08}_{-0.16}$	−1.451	0.540
XBS J021923.2−045148	0.632	$2.41^{+0.07}_{-0.04}$	$2.20^{+0.23}_{-0.22}$	$1.63^{+0.10}_{-0.08}$	$8.81^{+0.07}_{-0.05}$	$-0.11^{+0.10}_{-0.08}$	$-1.28^{+0.12}_{-0.09}$	−1.470	0.757
XBS J024200.9+000020	1.112	$2.03^{+0.05}_{-0.04}$	$1.91^{+0.13}_{-0.17}$	$1.38^{+0.07}_{-0.04}$	$9.79^{+0.06}_{-0.04}$	$0.57^{+0.07}_{-0.04}$	$-1.58^{+0.09}_{-0.06}$	−1.439	0.587
XBS J024207.3+000037	0.385	$2.52^{+0.12}_{-0.08}$	$1.93^{+0.31}_{-0.27}$	$1.52^{+0.06}_{-0.07}$	$8.42^{+0.10}_{-0.10}$	$-0.79^{+0.06}_{-0.07}$	$-1.57^{+0.12}_{-0.12}$	−1.368	0.497
XBS J031015.5−765131	1.187	$1.91^{+0.02}_{-0.02}$	$1.84^{+0.06}_{-0.06}$	$1.26^{+0.09}_{-0.12}$	$10.02^{+0.08}_{-0.10}$	$0.99^{+0.09}_{-0.12}$	$-1.39^{+0.12}_{-0.16}$	−1.364	0.385
XBS J033208.7−274735	0.544	$1.99^{+0.09}_{-0.07}$	$1.92^{+0.19}_{-0.24}$	$1.37^{+0.07}_{-0.13}$	$9.60^{+0.07}_{-0.11}$	$-0.45^{+0.07}_{-0.13}$	$-2.41^{+0.10}_{-0.17}$	−1.441	0.587
XBS J050446.3−283821	0.840	$1.97^{+0.11}_{-0.08}$	$1.87^{+0.46}_{-0.38}$	$0.97^{+0.08}_{-0.07}$	$8.20^{+0.35}_{-0.36}$	$-0.44^{+0.08}_{-0.06}$	$-1.00^{+0.36}_{-0.36}$	−1.178	−0.037
XBS J050501.8−284149	0.257	$2.18^{+0.05}_{-0.05}$	$2.15^{+0.39}_{-0.35}$	$1.29^{+0.14}_{-0.11}$	$7.44^{+0.11}_{-0.09}$	$-1.33^{+0.14}_{-0.11}$	$-1.13^{+0.18}_{-0.14}$	−1.350	0.457
XBS J051955.5−455727	0.562	$2.09^{+0.04}_{-0.04}$	$2.00^{+0.38}_{-0.33}$	$1.21^{+0.08}_{-0.10}$	$8.51^{+0.07}_{-0.08}$	$-0.31^{+0.08}_{-0.11}$	$-1.18^{+0.11}_{-0.14}$	−1.262	0.351
XBS J065400.0+742045	0.362	$2.30^{+0.19}_{-0.12}$	$2.37^{+0.60}_{-0.49}$	$1.56^{+0.13}_{-0.13}$	$8.24^{+0.10}_{-0.10}$	$-0.61^{+0.12}_{-0.13}$	$-1.21^{+0.16}_{-0.16}$	−1.456	0.694
XBS J074352.0+744258	0.800	$2.03^{+0.07}_{-0.06}$	$1.92^{+0.20}_{-0.25}$	$1.39^{+0.09}_{-0.12}$	$9.06^{+0.08}_{-0.09}$	$0.21^{+0.10}_{-0.12}$	$-1.21^{+0.13}_{-0.15}$	−1.418	0.638
XBS J080504.6+245156	0.980	$2.08^{+0.10}_{-0.10}$	$1.77^{+0.32}_{-0.28}$	$0.96^{+0.04}_{-0.04}$	$8.39^{+0.14}_{-0.17}$	$-0.33^{+0.03}_{-0.05}$	$-1.08^{+0.14}_{-0.18}$	−1.155	−0.075
XBS J080608.1+244420	0.357	$2.49^{+0.04}_{-0.03}$	$2.21^{+0.18}_{-0.23}$	$1.53^{+0.06}_{-0.07}$	$8.15^{+0.07}_{-0.07}$	$-0.25^{+0.06}_{-0.07}$	$-0.76^{+0.09}_{-0.10}$	−1.380	0.540

Downloaded from http://mnras.oxfordjournals.org/ at INAF Brera Milano (Osservatorio Astronomico di Brera) on May 7, 2015

Table C1 – *continued*

Name	z	Γ	Γ_{2-10}	Log $K_{\rm bol}$	Log $M_{\rm BH}$	Log $\dot{M}$	Log λ	$\alpha_{\rm OX}$	Log($L_{\rm disc}/L_{\rm corona}$)
XBS J100100.0+252103	0.794	$2.20^{+0.07}_{-0.04}$	$2.12^{+0.17}_{-0.16}$	$1.25^{+0.08}_{-0.07}$	$8.78^{+0.06}_{-0.05}$	$-0.15^{+0.08}_{-0.07}$	$-1.29^{+0.10}_{-0.09}$	−1.346	0.385
XBS J100309.4+554135	0.673	$2.27^{+0.07}_{-0.06}$	$1.86^{+0.35}_{-0.42}$	$1.61^{+0.07}_{-0.08}$	$8.87^{+0.05}_{-0.05}$	$-0.01^{+0.08}_{-0.08}$	$-1.23^{+0.09}_{-0.09}$	−1.454	0.757
XBS J100828.8+535408	0.384	$2.04^{+0.12}_{-0.09}$	$1.29^{+0.64}_{-0.54}$	$1.49^{+0.07}_{-0.08}$	$8.75^{+0.30}_{-0.24}$	$-0.82^{+0.07}_{-0.08}$	$-1.93^{+0.31}_{-0.25}$	−1.491	0.757
XBS J100921.7+534926	0.387	$2.35^{+0.08}_{-0.05}$	$1.94^{+0.35}_{-0.34}$	$1.28^{+0.08}_{-0.10}$	$8.22^{+0.12}_{-0.12}$	$-0.83^{+0.08}_{-0.10}$	$-1.41^{+0.14}_{-0.16}$	−1.309	0.320
XBS J101838.0+411635	0.577	$2.36^{+0.07}_{-0.06}$	$2.09^{+0.30}_{-0.26}$	$1.45^{+0.06}_{-0.07}$	$8.79^{+0.05}_{-0.06}$	$-0.33^{+0.07}_{-0.07}$	$-1.48^{+0.09}_{-0.09}$	−1.332	0.540
XBS J101850.5+411506	0.577	$2.30^{+0.05}_{-0.03}$	$2.17^{+0.15}_{-0.20}$	$1.38^{+0.06}_{-0.07}$	$8.89^{+0.05}_{-0.04}$	$0.07^{+0.07}_{-0.08}$	$-1.18^{+0.09}_{-0.08}$	−1.372	0.540
XBS J101922.6+412049	0.239	$2.12^{+0.16}_{-0.05}$	n.d.	$1.04^{+0.05}_{-0.04}$	$8.90^{+0.08}_{-0.75}$	$-1.05^{+0.05}_{-0.04}$	$-2.31^{+0.09}_{-0.75}$	−1.186	−0.163
XBS J103120.0+311404	1.190	$1.85^{+0.12}_{-0.08}$	$1.76^{+0.20}_{-0.18}$	$1.09^{+0.09}_{-0.05}$	$9.27^{+0.09}_{-0.06}$	$0.35^{+0.09}_{-0.05}$	$-1.28^{+0.13}_{-0.08}$	−1.240	0.132
XBS J103154.1+310732	0.299	$1.88^{+0.13}_{-0.12}$	$1.42^{+0.84}_{-0.76}$	$1.20^{+0.06}_{-0.07}$	$9.25^{+0.26}_{-0.19}$	$-1.22^{+0.06}_{-0.06}$	$-2.83^{+0.27}_{-0.20}$	−1.369	0.385
XBS J103932.7+205426	0.237	$1.87^{+0.11}_{-0.09}$	$1.87^{+0.63}_{-0.54}$	$1.04^{+0.07}_{-0.05}$	$8.02^{+0.17}_{-0.13}$	$-1.36^{+0.07}_{-0.05}$	$-1.74^{+0.18}_{-0.14}$	−1.273	0.132
XBS J103935.8+533036	0.229	$2.08^{+0.15}_{-0.10}$	$2.22^{+0.56}_{-0.43}$	$1.34^{+0.09}_{-0.12}$	$8.70^{+0.07}_{-0.09}$	$-0.99^{+0.09}_{-0.12}$	$-2.05^{+0.11}_{-0.15}$	−1.333	0.587
XBS J104026.9+204542	0.465	$1.99^{+0.03}_{-0.03}$	$1.88^{+0.13}_{-0.13}$	$0.97^{+0.04}_{-0.05}$	$8.52^{+0.05}_{-0.08}$	$-0.01^{+0.04}_{-0.04}$	$-0.89^{+0.06}_{-0.09}$	−1.043	0.002
XBS J104509.3−012442	0.472	$2.14^{+0.11}_{-0.06}$	$2.13^{+0.29}_{-0.31}$	$1.19^{+0.06}_{-0.06}$	$8.00^{+0.06}_{-0.05}$	$-0.85^{+0.05}_{-0.06}$	$-1.21^{+0.08}_{-0.08}$	−1.301	0.320
XBS J104912.8+330459	0.226	$1.67^{+0.12}_{-0.09}$	$1.91^{+0.46}_{-0.39}$	$0.86^{+0.03}_{-0.03}$	$8.46^{+0.21}_{-0.18}$	$-1.40^{+0.02}_{-0.03}$	$-2.22^{+0.21}_{-0.18}$	−1.060	−0.603
XBS J105014.9+331013	1.012	$2.33^{+0.37}_{-0.20}$	$2.45^{+0.95}_{-0.69}$	$2.01^{+0.10}_{-0.13}$	$9.72^{+0.13}_{-0.09}$	$0.71^{+0.10}_{-0.13}$	$-1.37^{+0.16}_{-0.16}$	−1.643	1.146
XBS J105239.7+572431	1.113	$2.10^{+0.02}_{-0.02}$	$2.04^{+0.12}_{-0.16}$	$1.71^{+0.07}_{-0.09}$	$9.48^{+0.05}_{-0.06}$	$0.82^{+0.07}_{-0.09}$	$-1.02^{+0.09}_{-0.11}$	−1.550	0.914
XBS J105316.9+573551	1.204	$1.80^{+0.02}_{-0.02}$	$1.97^{+0.14}_{-0.18}$	$1.11^{+0.05}_{-0.05}$	$8.82^{+0.12}_{-0.14}$	$0.53^{+0.05}_{-0.05}$	$-0.65^{+0.13}_{-0.15}$	−1.285	0.109
XBS J105624.2−033522	0.635	$2.16^{+0.09}_{-0.06}$	$2.20^{+0.26}_{-0.23}$	$1.44^{+0.07}_{-0.08}$	$8.75^{+0.05}_{-0.05}$	$-0.20^{+0.07}_{-0.08}$	$-1.31^{+0.09}_{-0.09}$	−1.425	0.638
XBS J112022.3+125252	0.406	$2.22^{+0.09}_{-0.08}$	$1.75^{+0.38}_{-0.50}$	$1.26^{+0.06}_{-0.07}$	$8.26^{+0.06}_{-0.06}$	$-0.57^{+0.06}_{-0.06}$	$-1.19^{+0.08}_{-0.08}$	−1.295	0.420
XBS J120359.1+443715	0.641	$2.43^{+0.12}_{-0.12}$	$2.57^{+0.40}_{-0.34}$	$1.37^{+0.11}_{-0.10}$	$8.77^{+0.06}_{-0.06}$	$-0.34^{+0.11}_{-0.10}$	$-1.47^{+0.13}_{-0.12}$	−1.396	1.600
XBS J123116.5+641115	0.454	$1.92^{+0.05}_{-0.05}$	$1.91^{+0.25}_{-0.22}$	$0.98^{+0.04}_{-0.04}$	$9.21^{+0.18}_{-0.13}$	$-1.07^{+0.05}_{-0.04}$	$-2.64^{+0.19}_{-0.14}$	−1.217	0.002
XBS J123759.6+621102	0.910	$2.05^{+0.04}_{-0.04}$	$1.89^{+0.12}_{-0.15}$	$1.45^{+0.07}_{-0.08}$	$9.16^{+0.05}_{-0.05}$	$0.40^{+0.06}_{-0.08}$	$-1.12^{+0.08}_{-0.09}$	−1.443	0.638
XBS J123800.9+621338	0.440	$2.54^{+0.04}_{-0.05}$	$2.01^{+0.26}_{-0.33}$	$1.91^{+0.07}_{-0.09}$	$8.44^{+0.09}_{-0.10}$	$-0.48^{+0.07}_{-0.08}$	$-1.28^{+0.11}_{-0.13}$	−1.571	1.016
XBS J124214.1−112512	0.820	$1.81^{+0.05}_{-0.05}$	$1.60^{+0.16}_{-0.15}$	$1.32^{+0.10}_{-0.08}$	$8.89^{+0.07}_{-0.06}$	$0.12^{+0.09}_{-0.08}$	$-1.13^{+0.11}_{-0.10}$	−1.431	0.457
XBS J124607.6+022153	0.491	$2.46^{+0.12}_{-0.08}$	$1.81^{+0.57}_{-0.48}$	$1.42^{+0.06}_{-0.07}$	$8.40^{+0.10}_{-0.10}$	$-0.42^{+0.06}_{-0.07}$	$-1.18^{+0.12}_{-0.12}$	−1.326	0.420
XBS J124641.8+022412	0.934	$2.21^{+0.07}_{-0.05}$	$2.00^{+0.19}_{-0.23}$	$1.54^{+0.04}_{-0.08}$	$9.11^{+0.02}_{-0.06}$	$0.70^{+0.03}_{-0.08}$	$-0.77^{+0.04}_{-0.10}$	−1.485	0.757
XBS J124949.4−060722	1.053	$2.16^{+0.07}_{-0.06}$	$1.70^{+0.31}_{-0.28}$	$1.44^{+0.07}_{-0.08}$	$8.53^{+0.05}_{-0.06}$	$0.34^{+0.06}_{-0.08}$	$-0.55^{+0.08}_{-0.10}$	−1.422	0.638
XBS J132101.6+340656	0.335	$2.44^{+0.04}_{-0.04}$	$2.18^{+0.18}_{-0.20}$	$1.68^{+0.07}_{-0.08}$	$8.49^{+0.07}_{-0.08}$	$-0.39^{+0.06}_{-0.09}$	$-1.24^{+0.09}_{-0.12}$	−1.351	0.757
XBS J133807.5+242411	0.631	$2.08^{+0.10}_{-0.08}$	$1.84^{+0.32}_{-0.35}$	$1.82^{+0.07}_{-0.09}$	$8.93^{+0.04}_{-0.06}$	$0.18^{+0.07}_{-0.09}$	$-1.11^{+0.08}_{-0.11}$	−1.601	1.016
XBS J134749.9+582111	0.646	$2.20^{+0.02}_{-0.02}$	$1.93^{+0.06}_{-0.06}$	$1.51^{+0.07}_{-0.08}$	$9.65^{+0.07}_{-0.07}$	$0.84^{+0.06}_{-0.08}$	$-1.17^{+0.09}_{-0.11}$	−1.419	0.694
XBS J140102.0−111224[a]	0.037	$1.91^{+0.02}_{-0.02}$	$1.74^{+0.12}_{-0.12}$	$1.40^{+0.19}_{-0.35}$	$7.71^{+0.96}_{-0.82}$	$-2.06^{+0.07}_{-0.09}$	$-2.13^{+0.96}_{-0.82}$	−1.382	0.638
XBS J141531.5+113156	0.257	$1.85^{+0.02}_{-0.04}$	n.d.	$1.01^{+0.04}_{-0.05}$	$9.13^{+0.17}_{-0.15}$	$-1.06^{+0.05}_{-0.05}$	$-2.55^{+0.18}_{-0.16}$	−1.174	0.043
XBS J144937.5+090826	1.260	$1.81^{+0.07}_{-0.04}$	$1.80^{+0.11}_{-0.10}$	$1.19^{+0.08}_{-0.06}$	$9.50^{+0.07}_{-0.06}$	$0.56^{+0.08}_{-0.06}$	$-1.30^{+0.11}_{-0.08}$	−1.332	0.261
XBS J160706.6+075709	0.233	$2.42^{+0.09}_{-0.08}$	$2.02^{+0.62}_{-0.55}$	$1.40^{+0.06}_{-0.07}$	$7.70^{+0.10}_{-0.11}$	$-1.24^{+0.06}_{-0.07}$	$-1.30^{+0.12}_{-0.13}$	−1.382	0.420
XBS J160731.5+081202	0.226	$2.67^{+0.22}_{-0.13}$	$2.32^{+0.72}_{-0.87}$	$1.74^{+0.09}_{-0.08}$	$6.99^{+0.09}_{-0.11}$	$-1.09^{+0.09}_{-0.08}$	$-0.44^{+0.13}_{-0.14}$	−1.335	0.587
XBS J165406.6+142123	0.641	$1.88^{+0.12}_{-0.08}$	$1.93^{+0.39}_{-0.34}$	$1.61^{+0.13}_{-0.13}$	$8.90^{+0.09}_{-0.10}$	$0.04^{+0.13}_{-0.13}$	$-1.22^{+0.16}_{-0.16}$	−1.478	0.829
XBS J165425.3+142159	0.178	$2.11^{+0.04}_{-0.02}$	$1.97^{+0.13}_{-0.13}$	$0.89^{+0.05}_{-0.04}$	$7.61^{+0.26}_{-0.36}$	$-1.02^{+0.04}_{-0.04}$	$-0.99^{+0.26}_{-0.36}$	−1.124	−0.196
XBS J165448.5+141311	0.320	$1.81^{+0.07}_{-0.04}$	$1.78^{+0.20}_{-0.27}$	$0.81^{+0.02}_{-0.02}$	$8.75^{+0.05}_{-0.06}$	$-0.68^{+0.02}_{-0.02}$	$-1.79^{+0.05}_{-0.06}$	−1.016	−0.540
XBS J205635.7−044717	0.217	$2.40^{+0.10}_{-0.08}$	$1.83^{+0.52}_{-0.73}$	$1.43^{+0.11}_{-0.11}$	$7.60^{+0.10}_{-0.09}$	$-1.01^{+0.11}_{-0.11}$	$-0.97^{+0.15}_{-0.14}$	−1.347	0.497
XBS J213002.3−153414	0.562	$2.06^{+0.13}_{-0.12}$	$2.31^{+0.33}_{-0.30}$	$1.68^{+0.13}_{-0.14}$	$8.53^{+0.08}_{-0.07}$	$0.39^{+0.14}_{-0.13}$	$-0.50^{+0.16}_{-0.15}$	−1.567	1.016
XBS J214041.4−234720	0.490	$2.17^{+0.05}_{-0.05}$	$1.91^{+0.19}_{-0.24}$	$1.46^{+0.10}_{-0.08}$	$9.31^{+0.06}_{-0.06}$	$0.01^{+0.10}_{-0.08}$	$-1.66^{+0.12}_{-0.10}$	−1.400	0.694
XBS J225050.2−642900	1.251	$2.04^{+0.04}_{-0.04}$	$1.93^{+0.12}_{-0.12}$	$1.26^{+0.11}_{-0.11}$	$9.71^{+0.11}_{-0.08}$	$0.69^{+0.11}_{-0.10}$	$-1.38^{+0.16}_{-0.13}$	−1.374	0.457
XBS J231342.5−423210	0.973	$2.14^{+0.08}_{-0.04}$	$2.00^{+0.16}_{-0.15}$	$1.21^{+0.08}_{-0.06}$	$9.12^{+0.11}_{-0.11}$	$0.30^{+0.08}_{-0.06}$	$-1.18^{+0.14}_{-0.13}$	−1.309	0.351

Notes. Column 1: source name; column 2: redshift; column 3: X-ray spectral index between 0.5 and 10 keV; column 4: X-ray spectral index between 2 and 10 keV; column 5: logarithm of the bolometric correction; column 6: logarithm of the BH mass in units of solar masses; columns 7: logarithm of the absolute accretion rate in units of solar masses per year; column 8: logarithm of Eddington ratio; column 9: two-point spectral index; column 10: logarithm of the disc/corona luminosity ratio. All errors are at 68 per cent confidence level (please note that in Corral et al. 2011 the reported errors on Γ are at 90 per cent confidence level).

[a]The X-ray luminosity of XBS J140102.0−111224 reported here is different from the value that appears in Corral et al. (2011) because of a typo discovered in that paper. Therefore, also the derived quantities, like $K_{\rm bol}$, $\alpha_{\rm OX}$ are different from what reported in Marchese et al. (2012).

This paper has been typeset from a TEX/LATEX file prepared by the author.

Downloaded from http://mnras.oxfordjournals.org/ at INAF Brera Milano (Osservatorio Astronomico di Brera) on May 7, 2015

Mem. S.A.It. Vol. 84, 717
© SAIt 2013
Memorie della

The relationship between X-ray emission and accretion in X-ray selected AGNs

R. Fanali[1,2], A. Caccianiga[1], P. Severgnini[1], R. Della Ceca[1], M. Dotti[2], and E. Marchese[2,1]

[1] INAF - Osservatorio Astronomico di Brera, via Brera 28, I-20121 Milano, Italy
[2] Università degli Studi di Milano Bicocca, Piazza Della Scienza 3, I-20126 Milano, Italy
e-mail: rossella.fanali@brera.inaf.it

Abstract. We study the link between the X-ray emission in radio-quiet AGNs and the accretion rate on the central Supermassive Black-Hole (SMBH) using a well-defined and statistically complete sample of 70 type1 AGNs extracted from the XMM-Newton Bright Serendipitous survey (XBS). To this end, we search and quantify the statistical correlations between the main parameters that characterize the X-ray emission (i. e. the X-ray spectral slope and the X-ray loudness), and the accretion rate, both absolute ($\dot{M}$) and relative to the Eddington limit (Eddington ratio, λ). Here, we summarize and discuss the main statistical correlations found and their possible implications on current disk-corona models.

Key words. active galaxies, X-ray properties, accretion rate

1. Introduction

It is now accepted that the engine of AGNs is powered by the accretion of matter onto the SMBH, placed in the center of the host galaxy: the matter is heated ($\sim 10^6$ K) through viscous and magnetic process and forms an accretion disk around the SMBH emitting in the UV-optical region. A fraction of energy is also emitted in the X-ray band with a spectrum that can be represented, at a zeroth order, by a power-law from 0.1 to 100 keV. It is believed that X-rays are produced in a hot corona ($\sim 10^8$ K) reprocessing the primary UV-optical emission of the disk via inverse-Compton mechanism (Haardt & Maraschi 1991). The main properties of X-ray emission change significantly from source to source. Recent results suggest that the differences can be partly related to the value of accretion rate or to the black-hole mass (Grupe et al. 2010, Risaliti et al. 2009, Vasudevan & Fabian 2009). The aim of this work is to establish the actual link between X-ray properties and the parameters that quantify the accretion rate by analyzing a well defined sample of 70 type1 AGNs selected from the XMM-Newton Bright Serendipitous survey (XBS). In this work we study the spectral index Γ between 0.5 and 10 keV and the bolometric correction $K_{\rm bol}$, defined as the ratio between bolometric luminosity and 2 – 10 keV luminosity. Γ gives direct information about the energy distribution of the electrons in the corona, while $K_{\rm bol}$ quantifies the relative importance between disk and corona. The approach followed is to search for statistically

Send offprint requests to: R. Fanali

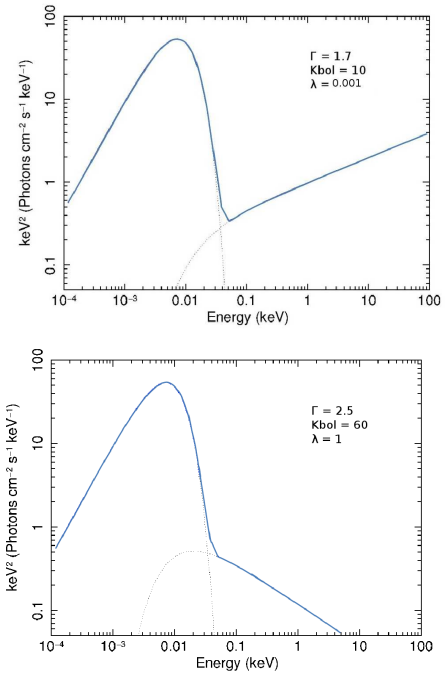

Fig. 1. Theoretical spectral energy distributions that represent two extreme cases of accretion: $\lambda \sim 10^{-3}$ (upper panel) and $\lambda \sim 1$ (lower panel). See text for more details.

significant correlations between these parameters and the value of accretion rate, absolute ($\dot{M}$) and normalized to Eddington limit (λ), presented in (Caccianiga et al. 2013).

2. Results

We find that Γ depends significantly on λ while the dependence on $\dot{M}$ is weak. By using partial correlation we demonstrate that the observed correlations are not induced by redshift. We find a similar $\Gamma - \lambda$ correlation also using the hard $2 - 10$ keV spectral index. Therefore the observed correlation is directly linked to the primary component of the X-ray emission and not due to secondary spectral component (e.g. soft excess). We also find a correlation between K_{bol} and λ while, again, the dependece on $\dot{M}$ is weak. We represent graphically the results of the $\Gamma - \lambda$ and $K_{bol} - \lambda$ correlations by showing the theoretical SEDs in two extreme cases of low and high Eddington ratios (Fig. 1): these SEDs were built using a Shakura & Sunyaev disk model plus a power-law in the range between 0.01 and 100 keV with a cut-off at 0.1 keV. The values of Γ and K_{bol} are taken from our fits of the $\Gamma - \lambda$ and $K_{bol} - \lambda$ correlations.

To simplify the comparison, we assume the same disk emission normalization in both cases. The comparison of the two SEDs suggests that the variation of $K_{\rm bol}$ could be entirely attributed to the variation of Γ. We also test this idea by using the partial correlation analysis and we conclude that the correlations observed in this work can be in principle explained by the $\Gamma - \lambda$ correlation alone. This result suggests a speculative interpretation based on the electron cooling of corona: for high values of λ, a large number of photons comes from the accretion disk and cools corona electrons rapidly, thus poducing steep X-ray spectra and high values of $K_{\rm bol}$. For low λ, less photons are available and this makes electron cooling inefficient, thus producing flat X-ray spectra and low values of $K_{\rm bol}$.

Full details are reported in Fanali et al. (2013).

Acknowledgements. We acknowledge Francesco Haardt for the useful discussions and ASI (grant n. I/008/06/0) for financial support.

References

Caccianiga et al., 2013, A&A, 549, A119.
Fanali et al. 2013, MNRAS, 1400.
Grupe et al. 2010, ApJ, 187, 64.
Haardt & Maraschi, 1991, ApJ, 380, L51.
Risaliti et al., 2009, ApJ, 700, L6
Vasudevan & Fabian, 2009, MNRAS, 392, 1124.